Reconstructing the topography and water level of the Mediterranean Sea during the Messinian Salinity Crisis

Directors:
Dr. Daniel García Castellanos
Dr. Ivone Jiménez Munt

Hanneke Heida

PhD Thesis

Barcelona, 2022

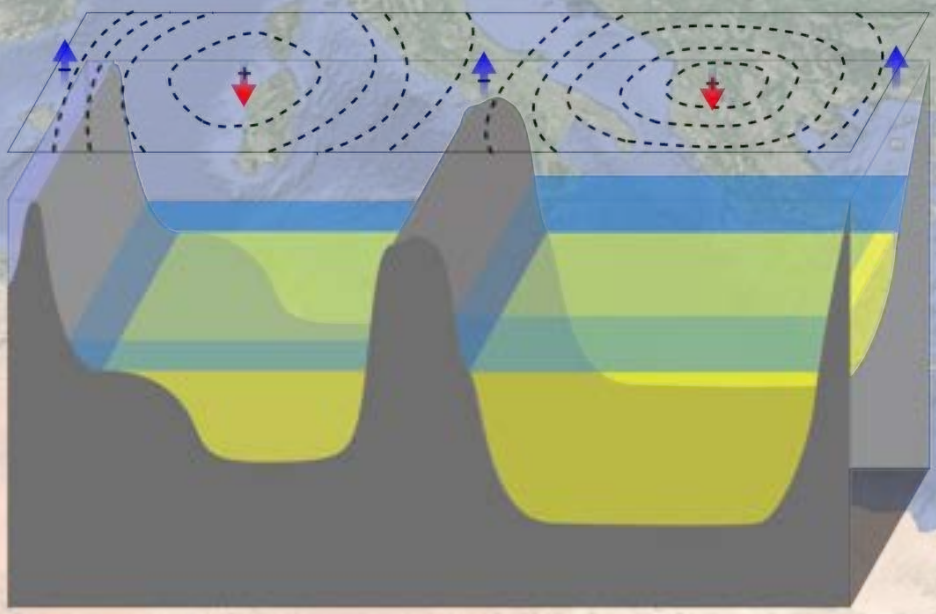

GEO3BCN Geosciences Barcelona - CSIC
CSIC Consejo Superior de Investigaciones Científicas
Universitat de Barcelona

Reconstructing the topography and water level of the Mediterranean Sea during the Messinian Salinity Crisis

Tesis doctoral presentada por

Hanneke Heida

al Programa de Doctorado Ciencias de la Tierra
de la Universitat de Barcelona
para optar al grado de
Doctor en Ciencias de la Tierra

Group of Dynamics of the Lithosphere (GDL)
Geociències Barcelona (GEO3BCN)
Consejo Superior de Investigaciones Científicas (CSIC)

Directores:

Dr. Daniel García Castellanos
Dra. Ivone Jiménez Munt

Tutor
Prof. Dr. Alberto Sáez Ruiz

Barcelona, September 2022

UNIVERSITAT DE BARCELONA

CSIC
CONSEJO SUPERIOR DE INVESTIGACIONES CIENTÍFICAS

GEO3BCN

Reconstructing the topography and water level of the Mediterranean Sea during the Messinian Salinity Crisis

Thesis presented at the PhD program for
Earth Science of the University of Barcelona
to obtain the Degree of
Doctor in Earth Sciences

PhD student: Hanneke Heida

Approved:

Dr. Daniel García Castellanos
GEO3BCN-CSIC, Supervisor

Dr. Ivone Jiménez Munt
GEO3BCN-CSIC, Supervisor

Prof. Dr. Alberto Sáez Ruiz
Universitat de Barcelona, Tutor

Gente di mare che se ne va
Dove gli pare dove non sa
- *Umberto Tozzi*

Summary

During the Messinian Salinity Crisis (MSC, 5.97 – 5.33 Ma), an environmental crisis unparalleled in recent geological history, thick evaporites were deposited in the Mediterranean Basin associated with major erosion of the continental margins. The MSC is thought to have led to a kilometre-scale water level drop by evaporation due to restriction of the Atlantic-Mediterranean marine connection, but the timing and amplitude of this drop have remained controversial. This is due to uncertainty in the post-MSC vertical motions and lack of clear correlations between the marginal and abyssal sedimentary records.

In this thesis I aim at constraining the Messinian water level by way of providing a paleobathymetric reconstruction of the Mediterranean sub-basins and depth estimates for the emplacement of evaporite deposits and erosional markers. I constrain the magnitude of vertical motions induced by the accumulation of evaporite and other sediment units, isostatic and thermal subsidence, and tectonic deformation in three key regions, being: the Alboran Basin, the rest of the Western Mediterranean, and the Nile Delta.

In the Alboran Basin (Chapter 3), erosional terraces were formed originally at a wide depth range. The shallowest terrace is reconstructed to 250-550 m depth, while the deepest terrace has a reconstructed depth range of 750-1500 m. This variation is interpreted as the result of fluctuating water levels during the drawdown phase and to a high-energy basin reflooding event. In the Western Mediterranean (Chapter 4), we use the MSC “Mobile Unit” halite and “Upper Unit” gypsum as markers for paleoshorelines, and we estimate them as having formed at depths of 1500 m and 1100 m respectively. In addition, halite is found in small silled basins originally as shallow as 500 m along the Balearic Promontory, suggesting that halite deposition during the evaporative drawdown spanned a wider depth range than suggested by its current preservation, and was subsequently removed by erosion during subaerial exposure during the drawdown and lowstand phase of the Messinian Salinity Crisis. Physics-based box modelling (Chapter 6) of water and salt fluxes to the Central Mallorca Depression on the Balearic Promontory allow to further evaluate this hypothesis, showing that the gypsum identified in this silled basin could only have formed by overall salinification of the Western Mediterranean at high water level, while the volume of halite suggests that its precipitation started only after the water level had dropped by at least 850 m. Also, the new, smaller, estimate of halite volume in the deep Western Mediterranean is in agreement with precipitation starting at or soon after the onset of drawdown, in contrast to that in the Eastern Mediterranean. In the Nile Delta (Chapter 5) topographical restoration shows the original depth of the geomorphological base level of the Nile River at ~600-m below present sea level, with a 400 m waterfall separating the downstream Messinian canyon from the older upper valley. This baselevel drop is 2-4 times smaller than derived from other criteria for the Eastern

basin, again suggesting fluctuations and diachronism of the MSC erosion episodes between the Western and Eastern Mediterranean.

I show that the bathymetry of the Mediterranean basins was not radically different from the modern day in areas unaffected by fault tectonic deformation or plate subduction. Both the evaporites and the erosional features are found to have formed at a wide range of depths, not clearly linked to a single stable basinwide base level but rather affected by fluctuating water budgets in each subbasin. I propose that these variations in time and between subbasins were driven by variations in runoff from the continent and possibly by the capture of Paratethyan waters, during a stage of complete disconnection from the Atlantic.

Resumen

Durante la Crisis de Salinidad del Messiniense (MSC, 5,97 – 5,33 Ma), una crisis ambiental sin precedentes en la historia geológica reciente, se depositaron gruesas evaporitas en el Mar Mediterráneo asociadas con una gran erosión de los márgenes continentales. Se cree que el MSC provocó una caída del nivel del agua alrededor de un kilómetro debido a la evaporación provocada debido a la restricción en la conexión marina entre el Atlántico y el Mediterráneo. Debido a la incertidumbre en los movimientos verticales posteriores a la MSC y la falta de correlaciones claras entre los registros sedimentarios marginales y abisales, la amplitud de esta caída y su ubicación en el tiempo siguen estando en discusión.

En esta tesis, mi objetivo es determinar el nivel del agua del Mediterráneo durante la MSC proporcionando una reconstrucción paleobatimétrica de las subcuencas mediterráneas y estimaciones de profundidad para el emplazamiento de depósitos de evaporita y marcadores de erosión. Estimo la magnitud de los movimientos verticales inducidos por la acumulación de evaporita y otras unidades de sedimentos, el hundimiento isostático y térmico y la deformación tectónica en tres regiones clave, que son: la cuenca de Alborán, el resto del Mediterráneo occidental y el delta del Nilo.

En la Cuenca de Alborán (Capítulo 3), las terrazas erosionales se formaron originalmente en un amplio rango de profundidad. La terraza menos profunda se reconstruye a 250-550 m de profundidad, mientras que la terraza más profunda tiene un rango de profundidad reconstruido de 750-1500 m. Esta variación se interpreta como resultado de la fluctuación del nivel de agua durante la fase de evaporación y de un evento de inundación de alta energía de la cuenca. En el Mediterráneo occidental (Capítulo 4), utilizamos la halita de la “Unidad móvil” y el yeso de la “Unidad superior” del MSC como marcadores de las paleo-líneas costeras, y estimamos que se formaron a profundidades de 1500 m y 1100 m respectivamente. Además, la halita se encuentra en pequeñas cuencas restringidas originalmente hasta a una profundidad tan poco profundo como 500 m a lo largo del Promontorio Balear, lo que sugiere que la deposición de halita abarcó una profundidad más amplia que el sugerido por su conservación actual y posteriormente fue eliminada por la erosión durante la exposición subaérea durante la fase de descenso y nivel bajo de la crisis de salinidad de Messiniense. El modelo de caja basado en la física (Capítulo 6) de los flujos de agua y sal en la Depresión Central de Mallorca en el Promontorio Balear permite evaluar más a fondo esta hipótesis, mostrando que el yeso identificado en esta cuenca restringida solo podría haberse formado por la salinización general del Mediterráneo occidental en el nivel alto del agua, mientras que el volumen de halita sugiere que su precipitación comenzó solo después de que el nivel del agua había descendido al menos 850 m. Además, la nueva estimación del volumen de halita en el Mediterráneo occidental profundo concuerda con la precipitación que comienza con el inicio de la bajada del nivel del mar, en contraste con la del Mediterráneo oriental. En el Delta del Nilo (Capítulo 5), la restauración topográfica muestra la profundidad original del nivel base

geomorfológico del río Nilo a ~600 m por debajo del nivel actual del mar, con una cascada de 400 m que separa el cañón Messiniense río abajo del valle superior más antiguo. Esta caída del nivel base es de 2 a 4 veces menor que la determinada por otros criterios para la cuenca oriental, lo que nuevamente sugiere fluctuaciones y diacronismo de los episodios de erosión de MSC entre el Mediterráneo occidental y oriental.

Mi trabajo demuestra que la batimetría de las cuencas mediterráneas no fue radicalmente diferente de la actual en áreas no afectadas por la deformación tectónica de fallas o la subducción de placas. Se encontró que tanto las evaporitas como las evidencias de erosión se formaron en una amplia gama de profundidades, no vinculadas claramente a un único nivel base estable en toda la cuenca, sino más bien afectadas por los balances de agua fluctuantes en cada subcuenca. Propongo que estas variaciones temporales y entre subcuencas fueron impulsadas por variaciones en la escorrentía del continente y posiblemente por la captura de aguas del Paratethys, durante una etapa de desconexión total del Atlántico.

Publications

First author publications:

Heida, H., Raad, F., Garcia-Castellanos, D., Jiménez-Munt, I., Maillard, A., & Lofi, J. (2021). Flexural-isostatic reconstruction of the Western Mediterranean during the Messinian Salinity Crisis: implications for water level and basin connectivity. *Basin Research*, *July*, 1–31. https://doi.org/10.1111/bre.12610

Heida, H., Garcia-Castellanos, D., Jiménez-Munt, I., Estrada, F., Ercilla, G., Do Couto, D., & Ammar, A. (Submitted). Paleotopography, sea level drop and erosion in the Alboran Basin during the Messinian Salinity Crisis from a flexural-isostatic reconstruction.

Co-authored publications included in this thesis:

Gvirtzman, Z., Heida, H., Garcia-Castellanos, D., Bar, O., Zucker, E., & Enzel, Y. (2022). Limited Mediterranean sea-level drop during the Messinian salinity crisis inferred from the buried Nile canyon. *Communications Earth and Environment*, 1–10. https://doi.org/10.1038/s43247-022-00540-4

Raad, F., Ebner, R., Heida, H., Meijer, P., Lofi, J., & Maillard, A., Garcia-Castellanos, D. (2022). A song of volumes , surfaces and fluxes : The case study of the Central Mallorca Depression (Balearic Promontory) during the Messinian Salinity Crisis. *Basin Research*, *March*, 1–27. https://doi.org/10.1111/bre.12702

Other co-authored publications not included in this thesis:

Maillard, A., Raad, F., Chanier, F., Heida, H., Lofi, J., Mas, G., & Garcia-Castellanos, D. (2022). Plio-Quaternary strike-slip tectonics in the Central Mallorca Depression, Balearic Promontory: Land–sea correlation. *Tectonophysics*, *829*(March), 229295. https://doi.org/10.1016/j.tecto.2022.229295

Andreetto, F., Aloisi, G., Raad, F., Heida, H., Flecker, R., Agiadi, K., Lofi, J., Blondel, S., Bulian, F., Camerlenghi, A., Caruso, A., Ebner, R., Garcia-castellanos, D., & Gaullier, V. (2021). Freshening of the Mediterranean Salt Giant : controversies and certainties around the terminal (Upper Gypsum and Lago-Mare) phases of the Messinian Salinity Crisis. *Earth-Science Reviews*, *216*(February), 103577. https://doi.org/10.1016/j.earscirev.2021.103577

Table of Contents

The SaltGiant ETN

The work in this thesis was performed within the context of the SaltGiant European Training Network (ETN), a cross-disciplinary network funded by the European Union's Horizon 2020 Research and Innovation Program under grant agreement N°765256. The project kicked off in 2018, centred around 15 PhD projects hosted at 13 different institutions all over Europe (see Fig. 1) across a wide range of topics with the universal aim of bettering our understanding of the Mediterranean Salt Giant.

Other stakeholders in the project were the 17 Partner Organizations in academia and industry responsible for hosting the Early-Stage Researchers (ESR) during trainings and secondments.

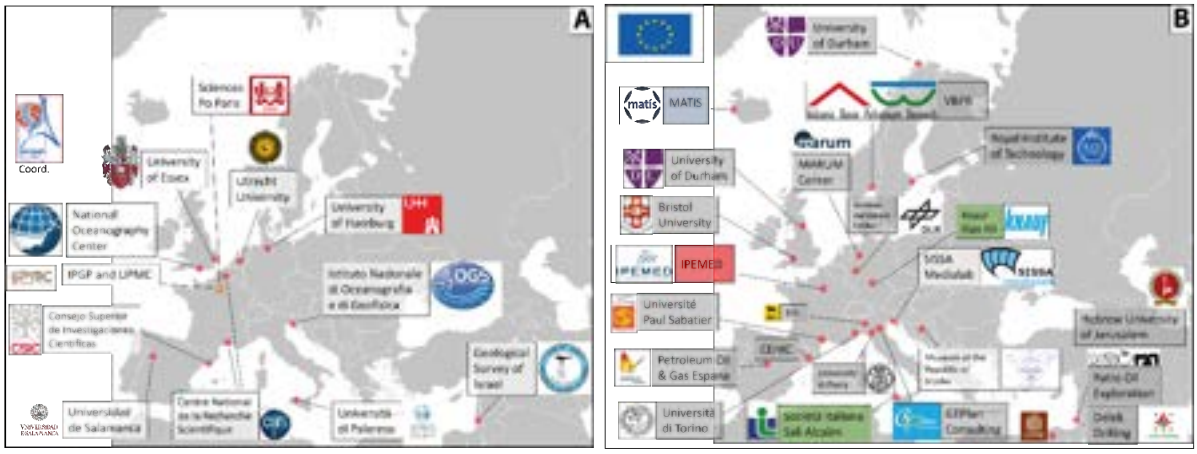

Figure 1. A: Benificiary institutions. B: Partner Organizations.

The project was coordinated by Dr. Giovanni Aloisi at the Institute Physique du Globe de Paris (IPGP), and structured in the following Work Packages (WPs):

WP1 – *Formation of the MSG:* focussed on the development of a unified model for the formation of the MSG through tectonic and hydro-geochemical evolution of the Mediterranean, and providing scenarios for the carbon and sulphur cycling during the MSC. Comprises ESR projects 1 through 7.

ESR 1: Late Miocene-Early Pliocene offshore onshore sedimentary records in the vicinity of Gibraltar

ESR 2: Marginal vertical motions (West. Med. and Levant) – this thesis

ESR 3: Balearic Basin Architecture

ESR 4: Sicilian Basin Architecture

ESR 5: Lago Mare revisited

ESR 6: Hydrology of Mediterranean Marginal basins during the formation of the MSG

ESR 7: Modelling the (bio-)geochemical evolution and circulation of Messinian brine

WP2 – *Deep Life:* aims to explain the development of the exceptional and poorly-understood deep microbial biosphere in the MSG, providing a terrestrial analogue for the hypersaline environments of Mars where life forms might have been preserved and characterize the microbial pathway for the formation of H2S ("sour gas") via the microbial reduction of the mineral gypsum.

ESR 8: The microbial sulphur-cycle in Messinian evaporites

ESR 9: Long-term survival of microbes in halite brine inclusions

WP3 – *Drilling Hazards:* with the goal to develop a mechanistic and quantitative understanding of early salt deformation and sub-salt overpressure development that can be used by the oil industry to mitigate the risks associated with drilling in salt-capped hydrocarbon provinces.

ESR 10: Mediterranean Salt Structures

ESR 11: Salt Tectonics in the Levantine Basin

ESR 12: Overpressure development in rapidly deposited salt basins. Application to the Salt Giant in the Mediterranean Basin

ESR 13: Analogue modelling of combined crustal and Messinian salt deformation in Mediterranean

WP4 – *Geo-Economics and History of Science and Technology:* Provides an integrated history of the discovery of the MSG, which contextualizes early research in this field in relation with paradigm shifts of mid-twentieth century geosciences, international oceanographic and prospecting campaigns and geopolitical tensions in the Mediterranean in the cold war, and a study on the economic and geopolitical implications of the mapping of big salt deposits because of their association with natural gas fields.

ESR 14: Natural Resource Windfalls, Growth and Income Inequality in Small Open Economies - Case Study of the Recent Natural Gas Discoveries in Egypt and the Eastern Mediterranean Region

ESR 15: Salt, Vessels and Maps: the Discovery of the Mediterranean Salt Giant

Through workshops, short courses and field courses organized by the beneficiaries and partner organizations on a wide range of topics valuable training has been provided, as well as a breeding ground for fruitful cross-disciplinary collaboration. The exchange of ideas between people working in geo-, natural and social sciences has greatly contributed to the success of this project.

Chapter 1: Introduction

This work aims at providing new quantitative understanding on the geological processes that led to the accumulation of the most recent salt giant on Earth, during the environmental, ecological and hydrological event known as the Messinian Salinity Crisis (MSC). The MSC has long fascinated the scientific community as it provides a unique opportunity towards deciphering the processes behind the formation of salt giants, as well as their impact on the global ocean and environmental conditions. Key controversies around the MSC remain concerning the timing and magnitude of water level drop, and its relation to salinity and evaporite deposition. By quantifying the vertical motions affecting the Mediterranean basins in response to MSC events and post-Messinian evolution, the original depth of Messinian erosional surfaces and evaporitic materials can be constrained. From the stratigraphic relationships between these erosional features and evaporitic units we can identify plausible paleoshoreline markers, which then inform us on the water level in the Mediterranean subbasins at the time of their formation.

In this Chapter I sketch the current understanding of the geodynamic setting of the Mediterranean Sea and the Messinian Salinity Crisis, the event during which the youngest salt giant on Earth was formed. I lay out the main open questions concerning this crucial stage in Mediterranean evolution and justify the need for paleotopographic reconstructions in the region to address such controversies. A short review of previous work on the topic of topographic and water level reconstructions is also provided.

In the final parts of this Chapter I lay out the objectives and an outline of this thesis.

1.1. The Messinian Salinity Crisis

1.1.1. Geodynamic setting of the Mediterranean Sea

The Mediterranean region, located on the Western end of the Alpine-Himalayan orogenic belt, is a region of astounding tectonic complexity. Containing simultaneously some of the oldest oceanic crust on earth (neotethyan crust of the Eastern Mediterranean, Granot, 2016) and young extensional basins formed in an overall convergent setting (Gueguen et al., 1998; Rosenbaum et al., 2002), it is a region characterized by apparently opposing processes and has been a fascinating natural laboratory towards understanding plate tectonics and ocean circulation processes. Steady convergence of the African and Arabian plates towards Eurasia, and progressive restriction and closure of the marine connection of this remnant of the Neotethys to the global ocean preconditioned the Mediterranean for one of the biggest environmental crises in recent geological history: The Messinian Salinity Crisis (MSC), the event that formed the Mediterranean Salt Giant.

The Mediterranean Salt Giant formed at the end of the Miocene between 5.98 and 5.33 Ma (Krijgsman et al., 1999) and consists of an accumulation of close to a million km^3 of evaporites (Haq et al., 2020). It is a unique example of a relatively young, pristine salt giant, and has fascinated geoscientists for over half a century due to its enigmatic formation relatively recent in geological history, and its many large-scale implications for environmental conditions (Hsü, 1983; see reviews by Ryan, 2009; Roveri et al., 2014a).

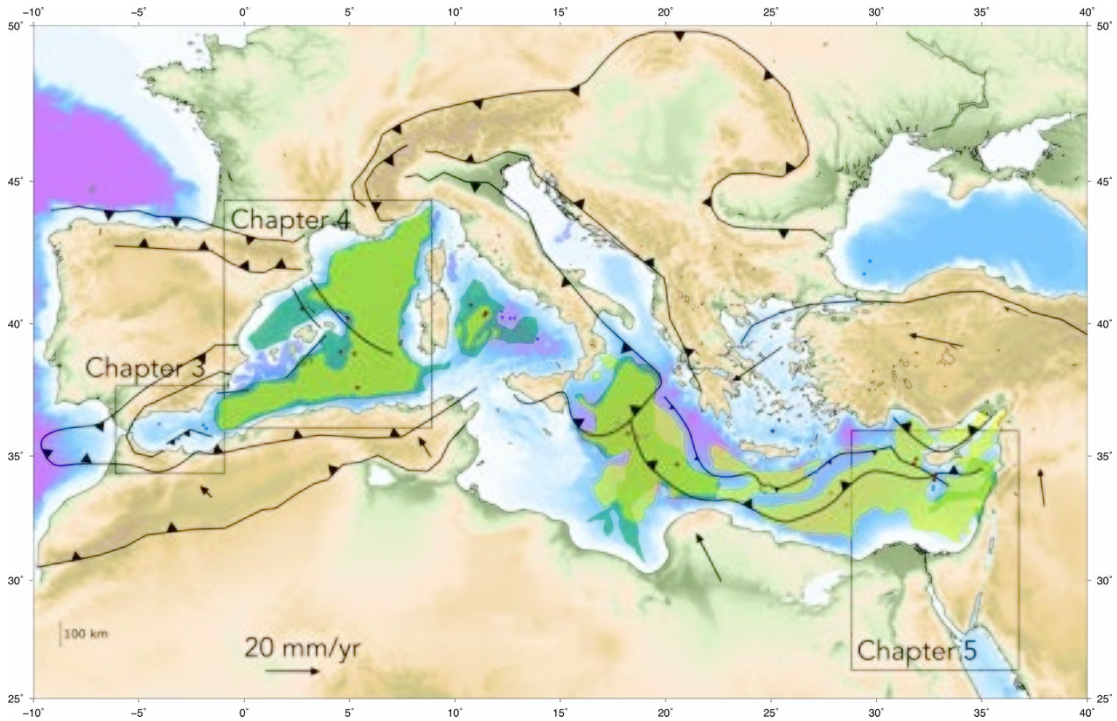

Figure 1.1. Simplified tectonic and bathymetric map of the Mediterranean including plate boundaries from Faccenna et al. (2014), horizontal plate velocities from Serpelloni et al. (2013) and Garcia-Castellanos et al., (2020), Evaporite distribution of halite (yellow) gypsum/anhydrite (green) and Complex (blue) units after Lofi (2018), location of IODP wells with (red) and without (white) Messinian evaporites. The location of the regions reconstructed in Chapters 3, 4 and 5 are outlined.

The Mediterranean Basin formation history is complex, because it encompasses simultaneous alpine compressional orogenic belts and extensional basins. This has been interpreted over the last decades as the result of the subduction of remnants of Neo-Tethyan oceanic crust and subduction-rollback back-arc extension basins formed coevally with various continental collisions (Faccenna et al., 2014). The overall geodynamic setting is that of convergence between the African and Eurasian plates, as a result of a clockwise rotation of Africa relative to Eurasia that amounts to a <4 mm/yr NW relative motion near the Strait of Gibraltar and a >20 mm/yr N motion near the Arabian Peninsula (Fig. 1.1). At the time of the MSC large parts of the Mediterranean had a configuration similar to today, with some notable regional exceptions. The Gibraltar Arc, crucial in the Atlantic-Mediterranean connectivity, had a less pronounced topography having since undergone rapid uplift (Corbí et al., 2017) related to trench retreat of the subducting slab leading to tearing, which has been recorded also in the Alps, Dinarides, Hellenides, and the Tyrrhenian. While most of the Western Mediterranean basins were opened by back-arc spreading well before the Messinian (Vergés and Sàbat, 1999; Faccenna et al., 2014) the Tyrrhenian Basin has undergone a phase of post-Messinian extension and volcanism and was thus narrower and shallower at the time of the MSC. A priori, the eventual fate of the Mediterranean should be its demise as the African and European plates collide, likely preceded by a new closure of the marine gateways and a period of salinification and evaporative water level drop.

Large evaporite deposits are frequent in earths geological history, recent exaples in the Mediterranean vicinity include the Badanian Salinity Crisis (Palcu et al., 2017) affecting the Central Paratethys during the Middle Miocene, and the Dead Sea where a modern evaporite deposit is being formed (see Fig. 1.2 for global distribution and ages of saline giants). They are linked to big events in the Wilson cycle, either by the initial rifting stage or birth of an ocean basin, or to its demise in continental collision and closure through subduction (Warren, 2010). The Mediterranean Salt Giant provides a unique opportunity to study a modern salt giant, formed in a setting of a deep open marine basin that underwent a period of restriction only to later reopen and re-establish its modern normal marine conditions.

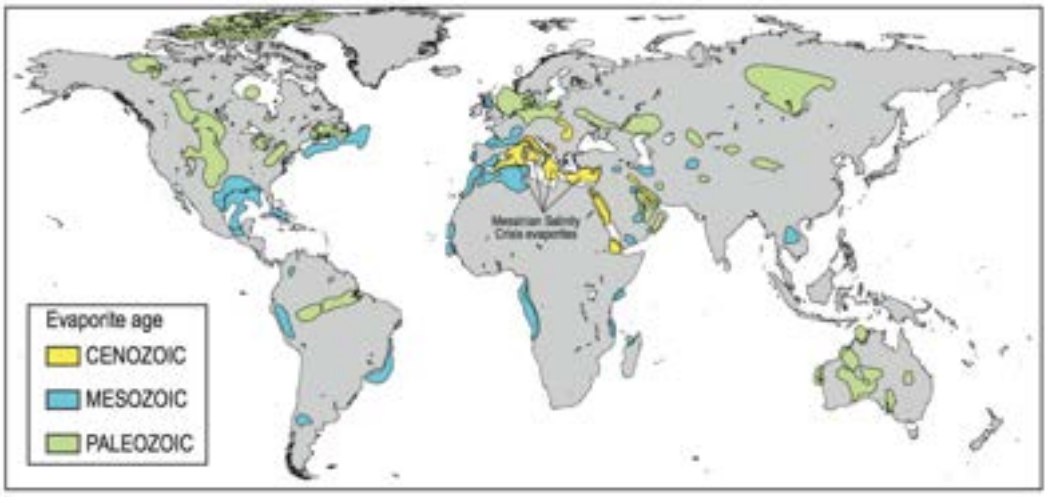

Figure 1.2. Geographical and age distribution of salt giants (modified by J. Lofi from Warren, 2010).

1.1.2. Mediterranean circulation and water budget in a semi-land-locked basin.

In its current configuration, the Mediterranean is connected to the global ocean through two relatively small gateways. The principal connection is at the Strait of Gibraltar, modulating the water and salt budget of the Mediterranean through inflow from the Atlantic to the Mediterranean and a more saline outflow of Mediterranean water that varies tidally. A second connection is human-made: the Suez Canal connecting the Eastern Mediterranean to the Red Sea and subsequently the Indian Ocean. Minimal water exchange takes place through this passageway, although a wider connection is known to have existed during the late Miocene (Ryan, 2008). At the Dardanelles Sill the Mediterranean is connected to the Black Sea, which has a positive freshwater budget, and a two-way exchange provides a net water contribution to the Mediterranean (Özsoy et al., 1996; Ozturk and Altas, 2021). Without the net inflow of marine water through the Strait of Gibraltar, the water level in the Mediterranean would fall drastically due to its negative freshwater budget (expressed as Evaporation minus Precipitation minus River discharge, or E-P-R), the present day value of which is estimated to be between 0.5 and 1.3 m/yr (Meijer and Krijgsman, 2005 and references therein). The net inflow, constrained by the E-P-R value multiplied by the surface area of the Mediterranean to the order of a few thousand km^3/yr compensates for the water lost to evaporation. The average salinity of the Mediterranean (which is slightly higher than that of the Atlantic, and increases West to East, [Sammartino et al., 2022]) is maintained by the export of excess salt ions by the Mediterranean Outflow Waters (Baringer and Price, 1999). Blocking the saline outflow would lead to a steady increase in salinity until saturation is reached for different evaporite minerals (progressively calcium carbonates, gypsum, halite, and potassium or bitter salts). In this scenario, the Mediterranean would act as a salt pan where ion concentration increases as ions are supplied by saline seawater while the water exiting the basin through evaporation contains no ions. Further restriction blocking also the inflow of Atlantic water would lead to the aforementioned evaporative drawdown, initially fast as the E-P-R is large, then slowing down as the surface area and thereby evaporation decreases, until an equilibrium is reached where E-P-R=0 (estimated at >2 km below modern sea level by Meijer and Krijgsman, 2005).

This equilibrium level is dependent on the organization of the various hydrological catchments in the Mediterranean and central Eurasian region, as he R component (River discharge, including also the net contribution of the Black Sea to the Mediterranean) can be heavily affected by changes in the Black Sea and Caspian Sea (formerly Paratethys) region. While the Mediterranean hydrological catchments are relatively limited in size, the Paratethys catchments, consisting of the modern Volga, Danube and Denpr river basins, are large (see Figure 1.3) and subject to wetter climates compared to the Mediterranean. Although in the past large water level drop linked to the MSC has been proposed for most of the Paratethys Basin, the timing and magnitude has been controversial from the moment the first studies were published, and recent review suggests that the Paratethys underwent only minor water level drop and supplied brackish water to the Mediterranean throughout the Lago Mare stage

(van Baak et al., 2017). A simulation of the Mediterranean freshwater budget in the Late Miocene suggested enhanced monsoon runoff in this period in order to explain the formation of sapropels, and proposes that the Chad-Eosahabi river system (see Figure 1.3), that does not currently provide freshwater into the Mediterranean, may have drained into the basin to explain this freshwater contribution (Simon et al., 2017). During the late Miocene, the Mediterranean and Paratethys might be considered an interconnected hydrological system, where water levels and exchanges of water between the basins vary, driven by Mediterranean isolation from the Atlantic and climatic variation. The extent of these combined catchments implies the temporary endorheism of an area spanning over 15 million km^2, over 10% of the globe's continental surface area (see Figure 1.3) during the disconnection between Mediterranean and Atlantic.

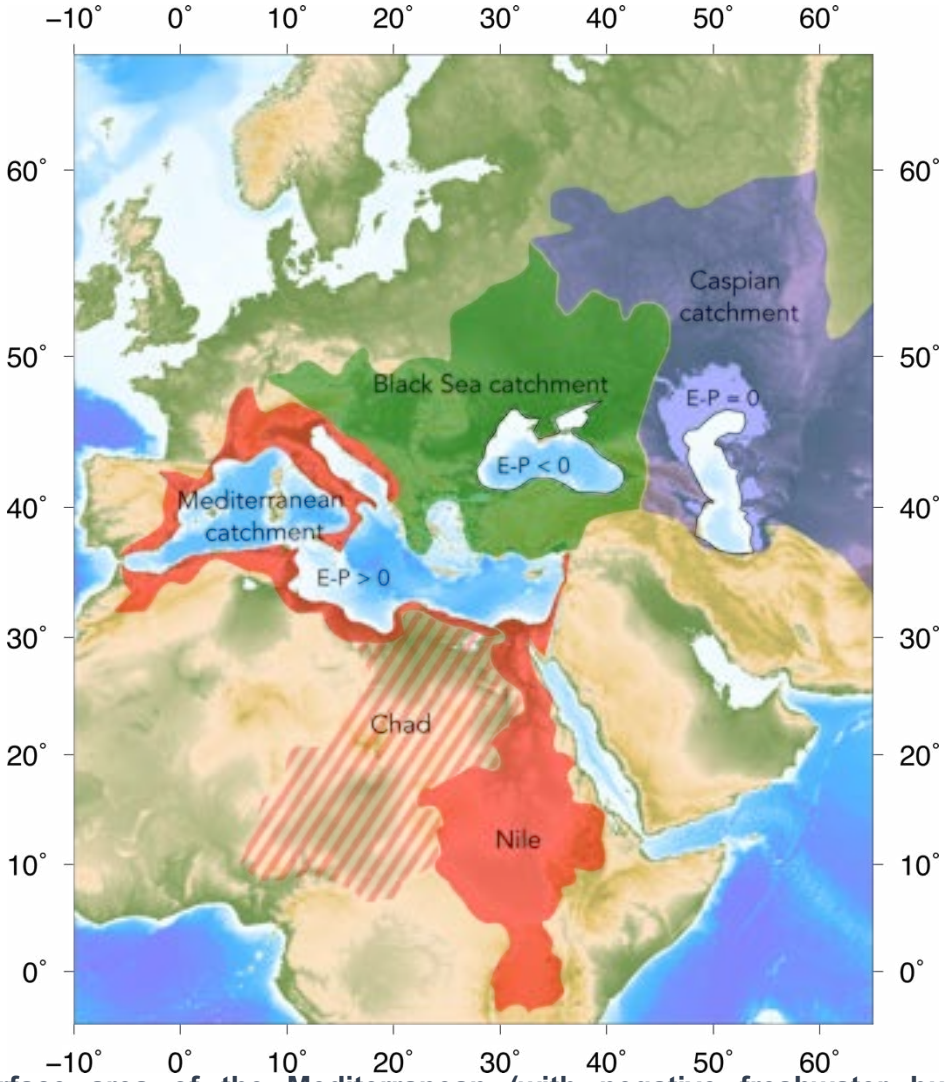

Figure 1.3. Surface area of the Mediterranean (with negative freshwater budget, E-P>0, compensated by Atlantic inflow), Black Sea (positive water budget, E-P<0) and Caspian (neutral water budget or E-P=0) hydrological catchments. The catchments of the Black Sea and Caspian Sea (from van der Baak et al., 2017) together form the catchment for the Miocene Paratethys. The Chad basin (red arced area) does not currently drain into the Mediterranean, but can at times have contributed to the Mediterranean freshwater budget. The total surface area of these basins which would have formed an endorheic system during the Messinian disconnection from the Atlantic Ocean covers approximately 15x10^6 km^3, or roughly 10% of the worlds continental surface area.

1.1.3. The Messinian Salinity Crisis: five decades of controversy.

The Messinian stage was first named by Mayer-Eymar (1867) after the town of Messina, Sicily, Italy. By the 1950s geologists observed the presence of evaporitic deposits of Miocene age surrounding the entire Mediterranean region (Ogniben, 1957; Kozary et al., 1968; Rios, 1968; Tortochaux, 1968; cited in Hsü et al., 1971), leading to the postulation that the Mediterranean had passed through a stage of isolation from the Atlantic or a *Messinian Salinity Crisis* (Selli, 1960) although the true extent of this crisis was not yet within the realm of imagination at that time. Besides the onshore marginal deposits, the presence of salt domes offshore was revealed by diapiric structures in seismic profiles in the 60's (Hersey, 1965). The age and formation process of this salt was not well understood, though prior to direct sampling of the basin, two popular models were proposed (Ryan, 2009):

i. Deposition in shallow rift valleys; or
ii. Precipitation in deep depressions separated from the external oceans

These models did not envision deposition of salt in an already deep, marine domain, but rather more local, restricted depressions prior to the formation of the Mediterranean.

It was during the first Mediterranean drilling campaign of the international Deep Sea Drilling Project in 1971 led by Kenneth Hsü and William Ryan (Hsü et al., 1971) that the hitherto mysterious "M reflector" (a ubiquitous erosional unconformity observed in many of the Mediterranean seismic surveys) was confirmed to be the base of the Pliocene marine sediment and the top of a vast evaporite deposit in the deep Mediterranean basins. In addition to this stratigraphic relationship, the drilling also discovered the presence of nodular anhydrite today only found in *Sabhka* environments, desiccation cracks, and gravels containing carbonates and anhydrite with a marine origin suggesting exposure of the shelf areas.

It was during this drilling campaign, rivetingly described by Kenneth Hsü in his book *The Mediterranean was a desert* (Hsü, 1983) that the idea of a deep, desiccated Mediterranean desert (see Figure 1.4) floored by a salt plain situated kilometres beneath the level of the global oceans was born, igniting a flood of scientific interest in this impactful event in recent geological history. This "deep-basin, shallow water" model was partially ignited by the description of a km deep incised fluvial network of the Rhône Valley extending over 300 km into France (Denizot, 1952), and a similar discovery along the Nile valley (Chumakov, 1967).

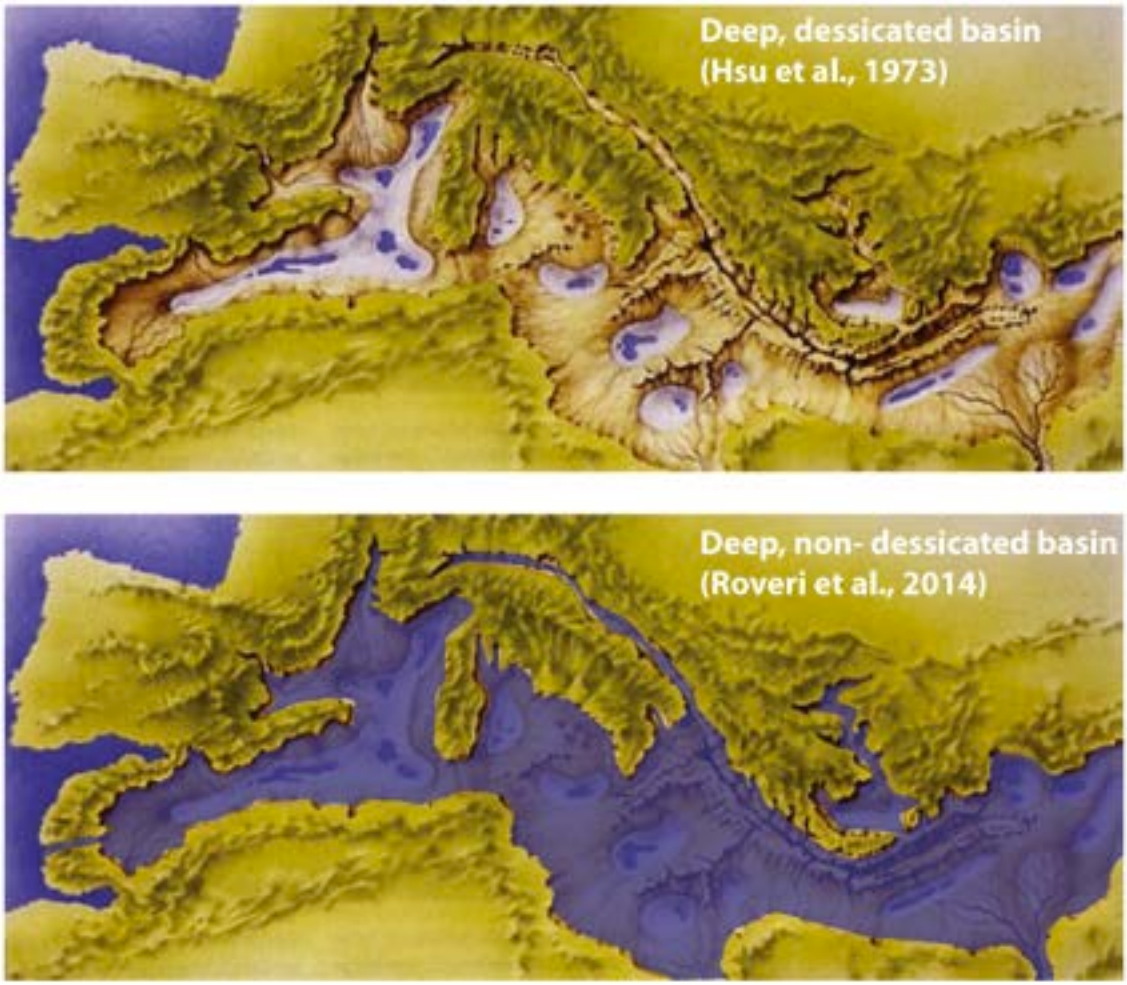

Figure 1.4. Cartoon depicting two initially proposed MSC scenarios for the deposition of the Mediterranean Salt Giant. Top panel: evaporite formation under a 1500 m sea-level drop, or the "deep-basin, shallow water" model; bottom panel: deposition with normal sea-level, or the "deep-basin, deep water" model. Modified after "The First Eden: The Mediterranean World and Man" by David Attenborough (1987). From: Krijgsman et al. (2018).

Although the idea of a closure of the Atlantic-Mediterranean connection causing the desiccation and deposition of evaporites seemed an elegant and simple model to explain the initial observations, controversy soon crept into the community of scientist dedicated to solving the mystery of the Messinian Salinity Crisis. From mapping of the Mediterranean Salt Giant it became obvious that the amount of salt was far too large to have been deposited from a single evaporation event of normal marine waters, as the salt layer was thought to be kilometres thick in places (Hsü et al., 1973), while the evaporation of 2-3 km of water would only yield an evaporite layer ~50 m thick. Thus, either a succession of evaporation and refilling events or a highly saline brine formation at high water level before desiccation would be required to explain the observed salt volume. A first attempt to estimate the total volume of salt, extrapolated from thickness reported by Montadert et al., (1978) yielded a volume of over 3.5 million km^3 (Blanc, 2006). Later, a more detailed investigation based on a compilation of reflection profiles yielded a volume of about 2 million km^3 (Ryan, 2008), and the most

recent estimate by Haq et al. (2020) reduces the total evaporite volume even further to between 0.82 and 0.93 million km^3. Still, this estimate constitutes about 5% the salt content of the global oceans.

In the wake of the IODP Leg 13 expedition, extensive study of the onshore MSC deposits gave rise to a number of arguments against the desiccation theory. In marginal basins (such as the Chelif and Vera basins) the evidence for a substantial water level drop recorded in the stratigraphy in the form of subaerial erosion is scarce and disputed, and the genesis of the marginal evaporites could be envisioned as evaporative salinification of a full Mediterranean basin (Ryan, 2009). Recently, several studies have cast doubts on the validity of the deep desiccation theory by suggesting that the deep evaporitic facies and the erosional morphological features may have been produced without a significant drop of the Mediterranean Sea level, therefore promoting the persistence of a relatively deep-water Mediterranean basin even during halite deposition, or a deep-basin, deep water model (Roveri et al., 2009; Lugli et al., 2013, 2015; Vasiliev et al., 2017; García-Veigas et al., 2018). For example, in the Sorbas Basin the Terminal Carbonate Complex is suggested to record continuous sedimentation throughout the MSC and only moderate sea-level fall (Roveri et al., 2009). Alternative (non-subaerial) formation of the erosional surfaces observed in the seismic record by submarine canyons has been proposed (Roveri et al., 2014b).

A fundamental obstacle towards the development of an integrated MSC chronology has been the physical disconnection between the onshore deposits and the offshore succession. While the onshore deposits have been studied in great detail and are able to provide a host of insights on the local environmental conditions during their deposition, they represent a small fraction (<5%) of the total volume of MSC deposits. The offshore sequence represents the bulk of the evaporite volume, and contains a more continuous record of the MSC as it was more protected from subaerial exposure during the crisis events. It has not been directly sampled beyond its topmost layer in the Western Mediterranean, and shows distinct variations between the Western, Central and Eastern Mediterranean subbasins.

Several attempts at arriving at a comprehensive model for the MSC integrating onshore and offshore data have been undertaken over the years (CIESM, 2008; Ryan, 2009; Roveri et al., 2014a), based on the original two-stage model by Clauzon et al. (1996) leading to the formulation of a “consensus model” dividing the MSC events into three stages:

- Stage 1 (5.97 – 5.60 Ma): Synchronous onset of evaporite deposition, recorded in up to 16 precession-driven cycles of gypsum-marl alternations in shallow/marginal basins known as the Primary Lower Gypsum (PLG) (Lugli et al., 2010).
- Stage 2 (5.60 – 5.55 Ma): Thick halite is deposited in the deep basins (Mobile Unit or MU) associated with a significant drop in water level or desiccation, the amplitude of which is highly debated. On the margins, erosional surfaces form and PLG deposits are eroded and redeposited as Resedimented Lower Gypsum (RLG)(Roveri et al., 2006)
- Stage 3 (5.55 – 5.33 Ma): divided into sub-stages 3.1 (5.55 – 5.42 Ma) with deposition of Upper Gypsum (UG) in the marginal basins and the Upper Unit also containing

gypsum/anhydrite (UU) in the deep basins (Rouchy and Caruso, 2006) and 3.2 (5.42 – 5.33 Ma), the *Lago Mare* stage of brackish water conditions marked by fauna of Paratethyan affiliation (Stoica et al., 2016).

The questions regarding the magnitude and duration of the Mediterranean water level drop are closely related to the original depth at which salt deposits and erosional features where formed. However, many interpretations so far missed a basic estimation of the isostatic compensation of post-MSC basin fill and compaction of sediment, and hence the estimates of the water level drop yield a wide range of uncertainty and their internal consistency is difficult to resolve.

In this thesis I provide a new assessment of into the configuration of the Mediterranean basins during the MSC, their original depth and connectivity, and the vertical and horizontal distribution of MSC markers in the form of evaporite deposits and erosional surfaces. This is done by restoring erosional and depositional MSC markers to their original depth through quantitative estimation of subsidence and uplift due to isostasy, tectonic processes, and sediment compaction since the onset of the MSC. The results imply variations in water level and over time and between sub-basins, and I propose a model where water level in each sub-basin is controlled by freshwater budget changes due to climate variations and reconfiguration of catchments while the Mediterranean is fully disconnected from the Atlantic until restoration of normal marine conditions at the base of the Pliocene.

1.1.4. Review of previous topographic reconstructions and water level estimates.

The erosional surfaces and evaporite deposits observed in the basin from borehole and reflection seismic data are found buried underneath hecto- to kilometric-scale thicknesses of post-Messinian sediment, and in some regions have been strongly affected by tectonic processes since the MSC. In order to understand the implications of the presence of such features for Messinian water levels, their original depth must be constrained. Here I give a brief overview of the results of previous work on regional or local scale, based on various techniques restoring the original geometry of MSC-related features.

A number of studies have previously quantified the base level during the MSC lowstand by compensating for the isostatic vertical motion since the Messinian to obtain the original depth of erosional features and Messinian deposits. In the Western Mediterranean the first backstripping analysis was performed by Ryan (1976) in the Gulf of Lions based on borehole data and seismic sections, and accounting for isostasy and the thermal history of the basin. This resulted in an early Pliocene bathymetry of 2500 m at the Rhône Delta, which is considered subaerially exposed during the crisis acme (Denizot, 1952). A minimum estimate of 400 m base-level drop is provided by Martinez et al., (2004) based on the modern relief on the MES in a 3D seismic dataset in the Ebro delta although this topography is not restored for isostatic subsidence. Urgeles et al., (2011) derived a drop of 1300 m based on changes in

fluvial network characteristics in a 3D seismic dataset in the same region, restored for post-MSC sediment accumulation. Mas et al. (2018) arrive at a minimum base-level drop of 800-1200 m in order to allow for the observed terrestrial colonization of the Balearic Islands during the MSC based on backstripping of a 2D section across the Balearic promontory.

In the Adriatic foredeep and Po plain, tectonically reconstructed pseudo-3D backstripping fitting modelled paleoshorelines to the coastal wedge position, fluvial network and the Messinian Erosion Surface resulted in a best fit for a base-level drop of 850 m (Amadori et al., 2018). The restored topography of the area suggests that it consisted of at least two hydrologically distinct subbasins during the lowstand stage of the MSC.

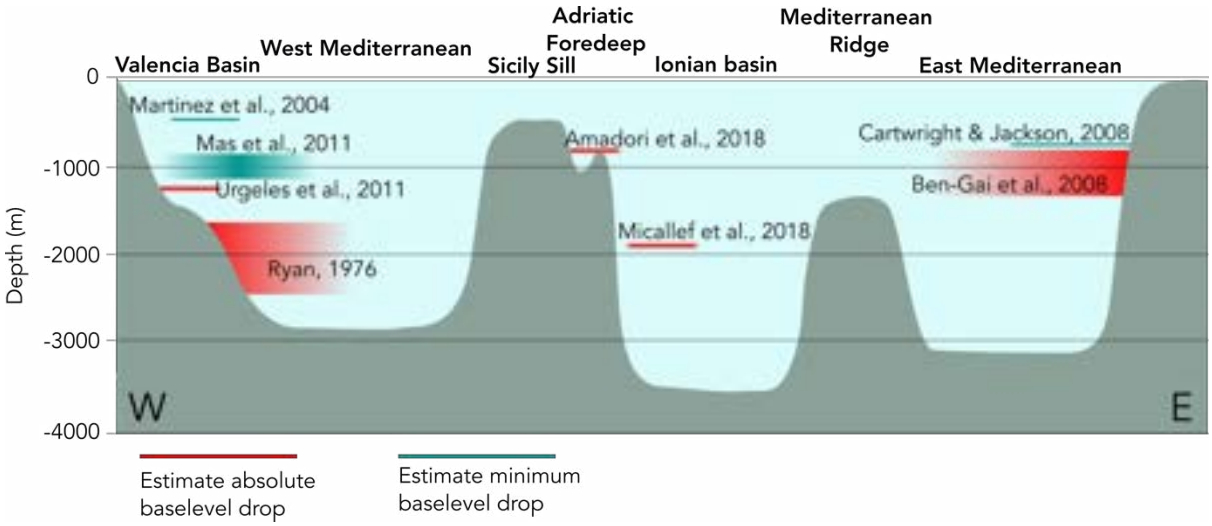

Figure 1.5. Water level drop estimates from previous studies across the Western and Eastern Mediterranean, based on isostatic reconstructions, morphology of erosional features, and forward modelling.

A first quantitative estimate of Messinian base-level in the Eastern Mediterranean was obtained from a deep erosional channel under the Nile delta, which when corrected for isostatic load of the Pliocene and Quaternary fill was found to form at a depth of 3.5-4 km below the present sea level (Ryan, 1978), although the subaerial nature of this horizon and its marine infill inland is disputed (Roveri et al., 2014a). In this work, the Nile Canyon will be revisited in Chapter 5 providing an updated base-level estimate for this erosional feature. In the Levant Basin, a wealth of data has allowed for analysis by a wide range of approaches. A forward modelling approach assuming shallow water-deep basin evaporite deposition yielded a range of 800-1300 m of base-level drop (Ben-Gai et al., 2005). Flexural and Airy backstripping applied to the Levant margin to reconstruct the seafloor depth before and after deposition of Messinian evaporites, resulted in paleodepths of ~2000 m (Tibor and Ben-Avraham, 2005) and 1500 m (Netzeband et al., 2006) in the deep basin, but as no shoreline information is incorporated the absolute drawdown magnitude cannot be estimated. Cartwright and Jackson (2008) combine relief measurements from the frontal scarp of the margin and the Ashod and Afiq canyons to arrive at a base-level drop of 800 m before evaporite deposition. They use independent constraints on sea-level and bathymetry rather than simple isostasy, as the Levant has been subject to tectonic uplift since the Messinian.

Just east of the Sicily Sill, Micallef et al. (2018) applied a backstripping approach to landforms comprising a dense fluvial network, where slope breaks and terraces were assumed to represent paleoshorelines buried on the Malta escarpment. They arrive at a 1800-2000 m water level drop in the Ionian basin.

The timing of Mediterranean sea-level fall relative to MSC stratigraphy has remained ambiguous (Ryan, 2009). A two-step base level fall in the Western basin was proposed, with the thick evaporites of the Mobile Unit and Upper Unit forming respectively during and immediately after the second event (Blanc, 2000; Lofi et al., 2005). Many authors converge on placing the maximum sea-level fall at the end of the deposition of the Mobile Unit in the deep western and eastern Mediterranean basins (Bertoni and Cartwright, 2007; Ryan, 2009; Lofi et al., 2011b) i.e. during of MSC Stage 2. Other authors (i.e. Bache et al. 2009, 2012) consider the whole deep basin evaporitic suite as having been deposited after the main sea-level drop, based on the seismic facies of the Lower Unit in the West Mediterranean which they interpret as the detrital product of margin erosion, requiring a continuous input of marine waters to an almost desiccated basin (Krijgsman and Meijer, 2008).

1.1.5. Motivation of this thesis

The large spread in drawdown estimates in all areas of the Mediterranean (see Fig. 1.5) suggest that a single drawdown of uniform and constant depth is not consistent with the current knowledge of the Messinian sequences spread throughout the basin. There is also a poor constraint om the potential for evaporite deposition in isolated basins, as the hypsometry of the Mediterranean during the MSC is not well known. The development of regional topographic reconstructions, taking into account the timing of formation of various Messinian evaporite units and erosional surfaces, can aid towards a better understanding of the MSC.

1.2. Objectives

The Messinian Salinity Crisis has provoked many decades of debate centred around the depositional environment and water level during the formation of the Mediterranean Salt Giant and associated sediment units. Although large achievements have been made regarding the chronology, mechanisms and stratigraphic relationships of the MSC sedimentary record, solid constraints on the Mediterranean water level evolution throughout the MSC are largely based on local studies addressing single (usually erosional) features, and results show limited internal consistency (see section 1.1.4). In order to better understand the progression of the MSC and the impact on the peri-Mediterranean environment, regional scale studies are crucial.

The objectives of this thesis can be summarized as follows:

1. Quantitively constrain vertical motions affecting the Mediterranean Basins during and after the MSC, to obtain a better understanding of the Mediterranean paleobathymetry and connectivity between subbasins. From the restored Messinian topography, we can investigate the relationships between basin hypsometry and the volume of evaporite deposits. Such relationships can clarify whether ion sources were necessary during the evaporite formation stage or whether the evaporites could have been formed from a completely disconnected basin.
2. Match suspected paleoshoreline indicators from the sediment/seismic record to water levels in the reconstructed bathymetry, quantitatively constraining the drop in water level required to form these features by subaerial exposure. This provides a constraint on the environmental conditions during the MSC, and allows for comparison of the water level both between different sub-basins and over time, as the different sedimentary and morphological features used as paleoshoreline markers can be linked to different stages of the MSC.
3. Connect the results obtained in the Alboran, Western Mediterranean and Nile Delta regions and synthesize a general model explaining my observations. Placing these results in the broader context of the MSC we can further constrain the mechanisms and timing of salt precipitation, the required water budgets and sources, temporal variations and imagine promising lines of investigation for furthering our understanding of the MSC.

In addition to these quantitative reconstructions of basin geometry and water levels, Chapter six shows how these reconstructions can be used to perform better constrained modelling studies of the MSC. Using the restored Messinian hypsometry of the Balearic Promontory and the Western Mediterranean, as well as the depth of marine channels, the salinity, water level and connectivity of the Central Mallorca Depression during the first and second stages of the MSC are investigated.

1.3. Outline

This work is organized as follows:

Chapters 1 and 2 (Introduction and Methods) provide context for the open questions surrounding the Messinian Salinity Crisis and the need for topographic reconstruction in the Mediterranean, and an introduction to the methodology used in subsequent chapters.

Chapters 3, 4 and 5 are focussed on reconstruction of the Messinian paleotopography and the vertical motions caused by MSC-related events, including water level estimates from the reconstruction of paleoshoreline markers.

Chapter 3 is dedicated to the Alboran Basin, a region crucial in deciphering MSC events due to its position at the Atlantic-Mediterranean gateway. Although thick MSC deposits are absent in this basin, the erosional surface excavated during the lowstand and reflooding of the basin bears features of great interest for topographic restoration. This Chapter also investigates whether the Messinian gateway could be positioned in the Alboran Volcanic Arc east of the basins main depocenter, instead of in the Gibraltar Arc region as generally assumed. Results from this chapter a have been submitted for publication and is currently undergoing peer-review (Heida et al., Submitted).

> **Heida, H**., Garcia-Castellanos, D., Jiménez-Munt, I., Estrada, F., Ercilla, G., Do Couto, D., & Ammar, A. (Submitted). Paleotopography, sea level drop and erosion in the Alboran Basin during the Messinian Salinity Crisis from a flexural-isostatic reconstruction.

Chapter 4 focuses on the Western Mediterranean subbasins, with special focus on the Valencia Basin where the stratigraphic record allows for the identification of MSC related paleoshorelines, and on the Balearic Promontory where a unique MSC record of halite deposited at a wide range of depths is found. Chapter 4 has been published in *Basin Research* (Heida et al., 2021):

> **Heida, H**., Raad, F., Garcia-Castellanos, D., Jiménez-Munt, I., Maillard, A., & Lofi, J. (2021). Flexural-isostatic reconstruction of the Western Mediterranean during the Messinian Salinity Crisis: implications for water level and basin connectivity. Basin Research, July, 1–31. https://doi.org/10.1111/bre.12610

Chapter 5 presents a reconstruction of the Nile Delta region, where a reinterpretation of the Messinian Nile Canyon allows for the identification of a paleoshoreline indicator in a knickzone in the channel profile. This work provides a new perspective in the well-known incision of the Nile Canyon. The results presented in this chapter have been published in *Communications Earth and Environment* (Gvirtzman et al., 2022):

> Gvirtzman, Z., **Heida, H**., Garcia-Castellanos, D., Bar, O., Zucker, E., & Enzel, Y. (2022). Limited Mediterranean sea-level drop during the Messinian salinity crisis inferred

from the buried Nile canyon. *Communications Earth and Environment*, 1–10. https://doi.org/10.1038/s43247-022-00540-4

Chapter 6 builds on the paleotopographic results in the Western Mediterranean, applying hydro-geochemical box modelling to the Messinian evaporite succession observed in the Central Mallorca Depression. This chapter dives into quantitative constraints for salinity and water levels during evaporite deposition. This work has been published in *Basin Research* (Raad et al., 2022):

Raad, F., Ebner, R., **Heida, H**., Meijer, P., Lofi, J., Maillard, A. and Garcia-Castellanos, D. (2022), A song of volumes, surfaces and fluxes – The case study of the Central Mallorca Depression (Balearic Promontory) during the Messinian Salinity Crisis. Basin Res. Accepted Author Manuscript. https://doi.org/10.1111/bre.12702

In Chapter 7 (Discussion) I aim to tie together the water-level results obtained in Chapters 3-6 and to explore how these results point towards a general model for the progression of the MSC, and which mechanisms and timing of events could provide an explanation for the distribution of Messinian evaporites and erosional features.

Chapter 8 recaps the main conclusions of this work.

Chapter 2: Methods for the reconstruction of Messinian topography and water level

In this Chapter I will introduce the fundamental concepts at the base of our flexural-isostatic reconstructions, as well as the numerical method used to obtain the results presented in this work. I will explain the basic concepts applicable to all regions presented in this volume, while region-specific modelling workflows are further elaborated on in respective Chapters. Here I also comment on the identification of target regions and potential MSC-related paleoshorelines. The methodology of box-modelling applied in the Chapter 6 is briefly discussed.

2.1. Isostasy and Lithospheric Flexure

2.1.1. Local Isostasy

Isostasy, one of the fundamental concepts in solid earth science, describes the Archimedes equilibrium state of the crust and mantle when not disturbed by forces acting on the surface. In this equilibrium state, the lighter crust floats on the denser mantle with the elevation of the surface being determined by their respective thicknesses and densities, and the pressure at the base of the certain depth in the mantle (the "depth of compensation", see Fig. 2.1) is uniform across different regions. At compensation depth, the pressure underneath a mountain ridge is the same as underneath an oceanic basin, and elevation and gravity data can be used to infer information about thickness and density of the lithosphere. Geological

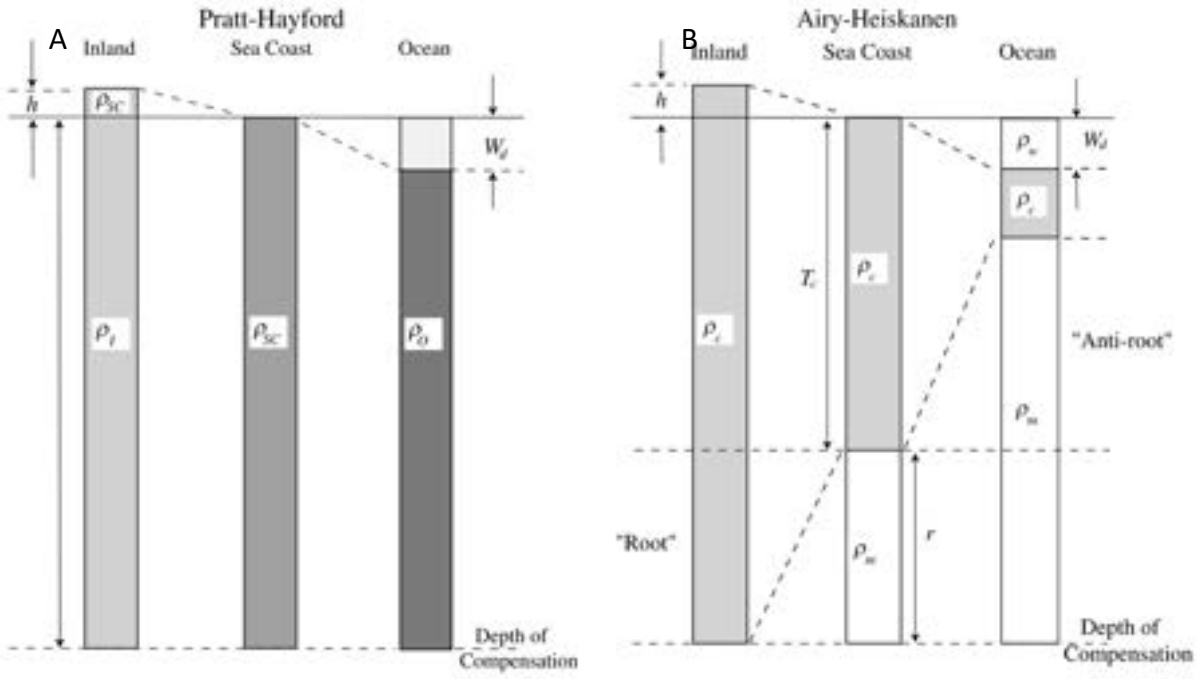

Figure 2.1. A: The Pratt-Hayford model of local isostatic compensation. Reproduced from Hayford (1909), Fig 1.17 from Watts (2001). B: The Airy-Heiskanen model of local isostatic compensation. Fig. 1.18 from Watts (2001).

processes such as mountain building, erosion and surface transport, volcanism and even the waxing and waning of ice sheets disturb this equilibrium state by altering the surface load. The concept of isostasy was developed over the course of the 19th and 20th centuries, leading to the development of theories of isostasy based on two fundamentally different ways in which such variations are compensated.

The Pratt-Hayford model (Fig. 2.1A) assumes that topographic features are underlain by regions of different density, so that the pressure at the compensation depth is equal for different regions (Hayford, 1909). This implies that the density of oceanic crust (underlying topographic basins and thus consisting of a column of smaller thickness) is higher than that at sea level, while the positive topography of mountain ranges is underlain by crust of lower

density (Watts, 2001). While this model was very effective at explaining geodetic observations in the United States, it assumes a base crust at a constant depth, it does not offer a mechanistic explanation for how a disturbance of isostasy can be restored. The topography is driven by the density of the crust, but the density of the crust cannot adjust to restore isostatic equilibrium after a change to surface loading by erosion or sedimentation.

In contrast, the Airy-Heiskanen model (Fig. 2.1B) assumes that mountains and ocean basins are underlain by crust with uniform density, where isostasy is reached by the formation of a crustal "root" under a mountain range where the lower density crust compensates for the excess mass of the mountain range, and a thinned crust or "anti-root" with higher density mantle compensated for mass deficiency at ocean basins. In this model, changes in the surface load are compensated by sinking of the crust into the mantle (subsidence) or a rise of the crust-mantle boundary (uplift/rebound) to restore isostatic equilibrium.

The Airy-Heiskanen model offers a useful first-order approach towards understanding the response of the crust to surface load changes due to its buoyancy relative to the underlying viscous mantle. It is controlled by the density contrast between the crust, mantle, the load being added or removed and the environment (being air or water).

When restoring the Messinian paleotopography, there are two basic load types that we consider:

- Accumulating sediment or evaporites in water;
- Changes in water depth due to evaporative drawdown

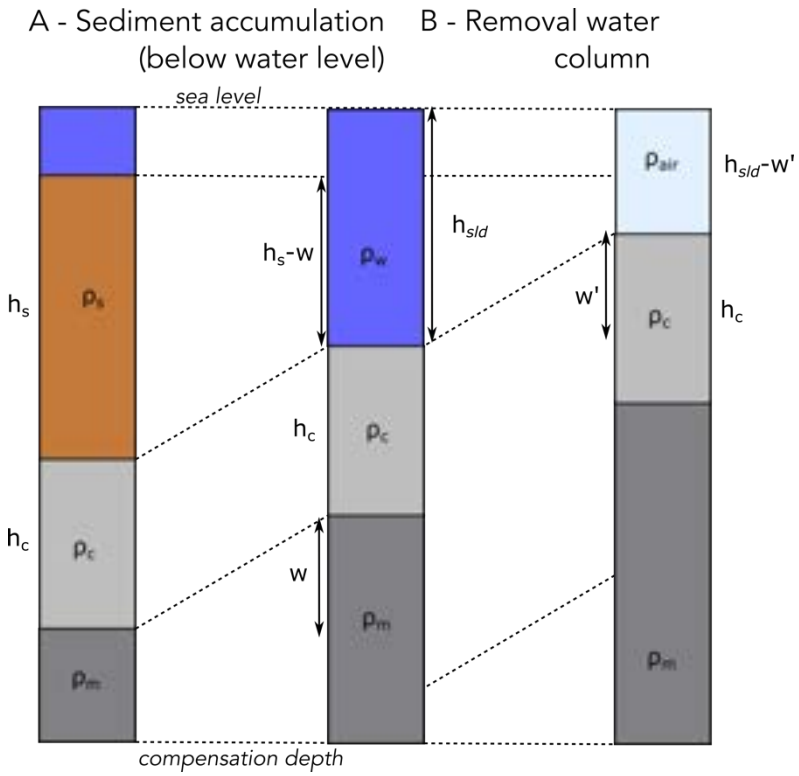

Figure 2.2. Isostatic deflection for each modelling step under local isostasy. A: Deflection due to sediment accumulation calculating by unloading the sediment. B: Deflection resulting from water level drop.

For the accumulation of sediment and evaporites under sea level the following relationship exists (Fig 2.2, local isostasy adopted):

$$h_s \cdot \rho_s + h_c \cdot \rho_c = (h_s - w) \cdot \rho_w + w \cdot \rho_m + h_c \cdot \rho_c \quad (2.1)$$

$$w \cdot \rho_m - w \cdot \rho_w = h_s \cdot \rho_s - h_s \cdot \rho_w \quad (2.2)$$

$$w \cdot (\rho_m - \rho_w) = h_s \cdot (\rho_s - \rho_w) \quad (2.3)$$

$$w = h_s \cdot \frac{(\rho_s - \rho_w)}{(\rho_m - \rho_w)} \quad (2.4)$$

While when calculating the isostatic response to a drop in water level (where h_{sld} is the height of the water column being removed) deflection (uplift/rebound) of the seafloor is related to the thickness of the removed water column as follows:

$$h_{sld} \cdot \rho_w = w' \cdot \rho_m + (h_{sld} - w') \cdot \rho_{air} \quad (2.5)$$

$$w' = h_{sld} \cdot \frac{\rho_w - \rho_{air}}{\rho_m - \rho_{air}} \quad (2.6)$$

Where:

w = subsidence due to sediment accumulation

w' = rebound due to sea level drop

ρ_w = water density (1030 kg/m^3)

ρ_m = mantle density (3250 kg/m^3)

ρ_{air} = air density (0 kg/m^3)

ρ_s = sediment/evaporite unit density

h_s = sediment thickness

h_{sld} = is the magnitude of water level drop

These relationships provide a first idea of the magnitude of vertical motions in response to the surface load changes during and after the MSC assuming local isostasy.

Isostasy has also played an important role in the development of models for the evolution of both ocean basins (Parsons and Sclater, 1977) and basins formed over extended continental crust (McKenzie, 1978) as they age and cool. Essentially, changes in density as hot, buoyant material cools and compacts affect the elevation of young basins, leading to a significant

amount of thermal subsidence in the first few Myr after the opening of a basin. In Chapters 3 and 4, I use these models to constrain the component of thermal subsidence that occurred after the Messinian in relatively young parts of the Mediterranean where post-extensional cooling could constitute a significant component of post-MSC vertical motions. For a more detailed description of the calculation of thermal subsidence, see the Methods sections of the respective chapters.

2.1.2. Flexure

Isostasy assumes that any surface load is completely compensated by displacement of mantle material to reach a situation of equilibrium, and that the crust has zero strength laterally supporting surface loads. In reality, the crust has a load-bearing capacity which will (partially) support surface loads over geological timescales. In this work, we assume that the behaviour of the lithosphere can be approached as a linearly elastic thin plate, in which strain is proportional to stress. When the dimensions of sedimentary basins and surface loads are much larger than the vertical thickness of the crust or "elastic plate", as in the case in the Mediterranean, where basin width and length exceed hundreds of km while the crustal thickness does not exceed a few tens of km, thin-elastic plate theory can be applied.

Thin-plate theory implies that the wavelength of deflection of a plate loaded at the surface is determined by the thickness of the equivalent elastic plate (equivalent elastic thickness,

T_e or EET), where the equivalent wavelength parameter of flexural bending λ is related to EET as follows (see also Figure 2.3):

$$\lambda = \left(\frac{(\rho_m - \rho_{infill}) * g}{4D}\right)^{1/4} \text{ (Walcott, 1970; Watts, 2001).} \quad (2.7)$$

Where:

λ = wavelength parameter (m)

g = gravitational constant (m/sec^2)

ρ_m = density mantle (kg/m^3)

ρ_{infill} = density contrast surface load (kg/m^3)

D = flexural rigidity

Rigidity D is related to EET by:

$$D(x,y) = \frac{E \cdot EET^3(x,y)}{12(1-\nu^2)} \quad (2.8)$$

Where E is the Young's modulus (assumed to be $7 \cdot 10^{10}$ N/m^2) and ν is the Poisson coefficient set at 0.25.

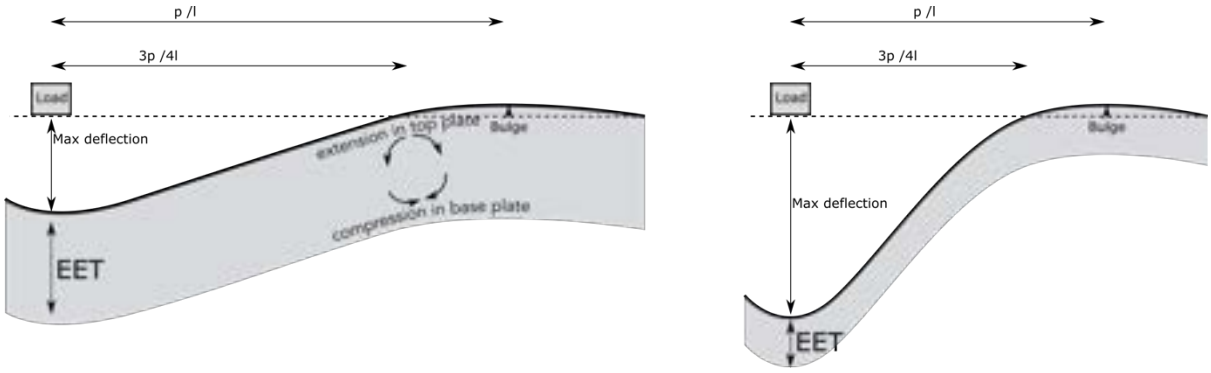

Figure 2.3. Flexure of a beam by a unit load, illustrating how flexural wavelength increases when EET decreases, after Watts (2001).

This means that the wavelength over which loads are supported is related to EET, a parameter that captures the effects of lithosphere thickness, age, rheology, thermal structure and pre-existing weaknesses. Determining the plausible range of EET for a region is one of the most important steps when calculating flexure. On a continental scale EET for continental lithosphere can be inferred by comparing gravity anomalies to their expression in surface topography, inferring EET from the degree to which such gravity anomalies are expressed by surface deformation over long timescales. Analysis by Pérez-Gussinyé & Watts, (2005) yielded values of 5 to 25 km EET in the Mediterranean west of Sardinia, with the lowest values occurring in the deep Provençal and Algerian basins and the highest in the Valencia Basin, consistent with variations in crustal thickness. The Alboran Basin, with high heat flow, volcanic domains and highly extended crust is expected to have even lower EET values. In Chapter 4 EET for the Western Mediterranean is determined in more detail based on thermal-rheological modelling, and in chapters 3 and 4 the regional EET is discussed in more detail. In chapters 3,4 and 5, I illustrate the sensitivity of our results to variations in EET by testing for a range of values.

2.2. Backstripping

The formation and evolution of marine basins is associated with large vertical motions which affect the depth of stratigraphic features up to millions of years after their deposition. During the original opening of the basin by extension, subsidence is controlled by tectonic and thermal characteristics of the crust, and potentially the formation of oceanic crust. From this point on, the basin is loaded with sediment causing subsidence due to isostatic compensation of their weight pressing down on the crust. In addition, the build-up of sediment causes a reduction of pore space (compaction) in the lower part of the sediment column reducing its thickness and further contributing to sinking of the seafloor.

In basin analysis the classic backstripping technique uses paleobathymetry (from lithological and palaeontological data), known variations in the global sea level curve and sediment thickness, lithology and porosity info from well data to quantify the tectonic and isostatic components of subsidence. The method was originally introduced in analysis of borehole data from the Gulf of Lions and the East Coast of the U.S.A. by (Watts and Ryan, 1976), providing time-depth sequences of these basins allowing for the identification of tectonic pulses. This type of analysis has been fundamental both for quantifying the component of subsidence related to tectonic loading (e.g. in foreland basins) and developing understanding of the processes driving the evolution of sedimentary basins (Bessis, 1986).

For the case of the Messinian Salinity Crisis, a lack of palaeontological water depth information and the plausible disconnection from the global ocean mean that the absolute bathymetry is not known for the evaporitic and lowstand stages of the MSC. By assuming the tectonic load as far as it can be constrained, and implementing a water level change to match the depth of paleoshoreline markers, we effectively invert the backstripping analysis. In this analysis, a few of the basic principles of backstripping are applied, with the fundamental difference that instead of using paleodepth to constrain components of vertical motions, we compute the magnitude of expected vertical motions since the onset of the MSC in order to obtain the paleodepth, effectively using an inverted backstripping approach, similar to Amadori et al. (2018).

The underlying assumptions to this technique are:

- The tectonic component of vertical motions is minimal or can be accurately constrained
- The position of the shoreline at a certain moment in time can be identified in the geological record and is representative for regional base level.

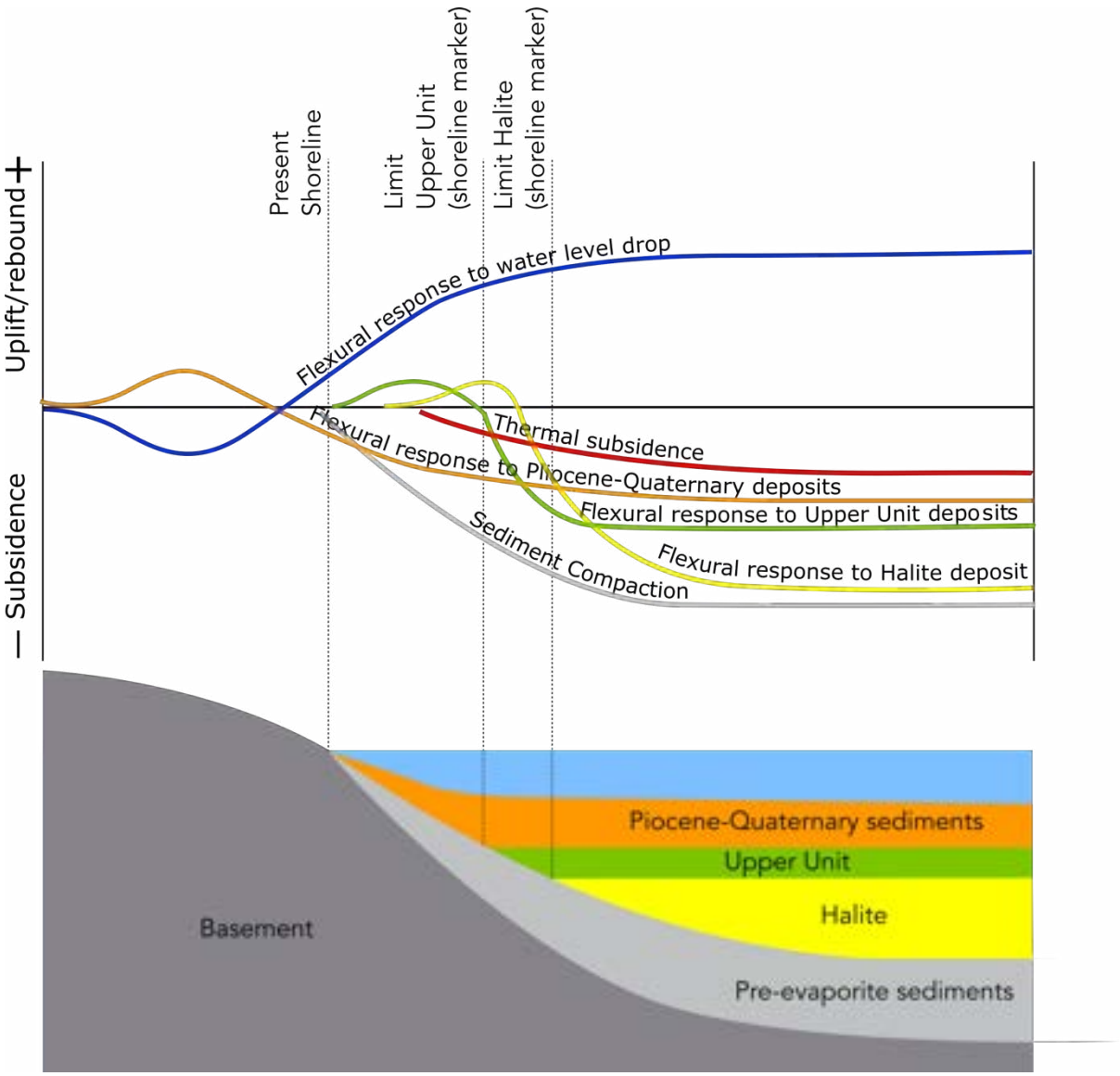

Figure 2.4. Schematic profile showing the contributions to (post-)Messinian isostatic vertical motions considered in the paleotopographic reconstruction.

Where these conditions are met, we can reconstruct both the depth of the basin for each key sediment horizon (Top Messinian/Base Pliocene, Top Mobile/halite unit, Base halite unit) by calculating vertical motions induced by the following processes (see Figure 2.4):

- Sediment and evaporite accumulation (performing a calculation of flexural-isostatic compensation for each surface load component, see section 2.3)
- Compaction of underlying Miocene sediment (following the classic depth-porosity relations by Sclater and Christie (1980).
- Thermal and tectonic subsidence constrained from geophysical properties of the lithosphere.

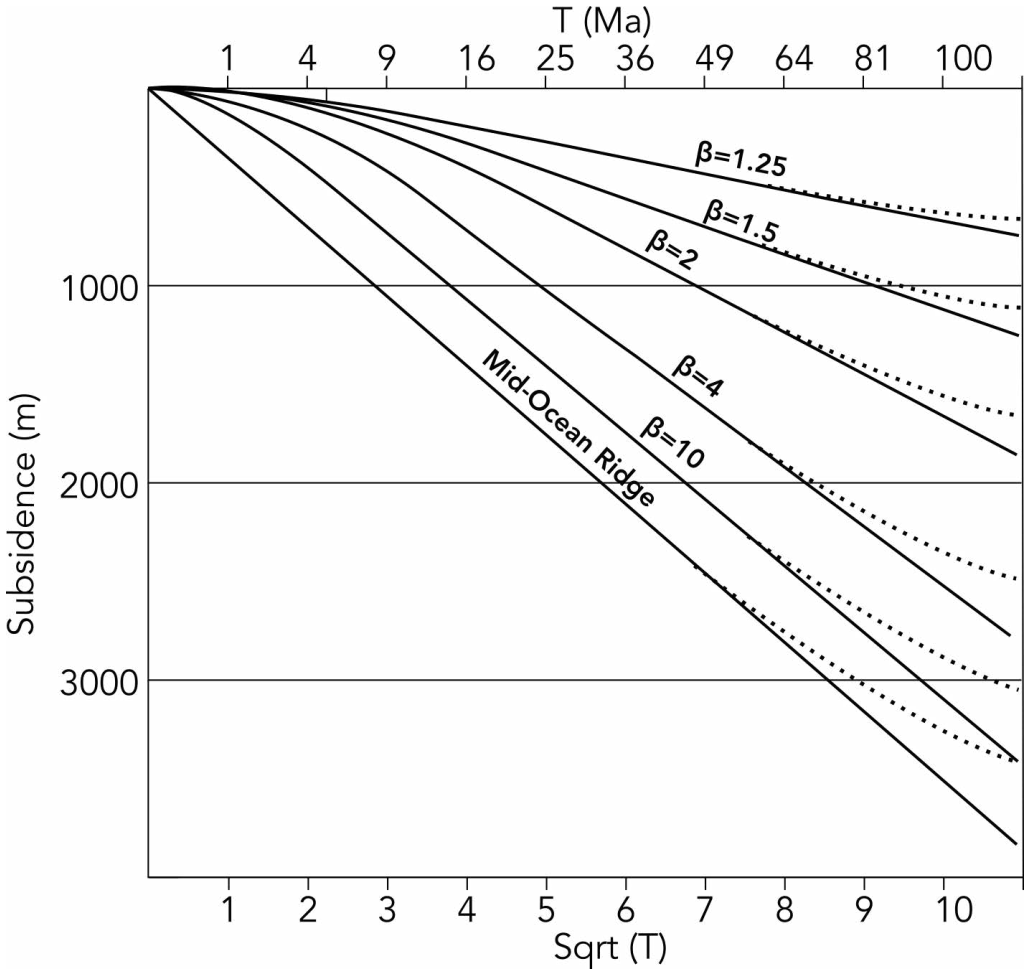

Figure 2.5. Thermal subsidence as a function of time after extension, according to the instantaneous rifting model from McKenzie (1978) (see their figure 4). In Chapters 3 and 4 potential thermal subsidence is calculated by fitting current age and age during the MSC to the appropriate extension curve to determine thermal subsidence that might have occurred since the MSC in any given basin.

In Chapters 3 and 4 the restoration of relatively young extensional basins calls for a calculation of the thermal subsidence that occurred since the MSC in response to stretching of the lithosphere and passive upwelling of asthenosphere. This is done by fitting the age of the basin and during the MSC (current age –6 Ma) to the thermal subsidence curve for the appropriate extension factor (β) based on the instantaneous continental stretching model by McKenzie (1978) (see Figure 2.5). The stretching factor is based on estimates of crustal thickness or lithosphere studies from refraction seismics, according to availability of such data in the subbasins studied. For oceanic crust, we apply the same principle using the cooling curve for the Mid-Ocean Ridge model by Stein and Stein, (1992) which for basins with an age of <50 Ma is almost identical to the curve by Parsons and Sclater (1978). These oceanic cooling models correspond to the curve for $\beta=\infty$ (see Figure 2.5).

2.3. TISC (numerical model for flexure calculation)

The bulk of this thesis (Chapters three, four and five) are based upon flexural-isostatic-reconstruction of the Mediterranean topography during various stages of the MSC. Chapter six uses a completely different modelling approach, namely hydrogeochemical box modelling, building upon the Messinian paleotopography obtained in the Central Mallorca Depression in Chapter four. Here I will outline the theory and methods used to obtain a flexural-isostatic reconstruction that accurately reflects the depth of the various Mediterranean sub-basins. As the procedure for reconstruction in each regional study differs slightly depending on available data, geodynamic setting of each study area, and local context of the MSC-related sedimentary record, each Chapter contains a section outlining the specific modelling procedure applied.

The flexural-isostatic component of vertical motion caused by sediment deposition can be calculated in pseudo-3D (planform) by application of a finite-difference method algorithm called TISC. It solves for the fourth order differential equation that describes the flexural-isostatic deflection of a thin elastic plate as a response to surface loads (Wees and Cloetingh, 1994; Garcia-Castellanos, 2002; Garcia-Castellanos and Jiménez-Munt, 2015), allowing for lateral variations of EET. The calculation of the vertical deflection of a bended thin elastic plate flexure (w_d) is based on the following expression (Garcia-Castellanos and Jiménez-Munt, 2015):

$$\Delta\big(D(x,y)\cdot\Delta w(x,y)\big)+\rho_a g w(x,y)=q_i(x,y) \qquad (2.9)$$

Where q_i is the load distribution (lateral pressure difference in Pa), D is rigidity of the lithosphere, w is the vertical deflection of the plate, ρ_a is the density contrast between the underlying mantle and environment overlying the plate (air or water), and x, y describe the horizontal position where deflection is being calculated. The surface load (q_i) is defined from the thickness of sediment and evaporite units or the water fill loading the basin, and the contrast between their density and that of the material they substitute (either water or air).

The required input for the numerical model (q[x,y]) needed to calculate the planform distribution of vertical motions in response to surface loading are provided in grid format with a resolution depending on the density of data available, the size of the studies region and the size of the investigated features. In the Alboran Basin (Chapter 3), where a relatively small region with a very high data density is reconstructed, a resolution of 1x1 km per cell is used, while in the larger Western Mediterranean study region (Chapter 4) and in the Nile Delta region (Chapter 5) the reconstruction is based on grids with a resolution of approx. 4x4 km per cell.

2.4. Time-depth conversion

To obtain the surface load distribution we need a reliable current depth distribution of the Pre-, Post- and Messinian sediment and evaporite units. These are obtained from (re)interpretation of seismic datasets obtained over the previous decades. In the Alboran Basin (Chapter 3) and Western Mediterranean (Chapter 4) a conversion from Two-Way Travel Time (TWTT, sec) to depth is obtained using seismic velocities compiled from literature where available and reported in Table 2.1. In the case of the Nile Delta, the Base Pliocene was constrained from a compilation of well and seismic data (Zucker et al., 2020).

In the Western Mediterranean, a uniform velocity profile in (pre-)Messinian sediment is justified considering that the evaporite-dominated sediment units are characterized by a uniform porosity expected in such materials, and a lack of lithological constraints from well data as the deep basin sequence has not been sampled beyond the topmost evaporite layer. The composition of the Lower Unit has been subject to debate, interpreted as either a partially clastic unit (Bache et al., 2009) related to a pre-evaporite drawdown, or as the deep-basin equivalent of the Primary Lower Gypsum, where the presence of evaporites in this unit would depend on availability of oxygen (Krijgsman and Meijer, 2008). Once the depths of all horizons of interest are established, we can use the sediment thicknesses and their density derived from well and seismic data to compute vertical motions induced by their deposition.

Unit	Alboran Basin		Western Mediterranean		Nile Delta	
	Velocity (m/s)	Density (kg/m^3)	Velocity (m/s)	Density (kg/m^3)	Velocity (m/s)	Density (kg/m^3)
Pliocene-Quaternary	1750 (Comas et al 1996)	2100 (Docherty&Banda 1992)	Power Law (Urgeles et al.2011)	2100 (Docherty& Banda 1992)	*	2000
Upper Unit gypsum/anhydrite	-	-	3400 (Maillard et al. 2006)	2500	-	-
Mobile Unit Halite	-	-	4800 (Samperi et al., 2020)	2170 (Samperi et al., 2020)	-	-
Pre-MSC sediment/Lower Unit	2500	-	2440 (Camerlenghi et al. 2019)	-	*	-

Table 2.1. Seismic velocity used in time-depth conversion and density used for computing isostatic motions. *In the Nile Delta region, the Base Pliocene and Basement depth were not converted with a uniform velocity.

2.5. Evidence for subaerial exposure in the Mediterranean seafloor: data and assumptions

This study focuses on the reconstruction of the original depth of erosional and stratigraphic coastline features of three regions in the Mediterranean. These span a total surface area of approximately $650x10^3$ km^2 of the offshore region in the Western Mediterranean (the entire basin from the Strait of Gibraltar to Sardinia, see Chapters 3 and 4). In the Eastern Mediterranean the reconstruction in Chapter 5 spans about $300x10^3$ km^2 of the offshore region, which covers approximately 35% of the deep Eastern Mediterranean Basin surface area. The suitability of a region for the type of reconstruction proposed in this work depends on the following factors:

- Availability of 2D (or 3D) seismic data with a high coverage, allowing for the accurate identification of the target horizons on the regional scale.
- Limited or well-quantified tectonic alteration since the MSC.

One of the main objectives of this thesis is the identification of paleo water levels by the reconstruction of shoreline markers to their original position. In order to achieve this, a base assumption must be made that we are able to identify such shorelines, and qualify certain surfaces as affected by subaerial erosion. The shoreline markers reconstructed in this thesis are based various types of features, some related to sedimentary/evaporite units, and some purely to the morphology of erosional surfaces, but all are based in the extensive record of reflection seismic data (both in 2- and 3D) in the Mediterranean.

Subaerial exposure of the Messinian Surface ("M-reflector") and the top evaporite layer in the deep Mediterranean Basin was proposed already during the DSDP Leg 13 drilling campaign. The presence of "chicken-wire" and nodular anhydrite in the Upper Evaporites recovered at the base of the Menorca margin (site 124 of DSDP Leg 13) were thought representative of sabkha environments, forming subaerially above the groundwater table (Ryan, 2009). This information, coupled with the erosional surfaces encountered both in the Alboran Basin (site 121) and in the Valencia Basin (site 122) and identifiable in in seismic data covering the margins all around the Western Mediterranean, has been a strong basis for early desiccation scenarios in the Mediterranean during the MSC.

In the Valencia Basin the characteristics of the Messinian evaporite units, combined with their relationship with the erosional features bounding them, allow us to interpret their limits as a marker of paleoshorelines.

Due to the gentle slope of the seafloor from the margins to the deep basin in this region, it is easier to identify lateral changes in the MSC deposits, from purely erosional margin, to an UU bounded by BES and TES, to the limit of the MU. The internal seismic facies of the UU, which shows relatively continuous parallel beds (see Fig. 2.6 B) that *onlap* onto the BES according to Lofi et al. (2011) indicating an agradational deposition during a gradual rise in base level, close to water level, indicating that the top onlap marks a paleoshoreline.

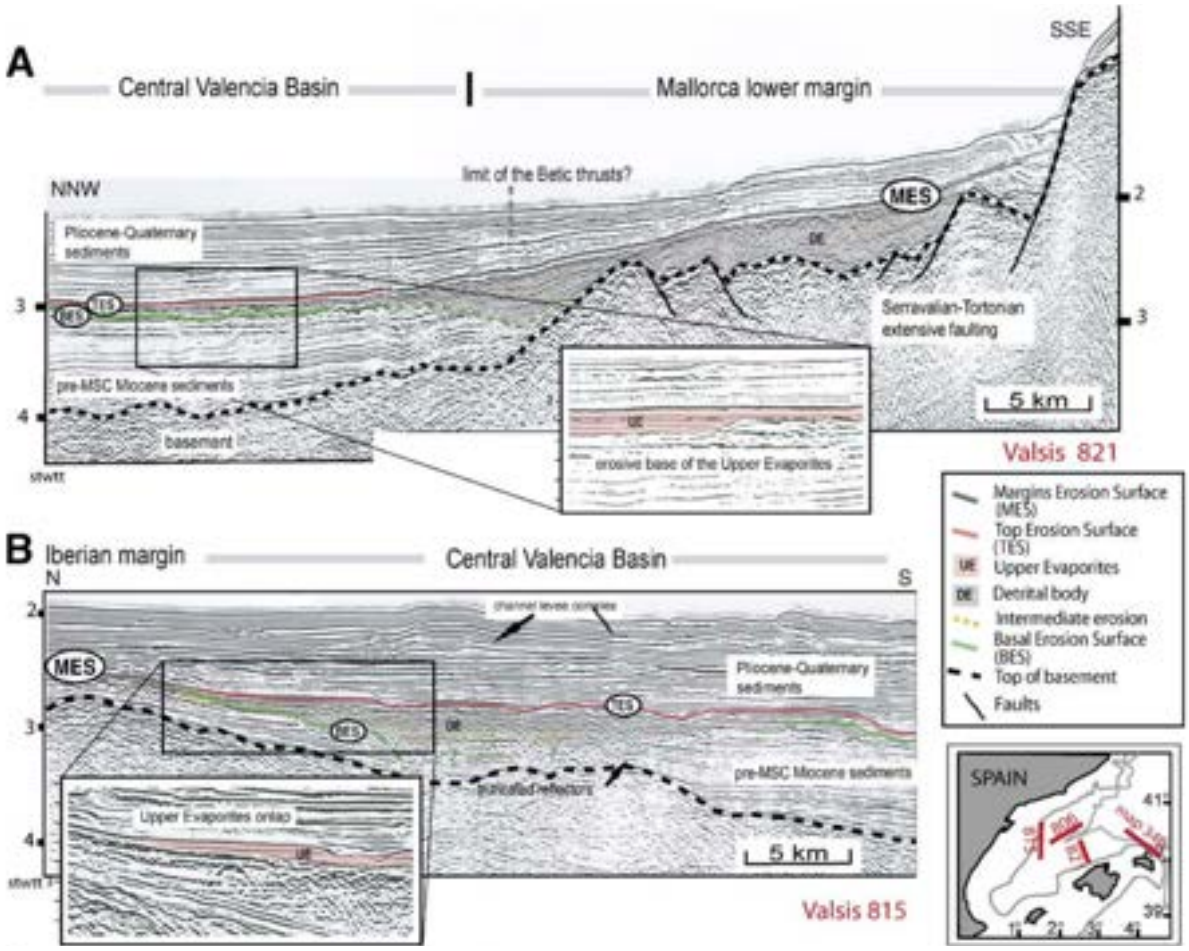

Figure 2.6. Seismic profiles in the Central Valencia Basin. illustrating the relationships between the MES, the Upper Evaporites, the BES and the TES along the slope. A: Seismic profile on the Mallorca margin, affected by recent normal faulting. This profile illustrates the transition between the thin Upper Evaporites sequence of the Central Valencia Basin, the detrital deposits and the erosion on the downslope domain of the margin B: Seismic profile on the Iberian margin showing the different acoustic facies of the Messinian deposits: chaotic facies, interpreted as detrital units, and layered seismic facies interpreted as the Upper Evaporites, both emplaced between two erosion surfaces. The truncations visible below the chaotic facies are equivalent to the upslope MES. From: Maillard et al., 2006.

The limit of the MU in the Valencia Basin is also considered a paleoshoreline marker due to it marking the limit of the Bottom Erosion Surface and the depth distribution of halite on other parts of the Balearic Promontory. The erosional character of these markers is further discussed in Chapter 4, and our results are also compared to a scenario where these features were formed under high water level.

In Chapters 3 and 5, the baselevel markers are based on morphological features in the MES/Base Pliocene surface, as they are not directly associated with primary evaporite deposits. The erosional and subaerial nature of these features is further elaborated on in the respective chapters.

2.6. Input data grids for the isostatic calculation

From the interpretation of extensive seismic datasets (see Figures 3.4 and 4.1 for location and density of seismic data in the Western Mediterranean) basin-wide depth distribution of a number of key horizons was mapped. These horizons include:

- The seafloor, which is a high-amplitude reflector marking the boundary between the water column (no internal reflectivity) and the sediment at the top of the seabed.
- The base of the Pliocene-Quaternary (PQ) unit. This horizon marks the Miocene-Pliocene boundary (5.33 Ma), and is marked by a strong reflection at the base of the often highly transparent lower part of the Pliocene sequence. On the Mediterranean margins, this contact often marks an angular unconformity with the underlying Messinian or older Miocene units. This horizon has been classically assigned the name “M-reflector” (Ryan, 1978).
- The base of the Upper Unit (UU), which is more easily identified as the top of the Mobile Unit (MU), which is a seismic unit with a high velocity, is very transparent and shows signs of viscous deformation or diapirism, as it is believed to consists mainly of halite. The UU itself shows strong internal reflectors, possibly caused by alternations of evaporite and sediment layers. In the Western Mediterranean, the UU covers a larger area than the underlying MU (Maillard et al., 2006; Lofi et al., 2011) (see Fig. 4.1), from the intermediate depth Valencia Basin to the deep basin. The contact between the UU and MU is conformable in the deep basin, but towards the margins this contact becomes erosional, classified as the Intermediate Erosion Surface (IES) (Lofi, 2018) see Fig. 2.6, then the Bottom Erosion Surface beyond the limit of the MU where UU directly overlies the pre-MSC sediment.
- The base of the Mobile Unit or base Messinian (in the deep basins the base Messinian cannot be accurately identified everywhere due to uncertainty with regards to the nature of the Lowe Unit). In the more marginal or intermediate basins the base of the first evaporite units is marked by a high amplitude contrast, previously known as the “N-reflector” (Ryan, 1978). Towards the basin margins the MU pinches out and the Intermediate Erosion Surface merges with the Bottom Erosion Surface under the UU.
- The top of the Acoustic Basement. This horizon is mainly used to constrain the thickness of the pre-evaporite sediment, needed to determine the compaction of these sediment during the deposition of the (post-)Messinian sediment and evaporites. It is identified as the deepest continuous reflection. In some places, the acoustic basement coincides with the top of the volcanic or metamorphic basement, but in other regions it is located inside the sediment column.

2.7. Hydrological box modelling

In Chapter 6, I present the results of a physics-based box model applied to the restored Messinian bathymetry of the Central Mallorca Depression in order to calculate the potential rate and quantity of evaporite deposition in basin. The basic principle relies on the dynamics of a basin with a negative freshwater budget that is compensated by inflow of water from the surrounding basin. This model is based on the exchange of water across a restricting sill between basins, with the efficiency of sill exchange constraining the degree of mixing between the water masses and thereby their potential difference in salinity. Using the restored geometry of the Central Mallorca Depression as reconstructed in Chapter 4, and the volume of Messinian Evaporite units in the CMD constrained from high-resolution seismic data we investigate the degree to which this subbasin would be able to salinify compared to the surrounding basin, and thereby we constrain the required salinity of Mediterranean surface waters during the stages of deposition of gypsum and halite in the CMD. This allows for comparison between scenarios for a basin undergoing a 2-way exchange of water between the CMD and surrounding basins, an inflow-only scenario and a scenario where the basin is fully disconnected by drawdown. The full methodology and derivation of water and salt fluxes is presented in Chapter 6.

Chapter 3: The Alboran Basin

The Alboran Basin is located in the very western extremity of the Mediterranean Sea, where it is currently connected to the Atlantic Ocean through the relatively narrow and shallow Strait of Gibraltar. In this Chapter, I present a flexural-isostatic reconstruction of the topography of the basin during the MSC, investigating the circumstances of formation of erosional terraces recognized in the Messinian Surface, the channel excavated by Zanclean Flood, and the impact of vertical motions on the Mediterranean-Atlantic connection. I also investigate the possible role of the East Alboran Volcanic Arc in controlling Atlantic-Mediterranean connectivity during the MSC.

This chapter has been submitted for publication in a peer-reviewed journal.

3.1. Chapter summary

The Messinian Salinity Crisis (MSC) was triggered and terminated by changes to the Atlantic-Mediterranean connectivity in the Alboran Basin, a region with a complex and debated geodynamic configuration. Since the MSC, basin topography and the geometry of the Messinian Erosional Surface have been subject to vertical motions due to sediment accumulation, tectonic deformation, and cooling after extension and magmatic arc formation. The objective of this work is to restore these contributions to post-Messinian subsidence in order to quantify the depth of the Alboran Basin during the MSC. We do this by performing a psuedo-3D planform flexural isostatic reconstruction of the Messinian Erosion Surface mapped from an extensive set of seismic reflection data. We focus on identifying the most likely position of the gateway between Atlantic and Mediterranean, the effect of a drawdown on gateway topography and connectivity, and the depth of proposed erosional features related to the Messinian lowstand. We evaluate the results of this restoration also considering the potential dynamic topography contribution from the rollback and tearing of the subducting Gibraltar slab imaged underneath the Gibraltar arc. Our results indicate that the depth of the Alboran Basin during the Messinian was slightly shallower than nowadays, but was on average still over 500 m reaching depths of at least 1000 m in most all subbasins. If the basin was desiccated, the topography was up to 300 m shallower. From our results, a hydrological barrier at the East Alboran Volcanic Arc with a Mediterranean drawdown affecting only the basins to the east is unlikely, unless the basin saw dynamic topography contributions of over 500 m in the arc region. In the Strait of Gibraltar area desiccation would lead to uplift of up to 100 m, with uplift rates too high to be counteracted by erosion, leading to a sustained isolation of the Mediterranean after the initial onset of drawdown. The terraces and canyons in the West Alboran are restored to depths between 250-550 m (shallowest terrace) and 750-1500 m (deepest terracea), and cannot be clearly linked to a single, stable water level during the MSC, suggesting possible variations in the water level during the isolation phase.

3.2. Introduction

3.2.1. The MSC in the Alboran Basin

The Alboran Basin constitutes the 200 km wide, 400 km long westernmost domain of the Mediterranean Sea. The Strait of Gibraltar, which is 15 km wide and 300 m deep at its narrowest point, connects the Alboran Basin with the Atlantic Ocean. It modulates the inflow of Atlantic water and the outflow of the more saline Mediterranean Bottom Water, thus maintaining the hydrological balance of the Mediterranean. Between 5.97 and 5.33 Ma (Krijgsman et al., 1999), this balance was disrupted during the Messinian Salinity Crisis (MSC).

The end of the MSC was marked by a reestablishment of normal marine conditions, proposed to have happened abruptly (Hsü et al., 1971; Blanc, 2002; Loget and Van Den Driessche, 2006), caused by a megaflooding event forming the Strait of Gibraltar and excavating an erosional channel up to 500 m deep across the Alboran Basin (Garcia-Castellanos et al., 2009, 2020; Estrada et al., 2011), illustrated in Figure 3.1. Other scenarios for the end of the MSC envision high water levels in the Mediterranean with reconnection marked by only minor sea-level rise (Loget et al., 2005; Roveri et al., 2006; Marzocchi et al., 2016; Andreetto et al., 2020). The magnitude of the water level drop during the MSC has been estimated in various subbasins from restoration of paleoshoreline markers at around 1800 m [Malta escarpment, Micallef et al. (2018)], 800 m [Po plain, Amadori et al., (2018)], 1100-1500 m [Valencia Basin, Heida et al., (2021)], and 600 m [Nile Canyon, Gvirtzman et al., in press], while other authors question high-amplitude water level drop during the MSC (Manzi et al., 2005; Roveri et al., 2009) and suggest that erosional features have a subaqueous origin (Roveri et al., 2014b).

The Alboran Basin does not contain evidence of in-situ Messinian evaporite deposits like the ones identified in the deep Mediterranean basins (Comas et al., 1999). In the West Alboran basin terraces and canyons partially terminating on these terraces have been identified truncating Miocene deposits on both the Spanish and Moroccan margins. These terraces reach dimensions of several km width and tens of km length, and were proposed to be linked to several stages of stable water level during reflooding of the basin (Estrada et al., 2011).

Similar terraces have also been identified on the Alboran Ridge, in the Bay of Oran (Algeria) and southwest of Mallorca (Balearic Islands) proposed to mark a stable water level linked to the depth of the Sicily Sill between 320 and 380 m during the MSC (Just et al., 2011).

Understanding the causes of both the onset and termination of the MSC hinges on accurate knowledge of the geometry of the Alboran region, as it is where the connectivity between Atlantic and Mediterranean is modulated. A number of Miocene marine gateways have been identified (Esteban et al., 1996; Flecker et al., 2015; Capella et al., 2018; Krijgsman et al., 2018) in the Betic and Rif tectonic arc that encapsulates the Alboran Basin (see Figure 3.1). These gateways underwent continentalization leading up to the MSC progressing from east to west due to regional uplift. The location of the last marine connection before the MSC remains unclear, having been proposed to be positioned in the Rifian Corridor (Martín et al., 2001),

the Gibraltar area (Capella et al., 2018; Krijgsman et al., 2018; Bulian et al., 2021) or in the East Alboran Volcanic Arc (Booth-Rea et al., 2018).

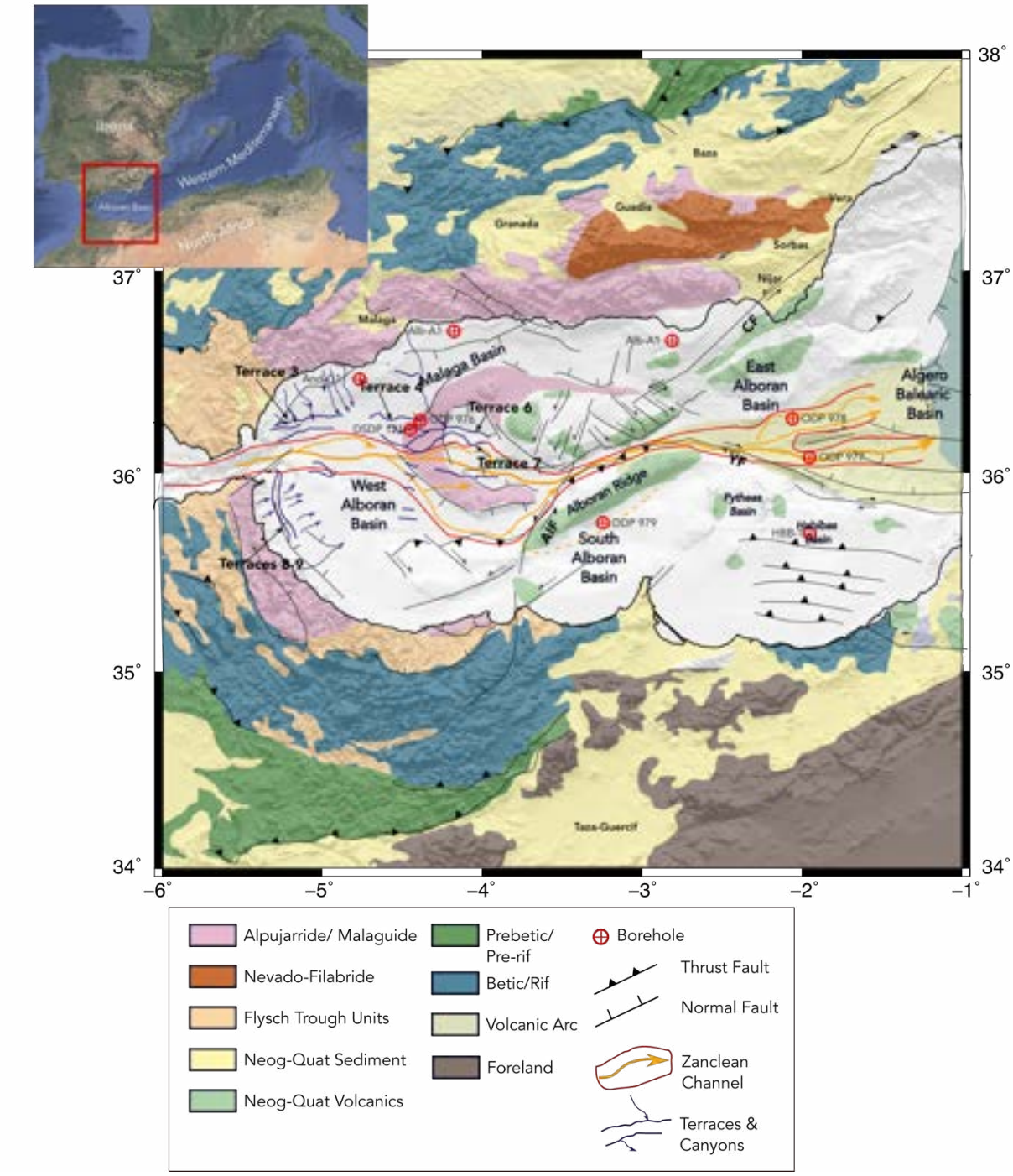

Figure 3.1. Geological map of the Alboran Basin and the Gibraltar Arc after Mancilla et al. (2015) and Jolivet et al. (2021). In red the Zanclean channel, in orange the main flood paths and in purple the Messinian Terraces from Estrada et al. (2011). AIF = Al-Idrissi Fault, YF = Yusuf fault, CF = Carboneras fault.

Depending on the position of the gateway, contrasting scenarios are proposed for the water level in the Alboran Basin (see Figure 3.2). If the gateway was positioned in the Betic-Rif tectonic arc, the entire Alboran basin would have been subject to desiccation, allowing for the formation of erosional terraces and the excavation of the Zanclean Channel in the West Alboran Basin (WAB) by subaerial exposure and flooding (Estrada et al., 2011). In this scenario gradual restriction would have occurred in the West Alboran Basin leading up to complete isolation, as reflected in changes towards warmer foraminifer assemblages, an increasingly stratified water column and sharp increase in terrestrial input due starting at ~7.2 Ma recorded in boreholes (Bulian et al., 2021). Alternatively, if the gateway was positioned in the Alboran volcanic arc east of the WAB, desiccation would only have affected the basins east of the Alboran, leaving the WAB connected to the global ocean as a marine refuge during the MSC, and with the volcanic arc providing a path for mammal migration that occurred between Iberia and Africa both before and during the MSC (Gibert et al., 2013; Booth-Rea et al., 2018). Study of seismic data in the West Alboran has found a paraconformable contact between Miocene and Pliocene deposits over large areas of the WAB (Booth-Rea et al., 2018; Gómez de la Peña et al., 2021). In this scenario the Zanclean Channel imaged could be related to submarine channel formation by strong currents similar to channels in the modern Gibraltar region (Booth-Rea et al., 2018; Krijgsman et al., 2018).

In this work, we aim to restore the Messinian topography of the Alboran Basin. We use a pseudo-3D (planform) flexural-isostatic modelling approach similar to that used recently to restore the depth of shoreline markers in the Po plain (Amadori et al., 2018), Malta Escarpment (Micallef et al., 2018b), Valencia Basin (Heida et al., 2021) and Nile Delta (Gvirtzman et al., in press). We consider the magnitude and uncertainty of vertical motions induced by sediment loading, water level fluctuation, cooling after extension and magmatic activity, and tectonic deformation.

Through this restoration we provide quantitative constraints on the depth of the Alboran Basin during the MSC, and the vertical motions induced by MSC events on the Atlantic-Mediterranean gateway. The restored topography allows us to critically consider the position of the gateway and to distinguish which scenario presented in Figure 3.2 is more plausible. From the restored topography, we constrain a depth range of suspected MSC-related erosional features, informing us on the evolution of water level in the basin during the Messinian lowstand.

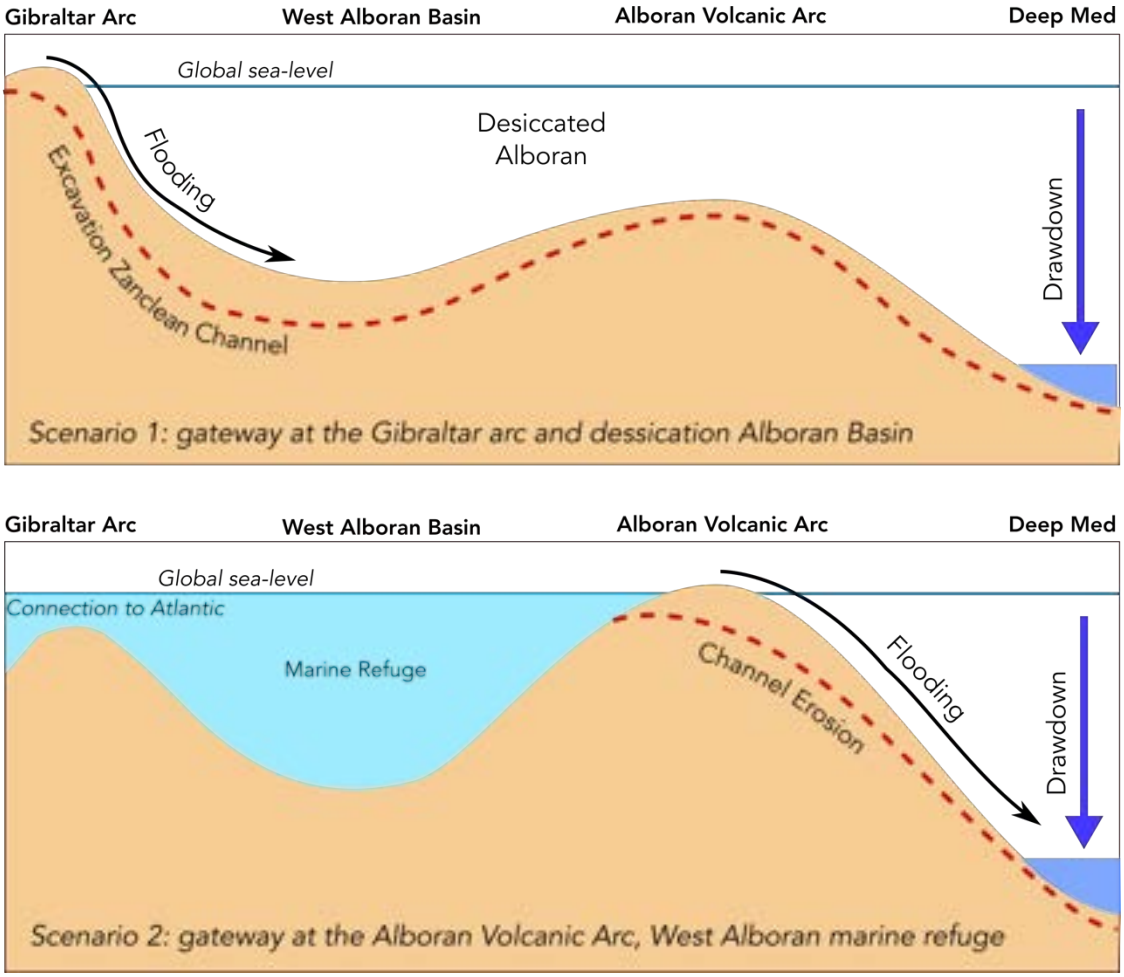

Figure 3.2. Cartoon profile of the Alboran Basin illustrating two contrasting scenarios for the Messinian lowstand and reflooding phase. The top panel shows the scenario where the entire Alboran Basin is affected by the Messinian lowstand until reconnection by flooding excavating a deep channel across the basin opening the Strait of Gibraltar (Garcia-Castellanos et al., 2020; Bulian et al., 2021). The bottom panel shows the alternative scenario where the Strait of Gibraltar was open during the MSC, while disconnection from the Atlantic took place at the subaerially exposed Alboran Volcanic Arc. The Alboran Arc would have formed a land bridge allowing for the migration of mammal species from Iberia to Africa before and during the MSC, as proposed by Booth-Rea et al. (2018).

3.2.2. Geodynamic setting

The Alboran Basin was formed in the context of extension due to the rollback of the subducting Gibraltar slab (Vergés and Fernàndez, 2012; Van Hinsbergen et al., 2014; Chertova et al., 2014) in the context of overall Africa-Iberia convergence (Dewey et al., 1989). It consists of several crustal domains or sub-basins, bounded by mayor structural features. The West Alboran Basin (WAB) (see Figures 3.1 and 3.3) consist of highly extended continental crust with a thickness of 4-6 km, and forms the main depocenter where the sediment cover reaches a thickness of 10-12 km. The WAB is has undergone extension and sediment fill since the Burdigalian (18 Ma) accompanied by a migration of the depocenter westward by

approximately 400 km. By Messinian time (6 Ma) the configuration of the depocenter was similar to the present day (Gómez de la Peña et al., 2021). Towards the Gibraltar arc, the thickness of the crust increases as the MOHO deepens to >40 km (Mancilla et al., 2015; Villaseñor et al., 2015; Diaz et al., 2021). The Malaga Basin (MB) shares a similar history to the WAB, albeit with considerably thicker basement of 18-20 km and a smaller sediment thickness. The WAB/MB domain is bounded by the Alboran Ridge and Carboneras Faults towards the east (see Figures 3.1 and 3.3).

South of the Alboran Ridge and Yusuf faults, the North African Margin containing the South Alboran, Habibas and Pytheas basins is underlain by African continental crust made up of Mesozoic (Medaouri et al., 2014) to Miocene (Negro et al., 2007) metamorphic basement with a thickness of 25-30 km (Gómez de la Peña et al., 2018), intruded by Late Serravallian-Tortonian volcanics (Duggen et al., 2004). The oldest observed non-volcanic sediment here are Tortonian-Messinian in age (Gómez de la Peña et al., 2021). This rigid domain acts as an indenter into the more easily deformed thinned continental crust of the WAB/Malaga basins, where the inherited crustal heterogeneities on the Al-Idrissi and Yusuf faults and in the Alboran Ridge antiform accommodate Eurasian–African plate motion.

North of the Yusuf Fault and South of the Carboneras Fault, the crustal nature changes to the arc magmatic crust of the East Alboran Basin of Late Serravallian-Tortonian subduction-related calc-alkaline volcanics (Duggen et al., 2004, 2008), related to the rollback of the Gibraltar slab. The thickness of the crust here is variable between 10 and 19 km (Grevemeyer et al., 2015; Palomeras et al., 2017; Gómez de la Peña et al., 2018). Towards the East the East Alboran Volcanic Arc crust transitions into the Algero-Balearic oceanic crust at 1^{o}W (Booth-Rea et al., 2007; Gómez de la Peña et al., 2021).

The Messinian surface has been affected by topographic expressions of deep mantle processes (Garcia-Castellanos and Villaseñor, 2011; Mancilla et al., 2015; Spakman et al., 2018; Jiménez-Munt et al., 2019; Faccenna and Becker, 2020; Capella et al., 2020). Here we will briefly summarize the plausible impact of these processes.

The Gibraltar Slab has undergone slab tearing propagating from east to west (Mancilla et al., 2015), leading to a westward propagating wave of uplift registered in the continentalization of intramontane basins in the Betic starting at 7.6 Ma in the Eastern Betics and continuing up to 5.3 Ma (Garcia-Castellanos and Villaseñor, 2011) in the westernmost, Gibraltar Arc. Modelling work by Boonma, (2021) suggests a magnitude of this dynamic topography wave of over 2 km, occurring mostly within 50 km surface distance from the slab tear. Garcia-Castellanos et al. (2002) report a similar value for the distance over which the subsurface load provokes a topographic response for realistic EET values of the region. Currently, the slab is attached to the Iberian plate only in the westernmost part of the Gibraltar Arc (Villaseñor et al., 2015), where the weight of the slab might be responsible for 1500-2000 m subsidence (Jiménez-Munt et al., 2019), the final portion of which might be linked to the opening of the Strait of Gibraltar (Garcia-Castellanos and Villaseñor, 2011). It should be noted that currently the Strait of Gibraltar area is undergoing uplift with shoreline markers found at 210 m

elevation (Rodríguez-Vidal et al., 2004), and uplifted Messinian marine sediment are present close to Gibraltar (Rico-García, 2007). Based on the identification of transgressive-regressive sedimentary cycles in the peripheral basins of the North Alboran subsidence-uplift wave is also registered from Málaga (5.4 Ma) to Gibraltar (3.2 Ma), which has brought latest- and post-Messinian deposits to elevations of over a hundred meters (Guerra-Merchán et al., 2014). Although the authors link this to tectonic activity on local faults, these data suggest a positive dynamic topography component in the Gibraltar region, and that the Strait of Gibraltar might have been a wider, deeper seaway leading up to the Messinian than nowadays.

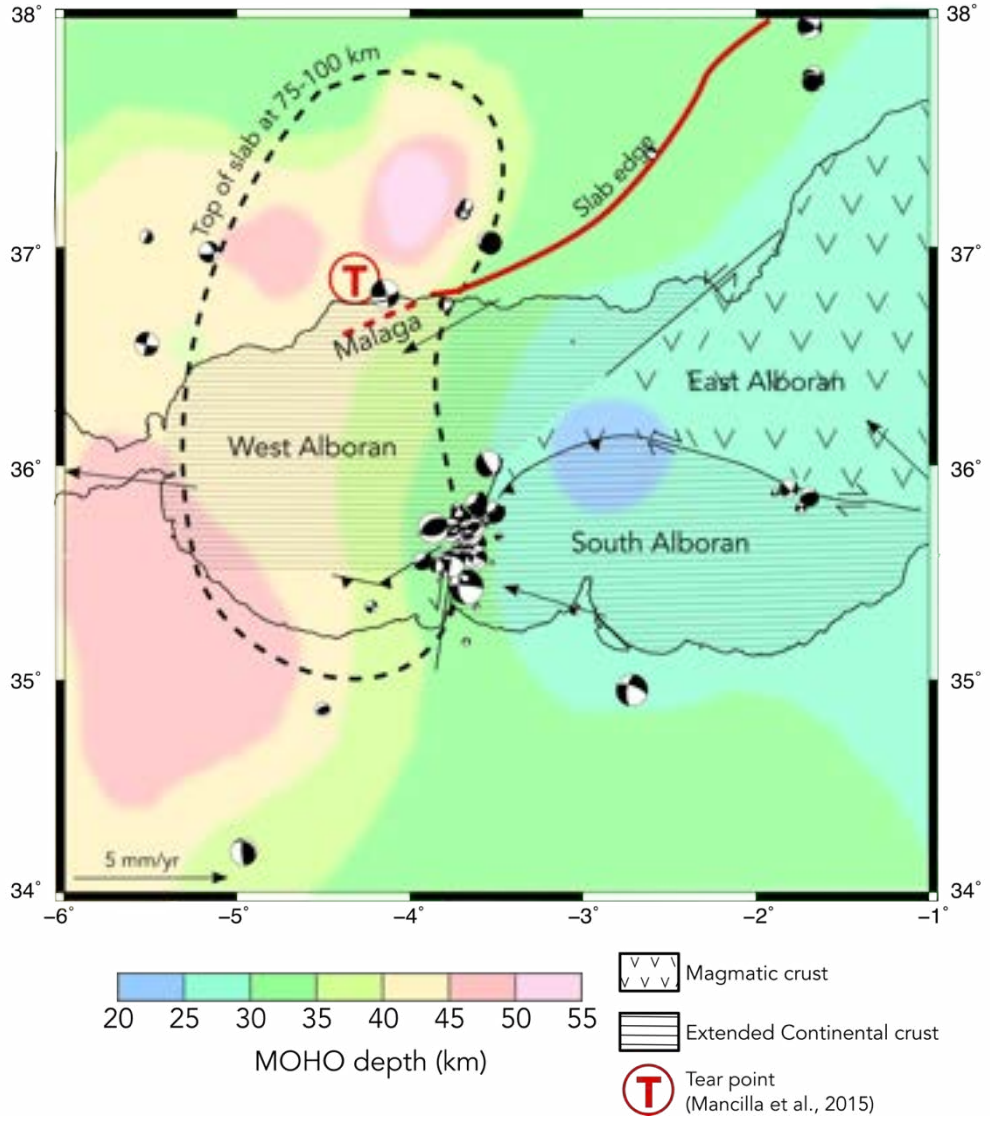

Figure 3.3. Moho depth map after Villaseñor et al. (2015). The dashed line shows the outline of the Gibraltar slab from the 1% velocity anomaly at 75-100 km depth, from Villaseñor et al. (2015). Edge of Iberian Moho (red line) and tear point from Mancilla et al. (2015). The position of the tear point corresponds to that suggested of Garcia-Castellanos and Villaseñor (2011). Mayor tectonic boundaries delimit crustal domains from Gómez de la Peña et al., (2021). Focal mechanisms for the period 2000-2010 (International Seismological Centre, 2022) show the main zones of seismicity along the Al-Idrissi and Yusuf faults

3.3. Data and Model Setup

3.3.1. Dataset and depth conversion

The depth of the Messinian Surface and acoustic basement used in the reconstruction of the Messinian paleotopography were determined from an extensive seismic dataset consisting of over 500 single- and multichannel seismic records in the Alboran Sea, partially reinterpreted and improved after Estrada et al. (2011) and Garcia-Castellanos et al. (2020). The extent of the dataset is presented in Figure 3.4.

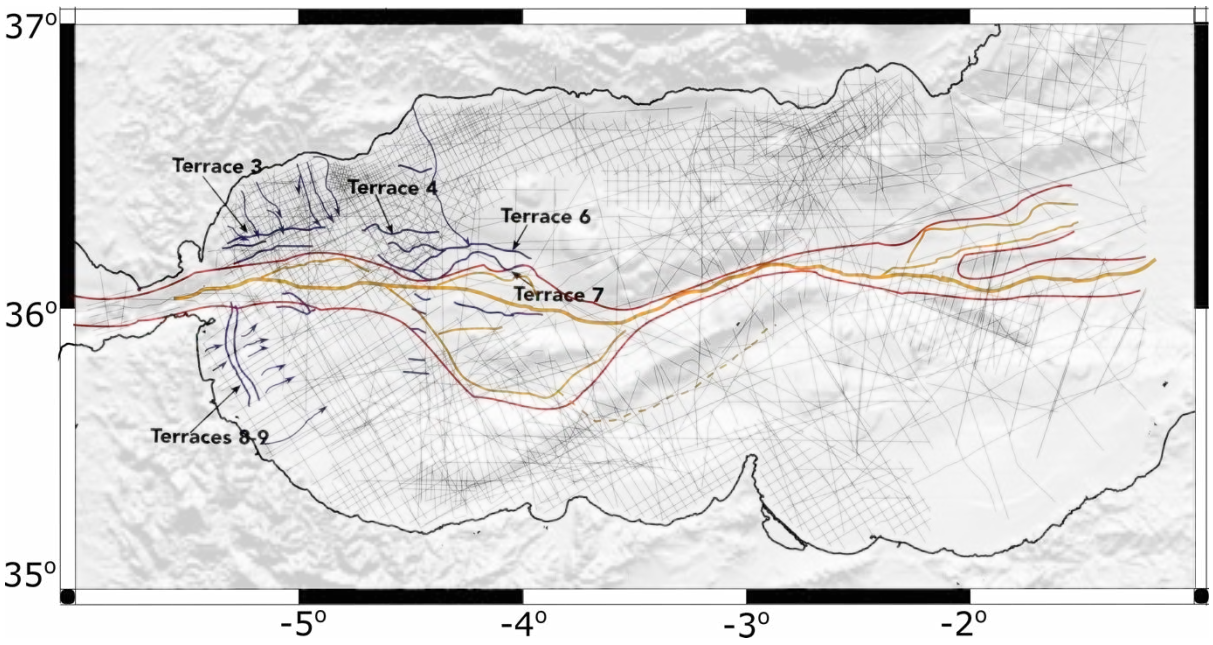

Figure 3.4. Map of seismic dataset used to determine the depth of the Messinian Surface and acoustic basement in the Alboran Basin.

The current depth of the Base Pliocene and Basement horizons are obtained by conversion from TWTT using a uniform seismic velocity for the sediment units (see Table 3.1). The applied seismic velocities are from Comas et al. (1996) and Camerlenghi et al. (2019). From these depths we can derive the thickness of the Plio-Quaternary and Miocene sediment load required to calculate flexure and compaction since the MSC (see Figure 3.5). The depth of the Base Pliocene (or Messinian Surface) is then restored by calculation of each subsidence component (as outlined in Figure 3.6), testing for a range of model parameters. The parameters that are tested for are: Effective Elastic Thickness (EET), porosity-depth curves for Miocene sediment lithology, thermal subsidence and tectonic uplift by shortening on the Alboran Ridge. The parameter ranges for these variables are listed in Tables 3.1 and 3.2.

Parameter	Reference model value	Minimum value	Maximum value
Marine water seismic velocity (km/sec)	1.5	-	-
Marine water density (kg/m^3)	1024	-	-
Pliocene-Quaternary seismic velocity (km/sec)	1.75 (Comas et al., 1996)	-	
Pliocene-Quaternary average density (kg/m^3)	2100 (Docherty & Banda, 1992)	-	-
Miocene seismic velocity (km/sec)	2.5 (Camerlenghi et al., 2019)	-	-
Miocene average density (kg/m^3)	2700	-	-
Miocene sediment surface porosity θ_0 (%)	56	49	67
Miocene sediment compaction coefficient (x10^{-5} cm^{-1})	0.39	0.27	0.51
Effective Elastic Thickness (km)	10	5	15
Asthenosphere density (kg/m^3)	3250		
Uplift Alboran Ridge (m)	1000	-	-

Table 3.1. Model parameters for reference model and tested parameter ranges.

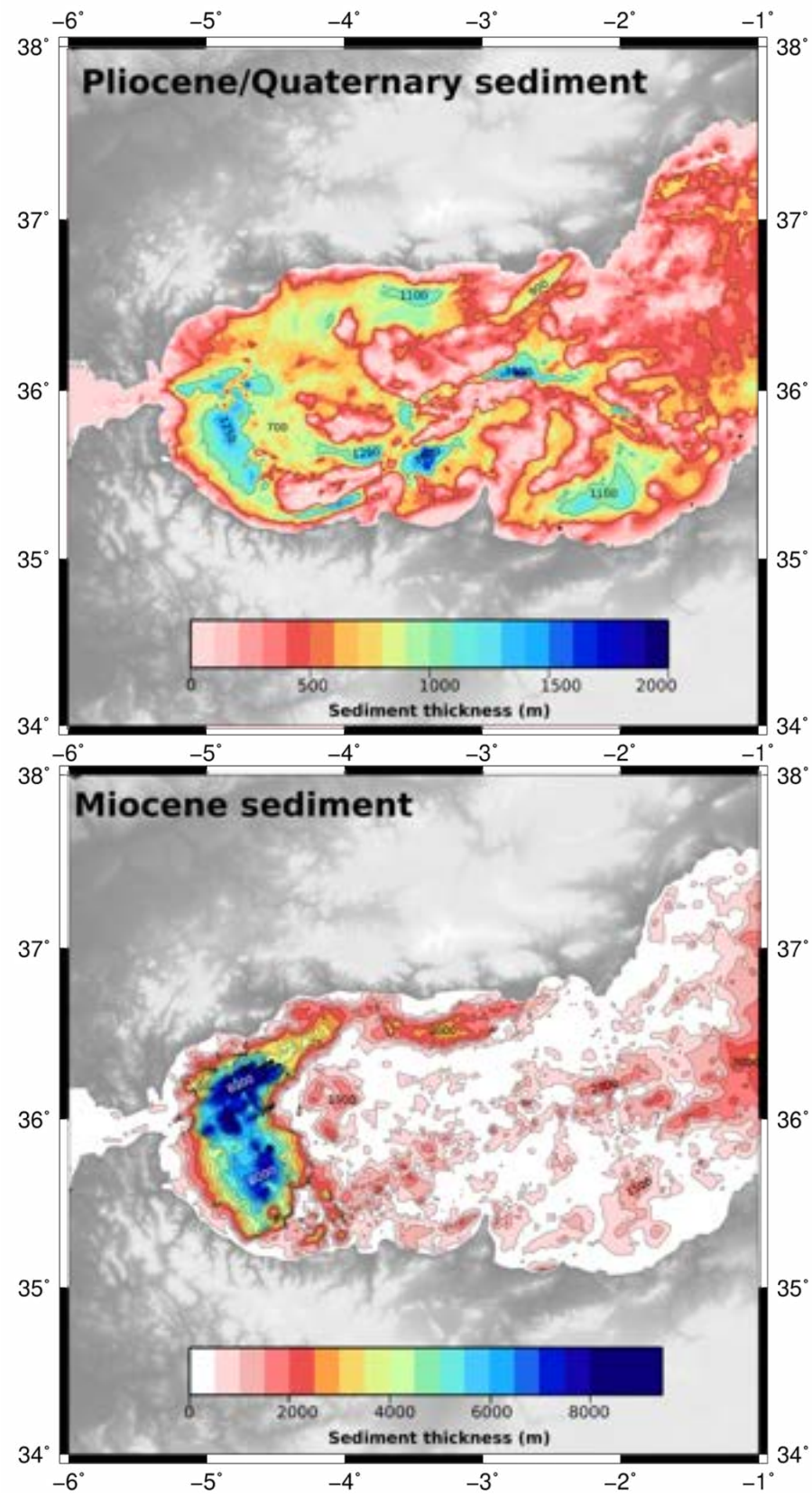

Figure 3.5. Thickness Pliocene/Quaternary (A) and Miocene (B) sediment, calculated by depth conversion of the Base Pliocene and Basement Top horizons in the seismic dataset, using uniform densities reported in Table 3.1, and subtraction of the horizon depth to obtain unit thickness.

3.3.2. Workflow and calculation of vertical motion

In Figure 3.6 I present an overview of the steps applied in the topographic restoration of the Alboran Basin, computing the various components of vertical motions (red boxes) based on the model inputs (blue boxes) that are described in more detail in this section.

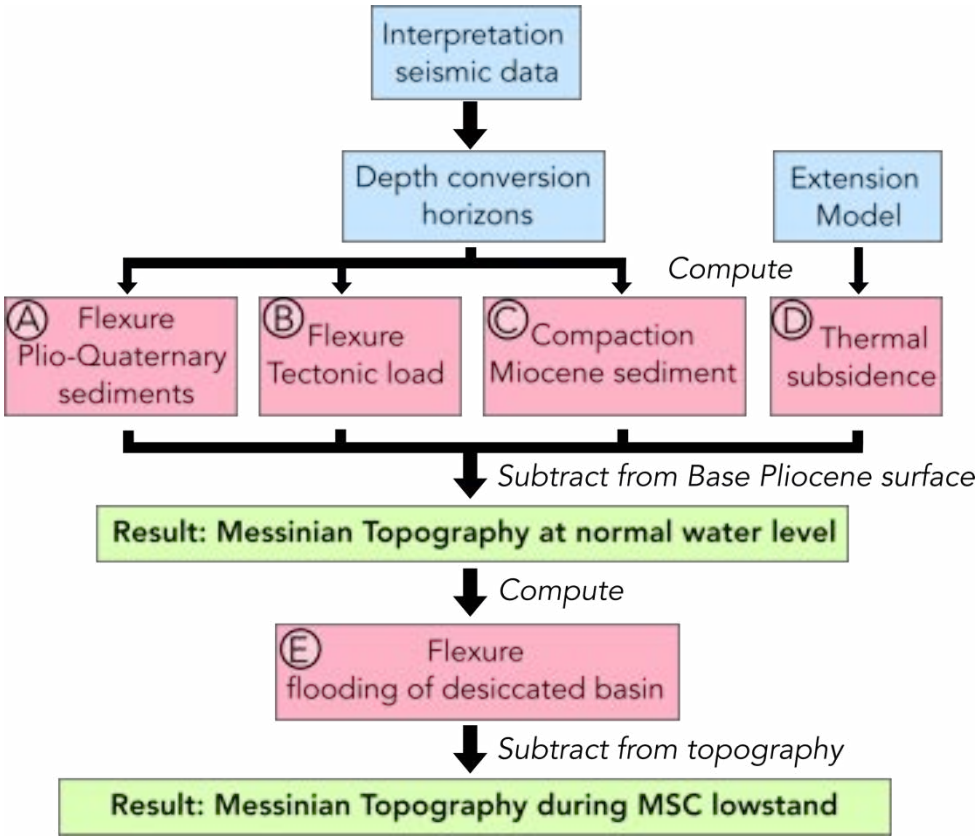

Figure 3.6. Workflow for topographic restoration (forward model). In blue: inputs. Red: calculation of vertical motions. Green: output topographies.

The calculation of the flexural-isostatic response to surface loading is performed using the pseudo-3D (planform) lithospheric flexure calculator function of TISC (Garcia-Castellanos, 2002; Garcia-Castellanos and Jiménez-Munt, 2015) adopting a thin elastic plate model. The model computes surface vertical motions on a grid with a resolution of 450x450 nodes (grid spacing 1 km). A key parameter in this analysis is the Effective Elastic Thickness (EET) the load-bearing capacity of the crust, or thickness of a theoretical purely elastic plate determining the lateral distribution of the response to surface loading. EET can be estimated based on the age of the lithosphere, its thickness and structural weaknesses (Burov and Diament, 1995). Tesauro et al. (2009) report EET values of 15-25 km based on lithospheric strength of the region. Alternatively, it can be estimated from cross-spectral analysis of gravity and topography anomalies, yielding values of 10 km in the Alboran Sea increasing to 30-40 km (with a 10-15 km uncertainty range) in the Gibraltar Arc (Kaban et al., 2018). Onshore in the Guadalquivir Basin indirect EET estimates have yielded values of 10 km or less (van der Beek and Cloetingh, 1992; Garcia-Castellanos et al., 2002). Thermophysical forward modelling shows that EET values required to fit elevation data are 30 km in the Atlas and Rif and 10 km

in the Strait of Gibraltar (Jiménez-Munt et al., 2019). In order to capture the influence of EET variations in the region we apply a range of 5-15 km uniform EET testing sensitivity, while for our reference model we apply a value of 10 km in the Alboran Basin increasing to 30 km in the onshore domain around the Strait of Gibraltar.

Another source of subsidence and deformation of the Messinian Surface is the burial and compaction of Miocene sediment after the MSC (step A in Figure 3.6). To calculate this contribution, we follow the classic depth-porosity relationship $\theta_z = \theta_0 \times e^{-cz}$ from Sclater & Christie (1980), where φ is porosity, z is depth below the seafloor and c is the compaction coefficient (see Table 3.1 for parameter values). The potential contribution of compaction to post-MSC subsidence is large due to the exceptional sediment thickness in the WAB. The presence of undercompacted shales in the WAB drives mud diapirism deforming the Messinian Surface, and is sourced from deep Langhian deposits (SU3 from (Do Couto et al., 2016). The depth of this unit (5 seconds TWTT, over 5 km depth) means that it was not in the depth range where significant compaction takes place in shales (top four kilometres), so the presence of these undercompacted sediment has a small effect on the accuracy of our post-Messinian compaction estimates. Above the Langhian shales, the WAB fill becomes more siliciclastic in nature, dominated by marls and sands intercalated by marine conglomerates (Do Couto et al., 2016). We test for sensitivity of compaction to Miocene sediment lithology by applying parameters ranging from pure sand to pure shale, while for our reference model we apply compaction parameters for a mixed sand-shale lithology from Sclater & Christie (1980).

Thermal subsidence occurred in the Alboran Basin since the MSC as a response to extension that varied in age and magnitude over the basin. We consider the domains consisting of extended continental crust (West Alboran Basin, Malaga Basin and South Alboran Basin) and constrain the magnitude of post-MSC subsidence applying the instantaneous stretching model by McKenzie (1978) (see section 2.2, Figure 2.5). Based on the recorded ages for extensional pulses described above, we place an upper and lower limit on the stretching age at 6 Ma and 21 Ma to test for the sensitivity of our reconstructed topography to this parameter. In order to estimate the amount of stretching each subbasin underwent, we assume a pre-stretching crustal thickness of 40 km, and compute the stretching factor (β) based on the current basement thickness as reported by Gómez de la Peña et al. (2018). We then calculate the end-member thermal subsidence values by applying the smallest β and oldest stretching age for the lower thermal subsidence limit, and the largest β and youngest stretching age for the upper limit. For our reference model, we apply a value in between the extremes calculated in this way. Ages and β values are reported in Table 3.2. In the East Alboran Basin, the magmatic nature of the crust means that a continental stretching model is not applicable and much higher thermal cooling values can be expected. As an upper limit for thermal subsidence on the volcanic arc, we apply the Mid-Ocean Ridge cooling and subsidence curve by Stein & Stein (1992). From this curve, applying opening at 6 Ma, we derive an upper limit of 900 m thermal subsidence since the MSC in the East Alboran Basin.

As volcanic activity started well before 6 Ma, we place a lower limit for the EAB at 400 m, and apply an intermediate value of 600 m for the reference model.

	Basement thickness range (km)	Stretching Factor range (-)	Extension age range (Ma)	Thermal subsidence (m) (reference model)	Thermal subsidence range (m)
North Africa	*25-55*	-	-	**-**	**-**
Iberia	*20-50*	-	-	**-**	**-**
West Alboran Basin	*4-6*	*6.6-10*	*6-21*	**350**	**150-485**
Malaga Basin	*18-20*	*2-2.2*	*6-21*	**140**	**100-185**
South Alboran Basin	*25-30*	*1.3-1.6*	*6-21*	**70**	**60-80**
East Alboran Basin	*10-19*	-	*6-11*	**600**	**400-900**

Table 3.2. Range of basement thickness, stretching factors, and plausible ages for extension tested in thermal subsidence calculation (inputs). Resulting thermal subsidence in bold.

The Messinian surface has undergone tectonic deformation due to convergence (García-Dueñas et al., 1992; Martínez-García et al., 2017). The Alboran Ridge is a mostly post-MSC tectonic feature that underwent shortening on reactivated faults by tectonic inversion (Comas et al., 1999; Martínez-García et al., 2017; Estrada et al., 2018). The total shortening on the ridge has been estimated as 16±4.7 km on the basement fault and an additional 2 km on minor faults (see Figure 3.7 A). The resulting uplift led to loading of the crust, which we restore using a block with a maximum height of 1 km and a density of 2700 kg/m^3. The geometry of the tectonic block used is illustrated in Figure 3.7 D, along with interpreted profiles based on seismic lines interpreted by (Gómez de la Peña et al., 2022) (Figure 3.7 A) and this work (Figure 3.7 B,C).

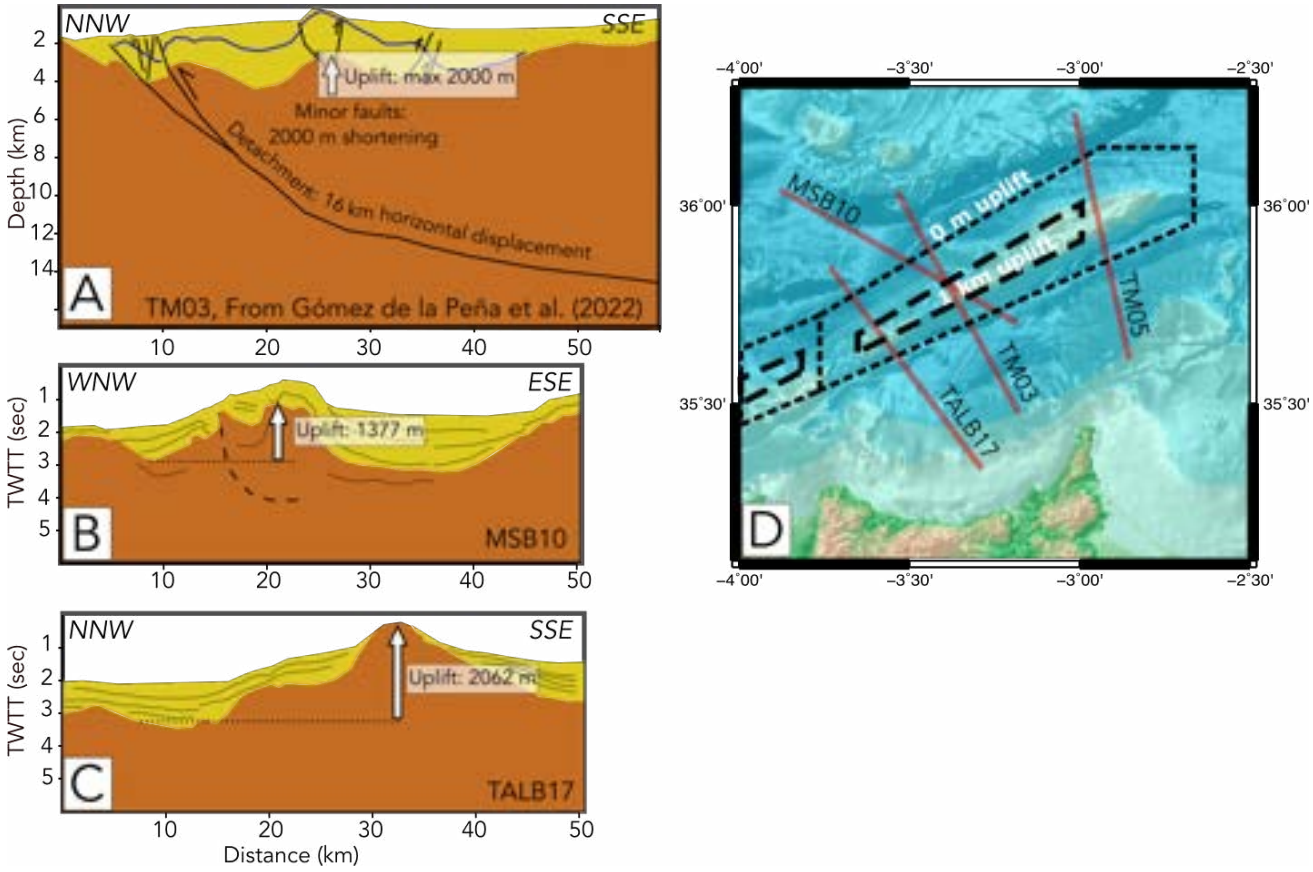

Figure 3.7. Estimation of vertical and horizontal tectonic deformation on the Alboran Ridge used to determine the tectonic load removed in topographic reconstruction. A-C: sketches from interpreted seismic profiles, including uplift estimates from this study. D: Map illustrating the geometry of the tectonic block used in our restoration, and locations of seismic lines crossing the Alboran Ridge.

3.4. Results

In this section we describe the main contributions to post-MSC vertical motions and restored topography for our reference model, as well as the uncertainty observed within our parameter range. For the reference model, as described above, we apply a EET value of 10 km in the offshore Alboran and 30 km around the Strait of Gibraltar, A mixed sand/shale compaction curve for Miocene sediment, and intermediate magnitude thermal subsidence as reported in Table 3.2. After restoration correcting the current depth of the Messinian surface for post-MSC sediment accumulation, tectonics and thermal subsidence (panels A, C, D and E in Figure 3.8) we obtain the topography of the Alboran Basin filled at normal global sea level (blue in Figures 3.9A, 3.9B and 3.10, Figure 3.11A). If we then compensate the topography also for subsidence in response to flooding of the basin after the MSC lowstand (panel B in Figure 3.8) we arrive at the potential topography while the basin was subaerially exposed (red in Figures 3.9A, 3.9B and 3.10, Figure 3.11B). In Figure 3.8, we see that in the West Alboran Basin the largest contributors to post-MSC subsidence are flexural-isostatic and compaction responses to Plio-Quaternary sediment accumulation (Figure 3.8A and D), while in the East Alboran thermal subsidence is the principal component of vertical motion (Figure 3.8E). A desiccated Alboran Basin would be shallower by up to 300 m than a basin filled at global sea-level (Figure 3.8B).

Figure 3.9 provides an overview of the depth and uncertainty of the restored topography across the Alboran Basin for a profile along the Zanclean Channel (Figure 3.9 A, C, D) and one crossing the East Alboran Basin North to South (Figure 3.9 B,D,F). Along with the restored depth range for both the full basin and desiccated basin (Figure 3.9 A, B) we provide the magnitude of subsidence contributions along these profiles for each step in our restoration (Figure 3.9 C, D). Both the West and East Alboran reach significant depths, being over 1000 m deep for the full basin scenario in every tested scenario (Figure 3.9A). The topography across the east Alboran Basin shows a potentially shallower basin, with part of the Malaga Basin and Alboran Ridge being subaerially exposed in a full basin scenario. The South Alboran Basin however reaches depths of over 1000 m in our restoration (Figure 3.9B).

In the East Alboran Volcanic Arc the uncertainty of our reconstruction is largest due to its poorly constrained thermal subsidence component that we estimate ranging from 400 to 900 meters. The uncertainties induced by variation of EET and compaction parameters are small in comparison, remaining in around the 100 m range (Figure 3.9 C, D) due to the relatively thin Miocene and Plio-Quaternary sediment cover in this region (Figure 3.5 B).

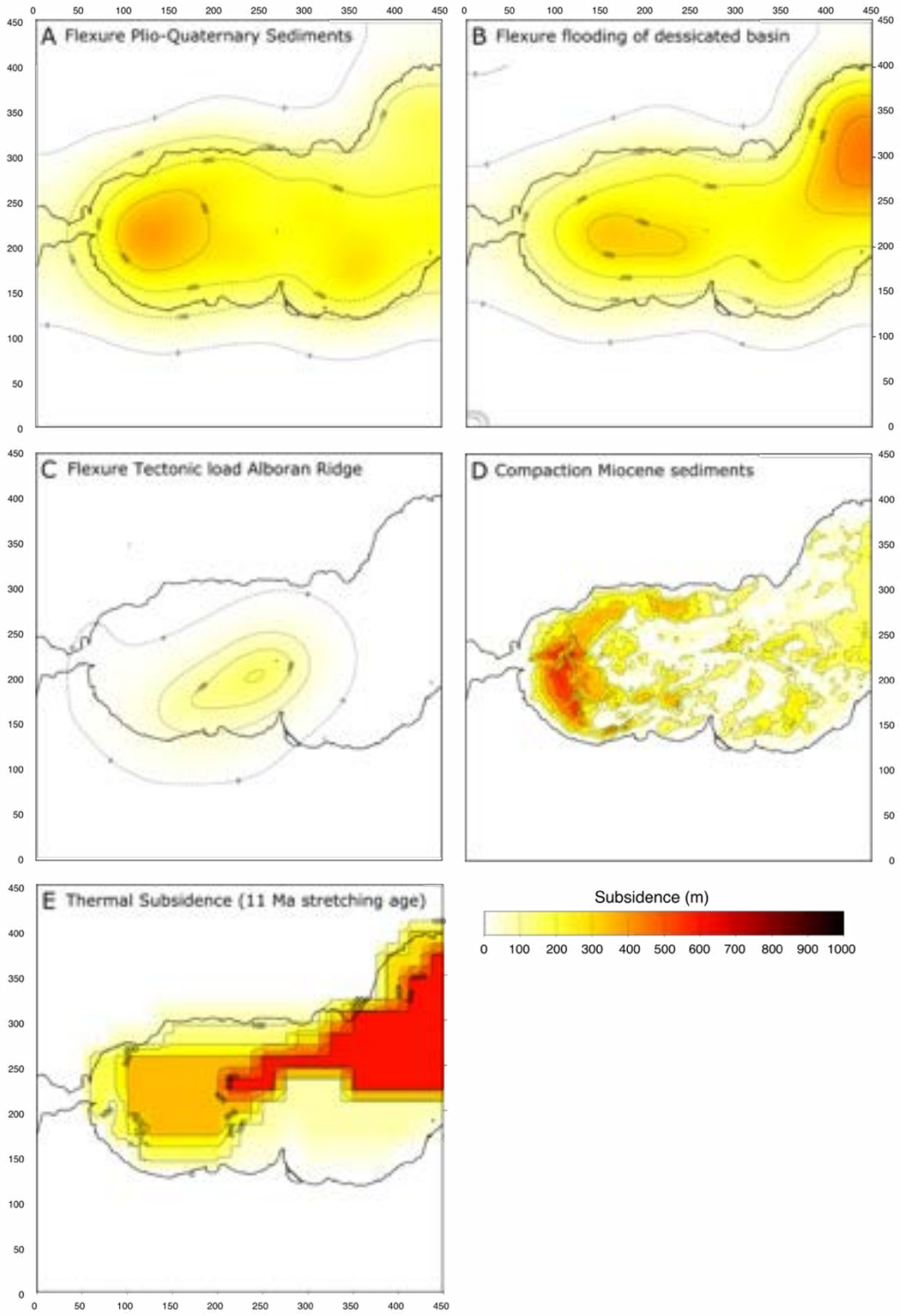

Figure 3.8. Subsidence components affecting the Alboran Basin since the MSC for reference model. A: Flexural-isostatic response to Pliocene-Quaternary sediment accumulation (step A in Figure 3.6). B. Flexural-isostatic response to the reflooding of the Alboran Basin from a -1500 m water level (step E in Figure 3.6). C: Flexural-isostatic response to tectonic shortening on the Alboran Ridge building 1 km topography (step B in Figure 3.6). D: Compaction of Miocene sediment by burial during the Pliocene-Quaternary (step C in Figure 3.6). E: Thermal subsidence after extension and magmatic activity (step D in Figure 3.6).

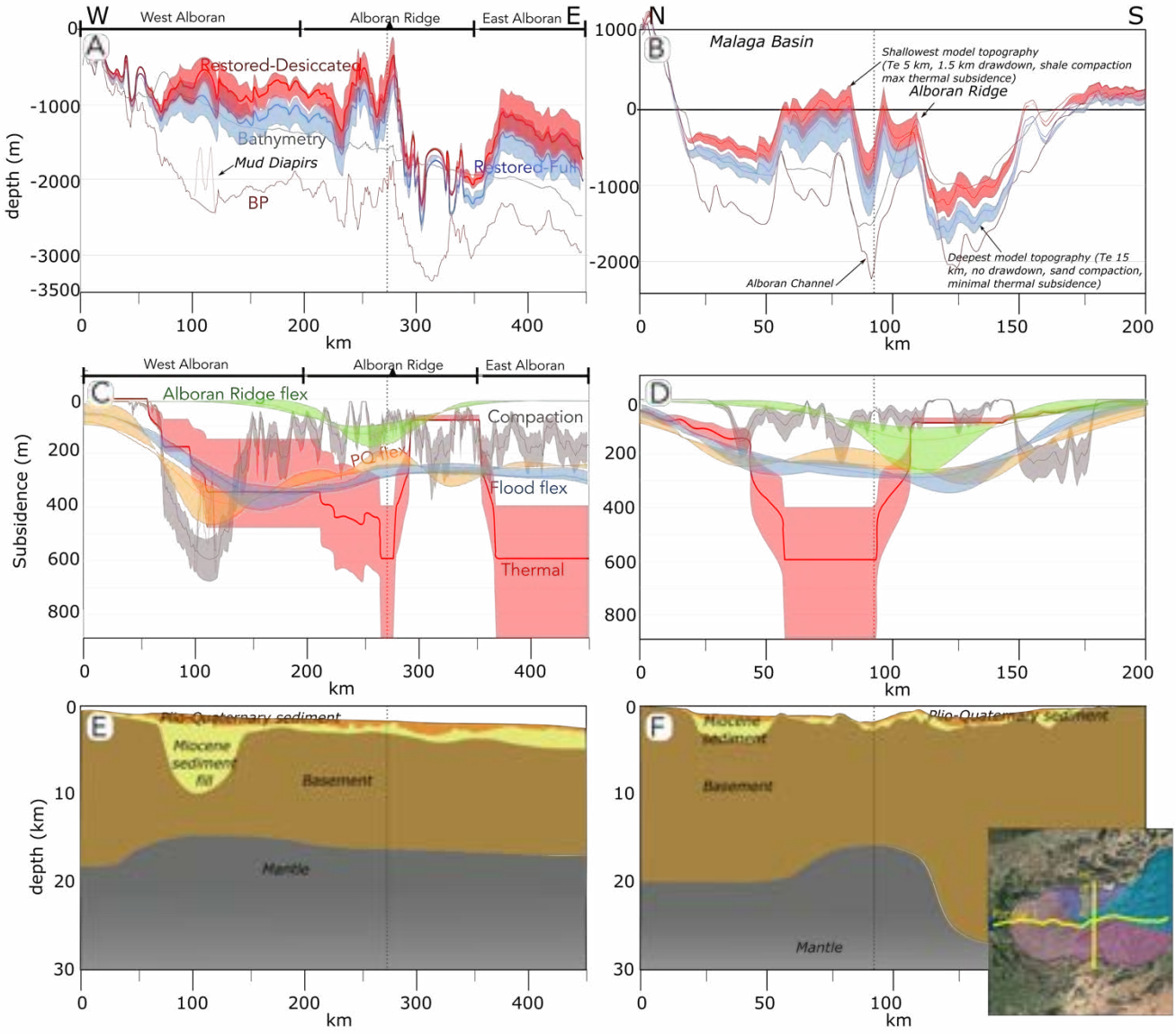

Figure 3.9. Results and uncertainty in Messinian topography and vertical motions, and current crustal structure along profiles following the Zanclean Channel and crossing the East Alboran North to South. See inset map for locations of Profile 1 (A, C, E) and Profile 2 (B, D, F). A,B: Depth of reference model (lines) and uncertainty (swaths) of modern and restored surfaces. Grey: current bathymetry. Dark red: current depth Base Pliocene(BP)/Messinian Surface. Blue: Restored depth of the Messinian topography for the water-filled basin at global sea level. Red: Restored depth of the Messinian topography for the basin during the Messinian lowstand with the water level at -1500 m. C,D: Magnitude in reference model (lines) and uncertainty (swaths) of post-MSC subsidence components. Yellow: Flexural-isostatic response to Pliocene-Quaternary sediment accumulation. Grey: Compaction of Miocene sediment by burial during the Pliocene-Quaternary. Green: Flexural-isostatic response to tectonic shortening on the Alboran Ridge building 1 km topography. Blue: Flexural-isostatic response to the reflooding from a -1500 m water level. Red: Thermal subsidence. E,F: Sketch crustal geometry with thickness after Gómez de la Peña (2018) and Miocene and Plio-quaternary sediment fill. Dashed vertical line: intersection point profiles 1 and 2.

The changes of the average depth along the basin across a 150 km wide swath for our parameter range is illustrated in Figure 3.10, for the full basin scenario (blue) and the desiccated basin scenario (red). We observe an increase of the basin depth in the West Alboran Basin and a basin depth varying within a range of approximately 500 in the Central/East Alboran domains. In all tested scenarios, the average depth is over 250 m over almost the entire basin. For the full-basin scenario, this depth is over 500 m.

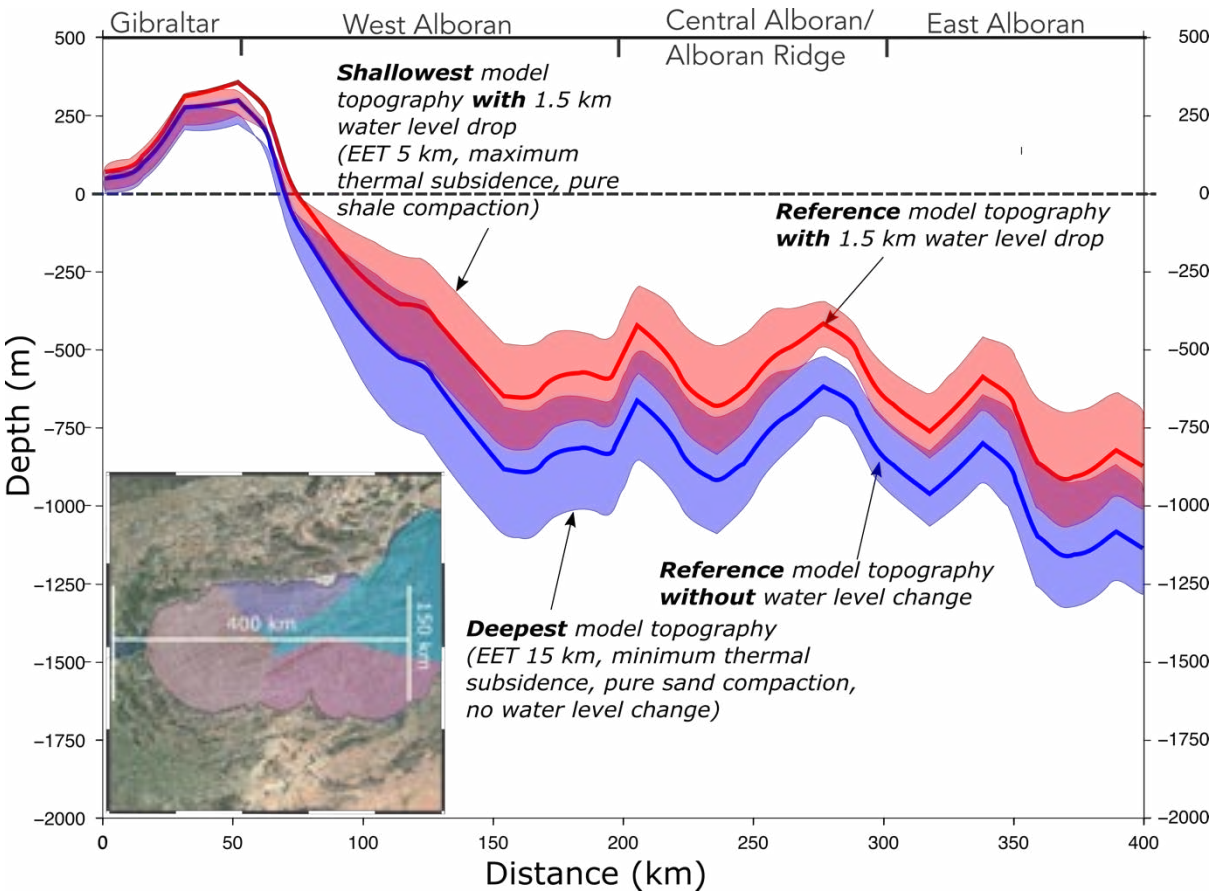

Figure 3.10. W-E profile of the average depth across a 150 km wide swath of the basin. Lines are for the reference model, swaths representing the uncertainty between the most extreme model scenarios within our parameter range as presented in Tables 3.1 and 3.2. Blue: Restored depth of the Messinian topography at normal global sea level. Red: Restored depth of the Messinian topography during the Messinian lowstand with the water level at -1500 m. From these profiles, the average depth of the basin is over 250 m even in the shallowest modelled scenario. These results do not support a topographic barrier preventing water exchange from the West to the East Alboran Basin during the MSC.

The Zanclean Channel topographic profile (Figure 3.9 A) shows very irregular topography between kms 200 and 350, with a sharp drop around km 275 where the Yusuf fault meets the Alboran Ridge and the channel bends from a SW-NE trend towards NW-SE. This abrupt topographic change is related to the activity of the Yusuf fault during the Plio-Quaternary and development of the Yusuf pull apart basin (Gómez de la Peña et al., 2022). The main branch of the Zanclean Channel has also been heavily deformed in this central sector by shortening

on the Alboran Ridge. The secondary southern branch of the Zanclean channel (dashed orange line in Figures 3.1 and 3.4) crosses the Al-Idrisi fault zone and the southern end of the Alboran Ridge. Along this southern channel branch, regions which were less tectonically affected are located at minimum depths of around 1 km for the desiccated basin scenario (see Figure 3.11 B)

Topography maps for our reference model are provided in Figure 3.11 for the full basin and desiccated basin scenarios. The full basin scenario (Figure 3.11 A) topography is over 500 m deep in the over 75% of the basins surface area, and reaches 1000 m in the eastern most part of the West Alboran, Malaga and large parts of the East Alboran basins. Parts of the East Alboran Volcanic Arc and the southern limit of the Malaga Basin would be subaerially exposed even at global water level.

In the desiccated basin (Figure 3.11 B), our restored depth is generally shallower by up to 300 m, and a drawdown of 1500 m would completely expose the West Alboran, Malaga and South Alboran basins. Potentially most of the East Alboran Basin would also be exposed.

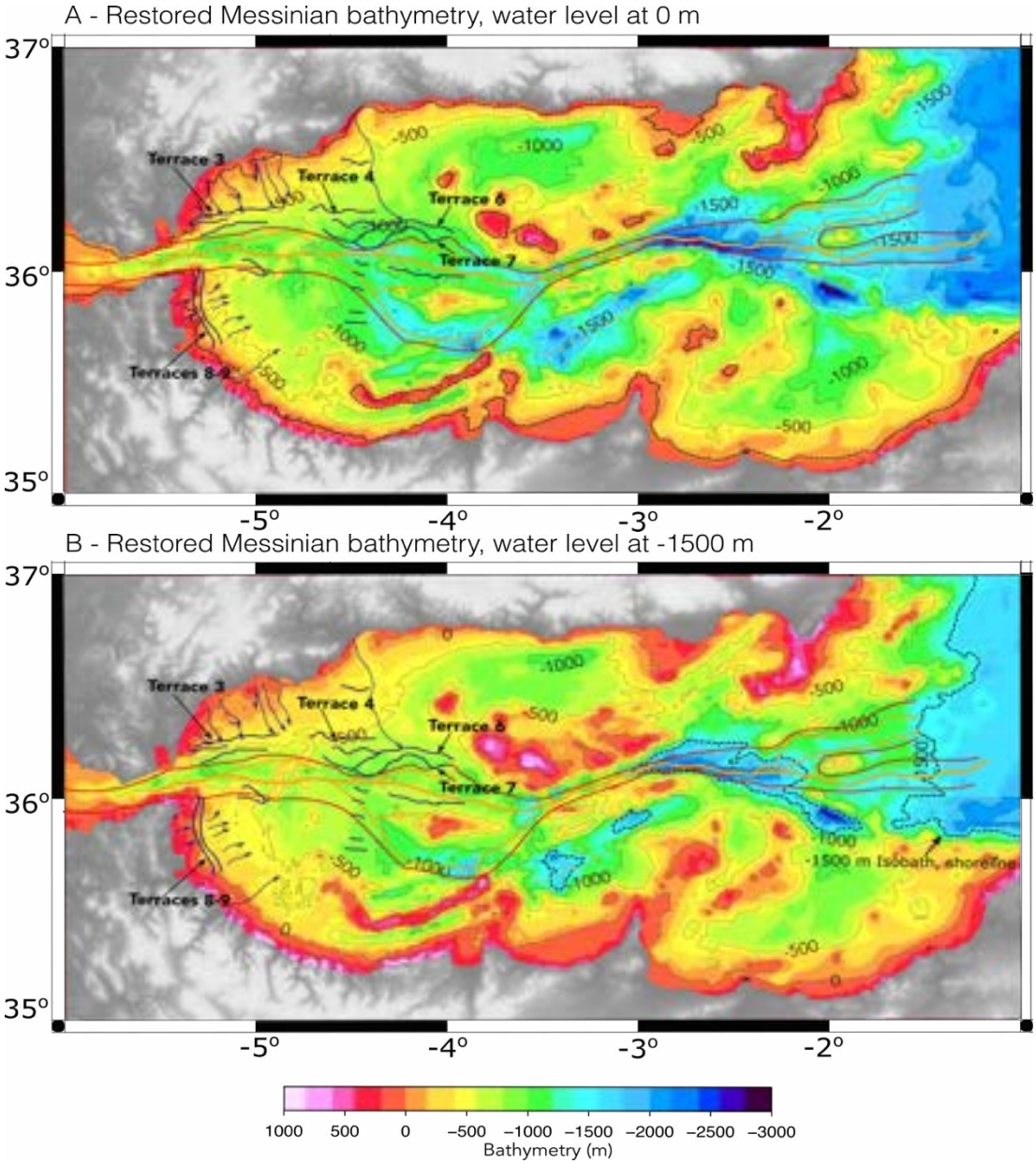

Figure 3.11. Restored Messinian bathymetry of the Alboran Basin for our reference model (EET = 10 km, mixed shale/sand compaction, thermal subsidence for extension at 11 Ma). In red the Zanclean channel, in orange the main flood paths and in purple the Messinian Terraces from Estrada et al. (2011). Panel A: Messinian bathymetry for a full Alboran Basin at global sea level (0 m). B: Messinian bathymetry for a desiccated Alboran Basin with the water level at -1500 m. The loss of the water isostatic load causes a shallower bathymetry during the lowstand.

3.5. Discussion

3.5.1. MSC paleotopography

The results of the topographic restoration indicate that parts of the Alboran Basin were up to 500 m shallower in Messinian times than the modern day for a water-filled basin scenario, but already reached depths of over a kilometre and was more than 500 m deep on average before the onset of the MSC. From the restored depth of the West Alboran Basin, we see that the basin locally reached depths of over 1 km if filled with water (Figure 3.11 B), and slightly shallower (between 500 and 1000 m deep) during a potential lowstand, implying the seafloor would be completely exposed in this region if disconnection occurred in the Strait of Gibraltar region and water level dropped by more than 1 km. Although large uncertainty in the East Alboran Basin depth arises from the thermal subsidence, it is possible that this region was significantly shallower than the Western Alboran Basin. This shallower East Alboran topography might have caused a pool of marine water at a relatively high level soon after the onset of flooding to form in the West Alboran, while water level rose to the level of the Volcanic Arc. Such intermediate pools or basins have been reported before in megaflooding scenarios such as the Kuray Basin for the Altay glacial outburst floods (Bohorquez et al., 2016). A variety of morphological features have been described related to this type of scenario, including large gravel dunes or mega-ripples related to flow whirls, although so far, such features have not been identified in the Alboran Basin and are probably too small to be identified in the currently available resolution of seismic data.

In the analysis presented in this work, the possible contribution of dynamic topography due to the subducting Gibraltar slab has not been accounted for. Although the methodology applied here does not allow to quantitatively analyse this contribution to topographic changes since the MSC, here we will briefly discuss its implications based on the timing and magnitude as constrained by other authors. The tearing Gibraltar slab and resulting flow of mantle material is the main plausible contributor to dynamic topography, and in addition an isostatic effect is expected above the region where the slab was originally attached, as the weight of the slab is suddenly removed upon tearing (Boonma, 2021). From the location of the slab edge along which tearing took place which is positioned underneath the Betics onshore (Garcia-Castellanos and Villaseñor, 2011; Mancilla et al., 2015) and the apparent short distance over which these isostatic and dynamic effects are expressed [approximately 50 km according to Garcia-Castellanos et al. (2002) and Boonma (2021)] it seems unlikely that these vertical motions had a large effect on the central part of the Alboran Basin, which is located about 150 km from the slab edge (see Figure 3.3). From the restored topography in a full-basin scenario, we can derive that the subsidence component by slab effects required to put the East Alboran region at global sea-level and form a topographic barrier restricting Atlantic-Mediterranean exchange is on average over 500 m (see Figure 3.10). As the restored topography in the region already accounts for a potential 900 m of post-MSC subsidence by

cooling of volcanic material, such a large subsidence component appears unlikely. Instead of a completely subaerially exposed Volcanic Arc region, the restored topography presented in this work envisions an archipelago of volcanic islands with deep seaways in between, facilitating mammal migration before and during the MSC (Gibert et al., 2013) but not presenting the bottleneck for Mediterranean-Atlantic water exchange. The erosion observed on these volcanic edifices (Booth-Rea et al., 2018) could be the result of the subaerial exposure during the Messinian lowstand phase, as a km-scale lowering of Mediterranean water level would potentially expose the region for over 200 kyr (see Figure 3.11B).

3.5.2. Where was the topographic barrier positioned?

Our results shed light on the plausibility of a MSC barrier disconnecting the east from the west Alboran basin during the MSC (Booth-Rea et al., 2018). In this scenario, the Western Alboran remained connected to the Atlantic forming a marine refuge throughout the MSC, and the land bridge between Africa and Iberia would explain the abundant transfer of terrestrial fauna from ~7 up to 3 Ma (see Figure 3.2 B). Geodynamically, the East Alboran land-bridge was supported by the consideration of isostatic equilibrium between a standard (6 km thick) oceanic crust formed at a Mid-Ocean Ridge at 2.5 km depth, and the present 16 km thick crust of equal density, which would be 2.5 km shallower and therefore subaerially exposed(Booth-Rea et al., 2018). For this, they follow a model similar to Lachenbruch & Morgan, (1990), calculating the depth at the volcanic arc as follows:

$$3.1)\ Hw_{arc} = Hw_{MOR} + \frac{\rho_m - \rho_c}{\rho_m - \rho_w} * (Hc_{MOR} - Hc_{arc})$$

Where:

Hw_{MOR}	= water depth at reference Mid-Ocean Ridge	(2.5 km)
Hw_{arc}	= water depth at volcanic arc crust	(km)
Hc_{MOR}	= crustal thickness at reference Mid-Ocean Ridge	(6 km)
Hc_{arc}	= crustal thickness at volcanic arc crust	(km)
ρ_m	= density mantle	(kg/m^3)
ρ_c	= density crust	(kg/m^3)

The water depth in the column in isostatic equilibrium with the reference Mid-Ocean Ridge is strongly dependent on the densities used for both the crust/lithosphere and the mantle/asthenosphere, as the contrast between these provides the buoyancy that determines its elevation. Booth-Rea et al. (2018) use a density of 2750 kg/m^3 for the crust and 3330 kg/m^3 for the mantle, yielding a strong buoyancy. In contrast, for the classic reference MOR column Lachenbruch and Morgan (1990) assign densities of 2800 kg/m^3 and 3200 kg/m^3 to the lithosphere and asthenosphere, respectively. Using these density values for crust and

mantle, calculated water depth at the Alboran Volcanic Arc crust would be around 600 m below sea level, instead of 0.

Kumar et al., (2021) apply coupled geophysical-petrological modelling to derive present-day thermal, density and compositional structure of the lithosphere and sublithospheric mantle. They obtain a density range in the mantle from 3295 kg/m^3 beneath the Moho to 3245 kg/m^3 at the LAB in the Alboran arc region (see Fig. 3.11 B, C). Applying this density range for the mantle, with a crustal density of 2800 kg/m^3 and a magmatic arc crustal thickness of 16 km results in calculated water depths at the arc of between 500 and 300 m according to equation 3.1. These calculations illustrate the strong sensitivity of calculated bathymetry to density contrast, and that assigning densities from previous model constraints yields a bathymetry substantially deeper than the results presented by Booth-Rea et al. (2018) Figure 3.12C also illustrates the high density of the lithospheric mantle underlying the Alboran Arc crust relative to the top of the asthenosphere, negatively contributing to the buoyancy of the arc and further increasing expected water depth.

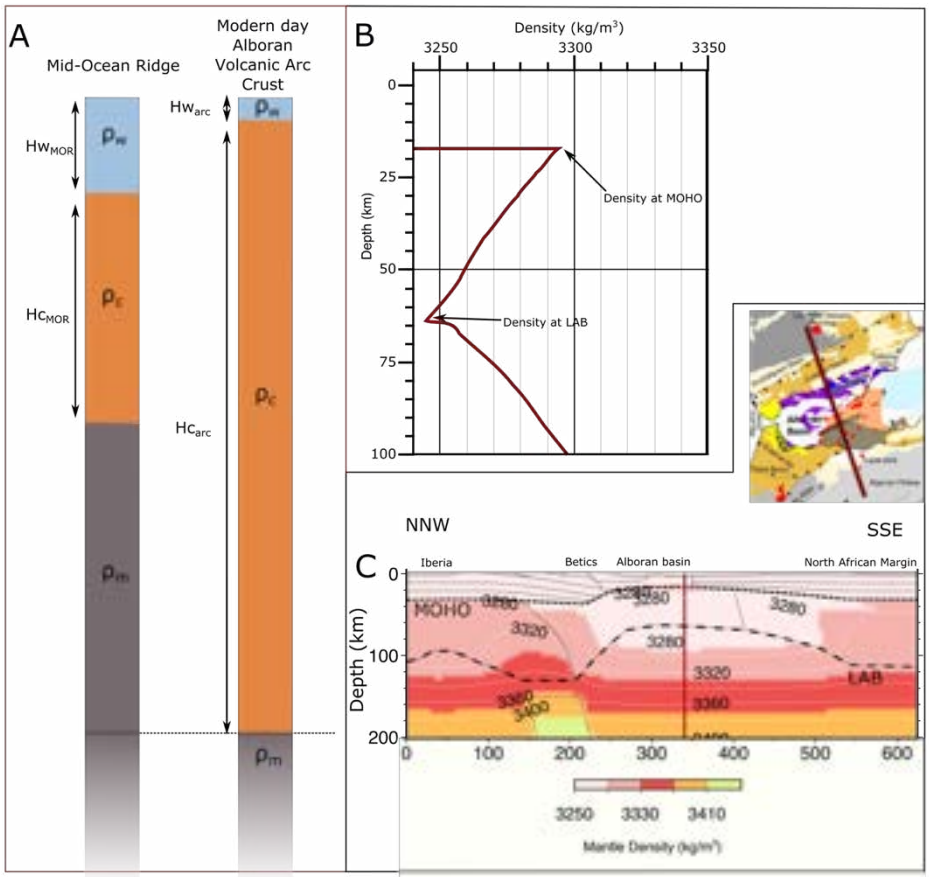

Figure 3.12. A: Comparative isostatic columns between a reference Mid-Ocean Ridge and the Alboran Volcanic Arc crust, illustrating the shallowing effect of increased crustal thickness compared to MOR following Airy isostasy, B: depth profile of mantle density at the Alboran Volcanic Arc at the position of vertical line in panel B, showing densities ranging from 3295 kg/m^3 at the Moho to 3245 kg/m^3 at the LAB. C: Profile of the modelled lithosphere and asthenosphere density based on geophysical-petrological modelling from Kumar et al. (2021) along a transect crossing the Alboran Basin (inset map).

Previous models have estimated the paleoelevation based on the crustal thickness and density as reported above, resulting in elevations at or above global sea level for the Alboran Volcanic Arc. The results presented here based on a reconstruction starting from the current depth of the Messinian Surface are strongly dependent on the thermal subsidence component. Although East Alboran heat flow is high at 100-150 mW/m^2 (Polyak et al., 1996), this corresponds to cooling ages of ~10-25 Ma, and plausible post-MSC thermal subsidence values for a MOR model certainly not exceeding our most extreme value of 900 m (for rapid cooling of a Mid-Ocean Ridge, see Methods section 2.2). In short, based on the crustal and lithosphere structure and thermal state of the Alboran Volcanic Arc, taking the current highly variable topography and 3-D geometry of the arc crust as a starting point and constraining the plausible contribution of each process causing subsidence in the region, our results indicate that the complete isolation of the East Alboran Basin from the West by this arc is highly unlikely.

3.5.3. Vertical isostatic motions at the Strait of Gibraltar

In the modern Strait of Gibraltar area, the topographic effect of the slab, which appears to be still attached slightly east of the strait (see Figure 3.3) (Garcia-Castellanos and Villaseñor, 2011; Mancilla et al., 2015; Jiménez-Munt et al., 2019) is not sufficiently understood. Whether the recent and ongoing uplift of the region recorded in the Rock of Gibraltar and nearby basins (Rodríguez-Vidal et al., 2004; Rico-García, 2007; Guerra-Merchán et al., 2014) was already active before the MSC determines whether the Strait of Gibraltar was open before the MSC, and possibly presented the last open Mediterranean-Atlantic gateway (Krijgsman et al., 2018; Bulian et al., 2021). Alternatively, if the strait was formed only at the end of the MSC potentially due to slab-driven subsidence (Jiménez-Munt et al., 2019) the Strait of Gibraltar area was a subaerially exposed tectonic arc and did not play a role in Atlantic-Mediterranean connectivity. While the exact position of the last connection is unknown, the impact of Messinian events on a shallow marine corridor in the Gibraltar Arc can be quantitatively examined from our results. Govers (2009) was the first to illustrate the isostatic effect of MSC events on the Strait of Gibraltar area, showing that the desiccation of the Mediterranean would lead to uplift in the gateway regions further isolating the Mediterranean. Coulson et al. (2019) highlight the additional effect of sea-level physics, illustrating that while global sea-level would rise by the addition of the water evaporated from the Mediterranean, sea-level in the vicinity of the Strait of Gibraltar would fall by up to 5 meters due to the loss of gravitational attraction of the Mediterranean water mass. From these considerations, the maximum uplift rate at the gateway that can be counteracted by erosion to keep the gateway open under fluctuating water level and salinity in the Mediterranean was refined to 1.5 mm yr^{-1} (Coulson et al., 2019). The uplift rate induced by desiccation from results presented here can be derived by evaluating the total uplift resulting across the Gibraltar Arc and dividing this by the time required for the development of a flexural response. This timescale for

development of flexure depends on Earth viscosity models, and ranges from 3 to 15 kyr according to Govers (2009). From the flexural-isostatic response to the flooding (which is the opposite effect of a desiccation) we can see that uplift in the Gibraltar arc ranges from around 40 +/- 10 m in the outer (towards the Atlantic) region of the Arc, and is >100 m in the inner (towards Mediterranean) parts (see Figure 3.8B). A minimum induced uplift rate using a 40 m uplift over 15 kyr, yields a rate of 2.67 mm yr^{-1}. This rate is higher than the critical uplift rate thought to be required to permanently close the gateway during uplift/erosion competition proposed to regulate connectivity during the MSC stage 1 (Garcia-Castellanos and Villaseñor, 2011; Coulson et al., 2019). Therefore, the sill rebound in response to an initial drawdown (possibly driven by temporal disconnection in response to tectonics or eustatic changes) is an efficient mechanism to prevent subsequent reflooding from the Atlantic until the sill is lowered either by erosion, tectonics, gravitational effects of the slab, or isostatic subsidence due to filling of the Alboran Basin by waters of a non-marine origin (i.e., Lago Mare). This confirms the “choking” effect proposed by Govers (2009).

3.5.4. Original depth of erosion in the West Alboran

The depth of the terraces observed in the West Alboran Basin Messinian Surface can potentially inform us on the water level during the MSC. The erosional features linked to the MSC in this region occur at a wide depth range in our reconstructed topography. Terraces 8, 9, 3 and 4, (Figures 3.1,3.4) which are located furthest from the WAB depocenter and towards its margins, are found at a range of reconstructed depths between 200 to 830 m, accounting for the uncertainty in our restoration (see Figure 3.13 E). Terraces 6 and 7 which are located in the deepest part of the basin and associated with the Zanclean Channel are restored to depths between 610 and 1450 m. If these terraces represent Messinian shorelines, their true depth of formation would be somewhere in between the desiccated and water-filled scenarios, as they would imply West Alboran Basin partially filled with water. The wide range of depths observed in our restored topography cannot be linked to a single, stable Messinian water level, as the variation of depths between terraces for each modelled scenario (>500 m, see Figure 3.13 E) is larger than the uncertainty range in the restoration within the tested parameter space. If the terraces were formed by coastal erosion (*ravinement*) during the Messinian drawdown stage, their various depths may reflect variable Mediterranean water level related to changes in the freshwater budget of the Mediterranean while it was disconnected from the Atlantic. The different features could also record different stages of the crisis, with the deepest erosion being related to a stage of complete exposure, while the shallower features record a base level during a stage of intermediate water level or were formed during reflooding.

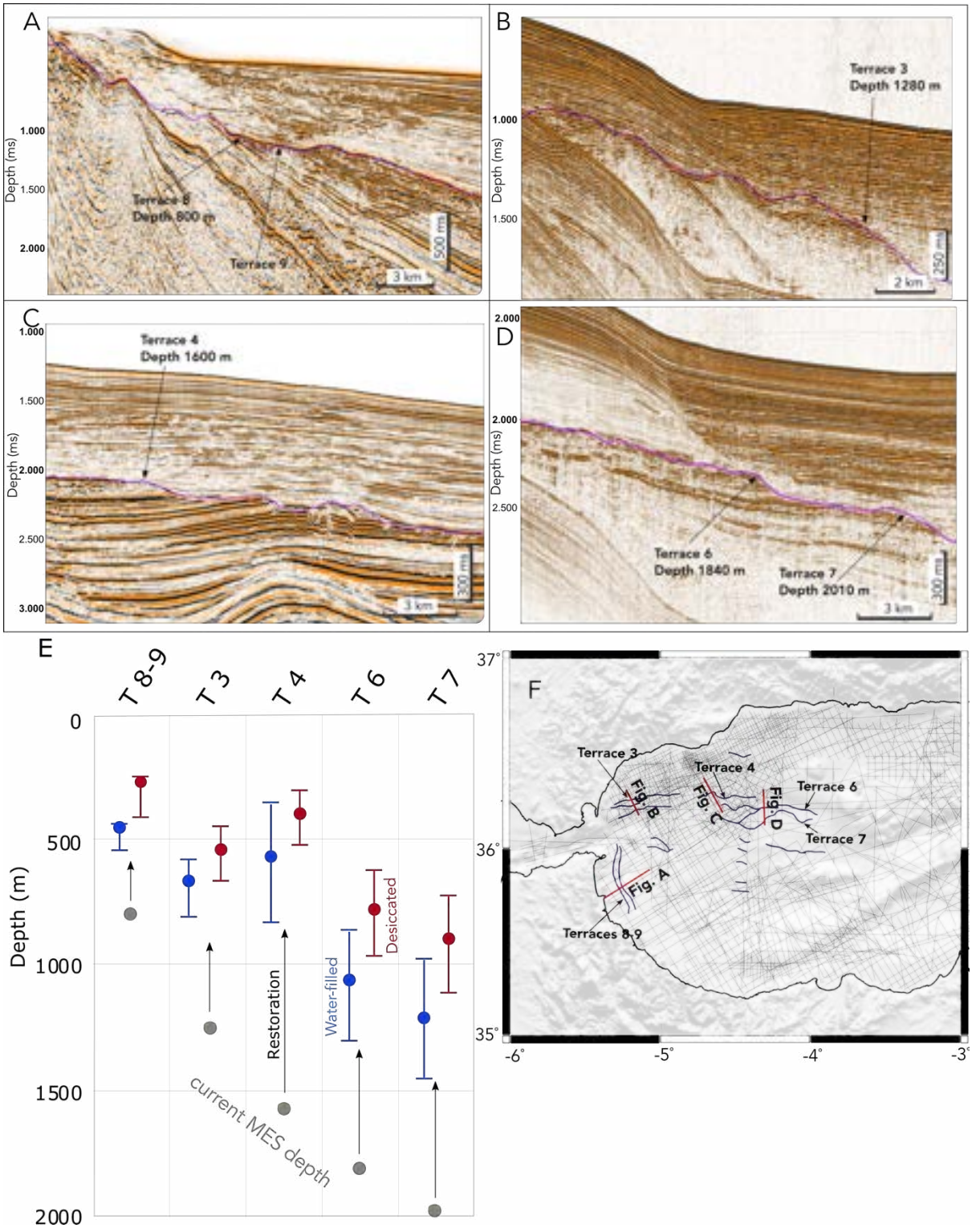

Figure 3.13. Depth restoration of terraces linked to subaerial erosion during the MSC lowstand and reflooding. A-D: Seismic profiles showing a selection of terraces in the Messinian Surface. E: Current (grey) and reconstructed depths of terraces for a water-filled Alboran Basin at global sea level (blue) and for a desiccated Alboran Basin (red). F: Locations of profiles.

3.6. Chapter conclusions

In the light of the results of our paleotopographic reconstruction and considering the uncertainties and limitations of my analysis, I draw the following conclusions:

1. How deep where the different regions of the Alboran Basin during the MSC?

The Alboran Basin reached a depth of over 1000 m both in the Western and Eastern Basins during the MSC in the reference model, with an average depth of over 500 m during the full-basin stage, and an average depth of over 250 m during desiccation.

2. What was the depth range of erosional features in the Alboran?

Within the parameter range explored in this study, my results show that the terraces identified in the West Alboran span a depth range of at least 500 meters. This range is larger than the uncertainty of the results and therefore the terraces cannot be related to a single stable Messinian water level. The shallowest restored terrace (T8 in Figure 3.13) was positioned at about 300 m (uncertainty 250-550 m) below modern sea level, while the deepest restored terrace (T7 in Figure 3.13) is found at 1300 m (uncertainty 750-1500 m) below modern sea level. The axis of the erosional channels linked to the Zanclean Flood ending the MSC are constrained to depths of over 1000 m (after incision) in the reconstructed topographies

3. Where was the topographic barrier located?

Within the limitations of our modelling methodology, the range of paleodepth obtained for the East Alboran Volcanic Arc makes this an unlikely location for the topographic barrier separating the Atlantic Ocean from the Mediterranean Sea and causing the Messinian drawdown. The arc represented a relatively shallow region of the Alboran Basin with parts of the arc likely subaerially exposed, but with corridors in between reaching depths of hundreds of meters in between (Figure 3.11) and an average depth likely no shallower than 250 m (Figure 3.10). A dynamic topography component due to slab dynamic processes cannot be excluded, as a driver of closure of the Mediterranean from the Atlantic at the East Alboran Volcanic Arc, although I deem this highly unlikely (see discussion section 3.5.1).

4. What was the impact of a large sea-level drop on the Strait of Gibraltar topography?

The sudden drop in water level in the Alboran Basin induced isostatic rebound in the Gibraltar region with uplift rates of over 2.6 mm/yr. This rate is higher than the critical uplift rate that can be compensated by erosion in the gateway, confirming the “choking” effect of Alboran desiccation as proposed by Govers (2009) provoking a prolonged stage of isolation of the Mediterranean from the Atlantic.

Chapter 4: The Western Mediterranean Basins East of Alboran

In this chapter, I focus on the paleobathymetry of the Western Mediterranean, excluding the Alboran Basin (see Chapter 3). The Western Mediterranean Basins contain the full Messinian "Trilogy", providing an opportunity to investigate the progression of the entire MSC, and furthermore it consists of basins with depth ranging from marginal, to intermediate (Valencia Basin, Balearic Promontory), to deep (Provençal, Algerian Basins) which show clearly the draping and pinching out of MSC-related units, as well as their relationship with erosional surfaces. On this basis I identify paleoshorelines which, upon restoration, quantitively constrain the required drop in water level associated to these shoreline markers. I also investigate the implications of the restored bathymetry on the depositional circumstances for the halite present both in large quantities in the deep basins and in smaller patches spread over a wide depth range on the Balearic Promontory.

Highlights:

- Restored topography during the Messinian Salinity Crisis, including and excluding effects of a large water level drop.
- Water level estimates from restored elevation of potential paleoshoreline markers at −1,500 m for the bottom erosion surface, and −1,100 m for the Upper unit deposition.
- Halite was deposited or preserved in local topographic minima at various depths on the Balearic Promontory, their thickness being controlled by the depth of such depressions.

Results from this chapter have been published as:

Heida, H., Raad, F., Garcia-Castellanos, D., Jiménez-Munt, I., Maillard, A., & Lofi, J. (2021). Flexural-isostatic reconstruction of the Western Mediterranean during the Messinian Salinity Crisis: implications for water level and basin connectivity. *Basin Research*, *July*, 1–31. https://doi.org/10.1111/bre.12610

4.1. Chapter Summary

During the Messinian Salinity Crisis (MSC, 5.97-5.33 Ma), thick evaporites were deposited in the Mediterranean Sea associated with major margin erosion. This has been interpreted by most authors as resulting from water level drop by evaporation but its timing, amplitude and variations between subbasins are poorly constrained due to uncertainty in post-Messinian vertical motions and lack of a clear time-correlation between the marginal basin and offshore records. The Balearic Promontory and surrounding basins exemplify a range of responses to this event, from margin erosion to up to a kilometre-thick Messinian units in the abyssal areas containing the majority of the MSC halite. The Balearic Promontory contains unique patches of halite with thickness up to 325 m at intermediate depths that provide valuable information on water level during the stage of halite deposition. We compile seismic markers potentially indicating ancient shorelines during the drawdown phase: the first is marked by the transition from the MES to UU based on seismic data. The second is the limit between the Bottom Erosion Surface and abyssal halite deposits. We restore these shorelines to their original depth accounting for flexural isostasy and sediment compaction. The best fitting scenario involves a water level drop of ca. 1100± 100 m for the Upper Unit level and 1500±100 m for the Bottom Erosion Surface level. According to our results, halite deposition began in the Central Mallorca Depression at 1300-1500 m depth, perched hundreds of meters above the deep basins, which were at 1500-1800 m (Valencia Basin) and >2900 m (Algerian Basin). The hypothesis that erosion surfaces were formed subaerially during the drawdown phase is consistent with a model of halite deposition before/during the water level drop of at least 1000 m, followed by the deposition of the Upper Unit until the MSC is terminated by reinstatement of normal marine conditions.

4.2. Introduction

4.2.1. The MSC in the Western Mediterranean

In the Western Mediterranean, the full Messinian "trilogy" of evaporitic units and sediment is present, but the chronology and environmental conditions during the various depositional and erosional stages are still under debate. For example, some authors suggest that deep-basin halite was formed synchronous to the PLG in stage 1 in a salinity-stratified water column (Van Ceuvering et al., 1976; Simon and Meijer, 2017; Meilijson et al., 2019). Evaporite deposits in the deep basins of the Western Mediterranean have not yet been drilled beyond their topmost layer, and due to the extreme conditions during their deposition they lack biostratigraphic water depth proxies. The main evidence supporting water level variations are erosional surfaces observed in outcrops in marginal basins (Decima and Wezel, 1967; Dronkert, 1976; Pagnier, 1976; Vai and Lucchi, 1977; Ott d'Estevou and Montenat, 1990; Riding et al., 1991; Rouchy and Saint Martin, 1992; Dabrio and Polo Camacho, 1995; Clauzon et al., 1996, 2015; Conesa and Badinot, 1999; Fortuin et al., 2000; Krijgsman et al., 2001; Bourillot et al., 2009, 2010; Roveri et al., 2009; Dela Pierre et al., 2011; Do Couto et al., 2015) and in the offshore seismic record underlying, intercalated in, and on top of the Messinian deposits, pointing to a kilometric water level drop or (near) desiccation of large parts of the Mediterranean (Ryan, 1976; Ryan & Cita, 1978;Lofi et al., 2005, 2011a, 2011b; Maillard et al., 2006; Raad et al., 2020). The MSC ended abruptly with a geologically-sudden reestablishment of open marine conditions, purportedly due to reflooding through the Strait of Gibraltar causing a deeply eroded channel in the Alboran basin and chaotic deposits associated with the flooding event (Blanc, 2002; Garcia-Castellanos et al., 2009, 2020; Estrada et al., 2011; Micallef et al., 2018a). However, some authors have argued for much smaller water level variations (<200 m) and alternative mechanisms for the formation of incised channels (Roveri et al., 2014b). The widespread occurrence of brackish lacustrine "Lago Mare" deposits on top of the deep and marginal evaporites has led other authors to suggest that the basins were already connected at high water level before the end of the Messinian (Stoica et al., 2016; Andreetto et al., 2020, 2021), which would be at odds with an outburst flood from the Atlantic Ocean.

Messinian erosional surfaces and deposits have been affected by subsidence and possibly phases of rebound since the start of the MSC due to loading by sediment deposition and water level changes (Ryan, 1976, 2011; Norman and Chase, 1986; Gargani, 2004; Govers et al., 2009). Backstripping (Watts and Ryan, 1976) is a classical technique used to calculate the isostatic and compaction effects due to sediment loading. Traditionally, this technique has been used to constrain the vertical motions related to tectonic loading by thrusting or extension, provided the availability of precise paleobathymetric measures. However, in areas where tectonic loading is negligible, it can a priori be inverted to constrain paleobathymetry (Amadori et al., 2018). The technique has been applied to constrain the original depth of the Messinian units and erosional surfaces in wells and along sections in the Gulf of Lions (Ryan, 1976), the Tertiary Piedmont Basin (Amadori et al., 2018), the Balearic Promontory (Mas et

al., 2018), and in the Ebro delta (Urgeles et al., 2011). This has led to drawdown estimates in the western Mediterranean of 1300 m of late-Messinian water level drop based on terrace formation in a fluvial erosion network (Urgeles et al., 2011) and a minimum of 800 m drawdown to facilitate faunal colonization of the Balearic Islands (Mas et al., 2018).

Except for Amadori et al. (2018), the aforementioned studies have been based on either local isostasy or 1D (cross-section) flexural isostasy. While a 2D (planform or pseudo-3D) technique was used by Govers (2009) and Govers et al. (2009), these studies were not designed to reconstruct the pre-MSC bathymetry nor reconstruct the shoreline positions. For this reason, paleobathymetric reconstructions based on erosional/depositional markers are only locally available in specific areas of the Western Mediterranean and their mutual consistency are difficult to evaluate.

In this paper, we aim at using a 2D (planform, pseudo-3D) flexural backstripping technique supported by an extensive set of seismic data to quantify Messinian and post-Messinian vertical motions, to constrain the paleodepth and the Messinian water level drop at the scale of the Western Mediterranean. To this purpose, we constrain the model with paleoshoreline indicators based on an extensive seismic dataset. The starting hypothesis of our study is therefore that these stratigraphic features were formed near the shore during the MSC. The depth range of the Valencia Basin and Balearic Promontory and their unique distribution of Messinian markers (Fig. 4.2) with erosion on the margins (Maillard et al., 2006, 2014; Urgeles et al., 2011; Driussi et al., 2015; Cameselle and Urgeles, 2017), Upper Unit in the Valencia Basin (Maillard et al., 2006) and a complete MSC trilogy in the deep basin (Fig. 4.2A) (Lofi et al., 2011a,b) provide an opportunity to constrain the progression of water level during the MSC in a region that covers the gap between shallow evaporite deposits (primary gypsum) and the deep (abyssal) salt deposits visible in the seismic record. A compilation of key MSC-related features including evaporite deposits and erosional features is presented in Figure 4.1.

4.2.2. Geodynamic setting

The Western Mediterranean comprises basins with distinct ages, tectonic styles and crustal nature. They formed as back-arc basins due to slab rollback of the retreating Apennines subduction in a general setting of N-S convergence between the African and Eurasian plates since the Miocene (Malinverno and Ryan, 1986; Mauffret et al., 1995, 2004; Martínez-Martínez and Azañón, 1997; Gueguen et al., 1998; Gelabert et al., 2002; Faccenna et al., 2004, p. 200; Jolivet et al., 2006; Schettino and Turco, 2006).

The Neogene Valencia Basin is a region of continental crust which was extended between 28 and 10 Ma (Bartrina et al., 1992; Roca and Guimerà, 1992; Watts and Torné, 1992a; Etheve et al., 2018), bounded by the Iberian Margin to the northwest and the Balearic Promontory to the southeast. To the east the Valencia Basin is bounded by the North Balearic Fracture Zone (Galdeano and Rossignol, 1977; Rehault et al., 1984; Maillard et al., 2020) which

accommodated the anticlockwise rotation of the Corsica-Sardinia-Calabria blocks with the emplacement of the oceanic crust of the Provençal basin between 22 and 16 Ma (Alvarez, 1972; Burrus, 1984; Gueguen et al., 1998; Speranza et al., 2002). Contrary to the Provençal Basin, the Valencia Basin extension did not attain the formation of oceanic crust but instead extension jumped to the southern side of the easternmost Betic range to form the Balearic promontory and open the Algerian Basin.

The Algerian Basin opening in the Miocene (16-8 Ma) has long been thought to be the result of the westward migration of the Alboran block due to rollback of the subducting Tethys plate (Lonergan and White, 1997; Rosenbaum et al., 2002). However, recent alternative models suggest that it can also be explained by back-arc spreading during the southwards retreat of the neotethyan subducted slabs (Vergés and Sàbat, 1999; Faccenna et al., 2004), ending before 8 Ma. It is separated from the Balearic Promontory by the Emile Baudot and Mazzaron Escarpments, structures that have been proposed to be the remnants of a transfer fault along which the Alboran domain migrated westward (Acosta et al., 2001; Mauffret et al., 2004).

With the exception of the Tyrrhenian Basin, all Western Mediterranean basins were mostly formed at the onset of the MSC (Ryan, 1976). The present-day thickness variations of the MSC units are therefore thought to be related to paleo-waterdepth and post-Messinian vertical movements (e.g. Lofi et al. (2011b)). Thin-skinned salt tectonics and subsequent deformation of the salt (diapirism) is another cause for the present-day thickness variation (CIESM, 2008; Dal Cin et al., 2016). Recent shortening has been reported between Alicante and Ibiza(Maillard and Mauffret, 2013), and post-MSC tectonics has also been reported in the Mallorca Island and in the CMD, interpreted in relation with strike-slip movements located in WSW-ENE narrow depressions. As these deformation affects the MSC markers only locally, so we do not consider this deformation in our basin-wide reconstruction.

Two distinct volcanic phases have been identified in the Western Mediterranean (Maillard et al., 1992; Martí et al., 1992). The first, mostly represented by calc-alkaline affinity, has been related to the emplacement of a volcanic arc of the SE-retreating subduction also observed in Sardinia, Corsica and Ligurian domains and is coeval to the Valencia rifting stage (late Oligocene-Early Miocene age), while the second stage is alkaline and represented by the Columbretes and the Southwest Mallorca Field on the Emile Baudot Escarpment (Late Miocene-Recent), and could be linked to regional decompression during extension (Martí et al., 1992; Acosta et al., 2001, 2004a; Réhault et al., 2012). This recent volcanism locally deformed the MSC deposits and erosion surface. The large extent of the volcanoes in the Valencia Basin surely affected the thermal history of the basin. Based on well data from the Catalan margin, these volcanic phases have been proposed to have counteracted general subsidence due to relaxation after the end of the main rifting phase at 10 Ma in the Valencia Basin (Watts & Torné 1992).

4.2.3. Messinian Salinity Crisis (MSC) stratigraphy

The distribution of the MSC sedimentary sequences is used to define paleoshoreline indicators that constrain our model. They have been identified and widely studied and described mainly from seismic datasets by several authors (Maillard et al., 2006; Camerlenghi et al., 2009; Lofi et al., 2011b; Urgeles et al., 2011; Driussi et al., 2015; Ochoa et al., 2015; Dal Cin et al., 2016; Cameselle and Urgeles, 2017; Lofi, 2018 and references therein; Pellen et al., 2019; Raad et al., 2020).

The deep basins of the Western Mediterranean (i.e. Provencal and Algerian Basins) contain the full MSC trilogy (e.g. Lofi et al., 2011b see also Fig. 4.1b), identified mainly through seismic reflection profiles with its components listed below:

- Lower unit (LU): age, origin and lithology remain unclear. It has been suggested to be a shale equivalent to Stage 1 PLG (Manzi et al., 2007, 2018).
- Mobile unit (MU): here considered representative of "Stage 2" lies conformably above the LU in the deep basins. Towards the limits with the intermediate depths (i.e. Valencia Basin), MU lies above pre-MSC sediment along a bottom erosion surface (BES) or Bottom Surface (BS) where conformable (Fig. 4.2A, C). Its upper boundary is conformable. The MU consist of up to kilometre-thick transparent seismic facies that is thought to contain mainly halite and it is highly deformed by salt tectonics. It pinches out everywhere on the borders of the deep basins (Fig. 4.2A-C, F).
- Upper unit (UU): deposited during "Stage 3" lies conformably above the MU in the deep basins, while towards the intermediate depths beyond the extent of MU it lies above the BS/BES. In the deep basins the upper boundary of the UU is conformable with the overlying PQ unit (TS), whereas in the intermediate Valencia Basin it is cut by a top erosion surface (TES) (Fig. 4.2A, D, E). The uppermost part of the UU has been drilled, and it is made of alternations of gypsum and clastic deposits (ODP initial reports volume 161; Ryan, 2009). Its thickness reaches ~1000 m in the deep basins (Fig. 4.2C; Lofi et al., 2011b), where it pinches out towards the slopes (Fig. 4.2B, F). In the Valencia Basin, the UU thins gradually from 500 m thickness (Fig. 4.2D, E) pinching out towards the Catalan and Ebro margins. Here the Bottom and Top Erosion Surfaces bounding the UU merge into the polygenic Margin Erosion Surface (MES).

Several interpretations in terms of water level change exist to account for the observed geometries and extent of erosional surfaces. We briefly describe those interpretations and present the scenario we adopt to test in our model. The depositional environment for the Lower Unit is hard to constrain, as its lithology is not known beyond its seismic reflectivity. There are no indications of water level variations during the deposition of this unit, and therefore we do not consider it as a separate stage in our topographic restoration. It is evident from well data in the Alboran Basin that restriction of the Atlantic-Mediterranean connection started affecting the depositional environment at ~7.2 Ma, well before the onset of evaporite deposition (Bulian et al., 2021).

A water level drop leading to margin erosion occurred after deposition of the PLG in the marginal basins (Krijgsman et al., 1999) and the MU precipitated from a brine formed under

conditions of restricted, but probable continuous connectivity to the Atlantic. MU deposition possibly started before and surely continued during the stage of water level drop, but without supply of marine waters from the Atlantic cannot have continued throughout a prolonged lowstand. Evidence for a change of deep brine precipitates to playa lake facies inside the halite unit is found in the Realmonte salt mine in Sicily (Lugli et al., 1999) although this might not be representative for the deep basin deposits. The amplitude of the water level fall is controversial, as it varies between a few hundred meters for some authors (Roveri et al., 2014a and references therein, 2014b) and more than one kilometre for others (Lofi et al., 2011b). Maillard et al., (2006) believe that it is during this kilometre amplitude water level drawdown that the BES was formed, due to subaerial exposure of the entire Valencia Basin.

Most authors believe that the emplacement of the UU happened during a rise in water level during the final MSC stage, causing its aggrading and onlapping geometry (Lofi et al., 2011a, 2011b). The onlaps of the UU are interpreted as indicators of successive paleoshorelines (Lofi et al., 2005).

For some authors, the nature of the TES in the Valencia Basin could be a result of dilution during the Lago-Mare phase, and/or subaerial exposure preceding the Zanclean reflooding (Escutia and Maldonado, 1992; Maillard et al., 2006). For others, this erosion is minor and can be found only locally due to the dilution during the Lago Mare event (Cameselle and Urgeles, 2017). A significant water level drop in Valencia Basin with unclear timing and magnitude is agreed upon (Maillard et al., 2006; Urgeles et al., 2011; Cameselle et al., 2014; Cameselle and Urgeles, 2017).

In the southwestern Valencia Basin, Cameselle & Urgeles (2017) identified a widespread Complex Unit locally overlain unconformably by a thin UU. The Complex Unit is interpreted here as a mass transport deposit resulting from destabilization of the slope during the first Messinian lowstand exposing the shelf and upper slope. Complex Units with different origin and timing are also present at the downslope mouth of Messinian valleys (Lofi et al., 2005; Maillard et al., 2006) and especially in the Gulf of Lions (Lofi et al., 2005).

On the Balearic Promontory, recent studies show the presence of widespread bedded units (Bedded Unit) and relatively thin salt patches (Maillard et al., 2014; Driussi et al., 2015b, 2015b; Raad et al., 2020). These units seem to be discontinuous between the Balearic Promontory and the surrounding deeper basins.

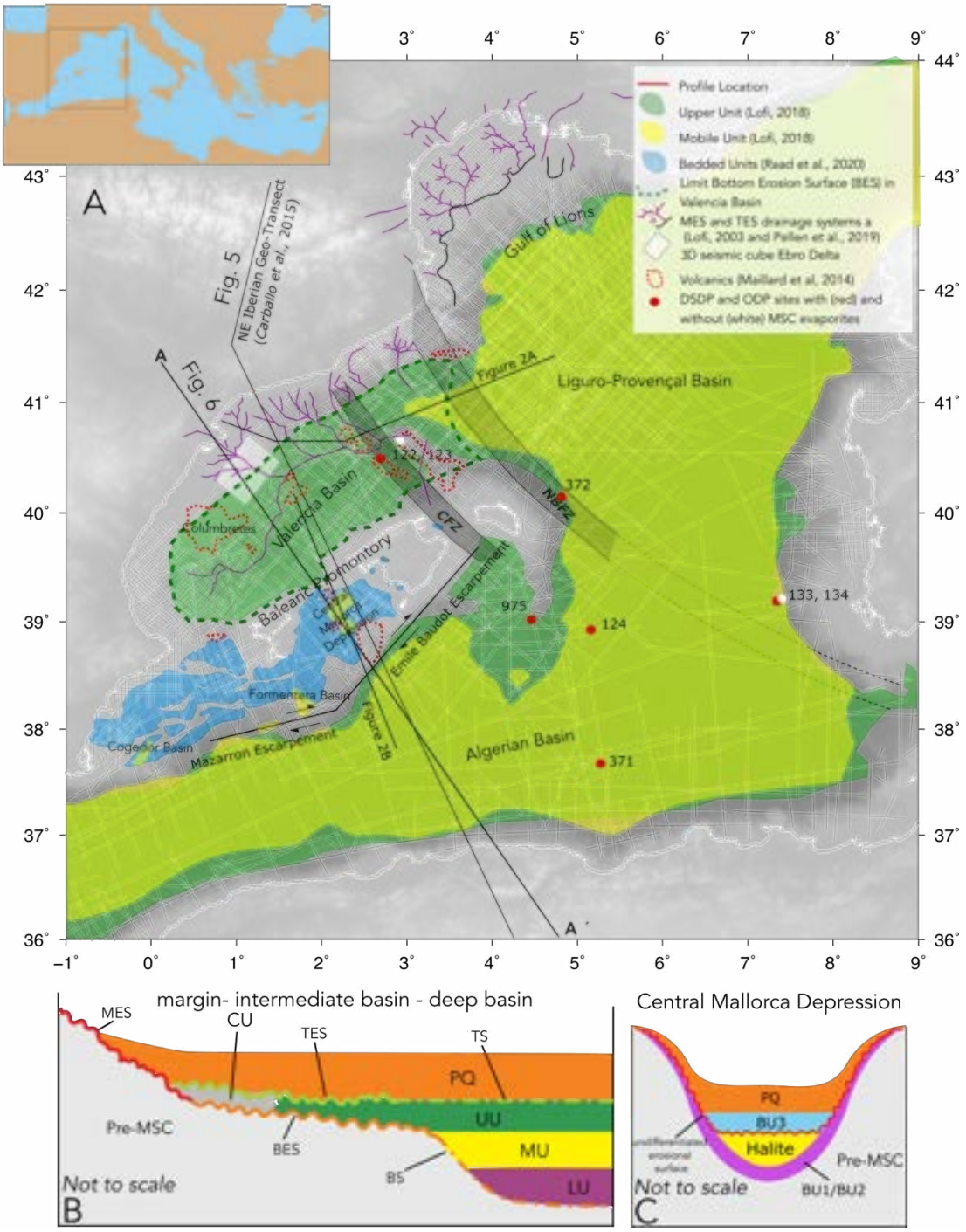

Figure 4.1. A: Topographic map of the Western Mediterranean area with the distribution of the main Messinian deposits and erosional features. It includes the main tectonic structures and locations of DSDP boreholes, seismic data used in this study (thin white lines), and location of the representative seismic profiles (Fig. 4.2) used for lithosphere characterization (Fig. 4.5) and the backstripping restoration (Fig. 4.6). CFZ: Catalan Fracture Zone; NBFZ: North Balearic Fracture Zone. B: Schematic cross section of the Western Mediterranean basin illustrating the present-day distribution of sedimentary units and surfaces after Lofi (2018). C: Schematic cross section of the Central Mallorca Depression (post) Messinian units (BU= Bedded Unit) and surfaces.

Raad et al. (2020) interpreted the MSC units of the Central Mallorca Depression as an undeformed analogue of the Sicilian MSC records. They recognized the equivalent of the PLG, salt and Upper Evaporites (UE). These authors suggest that the CMD was disconnected from the surrounding deep basins during the MSC water level fall. They identify a prominent erosional surface cutting the top of the PLG and of a salt unit in the depocenter (Fig. 4.1C). This surface lies at a present-day depth of ~1550 m below sea level (Fig. 4.2B)), and is interpreted as the result of an exposure or dissolution of salt in shallow water.

On Mallorca and Ibiza, the MSC record is mainly expressed by the terminal carbonate complex lying today between 30 and 60 m above sea level (Mas and Fornós, 2011; Maillard et al., 2020a). It is thought that the terminal carbonate complex formed close to sea level, starting from stage 1 of the MSC contemporaneous to the PLG (Cornée et al., 2004; Roveri et al., 2009; Mas and Fornós, 2013). Onshore drillings in the Palma de Mallorca basin also evidenced the presence of stage 1 PLG (Rosell et al., 1998; García-Veigas et al., 2018) lying below the PQ sediment, only a few tens of meters below sea level. Local water level recorded by phreatic overgrowths on speleothems in caves on the SE coast of Mallorca were recently established to have been at 33.3 and 31.8 m above modern just before and during the Stage 1 of the MSC respectively (Dumitru et al., 2021), although these were not corrected for vertical motions induced which the authors point out is necessary to properly interpret these water level results.

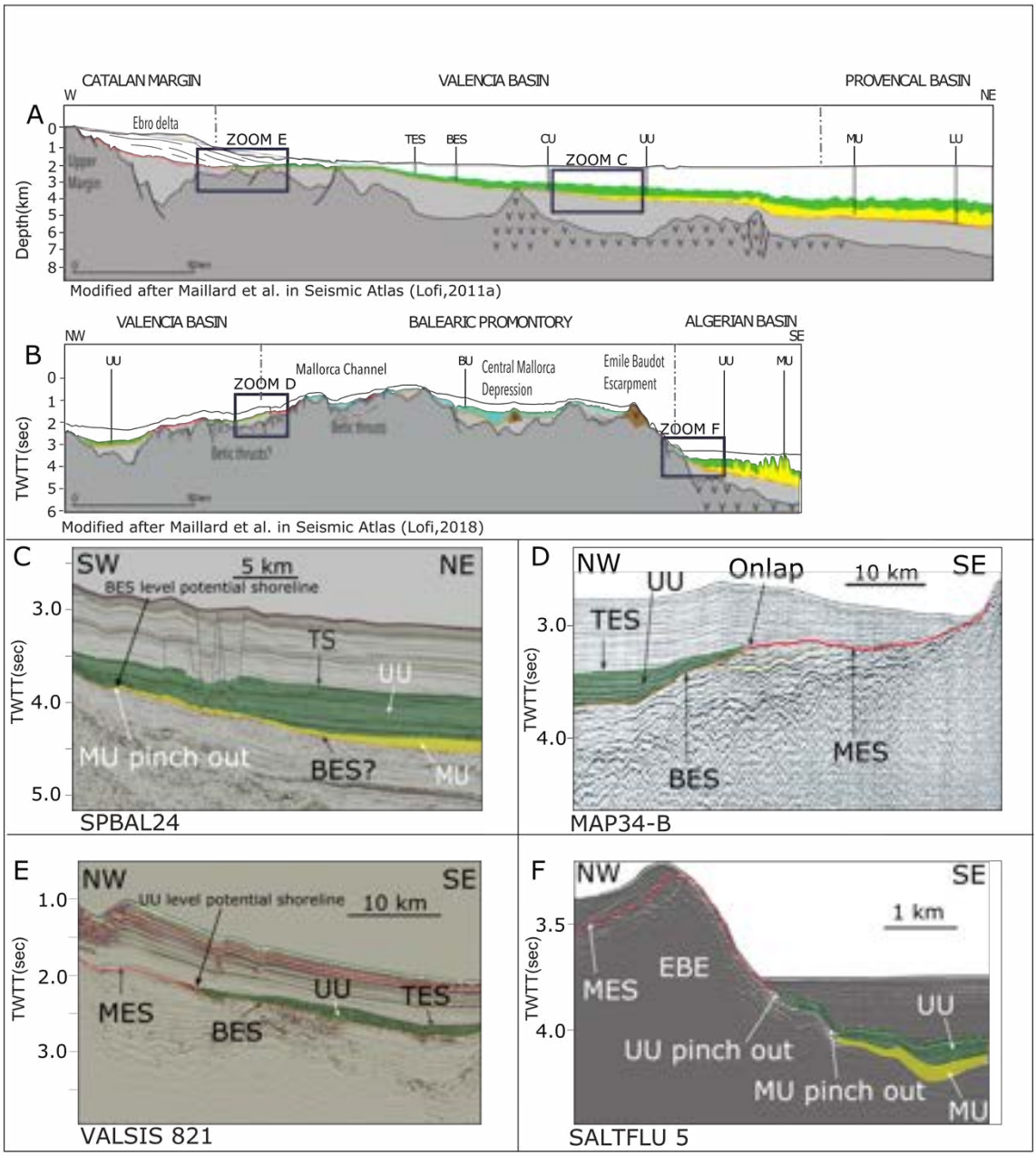

Figure 4.2. A, B: Line drawing composite profiles crossing key structural and sedimentary domains in the Western Mediterranean (from seismic atlases, Lofi, 2011a, 2018), position of profiles in Figure 4.1. C-F representative seismic lines with interpreted erosional features and MSC related evaporite units. D: modified after Maillard et al. in Lofi (2011a) F: modified after Camerlenghi et al. in Lofi (2011a).

4.3. Data and Model Setup

4.3.1. Paleoshoreline markers and tested scenarios

In this study, we constrain vertical motions and bathymetric changes during and after the MSC using pseudo-3D flexural-isostatic backstripping. We consider scenarios with and without a water level fall and investigate their implications for Mediterranean bathymetry, constraining the original depth of the proposed paleoshoreline markers. The first scenario relies on those by Maillard et al., (2006), Ryan, (2009) and Lofi et al., (2011b) which propose the following MSC seismic markers as potential paleoshorelines during the MSC:

- The onlap of UU onto the margins is considered the main paleoshoreline indicator towards the end of the MSC, where the MES splits into a BES and TES bracketing Messinian deposits. The deposition of UU is proposed to occur in shallow waters (Lofi et al., 2005; Maillard et al., 2006; Cameselle et al., 2014; Cameselle and Urgeles, 2017), before a rapid reflooding (Garcia-Castellanos et al., 2020 and references therein). The onlap of the top of the UU on the MES likely represents the highest water level during its deposition, although the top of the UU shows truncations (TES) that indicate possible variations around this water level. This stage is referred to as the UU level.
- The limit of the BES to MU on the margins is hypothesized to be another indicator of the paleo-shoreline after salt emplacement following an evaporative drawdown (Ryan, 2009). During this lowstand, the Bottom Erosion Surface developed in the Valencia Basin, where almost the entire region was subaerially exposed (Maillard et al., 2006). The elevation of the MU limit is variable due to the extensive erosion/dissolution that affected it after deposition. The shallowest preservation of halite limits the BES, and is therefore our reference point. The limit was also affected by halokinetic activity (Badji et al., 2015; Dal Cin et al., 2016). However, the distal limit of the imaged BES offers a constraint on the minimum amount of water level drop required to expose this region, although water level might have been lower, as a constraint on the maximum water level drop is not available. We therefore refer to this shoreline marker as the BES level.

The second tested scenario assumes no significant base level change, maintaining a deep Mediterranean basin throughout the formation of evaporites and erosional surfaces. We present the bathymetric implications of this scenario during the MSC compared to a scenario with considerable drawdown.

4.3.2. Flexural-isostatic backstripping

Pseudo-3D (planform) flexural-isostatic modelling of vertical motions due to surface loading was performed using TISC software (Garcia-Castellanos et al., 2002) allowing for a basin-wide evaluation of the topographic evolution during the MSC. The current basin state with the depth of bounding surfaces and the thickness of the various stratigraphic units is defined in grids of 200x200 resolution spanning an area of 860 by 890 km corresponding to the area in Figure 4.1. We perform backstripping accounting for the subsidence caused by sedimentation and rebound due to the removal of a water load during periods of low water level, as well as

compaction of the pre-Messinian sediment unit (Fig. 4.3). The flexural calculations adopt an elastic thin plate, assuming that loads are supported only by a strong lithosphere laying on a low-viscosity asthenosphere which behaves like a fluid. This approach does not allow for the evaluation of the initial time-dependent (transient) response to loading, which is rapid (10-30 kyr) compared to the geological processes we study here, which is why an equilibrium state for the basin is a valid assumption in most circumstances. Figure 4.3 illustrates the workflow and method for matching paleoshoreline positions to modelling results.

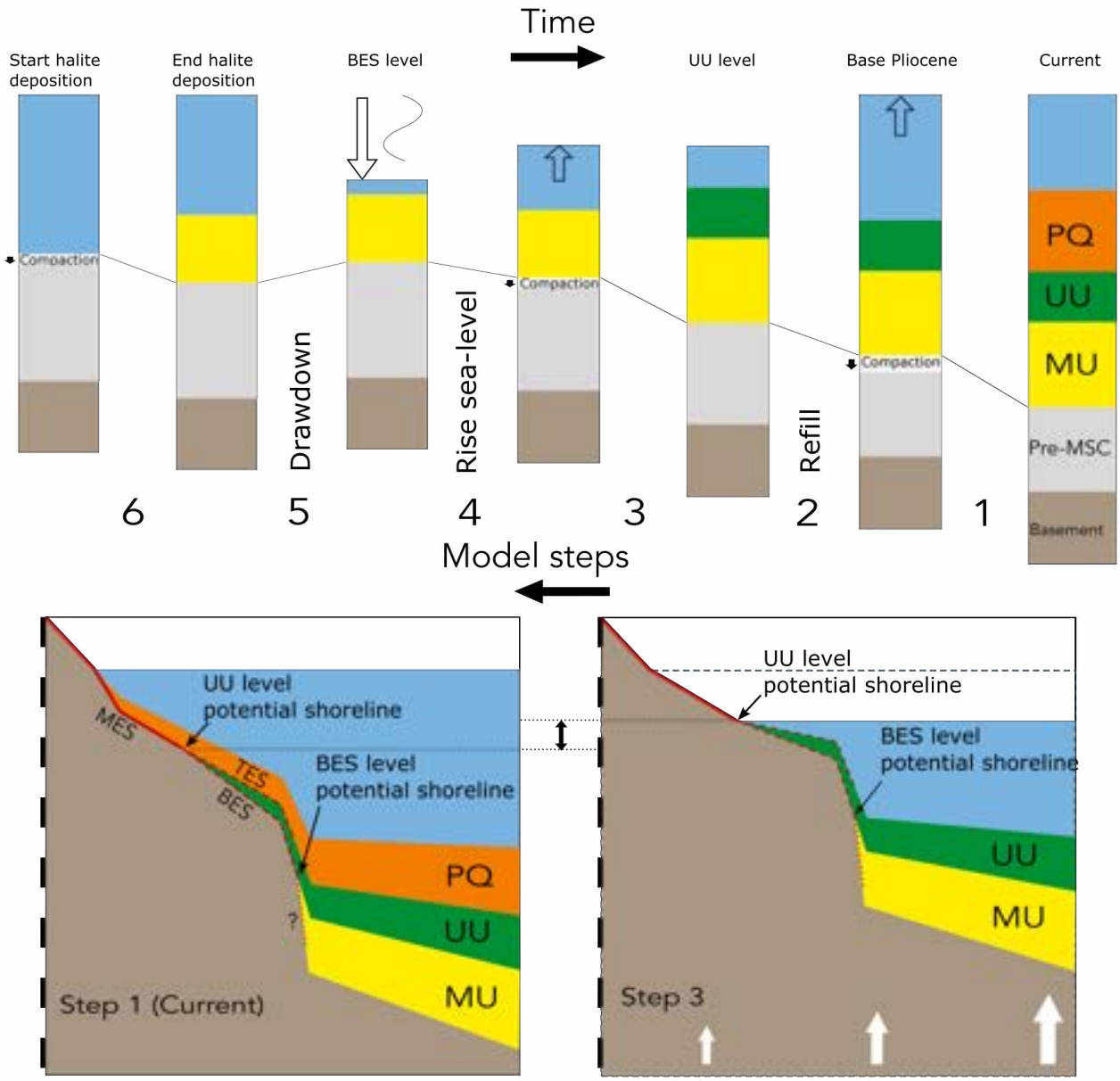

Figure 4.3. Schematic cross section showing step-by-step backstripping of sediment and water to determine flexural-isostatic response and match water level to paleoshorelines. 1: Removal of Plio-Quaternary sediment 2: Restoration of water level to pre-Zanclean flood level (UU lowstand) 3: Removal of UU sediment 4: Lowering of water level to lowest level at "acme" (BES lowstand) 5: Restoration of water level to pre-drawdown level 6: Removal of MU halite, to obtain bathymetry before the onset of stage 2 of the MSC.

The Effective Elastic Thickness (EET) of the lithosphere controls the magnitude of vertical motions as a response to tectonic and sedimentary loads (Burov and Diament, 1995; A.B. Watts, 2001), and is a crucial input parameter for flexural-isostatic modelling. For continental lithosphere, EET values are related to the thermal state (high geothermal gradients due to recent extension causing lower EET) and the state of the crust-mantle interface. *Decoupling,* meaning the existence of a low-strength zone between lower crust and upper mantle, prevents an applied load force from being transferred to and supported by the upper mantle. This reduces the EET value to solely that of the crust. In addition, local curvature of the plate inducing bending stresses can weaken the plate (Burov and Diament, 1995).

We first estimate EET values from the Yield Strength Envelopes of the lithosphere obtained from thermal and structural information (Fig. 4.5). Geotherms were calculated for the main domains along the NE Iberian Geo-Transect (Carballo et al., 2015, see Figure 4.1 for location), using MOHO and LAB depth, surface heat flow, average crustal and mantle compositions, crustal radiogenic heat production and average thermal conductivity. We test for a range of lithospheric strength parameters by using activation energy values from Govers and Wortel, (1995) and Cloetingh and Burov, (1996). Using the tAo code (Garcia-Castellanos et al., 1997) we calculate the effect of curvature due to sediment loading along a 2-D profile crossing the main crustal blocks (Fig. 4.6, see Fig. 4.1 for position profile A).

Bathymetry of the target region was derived from the GEBCO_2014 (IOC-IHO) grid. The thickness of the offshore Miocene to Quaternary deposits in the Western Mediterranean (Fig. 4.4) was determined from compilations of extensive seismic surveys (Fig. 4.1) including partially reinterpreted 2D seismic lines (Maillard et al., 1992, 2014; Roca and Guimerà, 1992; Maillard and Mauffret, 1993; Gallart et al., 1995; Mauffret et al., 1995; Sàbat et al., 1997; Acosta et al., 2001; Just et al., 2011; Leroux et al., 2019; Raad et al., 2020) and a 3D cube in the Ebro delta region (Urgeles et al., 2011). The seismic derived bathymetry, base PQ and the acoustic basement are available online as part of a wider dataset in the Western Mediterranean (Bellucci et al., 2021).

Although some sediment was deposited onshore their limited thickness and lateral distribution make for small effects when considering the regional scale, so we limit our investigation to offshore regions. In the north-eastern corner of our region data was not available, so grids were extended manually to be consistent with the deep basin thicknesses and prevent artefact shorelines in the Ligurian and Provençal basins. The reconstruction east of the Gulf of Lions and north of Corsica is therefore not accurate. The thickness of the MU (Fig. 4.4C) is locally higher in the Provençal basin (reaching up to 2 km) due to the presence of diapirs deforming the overlying UU (Fig. 4.4B) and Plio-Quaternary (Fig. 4.4A) units. The volumes of the MU and UU in our study area are 0.11×10^6 and 0.12×10^6 km^3 respectively, summing to 0.23×10^6 km^3. This is considerably lower than older estimates (0.5×10^6 km^3, Ryan, 2008) and still considerably lower than the 0.33×10^6 km^3 reported by Haq et al., (2020), but this can be due to the fact that volume from Haq et al. (2020) also includes the Lower Unit evaporites in the Western Mediterranean.

It should be noted that the distribution of the earliest sediment associated by some authors with the MSC (Lower Unit or LU) is not included in this reconstruction. No age control exists for the deep MSC record in the western Mediterranean and some authors question its age and origin (e.g., Raad et al., 2020). Moreover, the passage from pre-MSC sediment to evaporitic facies marking the onset of the MSC has been proven to be conformable all around the Mediterranean with no evidence of water level drop at this stage (Lugli et al., 2010; Dela Pierre et al., 2011; Ochoa et al., 2015). Therefore, unlike Bache et al., (2009) and Haq et al., (2020) we incorporate the LU in the pre-MSC sediment (Fig. 4.4D).

On the Balearic Islands we estimate the magnitude of post-MSC erosion by distributing the volume of clastic sediment in the Plio-Quaternary deposits on the offshore promontory onto the currently exposed surface area of the Balearic Islands (see Fig. 4.13), assuming the same area of subaerial exposure as in the modern day (the sum of the islands area is 4907 km^2) and a range of 30-70% for clastic provenance of sediment as found in the post-Messinian Unit I in ODP borehole 975 (M C Comas et al., 1996). This rough estimate allows us to describe the changes in surface topography since the MSC as well as the flexural-isostatic effect of this erosion. The onshore PQ sediment in the Palma graben (Capó and Garcia, 2019) is not considered as this was only transported over short distances, mostly sourced from the north-western Tramontana range and therefore had a negligible regional isostatic effect.

The full Messinian succession in the deep basin has not been drilled, which means it lacks a definitive constraint on density and other petrophysical characteristics required to convert the travel time of seismic waves to the key horizons to depth and determine the mass of the sediment and evaporite loads. Well data provides constraints for the top of the sequence, and we can assume a degree of similarity with the evaporite record found onshore. For the Pliocene-Quaternary sequence we assume a velocity function proposed by Urgeles et al., (2011) based on calibration from FORNAX-I well data on the Ebro margin. It takes the form :

$$depth[m] = 1135.1 * TWTT[s]^{1.343}$$

The UU is assumed to consist of intercalated gypsum/anhydrite and clays (Ryan, 2009), similar to the cycles observed in marginal basins which are proposed to have resulted from climate variations by precession cycles (Dronkert, 1985; Manzi et al., 2009). The MU, similar to the succession found in the Realmonte mine in Sicily is thought to consist of almost pure halite and potash salts (Lugli et al., 1999; Samperi et al., 2020), as evidenced by its seismic facies and the widespread halokinetic activity (Gaullier et al., 2008). Velocities and densities used in assessing our load distributions are listed in Table 4.1.

Unit	*Water*	*Plio-Quaternary*	*Upper Unit*	*Mobile Unit*	*Pre-halite*
Av. Seismic velocity (m/s)	1500	*Power law (see text)*	3400	4800	2440
Av. Density (kg/m3)	1030	2100	2500	2170	2700

Table 4.1: Average seismic velocities and densities used for each unit

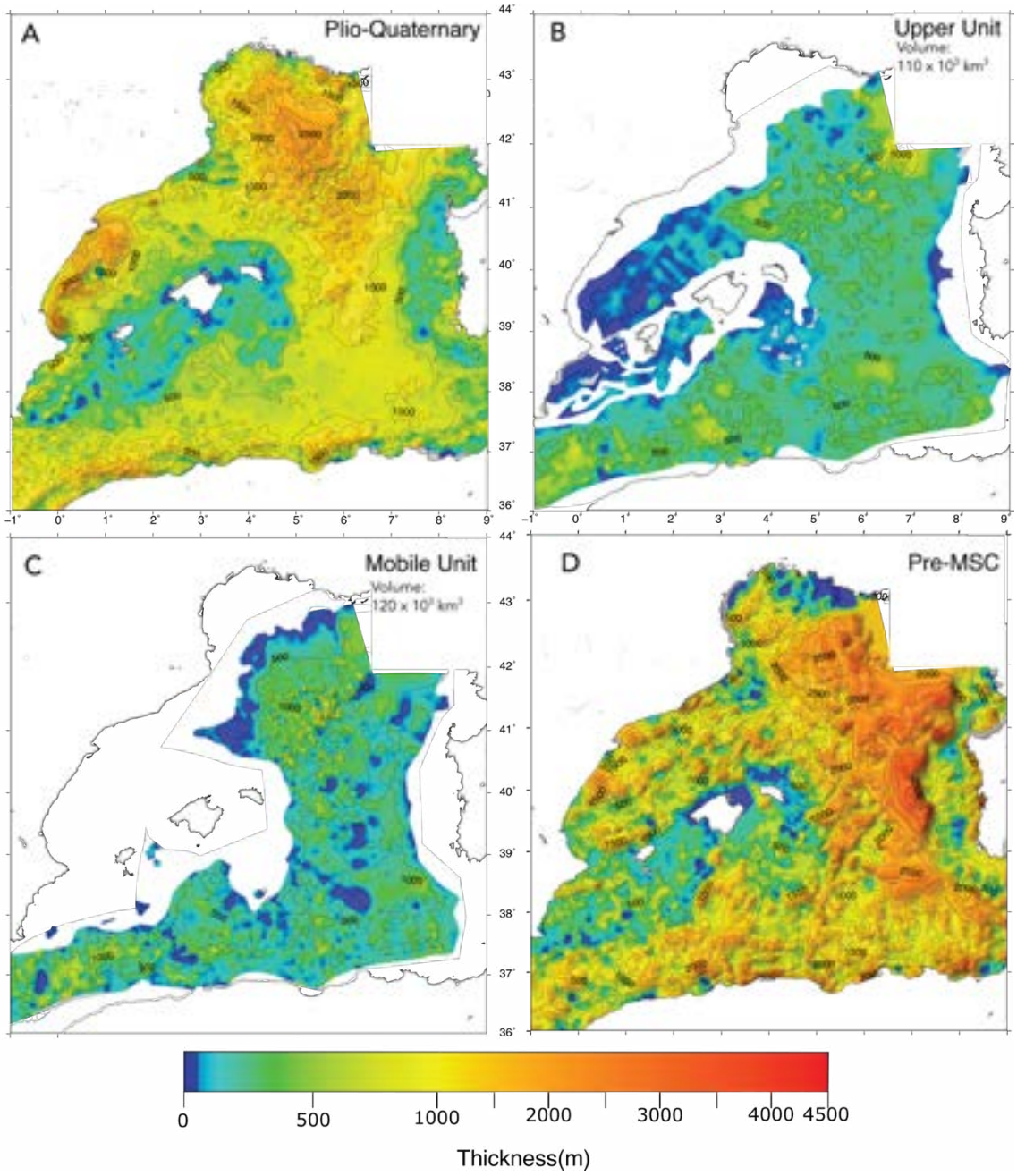

Figure 4.4. Thickness in meters of sedimentary units used in the reconstruction, as interpolated from the seismic dataset compilation in Fig. 4.1, using velocities presented in Table 4.1.

From these densities, we can derive the ratio of a response under *local isostasy* between the load thickness and induced subsidence or rebound for each step (see *Methods,* section 2.1, Fig. 2.2 and Table 2.1).

For long-wavelength and uniform loads, such as those in the deep Mediterranean basins the response will be close to local isostasy, but for more variable loads and close to load edges the response will be affected by the load-bearing capacity of the lithosphere.

The effect of compaction on the pre-halite bathymetry is determined for compaction following the standard porosity-depth relationship: $\phi_z = \phi_0 * e^{-bz}$.

Where Φ is porosity, z is depth below seafloor (km) and b is the compaction coefficient (km^{-1}), for shale Φ_0 = 0.67, b = 0.00051, and for sand Φ_0 = 0.49, b = 0.00027 (Sclater and Christie, 1980). Bessis, (1986) presents a porosity-depth curve based on three wells in the Gulf of Lions which fits a relationship of Φ_0 = 0.75 and b=0.00115, suggesting slightly faster compaction than the shale curve from Sclater & Christie (1980). We apply this range of porosity-depth relationships to correct the reconstructed bathymetry for compaction of pre-MSC sediment at each step in our reconstruction.

Water loads for drawdown and reflooding phases have a density of standard seawater in our models (1030 kg m^{-3}), although the real density during the evaporite deposition phases was likely higher due to the formation of more saline waters and brines (1200 kg m^{-3} at halite saturation). This has no significance for the pre-evaporite topographic reconstruction before brine formation at the Mediterranean scale, as the density increase cancels out with the later restoration of open marine conditions during the Zanclean flood.

An additional mechanism that modifies the depth of the Western Mediterranean basins is the cooling of the lithosphere. We use plate cooling models relating ocean floor depth to extensional age and heat flow (McKenzie, 1967; Parsons and Sclater, 1977; Stein and Stein, 1992) and continental extension models (McKenzie, 1967) to constrain this component of post-Messinian vertical motions. For the Provençal and Algerian Basins a MOR cooling model (Stein and Stein, 1992) is used, while for the Valencia Basin which consists of extended continental crust we use the McKenzie (1976) model. Dannowski et al. (2020) propose a failed rift and extended continental crust rather than full oceanic crust underlying the Ligurian Basin, which is the north-eastern continuation of the Provençal Basin. However, as this region is not covered by our dataset and the Provençal Basin represents the wider and older part of this extensional domain, we see no strong motivation to apply a continental crustal model to the Provençal Basin. The application of such a model would yield slightly smaller thermal subsidence values, and deeper estimates of Messinian bathymetry in the basin.

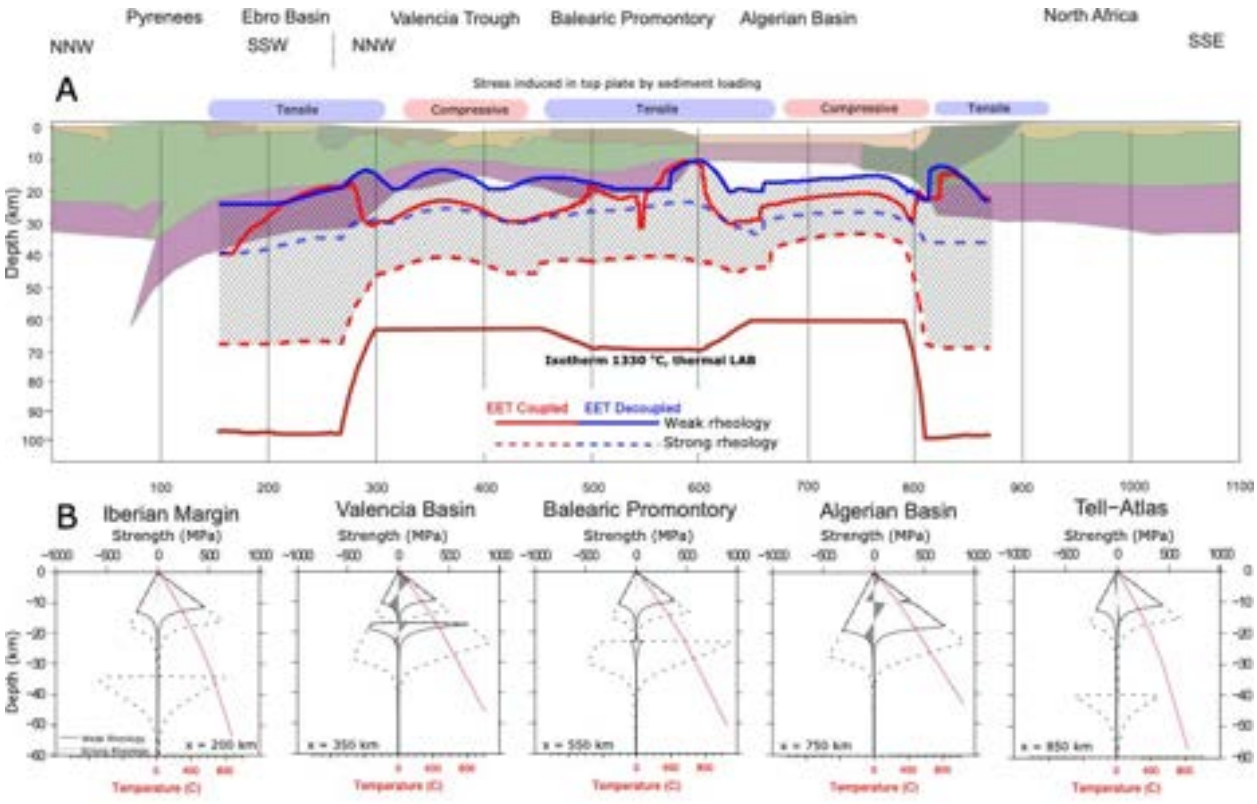

Figure 4.5. A: Effective Elastic Thickness variation from tAo model along a NE Iberia Geo-Transect (see Fig. 4.1 for location). Crustal units with different density, heat production and thermal conductivity used for constructing geotherms derived from a compilation of crustal structural data (colour filled bodies) and thermal lithosphere asthenosphere boundary (LAB, red-dark line) from Carballo et al., (2015). EET values determined for weak and strong rheological parameters for lower crust and upper mantle from Govers and Wortel, (1995) and Cloetingh and Burov, (1996) and for coupled vs decoupled crust and mantle. EET values are determined using tAo code by constructing Yield Strength Envelopes along transect based on rheology, geotherms and induced bending stresses by sediment loading since onset MSC. Range of plausible EET values hashed. Also shown is the stress regime induced on top of the plate by bending due to loading of sediment since onset MSC.

B: Yield Strength Envelopes constructed per region for weak and strong rheological parameters for lower crust and upper mantle from (Govers & Wortel, 1995) and (Cloetingh & Burov, 1996), showing decoupling in all regions but the Algerian Basin. Included are used geotherms and stresses (shaded grey area) at reference points along section.

4.4. Results

4.4.1. Thermal subsidence

Fitting the limits of the opening ages of the Algerian (8-16 ma) and Provençal (16-22) basins to the oceanic plate model GDH1 (Stein and Stein, 1992) yields post-Messinian thermal subsidence of 250 to 325 m in the Provençal basin, and 325 to 435 m for the Algerian basin.

The Valencia Basin has been studied extensively regarding its crustal structure and extensional mechanisms (Maillard et al., 1992; Torné et al., 1992; Watts and Torné, 1992a, 1992b; Maillard and Mauffret, 1999; Negredo et al., 1999). Best-fit basin histories suggest a finite rifting model with extension between 24 and 10 Ma, and the stretching factor (β) increasing from 1.4 on the basin flanks to 3 in the central basin (Watts and Torné, 1992a). Applying the McKenzie (1978) model yields a post-Messinian component of thermal subsidence in the range of 50-100 m on the flanks and 90-180 m in the centre depending on the applied post-rift age. Tectonic subsidence curves show a gradually decaying curve (Watts et al., 1990) meaning part of the thermal relaxation took place during the rifting phase and instantaneous rifting assumed in the McKenzie model does not apply to the Valencia Basin, so true values will fall towards the lower end of this range. Backstripping of wells in the Catalan margin area has yielded tectonic post-Messinian subsidence values ranging from 0 to 300 m (Bartrina et al., 1992; Watts and Torné, 1992a), with this variation in values possibly being related to ongoing activity on normal faults on the margin. Modelling of the basin evolution based on similar geodynamic data yielded maximum post-rift subsidence values of 380 m in the central part of the Valencia Basin since 10 Ma (Negredo et al., 1999). Due to the limitations of such 1D subsidence calculations we do not include the thermal component directly in our planform backstripping, as we are not able to constrain the lateral distribution of subsidence magnitudes accurately. However, we consider these subsidence values in the restored depths per basin presented in Table 4.2. Although thermal subsidence constitutes a considerable part of total vertical motions in the deep basins, because this effect diminishes towards the margins, we consider that it introduces a minor (<100 m) uncertainty in the reconstructed depths of our shorelines.

4.4.2. Effective Elastic Thickness

The results of our EET determination shown in Figure 4.5 yield an EET range of 10 to 45 km in the offshore domain with limited variation, with slightly lower values in the Algerian Basin. On the Emile Baudot Escarpment and the Algerian margin, we see sharp changes in EET values for weaker rheologies, likely due to bending stresses induced by boundaries of the sedimentary load in the deep basin.

European EET has been studied in this region by other authors using two principally different approaches. One is based on analysis of the spectral coherence of gravity anomalies and topography accounting for density variation in sediment, yielding values of 5 to 12 km in the western Mediterranean basins (Kaban et al., 2018). Alternatively, EET is inferred by

integrating the strength of the lithosphere derived from modelling based on thermal and rheological data, yielding values of <30 km for the Western Mediterranean (Tesauro et al., 2009).

The low strength estimated at the base of the crust along our 2D profile (from 0 MPa in the Iberian and north African margins to a maximum of 150 MPa in the Valencia Basin, see Figure 4.5) suggests a high degree of decoupling between crust and mantle in all regions except the Algerian Basin, which is the only region with true oceanic crust. This decoupling argues in support of using EETs towards the lower end value of our range, close to the 15 km value adopted for the 1D backstripping in Urgelés et al. (2011); and the Cenozoic evolution of the Catalan Coastal Ranges (5 km; Gaspar-Escribano et al., (2004). In addition, the generally low EET values (<20 km, Kaban et al., (2018) in the area derived from recent spectral analysis and the likelihood of decoupling between crust and lithospheric mantle in recently extended continental crust such as the Valencia Basin (Tesauro et al., 2009) point to values in the lower end of the range presented in Figure 4.5.

4.4.3. Sensitivity of paleotopography to EET

In Figure 4.6 the sensitivity of our reconstructed topography after removing the PQ sediment and a 1 km water column to the end-member EET values is presented along cross section A (see Fig. 4.1 for location). The reconstructed topography is strongly dependent on EET value in the Ebro delta region, where the Plio-Quaternary sediment load is largest. Here the localization of flexural-isostatic subsidence leads to a >700 m difference in post-MSC subsidence, also affecting the slope of the reconstructed bottom shelf which is nearly flat in the 10 km EET scenario but has significant basinward slope for a 45 km EET (Fig. 4.6). In the steepest areas of the MES on the Iberian margin where the onlaps of UU are located the sensitivity of topography is still around 500 m, illustrating the importance of the EET parameter when constraining the magnitude of water level changes. Considering the arguments for relatively low EET values in the previous section we adopt an EET value of 15 km for our reference model and vary this parameter between 10 and 20 km to test the uncertainty of reconstructed paleoshoreline depths due to lithospheric strength. Reconstructed shoreline depths vary by +/- 100 m as a result of this variation.

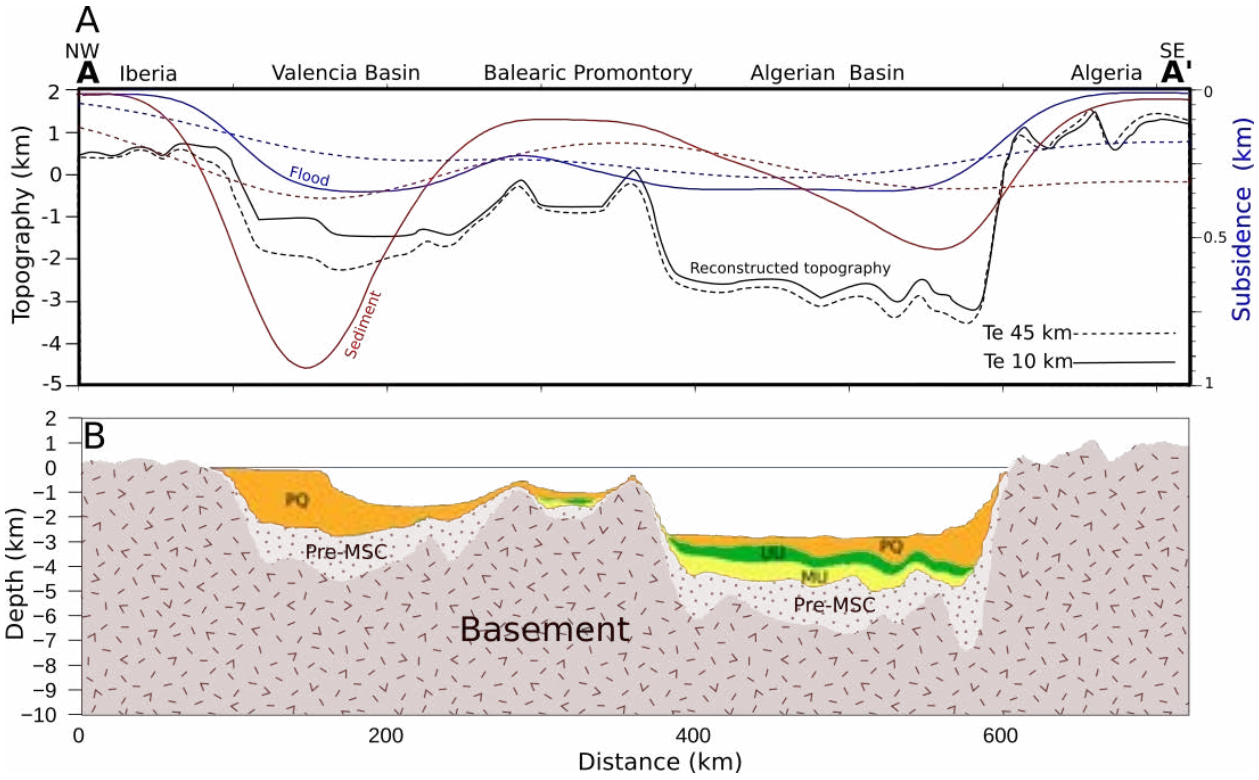

Figure 4.6. A: Schematic overview of results of backstripped profile A (see Fig. 4.1 for location) for 10 and 45 km EET. Black: Reconstructed topography at end MSC, before deposition PQ sediment and water level at -1000 m. Blue: vertical motions caused by 1 km change in water level (subsidence due to flooding). Orange: vertical motion due to sedimentation of Plio-Quaternary sediment (post-MSC subsidence).

B: Bathymetry and thicknesses of stratigraphic units used in backstripping along profile A. Orange: Plio-Quaternary sediment, Green: in deep basin: Upper Unit, on Balearic Promontory: Bedded Unit3, Yellow: Mobile Unit, Light Grey: Pre-MSC sediment, Dark Grey: Basement.

4.4.4. Sensitivity of paleoshoreline position to water level

The magnitude of a drop in water level during the MSC has a two-fold effect on the position of the reconstructed shoreline. First, it controls the magnitude of vertical motions affecting bathymetry, and secondly it determines the depth of the isobath followed by the shoreline. Figure 4.7 presents the sensitivity of the model output shoreline position at different drawdown magnitudes for our reference 15 km EET value, both for the UU level and the BES level. The reconstructed shoreline positions presented in Figure 4.7 are not corrected for thermal subsidence or tectonic deformation since the MSC. This is done due to the lack of lateral constraints on these components discussed in section 4.4.1.

In the Valencia Basin the most notable discrepancies in the paleoshoreline position for the UU level (Fig. 4.10B) are located at the Columbretes volcano, which caused Pliocene-recent deformation of the MES and Valencia Fault, active from Miocene to Pliocene which offsets the MES by about 0.5 seconds TWTT (Maillard and Mauffret, 2013). Accounting for the max value of 325 m post-MSC thermal subsidence in the Provençal basin (see section 4.4.1) would

shift the reconstructed shorelines slightly basinward, as the margin of the basin was in reality shallower than in our reconstruction. In the Valencia Basin this adjustment is not necessary for our UU level reconstruction considering that post-MSC thermal subsidence on its margins was negligible. On the Algerian margin the magnitude of the required adjustment is unclear, as subsidence in this area also carries a potential signal of tectonic origin due to subduction initiation and southward tilting of the basin (Auzende et al., 1972; Yelles et al., 2009; Leprêtre et al., 2013) affecting the depth of both the MU and UU limits. In the Valencia Basin, the UU limit in the Ebro delta region is likely not accurate, as Urgeles et al. (2011) showed the absence of an UU in their 3D dataset. Rather, they interpret the Messinian "Unit C" as a shallow water detrital fan. A water level of -1300 m is required to expose the Ebro margin in this region. However, water level cannot have been much lower as connectivity must have been maintained between the eastern Valencia Basin and the southwest Valencia Basin where the UU limit is clearly identified and mapped by Cameselle and Urgeles, (2017) varying around a reconstructed depth of -1100 m, although this connection is obscured by post-Messinian volcanic activity in the Columbretes. In the Gulf of Lions, the Upper Unit limit lies considerably deeper, close to the reconstructed shoreline for a -1500 m water level. In the steep Algerian Margin and Emile Baudot Escarpment, the UU limit lies further basinward than even the -2000 m isobath. Tentatively, we suggest this might be related to resedimentation of gypsum on steep margins, a process which does not require subaerial exposure (de Lange and Krijgsman, 2010) combined with tectonic processes mentioned above.

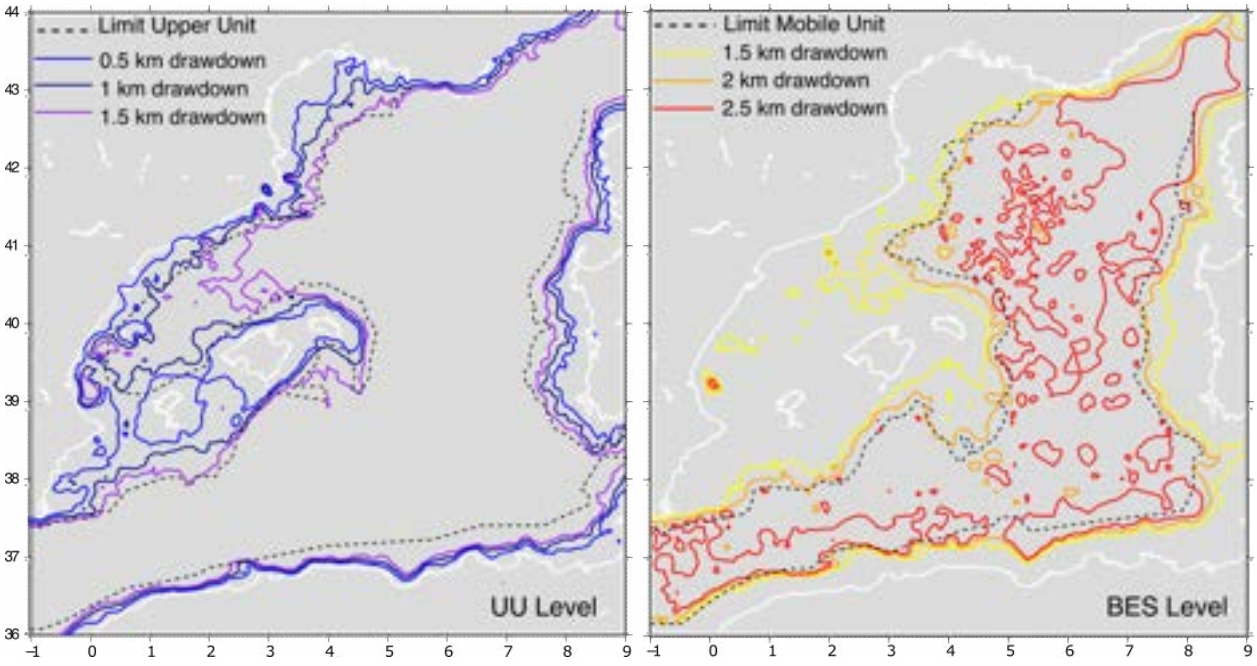

Figure 4.7. Sensitivity of the calculated paleoshoreline to the magnitude of water level fall (EET=15 km). Dashed black lines: position of paleoshoreline markers (see Fig. 4.1). Solid lines: reconstructed isobaths for various water levels. Left: UU level, Right: BES level.

As shoreline positions are better defined in the Valencia Basin where data availability is good and we can constrain our water level estimate against that of Urgeles et al. (2010) we consider this the more representative of paleo water level, rather than the deep basin margins where the depth of the UU limit is affected by the aforementioned processes. We therefore choose -1100 +/- 100 m as our reference water level for the UU level.

For the BES level, the limit of the MU fits well with a -1500 m water level in the shallowest MU limit towards the Valencia Basin, which indicated the minimum water level drop required to expose the top of the halite in that region. The depth of the salt limit shows strong variations between -1300 and -2000 m within the Gulf of Lions, while it is consistently deeper than -2000 m along the margins of the deep basins.

The modern salt limit is affected by significant halokinetic activity (Badji et al., 2015; Dal Cin et al., 2016). This, combined with the basin scale tilting of the Algerian Basin mentioned above could explain the discrepancy between our reconstructed shorelines and the limit of both UU and MU in the deep basin margins, but the larger (approximately 2200 m) drawdown required to obtain paleoshorelines in the position of the deep basin evaporite limit would imply a largely exposed sea floor in the Algerian basin (Fig. 4.7), with only small local lakes. We choose -1500 m for the BES level value as it allows for complete exposure of the BES in the Valencia Basin, but recognize that this constrains a minimum drop in water level which might still have been considerably lower at moments during the lowstand, as evidenced by the possible continuation of the BES underneath the MU.

4.4.5. Reference model

Based on the results presented above, our reference model assumes a 15 km EET and water levels of -1100 +/-100 m for UU level, which is the shallowest value for UU deposition found in places with a well constrained UU limit, although it should be noted that the UU is absent in some areas with a deeper reconstructed bathymetry, i.e., the Ebro Margin.

The BES level in our reference model lies at -1500 +/-100 m, which is the minimum water level drop needed to subaerially expose the BES to salt limit in the Valencia Basin, with the salt limit substantially deeper in other areas. In the Gulf of Lions our BES level shoreline along the ´Christiane' profile presented by Ryan (1976) is located at -2050 +/- 100 m, which fits well with their result of -1900 depth for the Late Messinian, even though we do not account for the isostatic effects of erosion in this region.

In the no-drawdown scenario our potential shorelines are positioned approximately 200 m deeper than when the flexural effect of removal of the water column is considered.

Basin		Liguro-Provençal	Algerian	Valencia	Halite CMD	Formentera	Cogedor
Average Bathymetry	**Modern**	**2700**	**2820**	**1500**	**950**	**1680**	**620**
	UU level (SL -1100)	**2300-2755**	**2120-2610**	**1110-1420**	**775-920**	**1302-1442**	**206-311**
	UU level (no SL drop)	**2650-3105**	**2470-2970**	**1460-1770**	**980-1125**	**1618-1767**	**455-560**
	BES level (SL -1500)	**2270-2690**	**2120-2575**	**1085-1395**	**825-970**	**1292-1432**	**127-232**
	BES level (no SL drop)	**2750-3170**	**2595-3055**	**1435-1745**	**1030-1175**	**1687-1827**	**422-527**
	Pre-halite (drawdown)	**3020-3325**	**2915-3255**	**1485-1795**	**1280-1425**	**1832-1972**	**543-648**
	Pre-halite (no drawdown)	**2800-3105**	**2695-3045**	**1435-1745**	**1235-1380**	**1687-1827**	**443-548**
Average Sediment thickness	Plio-Quaternary	1325	818	920	295	220	190
	Upper Unit	545	480	50	95	160	55
	Mobile Unit	665	505	-	215	70	75
	Total	**2535**	**1803**	**970**	**605**	**450**	**320**
Average Subsidence of Base MU	Plio-Quaternary	640	390	500	60	75	150
	Refilling	350	350	300	205	325	250
	Upper Unit	350	300	25	45	100	90
	Rise sea-level	130	125	50	0	70	45
	Mobile Unit	340	235	-	10	70	100
	Drawdown	-700	-695	-400	-250	-540	-395
	Compaction pre-MSC	550-780	340-570	150-410	45-190	55-195	30-135
	Thermal	250-325	325-435	50-100	0	?	?
	Total	**1910-2215**	**1370-1710**	**675-985**	**115-260**	**155-295**	**292-397**

Table 4.2 Bathymetry of Western Mediterranean sub-basins in modern day and at key moments during MSC, sediment thicknesses and vertical motion components. Average values are presented, but strong variations in sediment thicknesses and depths occur throughout the basins. In the CMD values correspond the average in the area of current halite occurrence. Paleodepth is determined by modern bathymetry - thickness sediment + decompaction pre-Messinian sediment + flexural-isostatic and thermal subsidence.

Each panel in Figure 4.8 represents a single step in our reconstruction, and can be interpreted as the flexural-isostatic effect on the Base MU surface of the applied load. The drop in water level at step 5 (Fig. 4.8E) results in a large rebound of up to 700 m in the deep basins, causing basin-wide shallowing even significantly affecting the margins and Balearic Promontory. The change in water level between BES and UU levels (Fig. 4.8D) and UU deposition (Fig. 4.8C) are not able to undo the entirety of this rebound, and the basins remain at their shallowest point throughout these steps. This strongly affects the bathymetry and depth of paleoshoreline markers formed during the BES and UU levels. The reflooding (Fig. 4.8B) and subsequent sedimentation (Fig. 4.8A) restore the basins to close to their pre-drawdown depth. The flexural-isostatic subsidence by sediment loading (Fig. 4.9A) was accompanied by compaction of the pre-halite sediment underlying the MSC units (Fig. 4.9B), and the total vertical motion on the Base MU surface since the onset of MU deposition is presented in Figure 4.9C.

The final resulting topography and shoreline positions, accounting for compaction and flexural-isostatic motions are presented in Figure 4.10. These maps exclude the thermal subsidence, which lateral variations are not accurately constrained. This explains the differences in reconstructed depths between Figure 4.10 and Table 4.2, where Table 4.2 represents the more accurate reconstructed depths. For the BES and UU levels the topography including (Fig. 4.10 B, D) and excluding (Fig. 4.10 C, E) water level drop are presented.

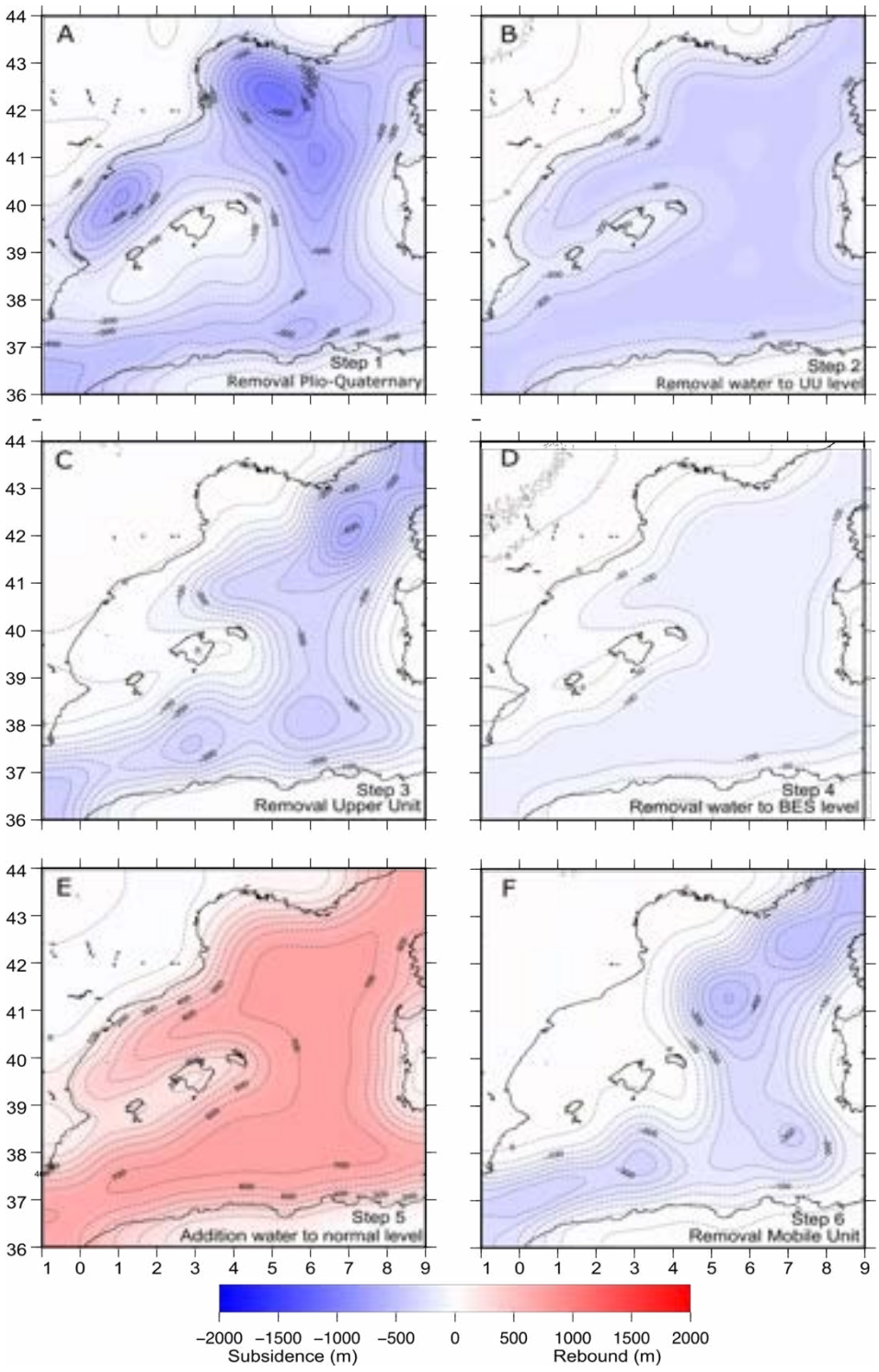

Figure 4.8. Flexural-isostatic vertical motions in m corresponding to each step of our reference model scenario. Sedimentation and floodings caused subsidence represented by negative values(blue), while water level drop caused rebound represented by positive values (red). Not included are effects of onshore erosion/sedimentation.

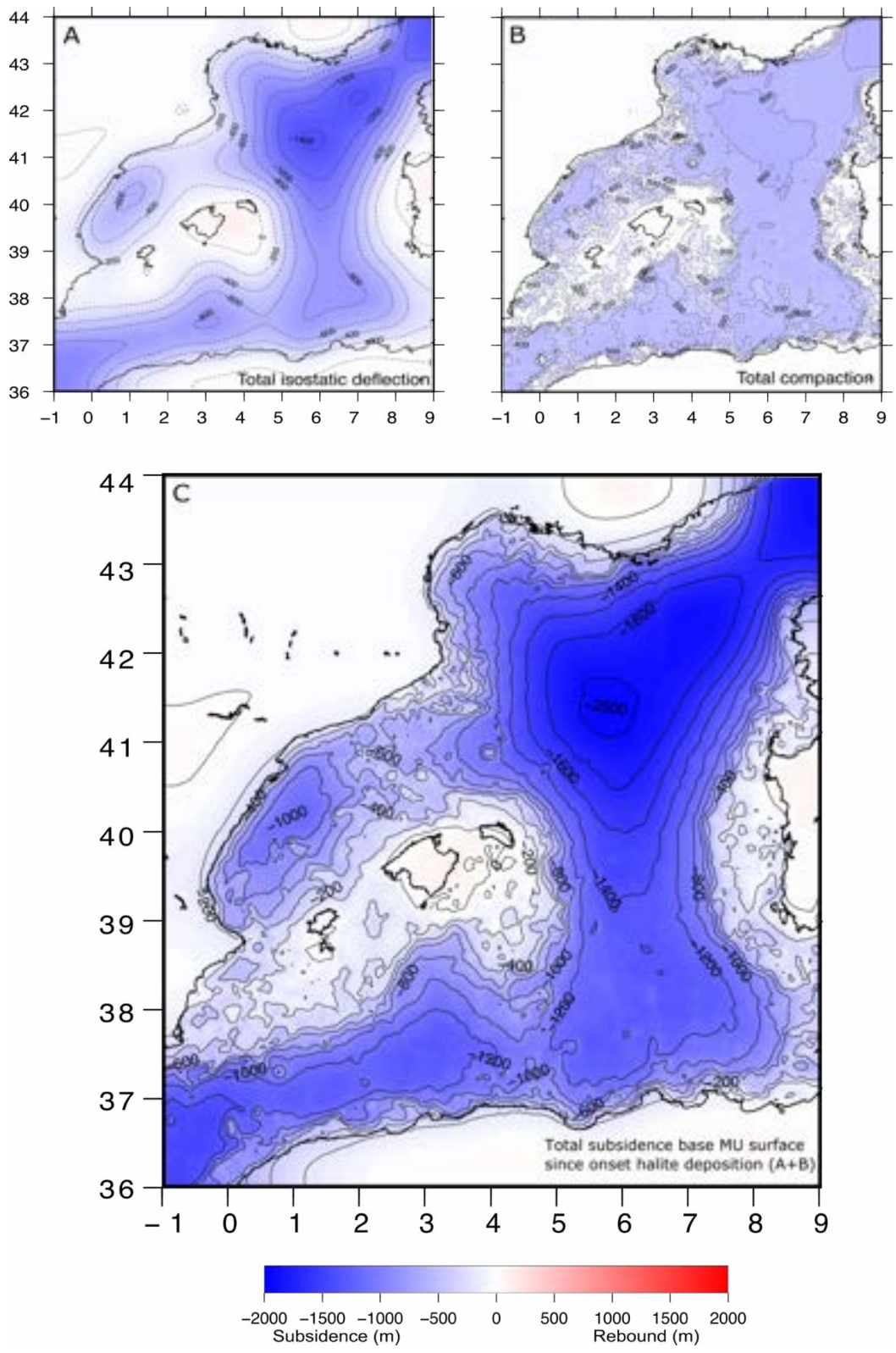

Figure 4.9. A: Sum of flexural-isostatic vertical motions in m since the onset of halite deposition, for the reference setup. B: total compaction of pre-halite sediment. C: Total subsidence of the base of Messinian sediment and MES since the onset of MU deposition (A+B). All values for reference model scenario. Not included are effects of onshore erosion/sedimentation and thermal subsidence.

4.5. Discussion

A key outstanding question around the MSC concerns the spatial distribution of evaporites and its link to paleo water depths. We describe the evolution of the Western Mediterranean basins from the perspective of our flexural-isostatic reconstruction for each sub-basin starting from the pre-Messinian bathymetry, and the implications for the paleoenvironmental changes during the MSC.

Assuming the paleoshoreline-based constraints on water level during the MSC are correct, our flexural-isostatic reconstruction shows that bathymetry of the intermediate basins before the onset of halite deposition (Fig. 4.10B) was slightly deeper than today, having since undergone subsidence by compaction, isostatic compensation and thermal cooling that combined was smaller than the sediment fill. The Valencia Basin reached 1500-1800 m depending on the chosen compaction curve (Table 4.2, Fig. 4.9B), and underwent a maximum of 1100 m of subsidence since the MSC (Fig. 4.9C). Because the UU in the Valencia Basin is relatively thin and MU is absent, its depth in our reconstruction during the MSC is controlled primarily by water level and the PQ load. The pre-halite depths of the Algerian and Provençal basins reached about 3 km depth on average (Fig. 4.10B, Table 4.2), which is similar to the present-day bathymetry. They underwent between 1200 and 2000 m of subsidence since the MSC (Fig. 4.9C) which is close to the sediment thickness accumulated in that same period. The significantly greater depth of the Provençal and Algerian basins compared to the intermediate basins can explain the much larger salt thickness, as they were not as extensively exposed during the drawdown stage. In addition, any exposed and dissolved salt would be trapped, in contrast to the Valencia Basin, from which it could be transported to the deep basins.

The water column above the top halite surface at the end of the MU deposition in the deep basins was approximately 2700-3300 m if halite was deposited in high water (Manzi et al., 2005), and 700-1200 m if the drawdown to BES level (of 1500 m) occurred. At the halite limit in the Valencia Basin this water column pre-drawdown was still 2 km, reducing to 0 after the drawdown.

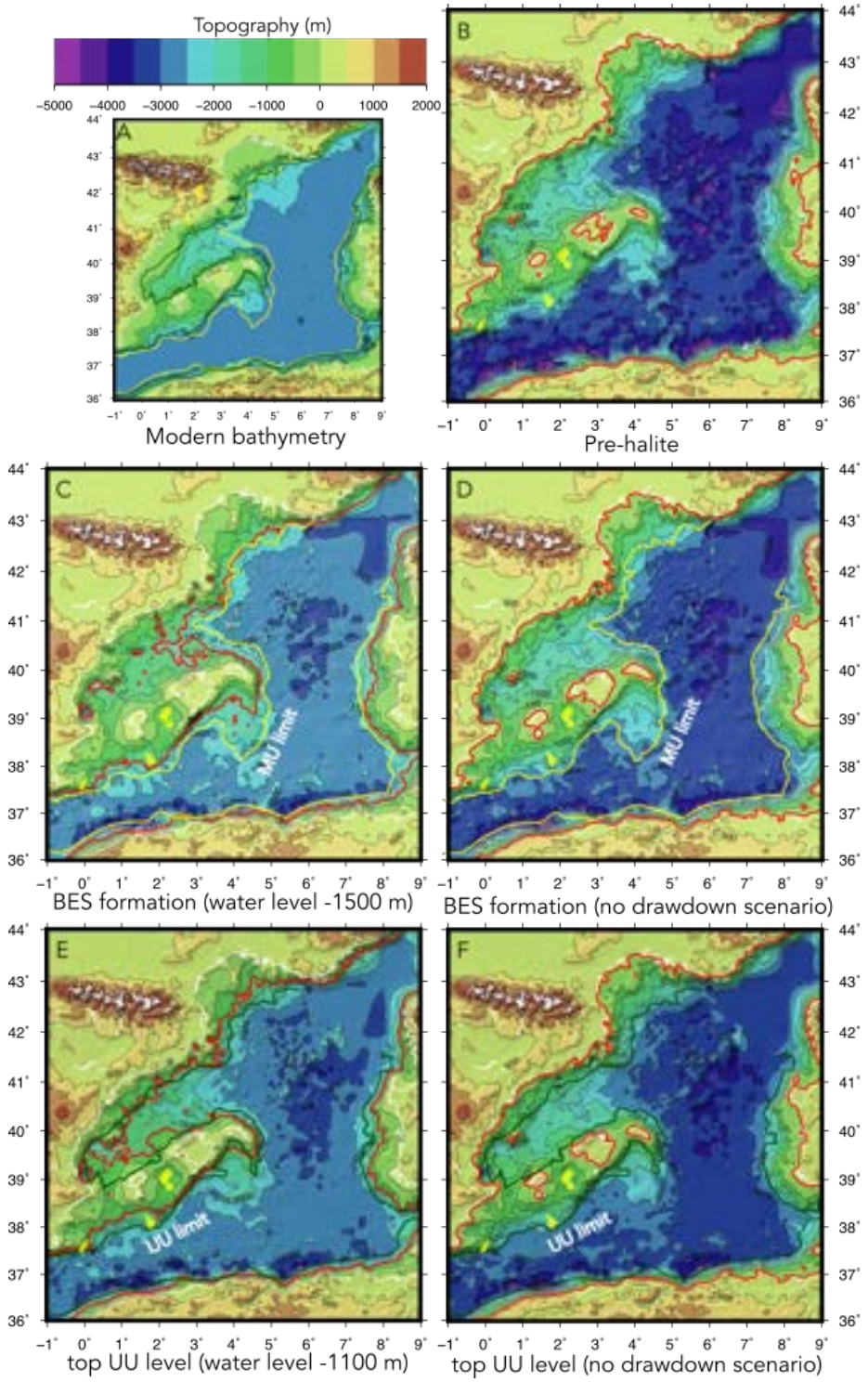

Figure 4.10. Modern topography (A) and reconstructed paleobathymetry results for our reference setup. These maps are not compensated for the thermal subsidence effect, overestimating the depth of the deep basins. B: pre-halite deposition. C: BES level (top MU) with water level at -1500 D: alternative BES level (top MU) for no-drawdown scenario. E: UU level (top UU) with water level at -1100. F: alternative UU level (top UU) with for no-drawdown scenario. Yellow line in B,C: limit MU, green line in D,E: limit UU). Solid red line: reconstructed shoreline. Yellow: halite isolated halite patches in CMD, Formentera and Cogedor basins. Note the discrepancy in required water level at the BES and UU levels of approximately 400 m in the drawdown scenarios (C vs. E).

In our reference model the uplift induced by the water level drop (Fig. 4.8E), yields basins shallower than today during the UU deposition. If our best-fit water level of -1100 m at the UU level is correct (in accordance with proposed values by [Maillard et al., 2006] and [Cameselle et al., 2014], slightly higher than previous estimates by [Urgeles et al., 2011] and [Mas et al., 2018]) this implies a maximum water depth of approximately 400 m at the transition from the Valencia Basin to the deep basin (Fig. 4.10E) at the end of UU deposition, and shallower (300-350 m) if we correct for thermal subsidence. At the same time, water depth in the deep basins reached 1000-1600 (average) to 2000 (max) m (Fig. 4.10E), which might suggest a different sedimentary environment and consequently a change in the nature of the UU between the Provençal Basin and the Valencia Basin. Without this drawdown isostatic effect, topography of the basins is 300 m deeper in the basin centres and water depths are therefore up to 3400 m (Fig. 4.10F).

In the no-drawdown scenario (Fig. 4.10E, F) we see that halite preservation occurs from laterally variable depths, from 1500 m (western Gulf of Lions), to 2500 m in the Valencia Basin and 3000-3500 m in the deep basins (Fig. 4.10E). These discrepancies could be explained by halokinetic activity, but the absence of halite in the Valencia Basin cannot be explained by such a mechanism alone, so either precipitation in that region must be prevented by a so-far unidentified mechanism, or halite must have been removed by submarine dissolution/erosion up to a very considerable depth (at least 2500 m) which we consider unlikely. The onlap depth of the UU in this scenario is also very variable, from 500-1000 m in the Valencia Basin to 2500 m in the deep basins, and considerable thickness of the UU is only reached at depths >2500 m. Considering the clastic nature of the UU, it is hard to explain these trends in a high water level scenario considering that the Valencia Basin and shallower margins would have had the biggest sediment supply. We therefore do not favor this scenario.

The main sources of uncertainty are the poor constraints on the EET and compaction of pre-halite sediment, as well as the magnitude of erosion in the exposed parts of the basin during the drawdown. We observe a disconnection between the UU and Bedded Unit3 lying on the Balearic Promontory (map in Fig. 4.11), onlapping on both sides of a topographic high situated between the CMD and Valencia Basin. Assuming this sill was exposed and considering the depth of this high when compensating for post-Messinian sedimentation, this indicates that the water level was at some point at least 600 to 750 m below modern sea level. Moreover, the onlaps of Bedded Unit3 in the CMD are positioned at a reconstructed depth of 750-900 m at the UU level, which is shallower than those of the UU on the southwest margin of the Valencia Basin (>1000 m). This supports the interpretation that stage 3 MSC deposits in the CMD (Bedded Unit3) were accumulated in isolated basins perched above the Valencia Basin water level. It implies deposition in an independent hydrological environment from the deep basin controlled by erosion and resedimentation on the Balearic Promontory.

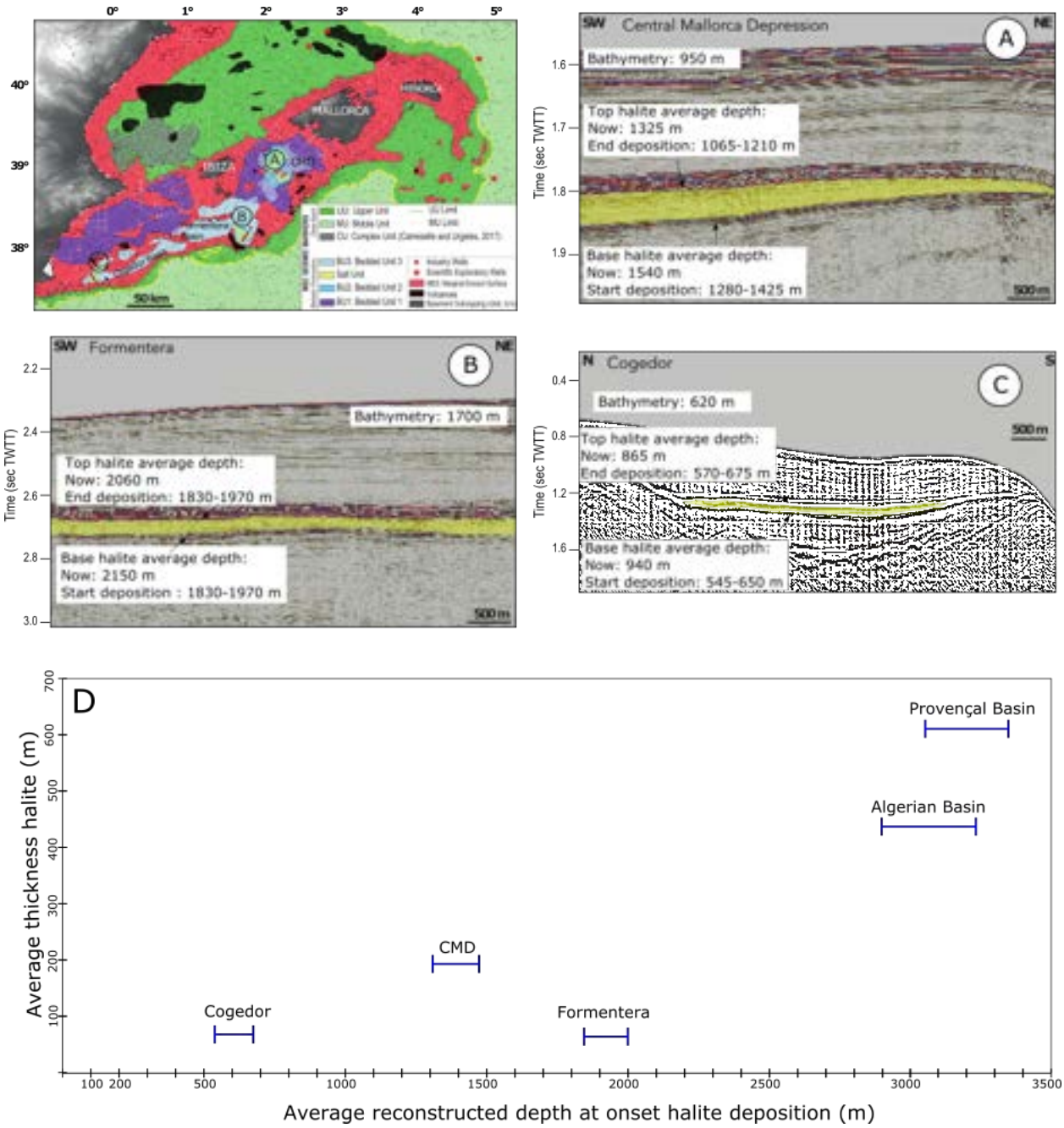

Figure 4.11. Seismic images of halite patches in CMD (A), Cogedor (B) and Formentera (C) basins showing current top and base depth of the halite (yellow) in TWTT (ms). Included are the reconstructed paleo-depths of both horizons not including the effect of water unloading. Map from Raad et al., 2020. D: Relationship of halite thickness to average reconstructed depth. Although the maximum thickness is reached in the deep basins, the smaller halite patches show no thickness-depth relationship.

On the Balearic Promontory, the halite patches (Figs. 4.1 and 4.11) occur at a wide range of present-day depths. Halite precipitation in the CMD depocenter started at a depth of 1280-1425 m, depending on the decompaction curve applied for the pre-halite sediment (see Table 4.2). Halite also deposited in basins with a restored depth as shallow as 550-660 m (Cogedor) which pre-halite depth could be as shallow as 450 m if we assume no drawdown ever

occurred, as this close to the margin the remnant uplift of the -1500 m change in water level in our reference model affects the pre-halite bathymetry. However, here we do not account for post-Messinian tectonics. Constraining these in this area is difficult due to the complex way the Balearic Promontory deformed, with large variations along its structure. Its western part (near Alicante shelf) was deformed by compression (Maillard and Mauffret, 2013) the vertical component of which would not have been more than 200-300 m. The true paleodepth might thus have been deeper, up to 960 m but the true magnitude of this effect is not well constrained. The aforementioned effect of residual shallowing due to the -1500 m drawdown also affects the Formentera Basin, which has a reconstructed depth of 1830-1970 m pre-halite, but could be 150 m shallower if no drawdown occurred.

A striking feature in these patches is the absence of any halite thickness vs. paleodepth relationship (Fig. 4.11D). The deepest pre-MSC basin (Fig. 4.11C, Formentera) has a much thinner halite unit than the CMD (Fig. 4.11A), which was lying up to 500 m shallower at the onset of the MU deposition (see Table 4.2 for depths and thicknesses). This could suggest that halite thickness in these patches was controlled by the local geometry of the basins and possibly the depths of their outlets. The open nature of the Cogedor and Formentera basins (Fig. 4.10), with respect to the completely silled-off CMD might have made them more susceptible to dissolution of the halite during the lowstand. Dissolved salt in Cogedor and Formentera would escape to the deep basin while in the CMD it is trapped inside the depression. This has been hypothesized by Raad et al. (2020) for the CMD, and a similar scenario has been proposed for the outcropping Sicilian halite (García-Veigas et al., 2018). It should be noted that especially on the western Balearic Promontory and potentially in the CMD, the effect of tectonic deformation since the MSC should be accounted for in order to achieve a higher accuracy in the paleodepth restoration. This is beyond the scope of this paper, but will shed more light on the role of the sills related to the halite patches during their formation.

Halite is conspicuously absent in the Valencia Basin, which had a pre-halite depth reaching at least 1500 m (Table 4.2). This can tentatively be explained as follows: it has been proposed by several authors that halite deposition occurred in deep water, in a strongly stratified water column (Yoshimura et al., 2016; Simon and Meijer, 2017). Any brine formed in the Valencia Basin may have sunk towards the deep Provençal Basin, as there was no topographic sill in between, although we could reasonably expect some salt trapping in the westernmost part of the Valencia Basin where volcanic edifices and structural highs were already present and depth variations allowed for the deposition of the MSC-related Complex Unit related to the lowstand (Cameselle and Urgeles, 2017). Alternatively, halite was deposited on the floor of the Valencia Basin but was later dissolved/eroded during the BES lowstand (-1500 m) when the basin floor was subaerially exposed. A combination of both processes is not excluded. These contrasting models are presented in Figure 4.12. Our results do not allow us to distinguish between these models, but the reconstructed depths of the basins do evidence the importance of explaining the observed halite distribution.

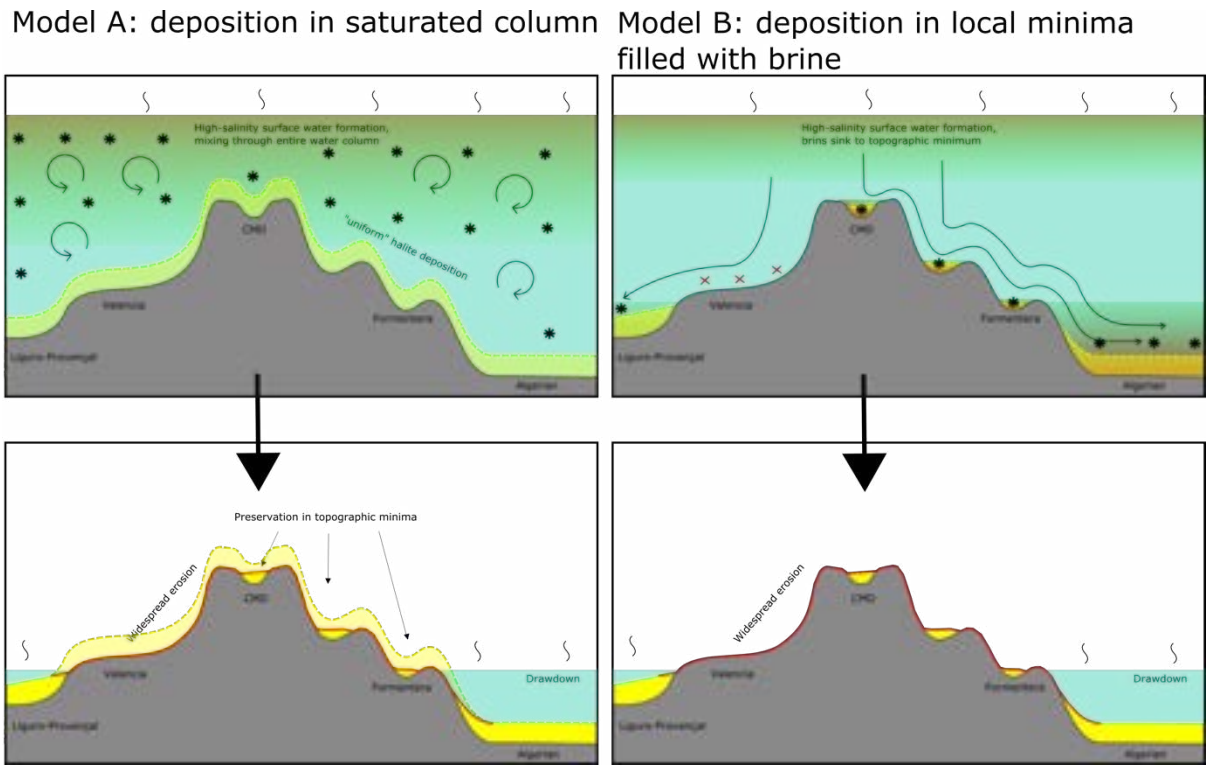

Figure 4.12. Contrasting models of halite deposition explaining the current depth-thickness distribution of halite. A: Halite is deposited throughout/in the top of the water column over the entire region, and subsequent drawdown exposes the intermediate basins removing all halite. In topographic minima some halite is preserved, as well as in the seep basins. B: Halite is deposited in local minima where dense brine can accumulate, while the Valencia Basin which is deeper than the CMD does not see halite accumulation because the dense brine sinks towards the deep basin. In this scenario the thickness of deposited halite in local minima depends on the geometry of the depressions.

The flexural-isostatic effect of the deep-basin isostatic loads on Mallorca Island suggest a close to zero effect (Fig. 4.9C) of vertical motion by MSC events, as rebound due to the drawdown (Fig. 4.8 E) was reversed by flooding and Plio-Quaternary sedimentation (Fig. 4.8 A, B). Based on the volume of post-Messinian sediment lying on the Balearic Promontory platform offshore (see Fig. 4.13), we estimate the isostatic erosional rebound assuming it was eroded from the current onshore Balearic Islands (effect not included in Figures 4.8, 4.9 and 4.10 due to their relative magnitudes). Using the constraints outlined in section 4.3.2, the eroded mass onshore is equivalent to a uniform load of 130-310 m. It should be noted that this height does not account for porosity changes from consolidated rock to sediment, so their true height would be smaller, but the mass removed from the islands is not affected by this simplification. We also do not account for the onshore post-MSC sedimentation in the Palma graben (see Capó and Garcia [2019] for thickness maps onshore), which suggest that the

central part of Mallorca island was not exposed to erosion until recently. This implies the rebound due to erosion would be more concentrated on the NW and SE regions of the island than shown in our results (see Figure 4.13). The erosion magnitude yields an average erosion rate of 0.03 to 0.04 mm/yr over the Pliocene and Quaternary, which is on the same order of magnitude as measured rates of seacliff erosion (Balaguer and Fornós, 2003). The rebound on the Balearic Islands due to erosion affects the pre-Messinian reefs on the eastern coast of Mallorca by up to 60 m since the MSC. We tentatively suggest that this explains the present-day elevation of the terminal carbonate complex on Mallorca island, originally formed near sea-level (Mas and Fornós, 2013), and that a higher eustatic sea-level before the MSC is not required to explain the elevation of phreatic overgrowths on speleothems as proposed by Dumitru et al. (2021). Previous estimates of long-term deformation on the eastern shore of Mallorca based on six Pliocene sea-level indicators yielded a median value of 0.002 mm/yr (Dumitru et al., 2019), which would yield a total post-MSC uplift of approximately 10 m, which is significantly below our estimate.

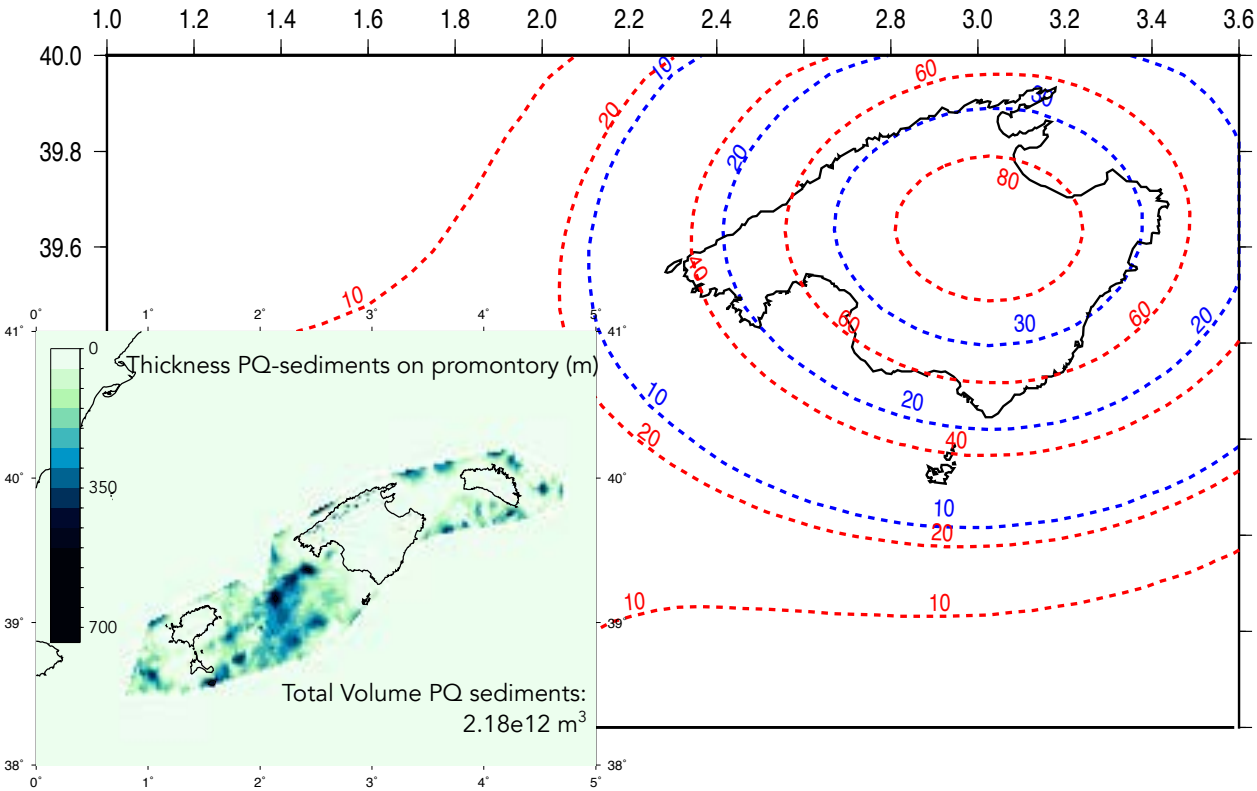

Figure 4.13. Thickness map of PQ sediment on the Balearic promontory and isolines for flexural-isostatic rebound effect in m for range of post-Messinian erosion values based on 30-70% clastic provenance sediment on Balearic Promontory. Blue: minimum volume clastics (0.65e12 m3, corresponding to the 30% clastic component limit and implying an average 133 m of erosion onland) Red: maximum volume clastics (1.52e12 m3, corresponding to the 70% clastic component limit and implying an average 310 m of erosion onland). Rebound calculated for EET value of 15 km.

Another important outcome of our results on the Balearic Promontory and the margins of the deep basins is the potentially large differential rebound and subsidence resulting from sudden drawdown and refilling events (see Figure 4.8B, D, E). While the subsidence and rebound induced by sedimentation and erosion develop gradually, the water level changes associated with the MSC are thought to have happened over very short time lapses (a few thousand years for the drawdown [Meijer and Krijgsman, 2005; Garcia-Castellanos and Villaseñor, 2011] and a few years for the reflooding [Garcia-Castellanos et al., 2009]), implying geologically-instantaneous changes in the surface isostatic loading. Thus, the isostatic time response is limited by the viscosity of the asthenosphere and forced to be also very rapid (stress relaxation in the asthenosphere takes place in time periods of about 20 kyr [Watts, 2001; Watts et al., 2013]). Since the density contrast between water, air and asthenosphere lead to a 0.3 to 0.4 ratio of the flexural response relative to the water level change, the kilometric drawdown imposed vertical motions in excess of several hundred meters in the aforementioned time scales. Because the uplift due to water level drop was reversed during subsequent stages, lasting effects on the deep basins is hard to distinguish in the modern basin, although it has been linked to a basin-wide magmatic pulse (Sternai et al., 2017). On the margins, these events caused differential motions of up to 700 m over a distance of about 100 km (Fig. 4.8), which could result in (re)activation of fault systems. Evidence for a tectonic response to this rebound would be very distinct from general normal fault activity, as it could be expressed as a phase of tectonic inversion. Although so far such evidence has not been described, it could independently strengthen the water level fall hypothesis for the MSC.

Our water level estimate implies a disconnection between the western and eastern Mediterranean at the platform between Sicily and Tunisia throughout a large part of MSC stage 3. The current depth of the Sicily Sill is 430 m, although its paleodepth during the crisis is not well constrained (Blanc, 2006). A recent study shows that the isostatic subsidence caused on the Malta platform due to sediment accumulation in the Ionian Sea during the PQ is very minor (Micallef et al., 2018a). Assuming the sill was there during the MSC, this means that water levels in the Eastern and Western basins were decoupled and dependent on local hydrological budgets, and that during the reflooding of the basin water level would have remained stagnant at the level of the Sicily Sill until water levels in the Eastern Basin reached that of the sill, as previously suggested by (Lofi et al., 2005; Meijer and Krijgsman, 2005; Blanc, 2006; Garcia-Castellanos and Villaseñor, 2011) and supported by terrace formation at various depths in different parts of the Mediterranean (Just et al., 2011; Micallef et al., 2018a) and references therein).

4.6. Chapter Conclusions

We present a reconstruction of Messinian paleotopography in the Western Mediterranean accounting for the flexural-isostatic response to sedimentation and water level variations since the onset of the Messinian Salinity Crisis. We test a scenario in which a main drawdown phase follows the emplacement of the MU (salt), and where the overlying UU emplaced in shallow waters, contrasted with a model without drawdown. Combining a thermo-mechanically constrained flexural-isostatic modelling we arrive at the following conclusions:

1. If the BES surface was formed by subaerial erosional processes, then the level of the western Mediterranean water surface was at least as low as -1500 +/-100 m prior to UU deposition.
2. If the extent of the UU deposits marks the coeval paleoshoreline, then the water level was no higher than -1100 +/-100 m at the end of the UU deposition.
3. The 1500-m-drawdown scenario would imply a 700-m rebound of the deep basins causing the basins to be significantly shallower during the final stage of the MSC compared to times preceding and following the MSC lowstand.
4. The isostatic subsidence, compaction and thermal subsidence since the Messinian largely compensate the accumulation of sediment, implying that the bathymetry of the various basins at the onset of MU deposition was similar to the modern day.
5. There exists no thickness-paleodepth relationship for halite in the perched CMD, Formentera and Cogedor basins. We interpret this lack of a trend, together with the absence of halite in the deeper Valencia Basin, as the result of halite being deposited or preserved only in local bathymetric minima, with the halite thickness being controlled by the depth of such depressions and their outlets (e.g., spillways of brine to deeper regions).

Chapter 5: The Nile Delta

This chapter is the results of a collaboration within the SaltGiant network (Geological Survey of Israel). In this chapter, we move to the Eastern Mediterranean, characterized by a very different expression of the Messinian Salinity Crisis, as a much thicker halite unit with notably absent/extremely limited Upper and Lower evaporite units. As the basin was disconnected from the Western Mediterranean at the Sicily Sill during the lowstand stage (see Chapter 4) water level is believed to have responded independently from the Western Mediterranean after disconnection from the Atlantic. We revisit the Messinian incision of the Nile Canyon, identifying a paleoshoreline marker at a knickzone of the channel just south of Cairo, and restoring this shoreline marker to its original depth. It becomes clear that the water level recorded in this morphological feature is much shallower (600 m depth) than the shorelines identified in the Valencia Basin (see Chapter 4), suggesting a possible role for variations in freshwater budgets between subbasins in controlling the Messinian water level.

Highlights:

- Original depth of the geomorphological base level of the Nile River at ~600-m below present sea level
- Water level drop 2-4 times smaller than previous estimates, but ca- 5 times larger than eustatic fluctuations.

This chapter has been published as:

Gvirtzman, Z., Heida, H., Garcia-Castellanos, D., Bar, O., Zucker, E., & Enzel, Y. (2022). Limited Mediterranean sea-level drop during the Messinian salinity crisis inferred from the buried Nile canyon. *Communications Earth and Environment*, 1–10. https://doi.org/10.1038/s43247-022-00540-4

5.1. Chapter Summary

The extreme Mediterranean water-level drop during the Messinian salinity crisis has been known for >50 years, but its amplitude and duration remain a challenge. Here we estimate its amplitude by restoring the topography of the Messinian Nile canyon and the vertical position of the Messinian coastline by unloading of post-Messinian sediment and accounting for flexural isostasy and compaction. We estimate the original depth of the geomorphological base level of the Nile River at ~600-m below present sea level, implying a drawdown 2-4 times smaller than previously estimated from the Nile canyon and suggesting that salt precipitated under 1-3-km deep waters. This conclusion is at odds with the nearly-desiccated basin model (>2 km drawdown) dominating the scientific literature for 50 years. Yet, a 600-m drawdown is ca. five times larger than eustatic fluctuations and its impact on the Mediterranean continental margins is incomparable to any glacial sea-level fall.

5.2. Introduction

5.96 million years ago (Late Messinian), when the connection between the Mediterranean Sea and the Atlantic Ocean was restricted, the entire Mediterranean became hypersaline, its marine fauna extinguished, and a kilometres-thick evaporite sequence was deposited on its floor (Hsü et al., 1973; Ryan and Cita, 1978) within a short period of ~640 ky (Krijgsman et al., 1999; Manzi et al., 2013). This Messinian Salinity Crisis (MSC) is an exceptional event in Earth's history. The MSC sea-level fall is strongly debated for >50 years; with high-end estimates of >1500 m (Hsü et al., 1973; Lofi et al., 2005; Madof et al., 2019; Micallef et al., 2018; Ryan, 1976) intermediate estimates of 800-1500 m (Ryan and Cita, 1978; Clauzon, 1982; Druckman et al., 1995; Bertoni and Cartwright, 2006, 2007; Cartwright and Jackson, 2008; Urgeles et al., 2011; Amadori et al., 2018) or 630-900 m (Ben Moshe et al., 2020), and even minor estimates of 200-500 m (Roveri et al., 2014a; Roveri et al., 2016). These estimates are ingredients of the applied depositional models: from a nearly desiccated Mediterranean, with salt deposited in residual shallow hypersaline lakes(Hsü et al., 1973; Ryan, 1976; Ryan and Cita, 1978), to a deep hypersaline-water body accumulating salt on its thousands-of-meters-deep floor (Schmalz , 1969; Roveri et al., 2014, 2016; Sirota et al., 2018).

A leading piece of evidence for a large MSC sea-level drop is the upstream canyon incision of rivers (e.g., the Nile and Rhone), buried under thick sequences of sediment (Clauzon, 1973, 1982; Ryan and Cita, 1978; Barber, 1981; Lofi et al., 2005; Ryan, 2009; Gorini et al., 2015). Elevation differences along (~2 km) and across (~1.5 km) the buried Nile canyon are considered as a measure for base base-level drop (Barber, 1981) ignoring the possibility that at least a part of the canyon may have been subaqueous; moreover, the thick Nile delta sediment also changed the vertical position of the buried canyon.

Here, we reconstruct the original elevation and shape of the Messinian Nile canyon, by correcting the buried Messinian erosion surface (MES, Lofi et al., 2005) for post-Messinian subsidence due to sedimentary loading (isostasy, lithosphere bending, and decompaction of underlying sediment). The results are the Messinian landscape immediately after its reflooding and before any Pliocene sedimentation, ignoring a few tens of m difference between the Early Pliocene and the present sea level (Miller et al., 2005). On the reconstructed landscape, we identify the geomorphologic base level of the MSC-Nile River, where river profile maintains a subhorizontal profile, and then, the paleo-shoreline where the river profile steepens again, when it turns into the submarine environment. With unloading the water above the base level, we restore the pre-flooding Messinian landscape, i.e, during maximal drawdown. Finally, we show that our conclusion about limited drawdown is beyond the uncertainties related to the restoration process, although we cannot exclude that the sea level was temporarily at different levels during the drawdown.

5.3. Geological observations

Near the present-day coast, the Messinian Nile canyon is buried 3000 m under the flat delta plain (Fig. 5.1a). About 100 km to the south, Near the city of Cairo, the canyon base is ~1500 m below the surface and its shoulders nearly reach the surface (Barber, 1981). Farther south, beyond the seismically-mapped plain, the canyon size and depth are uncertain. Approximately 1000 km south of Cairo, near Aswan, Early Pliocene brackish ostracods at the base of a 200-m deep canyon fill (Chumakov, 1967, 1973) raised the hypothesis that an Early Pliocene marine invasion of the canyon had reached Aswan, portraying the boundaries of the earlier MSC incision ~1200 km away from the present day coast (Said, 1981; Ryan, 2009). However, faunal re-examination (Roveri et al., 2014a; Roveri et al., 2016) showed a poor assemblage of rare and non-marine ostracods with a wide age range. This fauna could have been reworked from Cretaceous or Paleogene outcrops as observed in many Pliocene sediment along the Nile Valley (Philobbos et al., 2015), i.e., the near-Aswan canyon could have been subaerially excavated and buried before or after the MSC.

Examining stratigraphic data along the Nile Valley may clarify the uncertain inland extent of the MSC Nile canyon. Near Helwan, ~15 km south of Cairo, a water well reached the bottom of the canyon at 550 m (RIGW, 1997; Awad, 2019) below sea level (mbsl) and a few km south another well reached the bottom of the canyon at 200 m (Said, 1981). This abrupt depth change from 1200 m to 200-550 along only 15 km, indicates a paleo-knickzone, separating a deep gorge from a much shallower upper valley. Moreover, this knickzone approximately coincides with an Early Pliocene sedimentologic transition in the canyon fill from deep-water claystone (Said, 1981; Sallam et al., 2018) to shallow marine and tidal limestones that continue ~150 km farther south until Beni-Suef (Blanckenhorn, 1921; Sandford and Arkell, 1929; Little, 1936; Hassan et al., 1978; Sallam et al., 2018). Farther inland, Pliocene exposures consists of fluvial-lacustrine sediment (Tateo et al., 2000; Mahmoud and Tawfik, 2015; Philobbos et al., 2015; Sallam et al., 2018). These sedimentological data indicate that the early Pliocene marine invasion filled a deep gorge up to the Cairo-Helwan region, continuing ~150 km southward as a narrow and shallow marine embayment. From there, non-marine lacustrine environments extended further inland.

5.3.1. Flexure produced by the Nile delta isostatic load

Most MSC flexural studies (Norman and Chase, 1986; Gargani, 2004; Gargani and Rigollet, 2007; Govers et al., 2009; Gargani et al., 2010; Urgeles et al., 2011) are initiated with pre-MSC relief and forward model the vertical motions caused by deposition and erosion of pre-assumed masses of salt, water, and eroded material. Here we question the pre-assumed water mass and utilize a different approach; the present-day relief is the reference and we backward model (restore) the topography immediately after the MSC, by isostatically unloading sediment that accumulated since. Similar exercise (Amadori et al., 2018), conducted for the Po Plain and the north Adriatic Sea, concluded that an 800-900-m

drawdown best explains buried erosional features, and work applying the same method to the Western Mediterranean yielded water level estimated of -1500 m and -1100 m for stages 2 and 3 of the MSC respectively (Heida et al., 2021).

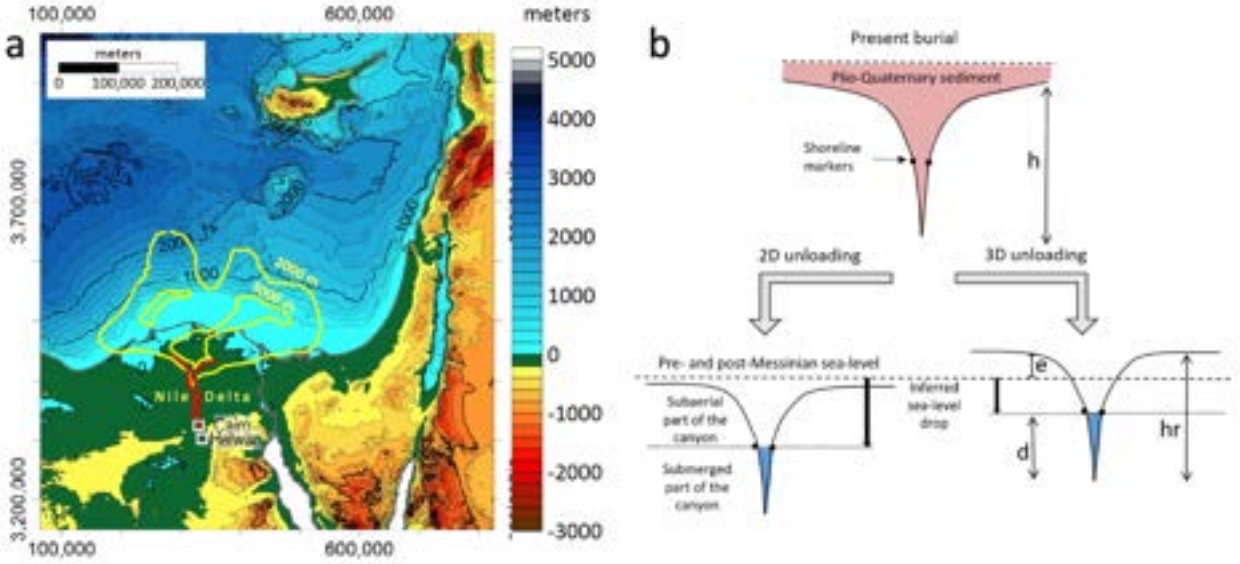

Figure 5.1. The expected influence of the Nile delta load on the adjacent Messinian canyon (a) Present-day topography and bathymetry. Red line outlines buried canyon walls[21]. Yellow lines are the 2000 and 3000 m (Zucker et al., 2020) thickness contour of the Pliocene-Quaternary section showing that the main sedimentary load is located north of the canyon. (b) Schematic illustration of the difference between 2D and 3D restoration of the original vertical position of the Messinian canyon. Upper panel shows the present day buried canyon under Pliocene-Quaternary rocks. Left panel illustrates that in 2D analysis, canyon remains fully below present-day sea level. Right panel illustrates that 3D analysis, considering the off-plane load, is expected to provide higher canyon shoulders. h - the height difference between canyon thalweg and shoulders. Hr - the same after sediment unloading (hr<h). E - elevation of canyon shoulders asl. d - water depth in the submerged part of the canyon. The inferred sea level drop is $\Delta_{sea\ level} = hr - e - d$.

The advantage in backward modelling is the well-known current relief and the unloaded sediment mass from seismic and well data. The source of uncertainty is the tectonic correction, which could be large (Amadori et al., 2018) particularly in tectonically active areas. Sicily, the Apennines, Crete, and Cyprus have uplifted thousands of meters since the end of the Miocene; the Ionian, Herodotus, and northern Levant basins subsided hundreds or thousands of meters towards nearby subduction zones (Robertson and Dixon, 1984; Faccenna et al., 2014; Faccenna and Becker, 2020). Fortunately, northern Egypt is far from any plate boundary with minimal tectonic activity. The continuous flow of River Nile along thousands of kilometers without significant post-Messinian incision, excludes the possibility of regional uplift. On the other hand, the lack of post-Messinian sedimentation outside of the Nile Valley indicates negligible regional subsidence. Moving offshore, the closest location of post-Messinian tectonic activity is observed 150-200 km north of the Messinian canyon along the Rosetta and Temsah fault systems (ref, Fig. 5.2A from Zucker et al., 2021). We estimate that this remote tectonic activity had minor influence on the restored canyon.

Taking advantage of the minor post-MSC tectonic activity in the Nile delta, we focus on the influence of the thick Nile delta load (2000-m and 3000-m contours, Fig. 5.1A) on the paleo-Nile canyon located >100 km to the south. 2D-treatment of this problem (Gargani and Rigollet, 2007; Gargani et al., 2010) provides uplifted canyon shoulders, but still below sea level (Fig. 5.1B). However, we hypothesize that a 3D-calculation considering a ~4-km-thick off-plane load should yield much higher canyon shoulders (*e* Fig. 5.1B). Our analysis indicates that the shoulders of the Messinian Nile canyon were significantly higher than the "normal" sea level before and after drawdown (*e* in Fig. 5.1B); due to the delta-load induced flexure, this positive topography was lowered after the Messinian. Without correcting for this pre-flexure topography, the magnitude of the sea-level drop is overestimated (Fig. 5.1B).

5.3.2. Geological markers for the fallen sea level

Another reason for overestimating the magnitude of the MSC drawdown is ignoring the possibility that the downstream portion of the canyon may have been, at least, partly submerged below the fallen sea level (*d* in Fig. 5.1B). The challenge is to recognize indicators of the fallen MSC level, including 1) Changes in the slope of the river thalweg as indicators of land-sea transition (Gargani and Rigollet, 2007). 2) Sedimentary facies characterizing continental-to-marine or shelf-to-slope transitions (Ghielmi et al., 2010, 2013; Amadori et al., 2018). 3) Buried scarps of shoreline terraces (Druckman et al., 1995; Bertoni and Cartwright, 2006; Cartwright and Jackson, 2008). 4) Flat truncations indicating subaerial erosion (Bertoni and Cartwright, 2006). 5) Geomorphic erosional surfaces/features distinguishing between subaerial and submarine channel (Ben Moshe et al., 2020).

Here we combine two observations constraining the amplitude of sea-level drop: a) the knickzone height generated by the upstream-migrating Nile incision, which constrains the minimal (partial) drawdown, excluding the downstream part of the valley. b) The transition from a sub-horizontal to a steeper river profile marking the transition from fluvial to submarine flow. Such a transition is observed in rivers continuously extending on-to-offshore as submarine canyons; e.g., the Gauping River-Canyon (Liu et al., 2016) (southwest Taiwan) and the LIobregat River-Foix Canyon (Amblas et al., 2015)(northwest Spain), with nearly horizontal thalweg approaching the coastline or shelf edge and much steeper thalweg offshore. Over geological time scales, near their base level and mouth, river profiles flatten. Therefore, the near-horizontal river profile and its slope break with the submarine canyon indicate the presence of a regional base level.

5.4. Data and Model Setup

For unloading the post-Messinian (Pliocene-Quaternary) sediment from the base Pliocene surface, we first expand the recently compiled base Pliocene map (Zucker et al., 2020) a few hundred kilometres south of Cairo. In practice this requires to reconstruct the depth of the buried canyon under the present-day Nile Valley. Outside the valley the thickness of post Messinian rocks is negligible. Based on the data presented above, we considered a linear gradient of 1/30 (1000 m over a distance of 30 km) between Cairo and Helwan and a much smaller gradient of 1/3333 (300 m per 1000 km) farther south. In this map the bottom of the canyon is 1200 m near Cairo, 550 m in Helwan (RIGW, 1997; Awad, 2019), and 400 m at the southern boundary of the map (Fig. 5.2a).

For decompaction of underlying sediment, we used a regional sediment thickness map (Loncke et al., 2006), which is >10 km deep in most of the study area. The decompaction results are insensitive to the accuracy of this map, because rocks deeper than ~5 km retain nearly negligible porosity (Sagy et al., 2015; Amadori et al., 2018). The uncertainty related to a range of decompaction parameters (shale, sand, and shaly-sand) are presented in Fig. 5.5.

For flexural backstripping we apply an elastic thin-plate approach with a pseudo-3D (planform) flexural procedure(Garcia-Castellanos et al., 2003; Amadori et al., 2018; Heida et al., 2021). For density of the post-Messinian sediment we use 2000 kg/m^3, consistent with seismic and well log data (Loncke et al., 2006; Sagy et al., 2015). For elastic thickness we use 20, 30, 40, and 50 km, and the associated uncertainty is illustrated in Figures 5.4 and 5.5.

5.5. Results

5.5.1. Restoring the original topography

Restoring the original topography requires the Pliocene-Quaternary thickness (Fig. 5.2A), and involves calculating the subsidence due to compaction of pre-Pliocene sediment (Fig. 5.2b) and the flexural deflection due to the weight of the Pliocene-Quaternary sediment (Fig. 5.2c) and the evaporated water layer (Fig. 5.2D). Figs 5.2e and 5.2f present the observed and restored base Pliocene surface. The restored landscape is a few hundred meters above the pre- and post-MSC sea level (Fig. 5.3B); its present depth below the flat delta plain expresses the post-Messinian subsidence due to flexural bending of the lithosphere and compaction of pre-Pliocene sediment (Fig. 5.2A, B).

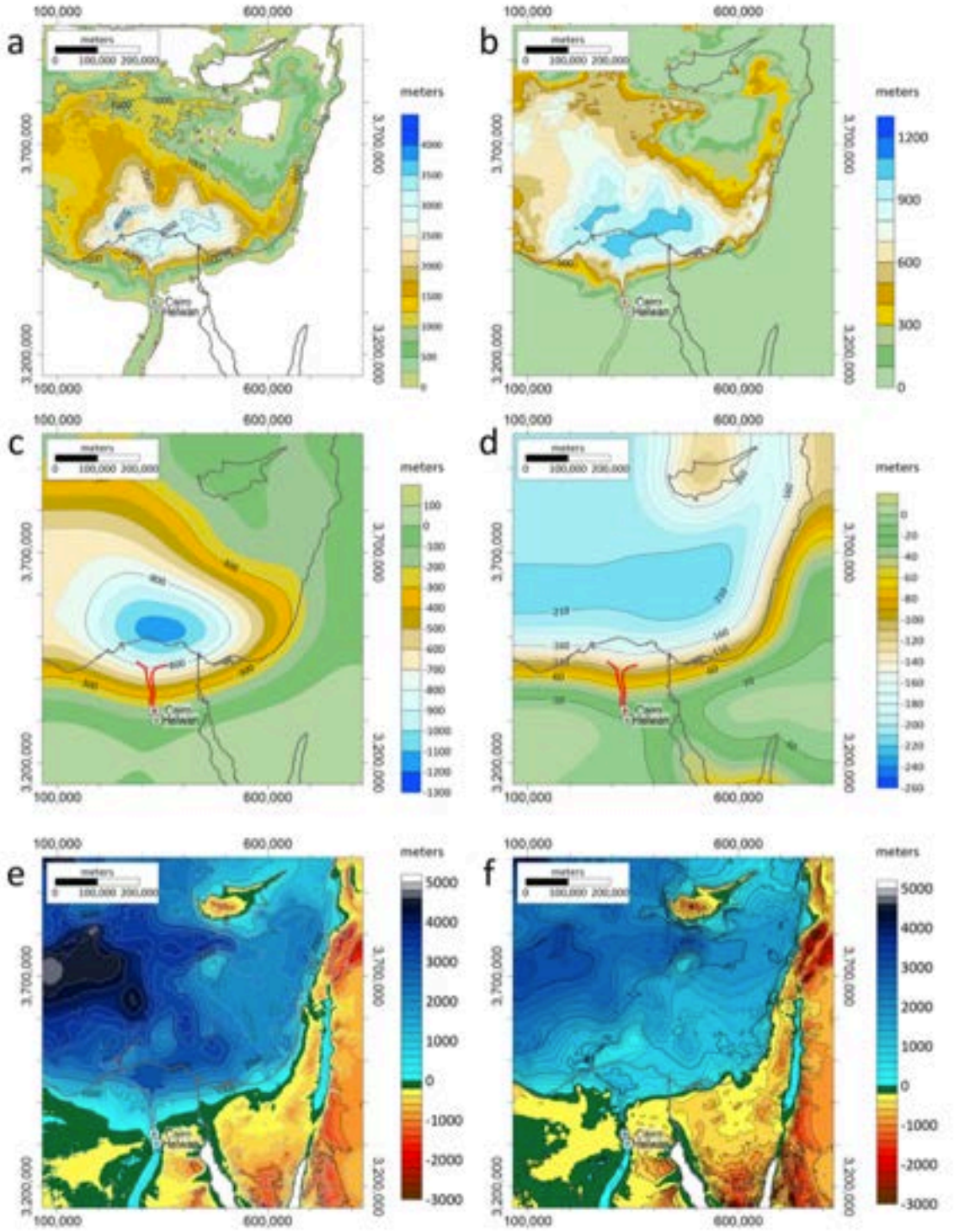

Figure 5.2. Maps illustrating how the Messinian erosional surface (MES ~ base Pliocene) is restored to its original vertical position. a) Thickness of rocks covering the base Pliocene surface. b) Calculated subsidence due to compaction of pre-Pliocene sediment assuming shale lithology. c) Calculated flexural deflection due to unloading of post-Messinian rocks, using elastic thickness, Te=30 km). d) Calculated flexural deflection due to unloading of a 650-m-thick water layer (Te=30 km. e) Observed base Pliocene structural map (modified after Zucker et al., 2020). f) Restored base Pliocene surface after correcting for compaction (shale) and deflection (Te=30 km) due to sediment unloading. No correction for water unloading has been applied here.

The canyon's longitudinal profile (Fig. 5.4A) illustrates that this upward restoration reached ~750 m near Cairo and ~2000 m at the base of the paleo-continental slope. Confirming our hypotheses, the restoration quantifies the elevated canyon shoulders (*e* in Fig. 5.1B) and the original canyon depth (*hr<h* in Fig. 5.1B). For example, 60 km north of Cairo (Section 4, Fig 5.4D), the restored shoulders are ~300 m above the pre- and post-MSC sea level, and the shoulder-to-thalweg relief drops from 1500 m in the buried surface to 1000 m in the restored landscape.

The longitudinal river profile further illustrates that the height of the Cairo-Helwan knickzone is reduced from 650 m in the buried profile to 400 meters in the restored profile (Fig. 5.4A). Downstream, the profile flattens to near horizontal with ±100-m elevation differences for the 20<Te<50 km range of elastic thicknesses. This nearly horizontal segment extends ~40 km downstream to a slope break (knickpoint), where the concave profile abruptly steepens and becomes convex.

We interpret the Cairo-Helwan knickzone as the southernmost location of the Messinian retrogressive incision, separating the MSC canyon gorge from the pre-MSC upstream valley. This knickzone most probably was characterized by a series of high bedrock waterfalls (Haviv et al., 2010) held by hard Mesozoic carbonates (Barber, 1981), accommodating most of the sea-level drop. From the base of this inferred knickzone, the river slope gradually decreased towards the inferred base level (Fig. 5.4A). The concave-convex knickpoint is interpreted as the coastline, where the subaerial river flow was transformed into a submarine turbiditic flow that formed a subaqueous canyon.

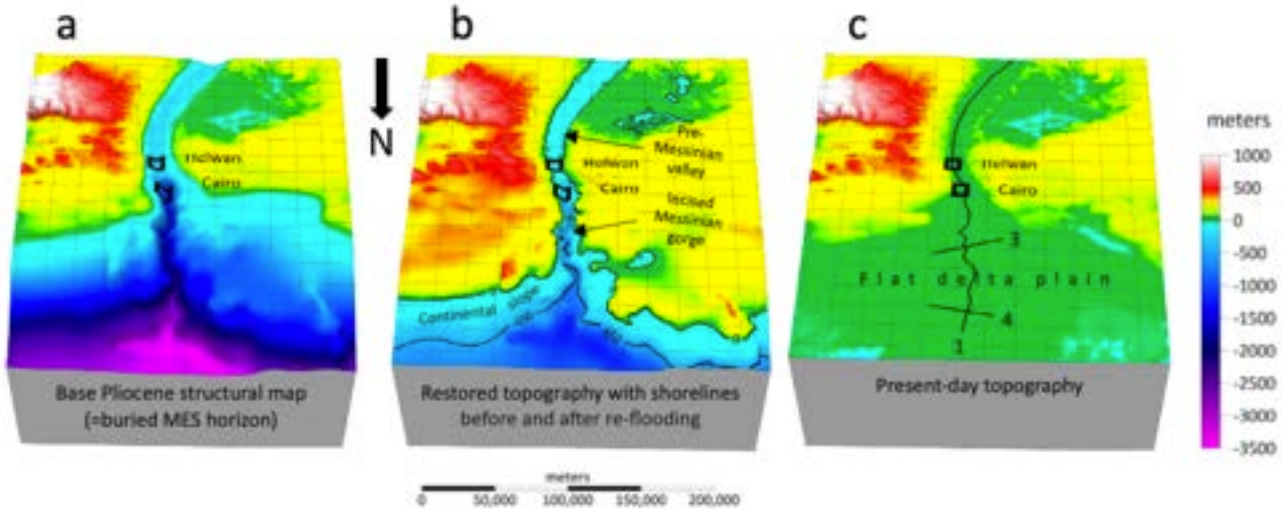

Figure 5.3. 3D view of the Nile delta and the buried Messinian canyon illustrating landscape evolution being restored. a) Base Pliocene structural map (=MES). b) Restored topography for the earliest Pliocene immediately after sea level recovery and prior to any Pliocene deposition (shale parameters for decompaction and Te=30 km for deflection, same as Fig. 5.2f). The isobath 650 m represents the fallen MSC shoreline. c) Present-day topography. Black lines mark locations of cross sections (Fig. 5.4). The area annotated as "flat delta plain" in the present topography (c) was a few hundred m asl in the earliest Pliocene (b).

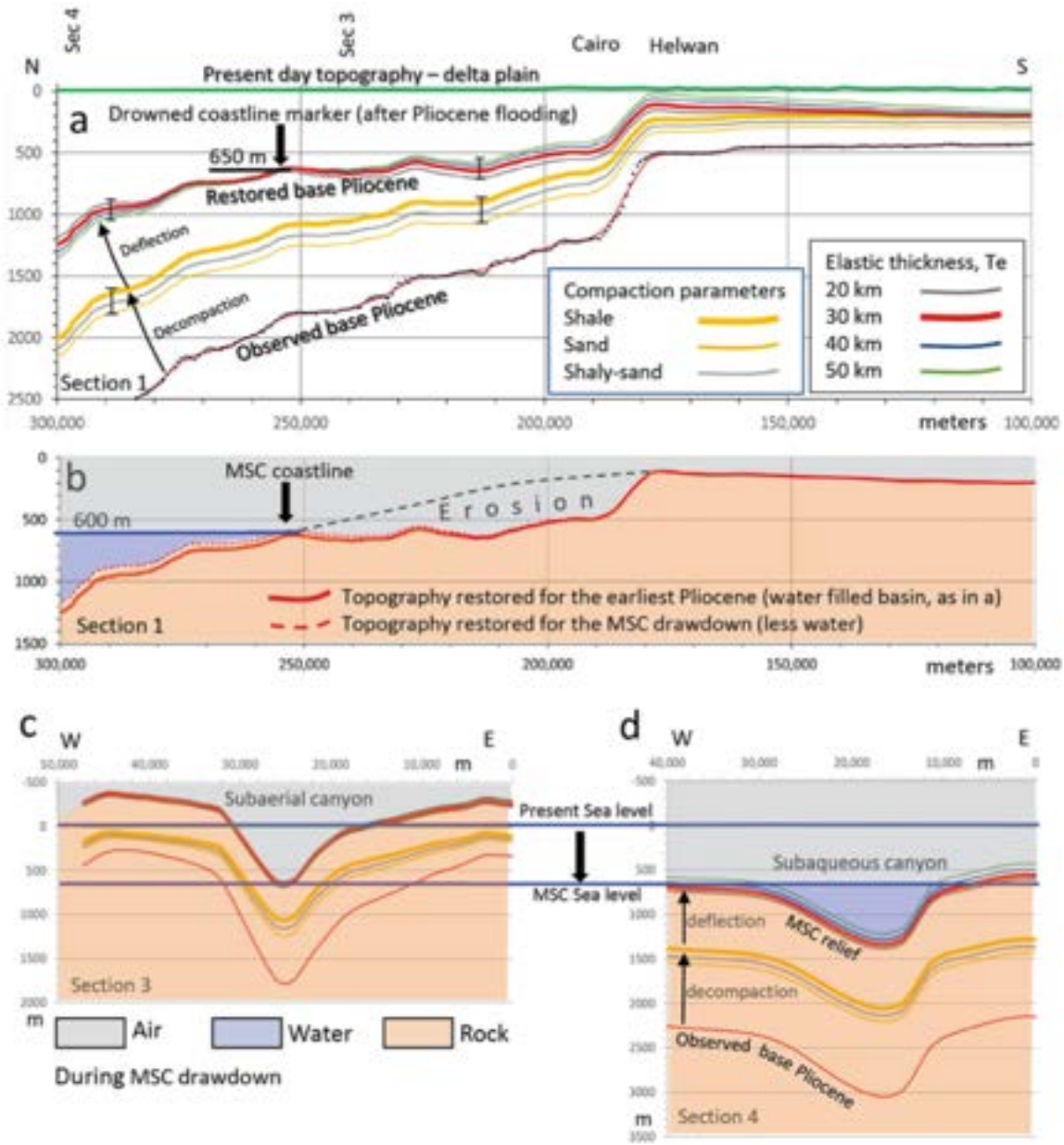

Figure 5.4. Topography restoration illustrated in cross sections. a) Along thalweg river profile (location in Fig. 5.3c) illustrating the combined effect of sediment decompaction (shale parameters) and flexural deflection. Error bars represent the range of uncertainty in the decompaction (shale, sand, shaly-sand) and elastic thickness (Te= 20, 30, 40, and 50 km). b) Interpretation of the restored river profile. The Cairo-Helwan knickzone is inferred as the southernmost location of the Messinian retrogressive incision, separating the MSC canyon gorge from the pre-MSC hanging valley. The transition from sub-horizontal to steeper gradient marks the MSC coast line 650 m below the present-day sea level. c) Restored profile across the subaerial segment of the canyon with incision down to 650 m below the pre- and post-MSC sea level. d) Restored profile across the subaqueous part of the canyon.

The depth of the inferred MSC coastline is ~650 mbsl for all curves calculated with elastic thickness 20<Te<50 km. Differences of 100-200 m between Te=20 and Te=50 km are observed at the far ends of the profile (Fig. 5.4A and Fig. 5.5A). This restoration is calculated for a filled Mediterranean, a short moment after it returned to "normal" (pre- and post-MSC) sea level (the absence of large glaciations at the time allows to assume Zanclean sea level close to present (Miller et al., 2005)). To restore the topography immediately before re-flooding, we unloaded a 650-m-thick water layer, generating an isostatic rebound that brings the MSC coastline to 600 mbsl (Fig. 5.4B) and, thus, conclude that a 600 m drawdown best explains the observations. Considering that sea level of a closed basins commonly fluctuates, we cannot rule out short episodes of lower or higher sea level. However, the observed sub-horizontal segment of the river profile indicates relative stability of the base level around 600 mbls for a duration that is long enough to produce such a profile.

5.5.2. Uncertainties related to decompaction and deflection

The unknown lithology and spatiotemporal distribution of the sediment buried under the Pliocene-Quaternary section, produces an uncertainty related to the parameters used for the decompaction correction. To illustrate the range of this uncertainty, we used parameters of three lithologies: sand, shale, and shaley sand. Considering that at least since the Late Eocene, huge amounts of clastics started arriving to the Egyptian continental margin, which accumulated mainly shales (Salem et al., 1976; Said et al. 1981; Steinberg et al., 2011; Macgregor, 2012; Bar et al., 2016), we corrected for decompaction using shale parameters and reached the conclusion of 600 m drawdown (Fig. 5.5B). In addition, we demonstrate that using shaly sand lithology for the pre-Pliocene sediment, the amplitude of the reconstructed drawdown may increase to 750 m (Fig. 5.5C).

Another source of uncertainty is related to the elastic thickness used for the deflection correction. Previous studies dealing with lithospheric strength in the studied region argued that rigidity increases along with decreasing crustal thickness(Steckler and ten Brink, 1986). Te=45 km was used for the Levant margin and Te=25 km for the Arabian plate(ten Brink et al., 1990), Te=30 km for the Levant Basin assuming that this is approximately the depth of the 350^0 isotherm(Segev et al., 2006), and Te of 10-35 km for the Levant continental margin(Steinberg et al., 2014).

In light of this uncertainty, here we calculated the deflection four times using Te = 20, 30, 40, and 50 km. This range significantly (±400 m) influences the results in the central basin, but its influence on the restored coastline is smaller than 100 m (Fig. 5.5B, C).

Unloading of a 650 m thick water layer causes an isostatic rebound of 210 m in the deep basin and zero inland (Fig. 5.4b). To further show this effect we recalculate water unloading for a 500 and 750 m thick water layer, for Te= 30 and 40 km. The effect of these variations on the restored river profile are negligible.

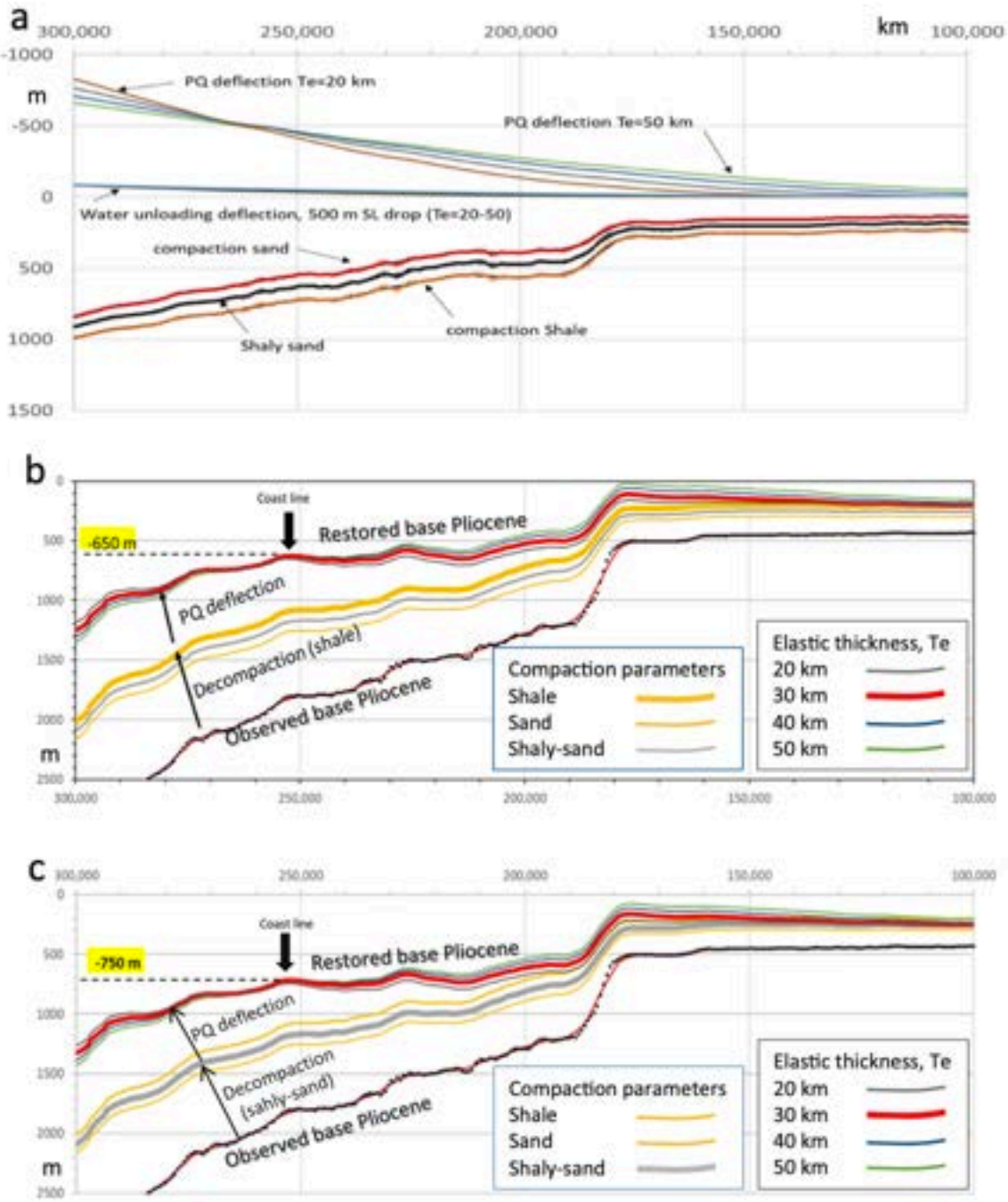

Figure 5.5. Uncertainties in river profile restoration. a) Calculated subsidence during burial of pre-Pliocene sediment using compaction parameters of shale, sand, and shaly-sand. Calculated deflection due to unloading of post-Messinian sediment using elastic thickness Te = 20, 30, 40, and 50 km. b) Restoration based on the assumption that pre-Pliocene sediment contains mostly shales (same as Fig. 5.4a). c) Restoration based on the assumption that pre-Pliocene sediment contains mostly shaly sand. The difference between b and c is 100 m in the sea level restoration (650 m versus 750 m, respectively).

5.6. Discussion and conclusions

The restored topography, during the time immediately after re-flooding and just before initial Pliocene deposition, indicates the existence of a deep-water embayment extending to the Cairo-Helwan knickzone, and a 200-m deep water body continuing farther inland (Fig. 5.2E, 5.3B). We argue that the deep embayment was excavated by Messinian incision whereas the upper valley south of the Cairo-Helwan knickzone, may have been shaped by pre-Messinian ancestors of River Nile and unaffected by the Messinian incision. This conclusion is consistent with the sedimentological data presented above indicating a transition from deep water deposits north of Cairo to shallow water and lacustrine and fluvial deposits in the Beni-Suef region and further south along the Nile Valley; it disagrees with suggestions that the Messinian incision and subsequent marine invasion had reached Aswan. Another indication for limited retrograde incision up to Cairo (~100 km) and not further upstream to Aswan (~1200 km) is the absence of a thick Messinian fan delta, which is expected in a case of enormous erosion along 1200 km. The Late Messinian Qawasim and Abu Madi Formations exceed thickness of 1000 m only in a limited (100x25 km) region at the mouth of the canyon(Rizzini et al., 1978; Barber, 1981; Said, 1981; Pigott and Abdel-Fattah, 2014; Leila and Moscariello, 2019). Outside this region these formations rapidly thin to a few 10s or 100s of m (<300 m) resembling distal deep-water deposits(Said, 1981; Ahmed et al., 2001; Kellner et al., 2018). Such a canyon fill with a relatively small lowstand fan is better reconciled with limited incision of the Messinian Nile canyon up to Cairo.

Messinian deposits of the Abu Madi and Qawasim Fm. overlying the MES offshore Egypt and the MSC Stage 3 deposits overlying the salt in the Levant Basin of 100-200 m thick, (Gvirtzman et al., 2017; Madof et al., 2019), indicate that the major drawdown occurred during the second stage of the MSC alongside massive salt deposition in the deep basin. However, since the thickness of the post salt Messinian deposits (MSC stage 3) are negligible in relations to the Pliocene-Quaternary section, here we assume that the top salt and the base Pliocene surfaces approximately coincide. Thus, the restored landscape at the end of Stage 2 (5.55 Ma) and at the end of Stage 3 (5.33 Ma) are practically the same.

The 200 m depth of the pre-Messinian upper valley south of Helwan is difficult to explain, considering that Oligocene-Miocene eustatic drawdowns only reached a few tens of meters (Miller et al., 2005). To reconcile this discrepancy geodynamically, ~150-m regional subsidence should be invoked, as proposed from modelling of mantle-flow-sourced topography (Faccenna et al., 2019); such post-Messinian tectonic correction implies reduction of the amplitude of drawdown from 600 m to 450 m. On the other hand, the presence of Pliocene marine rocks in the upper Nile Valley, 50 m above sea level (Sallam et al., 2018), indicates that northern Egypt has not been subsiding significantly, at least since the Pliocene and that therefore 450 m to explain the depth of the Base Pliocene surface seems unrealistic in our opinion.

Another possibility is that the canyon depth near Helwan is not 550 mbsl(RIGW, 1997; Awad, 2019), as we used for modelling, but only 200 mbsl as observed in a water well, located a few kn to the south (Said, 1981). Applying 200 mbsl in the model, the restored upper valley rises to ~100 mbsl; considering post-Messinian 50 m of tectonic subsidence, the base of the restored Miocene valley rises to 50 mbsl, which is within the range of eustatic falls. With such a tectonic correction (50 m), the inferred MSC drawdown is reduced from 600 to 550 m. It should be mentioned, however, that such details are within the uncertainties of the technique (e.g., sediment thickness, compaction, and elastic thickness).

Within the range of 550-750 m drawdown, we prefer the value of 600 m, which fits the assumptions of shale dominated lithology for pre-Pliocene lithology and tectonic stability of the Egyptian continental margin. ~600 m drawdown is 2-4 times smaller than previous estimations deduced from the Nile canyon (Barber, 1981; Gargani and Rigollet, 2007; Gargani et al., 2010). We claim that previous studies underestimated the post-Messinian subsidence by ignoring the compaction of the pre-Pliocene sediment and not considering the 3D-effect of flexure. For instance, the formerly estimated post-Messinian subsidence of 750-1000 m at the base of the continental slope (Gargani and Rigollet, 2007), becomes ~2000 m when including decompaction and flexural isostasy. We further propose that base level drop and incision depth were overestimated by ignoring the uplifted canyon shoulders (*e*) and its subaqueous downstream portion (*d*) (Fig 1B). For instance, Barber (1981) measured a >2000-m relief along the buried gorge and associated it with base-level drop. Here, we show that after isostatic unloading, the river profile reveals a flat region consistent with a steady lowered base level during the MSC at about -650 m.

The difference between our result of a 600 m drawdown and the 800-900 m drawdown inferred from the Po Plain and north Adriatic Sea (Amadori et al., 2018, same method) is within the range of uncertainty of the method. The discrepancy may therefore be related to 1) limitations of the technique (uncertainties are shown in Fig. 5.5 ;2) The possibility of disconnected Adriatic Sea from the Eastern Mediterranean, consequently having different base levels, or 3) Involvement of difficult-to-correct tectonic motions in the Po Plain, located between the active Apennines and Alps. We emphasize again that, in contrast, the tectonically-stable Egyptian continental margin provides ideal conditions for restoration.

Finally, we cannot dismiss the possibility that geomorphological markers identified at various depths below the Mediterranean seabed (Bertoni and Cartwright, 2006; Micallef et al., 2018a; Madof et al., 2019), represent different and possibly shorter-lived stages of the MSC. Our analysis is based on the incision along the Messinian Nile canyon, the largest erosional feature formed during the MSC and hence we interpret it as representative for the average sea level during most of the duration of the drawdown stage.

Chapter 6: Box modelling of evaporite deposition in the Central Mallorca Depression

After presenting the results of the bathymetric reconstructions of the various Mediterranean sub-basins in Chapters three, four and five, in this Chapter we illustrate how such reconstructions can be applied to constrain quantitative hydrogeochemical box modelling. We use the reconstructed hypsometry of both the Central Mallorca Depression and the deep West Mediterranean to compute the evaporite precipitation potential under a wide range of conditions, from fully connected with two-way water exchange to complete disconnection from the deep basin, and compare these to the observed volumes of halite and gypsum. We show a marked difference in the required environmental conditions during the deposition of gypsum (high water level, connected) and halite (rapid deposition from a disconnected basin). Halite volumes observed in the Western Mediterranean and CMD can be consistent with a water level drop of around 1.5 km, which matches the shoreline depth reconstructed in Chapter 4. However, the exact conditions (especially water level) at the onset of halite deposition remain unclear, considering its depth distribution in small subbasins apart from the CMD.

This Chapter is the result of an interdisciplinary collaboration with two SaltGiant ESRs (CNRS Montpellier and Utrecht University).

Highlights:

- Gypsum saturation was reached in the upper water layer of the Mediterranean during Stage 1 of the Messinian Salinity Crisis
- Primary Lower Gypsum deposition was not limited to shallow (<200 m) silled basins, as previously proposed
- A high amplitude drawdown of >850 m occurred in the Western Mediterranean during Stage 2 of the MSC
- During this drawdown, halite emplacement in the Western Mediterranean started from a deep, brine filled basin reaching halite saturation when drawdown was between 0 and 850 m below sea level.

Results from this chapter have been published as:

Raad, F., Ebner, R., Heida, H., Meijer, P., Lofi, J., & Maillard, A., Garcia-Castellanos, D. (2022). A song of volumes , surfaces and fluxes : The case study of the Central Mallorca Depression (Balearic Promontory) during the Messinian Salinity Crisis. *Basin Research*, *March*, 1–27. https://doi.org/10.1111/bre.12702

6.1. Chapter Summary

The Central Mallorca Depression (CMD) located in the Balearic Promontory (Western Mediterranean), contains a well-preserved evaporitic sequence belonging to the Messinian Salinity Crisis (MSC) salt giant, densely covered by high- and low-resolution seismic reflection data. It has been proposed recently that the MSC evaporitic sequence in the CMD could be a non-deformed analogue of the key MSC area represented by the Caltanissetta Basin in Sicily. This presumed similarity makes the CMD an interesting system to better understand the MSC events.

Physics-based box models of the water mixing between sub-basins, built on conservation of mass of water and salt, help constrain the hydrological conditions under which evaporites formed during the MSC. Those models have been widely used in the literature of the MSC in the past two decades. They have been mostly applied to the Mediterranean Sea as a whole focusing on the Mediterranean-Atlantic connection, or focusing on the influence of the Sicily Sill connecting the Western and Eastern Mediterranean Sea. In this study, we apply a downscaled version of such modelling technique to the CMD.

First, we quantify the present-day volumes of the MSC units. We then use a reconstructed pre-MSC paleo-bathymetry to model salinity changes as a function of flux exchanges between the CMD and the Mediterranean. We show that a persistent connection between the CMD and the Mediterranean brine near gypsum saturation can explain the volume of Primary Lower Gypsum under a sea level similar to the present. For the halite, on the contrary, the results indicate that the observed volume is smaller than that expected to have deposited if halite deposition started in a full basin, suggesting a drawdown of at least 850 m (sill depth) is necessary. Comparison between the deep basin halite volume and that of the CMD shows that it is possible to obtain the observed halite volume in both basins from a disconnected basin undergoing drawdown, although determining the average salinity of the basin at the onset of drawdown requires further investigation.

6.2. Introduction

6.2.1. The MSC units on the Balearic Promontory

The reduction of water exchange between the Atlantic and Mediterranean caused by the tectonic uplift of the Gibraltar arc during the Late Miocene Messinian Salinity Crisis (MSC; 5.97-5.33 Ma) led to the deposition of a large evaporitic body, also known as the Mediterranean Salt Giant, in a relatively short geological time interval of ~640 kyr (Hsü, 1973; Ryan, 1973; Krijgsman et al., 1999; CIESM, 2008). It has been suggested that deposition of the Mediterranean MSC salt giant has greatly affected the global oceans, by sequestering up to ~ 6-10 % of their salt content into the Mediterranean Sea (Garcia-Castellanos and Villaseñor, 2011; Haq et al., 2020) The mechanisms and time spans for the deposition of the MSC evaporites are still not clear and highly debated despite the numerous studies in the last half century, although a generally accepted chronostratigraphic model that divides the MSC events into 3 stages has been proposed (CIESM, 2008; Roveri et al., 2014a). According to this model, the onset of the MSC is marked, at least in marginal basins (<200 m paleo-depth), by up to 16 precession-driven cycles of gypsum intercalated with marls/carbonates, also called the Primary Lower Gypsum (PLG). The deposition of the PLG took place during the first stage of the MSC (stage 1; 5.971-5.60 Ma; (Krijgsman et al., 1999; Lugli et al., 2010). It was followed by stage 2 (5.60-5.55 Ma) in which part of the PLG was removed (by erosion and/or as mass transport deposit) and resedimented as Resedimented Lower Gypsum (RLG) (Roveri et al., 2006; Clauzon et al., 2015; Vinicio Manzi et al., 2021), and a halite unit was deposited in intermediate (~200 to 1000 m paleo-depth; e.g. Caltanissetta Basin and Central Mallorca Depression; (Lugli et al., 1999; Raad et al., 2021) to deep basins (>1000 m paleo-depth; e.g. Provencal and Levant basins; Lofi et al., 2011). During this stage, margins and slopes underwent intense erosion of subaerial origin according to some authors (e.g. Clauzon, 1978; Lofi et al., 2005) or of submarine origin according to others (e.g., Roveri et al., 2014b) . The third and last MSC stage is divided in 2 substages, substage 3.1 (5.55-5.42 Ma) in which the Upper Evaporites (UE) deposited in hypersaline conditions (Manzi et al., 2009), and substage 3.2 (5.42-5.33 Ma) which witnessed more hyposaline conditions, also known as the Lago Mare phase (Andreetto et al., 2021).

Several aspects and implications of the consensus model remain ambiguous and continuously questioned. For example, whether the halite deposition took place synchronously and exclusively during stage 2 (Roveri et al., 2014a; Manzi et al., 2018; Manzi et al., 2021) or started already during stage 1 (Meilijson et al., 2018, 2022). Another controversy is whether the isolated conditions persisted during the whole stage 3 or the Atlantic-Mediterranean connection was restored at the beginning of that stage (Andreetto et al., 2021), with a Mediterranean probably supplied also by Paratethyan brackish water (Marzocchi et al., 2016). Many more aspects continue to puzzle regarding the MSC: the amplitude and duration of the main water level drawdown, the reason for the absence of evaporites on most of the shelves and slopes of the open deep basins, the cause of lack of a clear paleodepth distribution of halite (e.g. deep halite-free Valencia Basin versus shallower Balearic Promontory containing halite; Heida et al., 2021).

The Balearic Promontory (BP), a prominent high in the Western Mediterranean (Figure 6.1), presents a unique opportunity place to investigate the formation of the MSC evaporites, thanks to the well-preserved evaporitic units deposited since the beginning of the crisis (Maillard et al., 2014; Ochoa et al., 2015; Driussi et al., 2015b; Raad et al., 2021). Lying between Mallorca and Ibiza, the Central Mallorca Depression (CMD), contains the most complete and least tectonically deformed evaporitic sequence in the BP, including halite (Raad et al., 2021; Maillard et al., 2022). This sequence has been studied and accurately mapped recently by several authors (Figure 6.1) (Maillard et al., 2014; Driussi et al., 2015b; Raad et al., 2021). Most recently, Raad et al. (2021) showed that the MSC evaporitic sequence in the CMD could be an undeformed analogue of the intermediate-depth Caltanissetta Basin in Sicily, a rare example of onshore record holding MSC halite, which makes the CMD an interesting place to study for furthering our understanding of the MSC.

Physics-based models help in examining some hydrological factors under which the MSC evaporites formed. Those models have been widely used in MSC research in the past two decades (Blanc, 2000; Meijer & Krijgsman, 2005; Blanc, 2006; Meijer, 2006; Krijgsman & Meijer, 2008; Topper et al., 2011; Meijer, 2012; Topper & Meijer, 2013; Simon et al., 2017). All those studies worked on a Mediterranean scale aimed at the Atlantic-Western Mediterranean and Western-Eastern Mediterranean connections through the Gibraltar and Sicily straits, respectively. In this study, we scale down as we apply models based on conservation of mass of water and salt and a simplified representation of strait dynamics, on a single sub-basin within the Western Mediterranean, the CMD (Figure 6.1). A similar approach has been applied recently in the Sorbas Basin using those models by Modestou et al. (2017). In the CMD, the availability of a good, high- and low-resolution seismic reflection data coverage, allows the determination of the thicknesses and respective volumes of the evaporites (Figure 6.2-A). In addition, the availability of a restored pre-MSC paleo-bathymetry, published recently by Heida et al. (2021), allows the establishment of the hypsometry of the basin during the MSC.

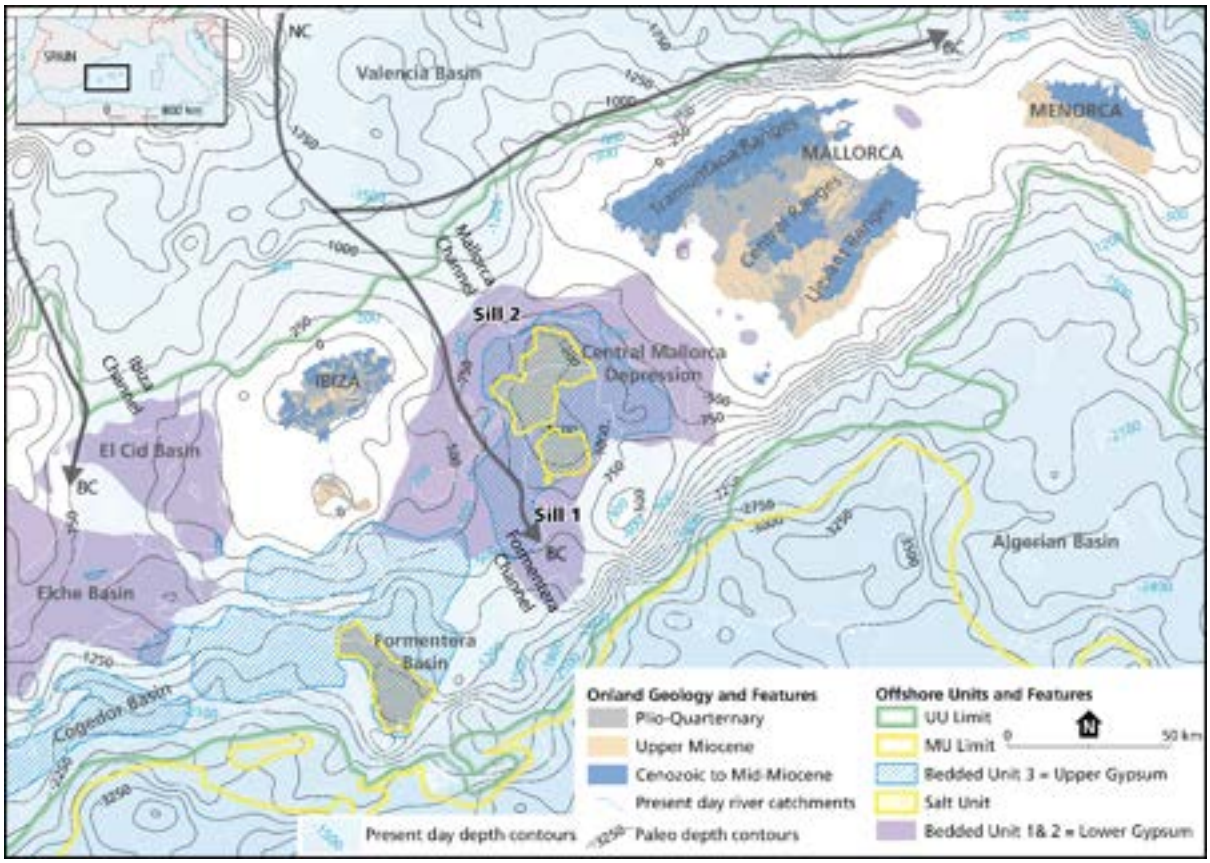

Figure 6.1. Map of the MSC units over the Balearic Promontory (BP), Valencia Basin and Algerian Basin. Our study area focusses on the Central Mallorca Depression (CMD) located between the islands of Mallorca and Ibiza, which contains several Bedded Units (BUs) and a Halite unit geometrically/attitudinally separated from the deep basin's Mobile Unit (MU) and Upper Unit (UU). MSC units of the BP are modified from Raad et al. (2021). Onland geology of the Balearic Islands is modified from geological map of Spain 1:50000 (IGME). Thin white lines in the background represent the present-day Bathymetry taken from the European Marine Observation and Data network (EMODnet) database available online (www.emodnet-bathymetry.eu). Thin black lines represent the paleo-bathymetry at the start of the MSC, modified after Heida et al. (2021). Arrows indicate the present day currents (from Pinot et al. (2002) and Lüdmann et al. (2012)). NC=Northern Current. BC=Balearic Current.

The main objectives of this study are to: (1) establish the hydrological conditions (salinity and fluxes) and mechanisms under which the evaporites (gypsum and halite) in the CMD formed during MSC stages 1 and 2, and (2) examine the amplitude of a potential water level drawdown in the CMD needed to explain the required hydrological conditions.

To reach these objectives, we use the calculated volumes of the MSC evaporites and the restored pre-MSC bathymetry to (1) make water budget calculations of the CMD and compare those with the observed evaporitic volumes, (2) test the factors (fresh water budget and fluxes) controlling the salinity of the CMD as an isolated basin, (3) calculate the fastest evolution possible of the CMD and Valencia Basin in terms of salinity and time to deposit the

observed evaporites, and (4) discuss our results and observations in the frame of the whole Mediterranean Salt Giant complex and compare them to the consensus model.

The present-day BP is characterized by a series of sub-basins lying at a wide range of depths (Figure 6.1; e.g. -650 m Elche Basin and -1700 m Formentera Basin). They show different levels of inter-basinal connection and all contain MSC sediment up to ~500 m thick (Figure 6.1 and Figure 6.2; Driussi et al., 2015a; Ochoa et al., 2015; Raad et al., 2021). The MSC sediments of the BP have been mainly studied through seismic reflection data due to the absence of exploratory scientific boreholes. They consist of Bedded Units covering most of the BP area (BU sensu Lofi et al., 2011; Lofi, 2018; divided subsequently into BU1, BU2 and BU3 by Raad et al., 2021; Table 6.1) as well as salt patches present in some sub-basins depocenters (Figure 6.1) (Mauffret, 1977; Acosta et al., 2004b; Maillard et al., 2014; Driussi et al., 2015b; Raad et al., 2021; Heida et al., 2021, Figure 6.1) The sub-basins are believed to have inherited their structure from the pre-Messinian tectonic evolution of the promontory, and thus to have been preexisting topographic lows during the MSC allowing the accumulation of evaporites (Sàbat et al., 2011; Driussi et al., 2015a).

In this work, we focus mainly on the CMD, an intermediate-depth (sensu Roveri et al., 2014a) sub-basin containing a well-preserved MSC sequence.

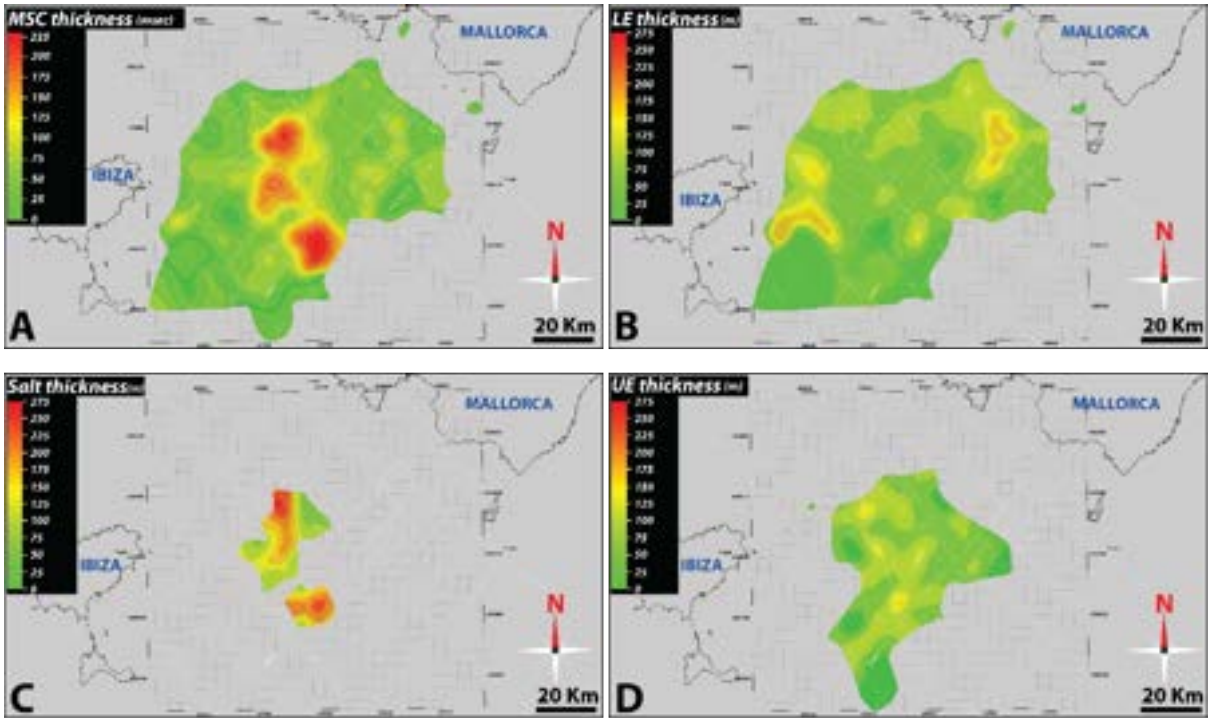

Figure 6.2. Thickness maps of the MSC units of the CMD. A: Thickness map in TWTT of the whole MSC units, including all BUs and Halite in TWTT. B: Thickness map in meters of BU1 + BU2 interpreted as stage 1 MSC Lower Evaporites (LE), with gypsum content ranging between of about 80% (see text and Table 6.1 for explanation). C: Thickness map in meters of the halite unit. D: Thickness map in meters of BU3 interpreted as MSC stage 3 Upper Evaporites (UE). The white thin lines mark the locations of seismic profiles used to map the deposits.

6.2.2. The Central Mallorca Depression: Present-day vs paleo-topography

Today, the maximum water depth of the CMD reaches -1050 m (Figure 6.1; Acosta et al., 2004). The CMD is surrounded by the gently dipping slopes of Mallorca and Ibiza to the NNE and WSW respectively. It is connected northward to Valencia Basin through the ~730 m deep, ~20km wide Mallorca Channel (Pinot et al., 2002), and southward to the Algerian Basin through the ~1000 m deep, ~30 km wide channel that we call the Formentera Channel (Figure 6.1). The CMD underwent limited post-MSC tectonics with some local deformation caused by extension and strike-slip motions (Acosta et al., 2004b; Sàbat et al., 2011), which guaranteed a good preservation of the MSC deposits. Other sources of vertical motions, such as isostatic subsidence, compaction and thermal subsidence, did not strongly affect the CMD due to the nature of the lithosphere below the BP and the limited extent and thickness of the sediment (Heida et al., 2021 and references therein). Heida et al. (2021) applied a pseudo-3D backstripping restoration of the Messinian paleotopography of a large area in the Western Mediterranean, including the BP. They obtained pre-MSC paleo-depths of the BP sub-basins ranging from ~550 m (e.g. Cogedor Basin) to ~1800 m (e.g. Formentera Basin). The CMD was at ~1500 m in its deepest part (Figure 6.1, Figure 6.3 and Table 6.3; Heida et al., 2021) whereas the Mallorca and Formentera channels were at 750 m and 850 m (±50 m; Heida et al., 2021) respectively (Sill 02 and sill 01, respectively, in Figure 6.1 and Figure 6.3).

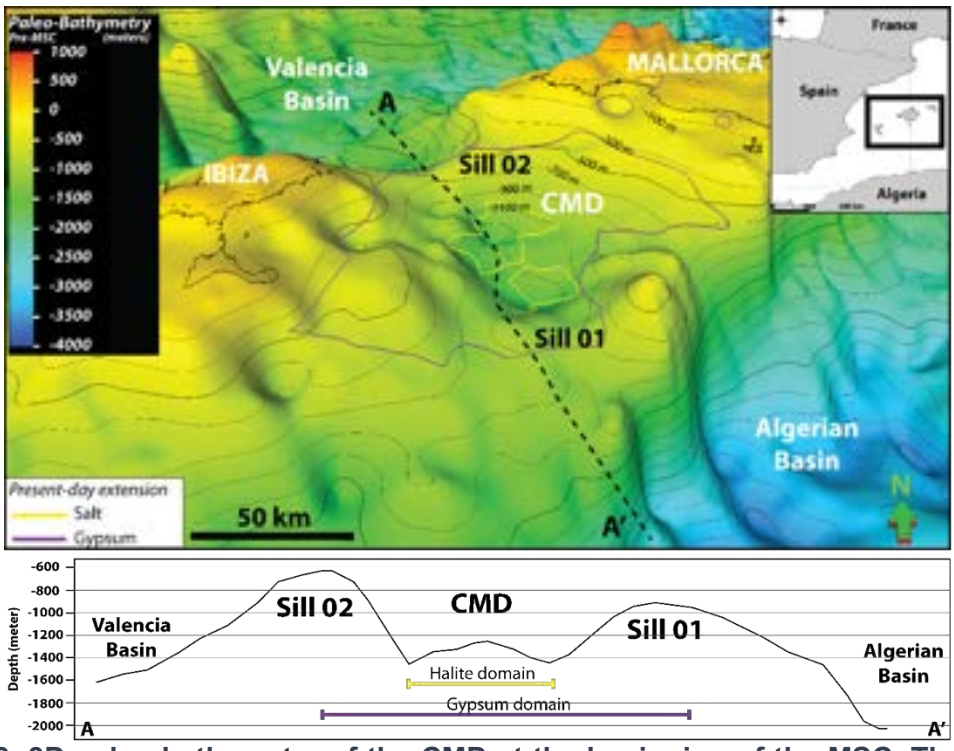

Figure 6.3. 3D paleo-bathymetry of the CMD at the beginning of the MSC. The CMD is connected to the deep basin through two silled channels/connections. Sill 01 is deeper and is the one that is used in the modelling as a connection between the CMD and the open Mediterranean. A-A' is a 2D profile highlighting the geometry of the CMD and the sills. The violet and yellow polygons represent the present-day extension of the gypsum and halite, respectively. They are 2D polygons projected above the 3D paleo-bathymetry.

6.2.3. Present-day Hydrography and Water Masses in the Central Mallorca Depression

Generally, four water masses can be distinguished in the Western Mediterranean: the Modified Atlantic Surface Water; the Levantine Intermediate Water; the Western Mediterranean Deep Water; and the Bottom Water (La Violette, 1994; Pinot et al., 2002; Lüdmann et al., 2012). The Mallorca and Ibiza channels play a main role in the regional water exchange and circulation of those water masses. In particular, the Northern Current carrying northern waters from the Gulf of Lions southward along the continental slope of the Valencia Basin, is in part blocked by the Balearic Islands and consequently bifurcates north of Ibiza. One branch, called the Balearic Current, passes through the Ibiza and Mallorca channels into the Algerian Basin (Figure 6.1). Several studies surveyed and quantified the present-day oceanographic parameters of these currents (water exchanges, fluxes, salinities) across the Mallorca Channel (Pinot et al., 2002; Barceló-Llull et al., 2019; Vargas-Yáñez et al., 2020). The fresh water from river runoff reaching the CMD is very limited (<<10 $m^3 s^{-1}$; Table 6.3) with minor river catchments draining from the Tramuntana and Central ranges onshore Mallorca, and the central part of Ibiza Island (Figure 6.1; Garcia et al., 2017 and references therein). Most of the catchments are draining mainly Mesozoic carbonates (Figure 6.1).

6.2.4. Messinian Salinity Crisis in the Central Mallorca Depression

So far, only two studies were dedicated to the MSC deposits in the CMD. Maillard et al. (2014) were the first to study and map the BUs and to image the salt offshore at an intermediate depth. The authors present all possible scenarios for the deposition of the MSC sediment based on the observed features and markers (see their Figure 12). In the most recent study dedicated to the MSC deposits in the BP, Raad et al. (2021) made a step forward by dividing the BUs into 3 sub-units (Table 6.1) based on their seismo-stratigraphic position and seismic facies. Including the salt unit, they performed a unit-by-unit comparison to the MSC evaporites outcropping in the Sicilian Caltanissetta Basin. Following their division and comparison, Raad et al. (2021) interpreted the MSC units of the CMD and proposed a depositional model as follows (see their Figure 10 and discussion for a detailed description and interpretation of each unit):

- BU1: equivalent to the PLG and deposited during stage 1 of the MSC (Table 6.1). It is the only drilled MSC unit of the BP and is made of a succession of precession-driven cycles of selenitic gypsum and marls (Ochoa et al., 2015). This unit is topped by a clear erosional surface everywhere on the BP (Maillard et al., 2014; Ochoa et al., 2015; Raad et al., 2021). In the CMD, BU1 reaches a maximum thickness of ~180 m in the proximal domain (Figure 6.2-B) when it is preserved. It thins towards the distal domain (~40 m), and/or where it is eroded by paleo-incisions (Figure 6.2-B; Raad et al., 2021).

- BU2: possible time equivalent of BU1 (i.e. MSC stage 1), it would represent its distal facies equivalent. According to Raad et al. (2021), this unit likely consists mainly of cumulate gypsum, alternated with non-evaporitic sediment. The cumulate gypsum is commonly known to form in a supersaturated water column in which gypsum crystals nucleate at the top or within water column and then precipitate and settle on the seafloor as laminar gypsum (Hardie and Lowenstein, 2004; Babel and Schreiber, 2014; Natalicchio et al., 2021). No erosional features mark the top or the base of this unit. Both BU1 and BU2 were deposited during a high stand, and were then followed by an important base level drawdown, during which only BU1 was exposed.

- Salt unit: it consists mainly of halite and might include more soluble salts (K- and Mg-salts), similar to the salts observed in Caltanissetta Basin (Lugli et al., 1999; Manzi et al., 2012). The salt unit in the CMD is truncated at its upper limit by an erosional surface, probably due to exposure and/or dissolution in relatively shallow water when the maximum base level drawdown was reached. It reaches a maximum thickness of ~280 m in the deepest depocenter (Figure 6.2-C).

- BU3: this unit is interpreted as the equivalent of the Upper Evaporites of the Caltanissetta Basin, and consisting of alternating terrigenous and gypsum beds deposited during stage 3 of the MSC (Table 6.1). It lies unconformably above the BU1 and the salt. It lies conformably below the lowermost Pliocene pelagic sediment. BU3 reaches thicknesses up to ~170 m (Figure 6.2-D). It shows no physical relationsh or continuation with the deep basin's MSC evaporites. For this reason Raad et al. (2021) and Heida et al. (2021) concluded that the CMD was disconnected from all the surrounding basins during the final stage of the MSC, before getting reconnected during the Zanclean reflooding with the rest of the Mediterranean at the end of the crisis (Garcia-Castellanos et al., 2009). In this scenario, the sulfate ions needed for gypsum precipitation are exclusively derived from dissolution of stage 1 PLG (Ryan, 2009; Andreetto et al., 2021).

MSC unit	Interpreted lithology	MSC stage and duration	Velocity for TWTT to depth conversion	Evaporites/clastic ratio	Total volume (m3)	Evaporitic volume (m3)	Thickness (meters)	Bounding surfaces
BU1 = LE (PLG)	Selenitic gypsum intercalated with marls	Stage 1 (5.97-5.60 Ma)	4500 m/s (Ochoa et al., 2015)	80%	3.73E+11	2.99E+11	40-180m	Base: Conformable Top: TES
BU2 = LE	pelagic gypsum intercalated with marls	Stage 1 (5.97-5.60 Ma)	4500 m/s	80%	3.73E+11	2.99E+11	40-180m	Base: Conformable Top: Conformable
Salt unit	halite	Stage 2 (5.60-5.55 Ma)	4780 m/s (Samperi et al., 2020)	100%	9.63E+10	9.63E+10	280m	Base: Conformable Top: IES
BU3 = UE + LM?	Alternations of gypsum and clastics	Stage 3 (5.55-5.33 Ma)	3500 m/s	50%	1.63E+11	8.14E+10	150m	Base: IES Top: Conformable

Table 6.1. Characteristics and parameters of the MSC units present in the CMD. BU=Bedded Unit; LE=Lower Evaporites; PLG=Primary Lower Gypsum; UE=Upper Evaporites; LM=Lago Mare; TES= Top Erosion Surface; IES= Intermediate Erosion Surf

6.3. Data and Model Setup

6.3.1. Seismic dataset and volume calculations

We use widespread high- and low-resolution seismic reflection profiles to calculate the volumes of the MSC units in the CMD (Figure 6.2-A). This dataset has been interpreted, described and used in several previous studies (e.g. (Maillard et al., 2014; Bellucci et al., 2021; Raad et al., 2021). Following the interpretation of the MSC units on the seismic profiles, a thickness map for each unit was created (Figure 6.2) using the internal velocities shown in Table 6.1 for the time to depth conversion.

For the volume calculations we consider 80% of the total volume of BU1 (=PLG) and BU2 as gypsum, since elsewhere around the Mediterranean the PLG cycles contain only thin non-evaporitic intercalations and much thicker gypsum beds (Table 6.1; e.g., Lugli et al., 2010; Ochoa et al., 2015 for the BP offshore area; García-Veigas et al., 2018; Mas & Fornós, 2020). For the BU3 (=UE) we consider only 50% of its volume as gypsum since the gypsum/non-evaporitic deposit ratio of the UE is lower than the PLG (Table 6.1; e.g., Manzi et al., 2009 for Sicily; Manzi et al., 2016 for Cyprus; Lugli et al., 2015 for the Upper Unit in offshore DSDP and ODP sites). No such assumptions are made for the halite volume as we consider the entire salt unit as made of halite with negligible amount of clastics (Lugli et al., 1999; Manzi et al., 2012; Samperi et al., 2020).

6.3.2. Theoretical model

Investigating the possible scenarios that could have led to the Messinian deposits of the CMD requires that we consider the salinity of the basin itself as well as the salinity of the surrounding waters. In this study, we define salinity (*S*) as dissolved mass of salts (*m*) per volume of water (*V*), ($S = \frac{m}{V}[\ kg\ m^{-3}]$).

We treat salinity as a sum of concentrations and differentiate between the salts of interest, i.e., gypsum and halite:

$$S = \frac{\sum m_{Salts}}{V} = \sum[salt] = \ c[CaSO_4] + \ c[NaCl] + \ c[other\ salts] \qquad (6.1)$$

Since the exact composition of seawater during the MSC is not known, we use a composition that has been used in previous studies (e.g., Gladstone et al., 2007; Krijgsman & Meijer, 2008; Topper & Meijer, 2013; Simon et al., 2017) and assume a proportional increase of the partial concentrations with increasing salinity, until saturation is reached. Saturation is defined as the salinity at which the water body cannot hold any extra ions of the salt in question. Adding the concentration of the three ion groups in Table 6.2 to eq. (6.1), we define our reference salinity to be $S_{reference} = 35.05 kg\ m^{-3} = \ 1.27\ kg\ m^{-3} + \ 27.21\ kg\ m^{-3} + \ 6.57\ kg\ m^{-3}$ (Leeder, 2009). Assuming seawater is saturated in gypsum at 145 $kg\ m^{-3}$ (McCaffrey et al., 1987; De

Lange et al., 1990) and in halite at 350 $kg\ m^{-3}$ (McCaffrey et al., 1987; Babel and Schreiber, 2014), we can then calculate the saturation concentration for gypsum, $c[CaSO_4]^{sat} = 5.25\ kg\ m^{-3}$ and halite $c[NaCl]^{sat} = 272.1\ kg\ m^{-3}$ (Krijgsman and Meijer, 2008; Topper and Meijer, 2013). A direct application of these values is to quantify the volume of water, at saturation concentration, that would be needed to form an observed volume of deposit. Since a lower concentration would require a bigger volume of water to precipitate the deposit, this water volume at saturation will be called V_{min}:

$$V_{min} = \frac{m_{salt}}{c[salt]^{sat}} = \frac{V_{deposit} * \rho_{deposit}}{c[salt]^{sat}} \quad \textbf{(6.2)}$$

In which m_{salt} is the salt mass that forms the deposit that can be derived from the volume of the deposit, $V_{deposit}$ in [m^3] and its density, $\rho_{deposit}$ $[kg\ m^{-3}]$ (Table 6.2).

The water volume of the CMD is defined by the physical limits of the basin as retrieved from the pre-Messinian paleo-bathymetry of the CMD (Figure 6.3) (Heida et al., 2021). From the same reconstruction, we draw cross sections through the southern and the northern connection between the CMD and the adjacent Mediterranean Sea. With a width of 70-80 km at sea level and a depth of up to 850 m, these connections are larger than the Strait of Gibraltar (12 km wide, 300 m deep; Lacombe & Richez, 1982). They are best described as wide openings with a sill that is elevated well above the seafloor north and south of the CMD but still located at significant water depth (Figure 6.3). The openings would form a narrow strait and/or shallow sill only when the water level is significantly lower than today. From modern measurements (Pinot et al., 2002; Barceló-Llull et al., 2019) it is known that there are both fluxes into and out of the basin through each of the two connections (see section 6.2.2).

It is possible to apply basic principles that allow us to learn about the CMD and its fluxes as a system while making as little assumptions as possible. One of these principles is the conservation of water volume for a system that is in balance. This means that the volume of water in the basin does not change when the sum of fluxes into the basin is of the same size as the sum of outward fluxes. In contrast, when there is a net outflux, the volume of water inside the basin will decrease over time, with a rate defined by the absolute difference between the in- and outflux. This is for example the case for a disconnected basin with a negative freshwater budget. This loss of fresh water is described by a volume flux [$m^3 s^{-1}$] (positive when the basin loses water) and named freshwater budget (fwb).

	Gypsum	Halite	Reference
Density (kg/m3)	2300	2200	Leeder, 1999
Fraction of longroup (-)	1.27/ 35	27.21/ 35	Leeder, 1999 Topper & Meijer (2013)
Saturation Concentration (kg/m3)	5.25	271.1	Leeder, 1999 Topper & Meijer (2013)
Area covered by deposit (m2)	5.33E+9	6.65E+8	This work
Volume in CMD (m3)	3.80E+11	9.63E+10	This work
Erosion rate (mm/a)	From 0.20[a] up to 3.16[b]	0.5–0.75[c] (for 50 mm/a precipitation) – 20[d] (for 100 mm/a rainfall)	[a] Sanna et al., (2015) [b] Calaforra et al., (1993) [c] Frumkin (1994) [d] Mottershead et al. (2005)
Precipitation rate (mm/a)	1[a]–100[b]	100[c, d]–150[e]	[a]Orti et al., (1985) [b]Schreiber & Hsu, (1980) [c] Lensky et al., (2005) [d] Sirota et al., (2018) [e] Manzi et al., (2012)

Table 6.2 Table showing the parameters used in our modelling for Halite and Gypsum with the corresponding references. Erosion rates are not used in the modelling but are used for considerations in the discussion.

$$\mathrm{Fwb} = (E - P) * A - R \quad \textbf{(6.3)}$$

In which E is the rate of evaporation [$m\ s^{-1}$], P the rate of precipitation [$m\ s^{-1}$], A the surface area of the basin [m²] and R the inflow of river water [$m^3 s^{-1}$]. In this scenario the basin experiences a drawdown due to the loss of water volume to the atmosphere until the surface area A is so small that the net evaporative loss is of the same size as the river inflow R. When the water volume decreases, the salinity increases until an equilibrium is reached, since neither net evaporation nor river inflow transport ions. In this case, the evolution of salinity *S* with time *t* is given by,

$$S(t) = \frac{m_{salt}}{V_0 - \mathrm{fwb} * t} \quad \textbf{(6.4)}$$

Where m_{salt} is the mass of salt [kg] contained in the basin at the start of drawdown (i.e., upon disconnection) and V_0 the initial volume of the basin [m^3].

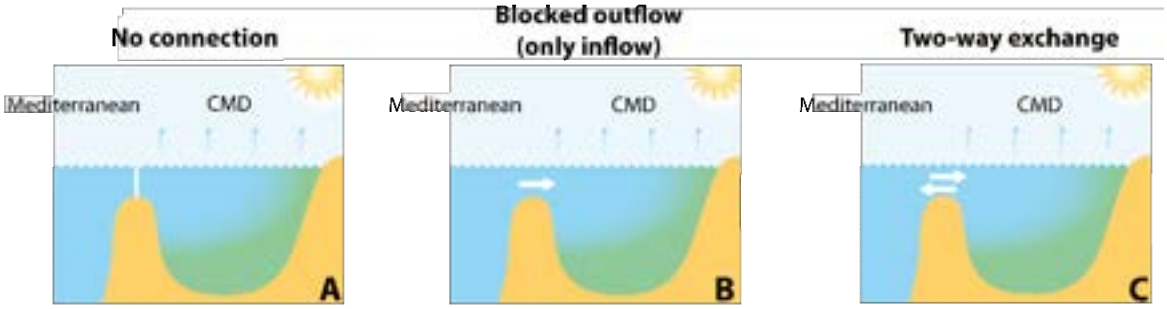

Figure 6.4. Different ways to approach the connection between the CMD and the open Mediterranean. A: No connection between the CMD and the Mediterranean and thus both influx and outflux are cut. B: The basin is connected to the open Mediterranean in a way that inflow compensates the loss of freshwater due to evaporation. C: There is a two-way exchange over the sill. The inflow now compensates the freshwater budget as well as the saline outflow. Those three 'approaches' should not be conflated with the 'scenarios' that we present and discuss in the text, as they are strictly theoretical.

During at least part of its MSC evolution, the CMD is likely to also have been subject to saline water fluxes through its connections. This means that the concentration of ions would have changed while the water volume stayed the same. For a basin with a negative freshwater budget that is fully balanced by a saline inflow (Figure 6.4-B), the concentration of dissolved ions, and hence the salinity, increases over time. If either gypsum or halite reaches its saturation concentration in the process, the mass that exceeds this threshold concentration is taken to be precipitated as a uniform layer without getting re-dissolved. In the following we use $\Gamma = \frac{m_{prec}}{t}$ [$kg\ s^{-1}$] to describe

the rate at which mass is precipitated. It is important to note that salinity can increase past the point at which precipitation begins since the ion group of the other salts can continue to concentrate (equation 6.1). In that scenario the evolution of salinity S with time t is dependent on the magnitude of the influx Q_{in} and its salinity S_{in}

$$S(t) = S_0 + \frac{Q_{in} * S_{in} - \Gamma}{V_0} * t \tag{6.5}$$

For a basin like the CMD, it is likely that the exchange through the two sections is more complex than only inflow to balance the freshwater budget. By assuming that the salinity of the inflow through the northern connection is the same or close to the salinity of the inflow through the southern connection, we can simplify the system by combining these two fluxes to one inwards flux. The same applies to the fluxes leaving the basin through the two connections (Figure 6.4-C). In this scenario the salinity of the basin, S_{out}, is dependent on the properties of these combined in- and outflows respectively.

$$S(t) = S_0 + \frac{Q_{in} * S_{in} - Q_{out} * S_{out} - \Gamma}{V_0} * t \tag{6.6}$$

A special case to consider is the situation where neither salinity nor water volume of the basin change in a system of this kind. These two conditions can be described as $\frac{dV(t)}{dt} = 0$ and $\frac{dS(t)}{dt} = 0$ and lead to two expressions

$$Q_{in} = Q_{out} + fwb \tag{6.7a}$$

$$Q_{in} * S_{in} = Q_{out} * S_{out} + \Gamma \tag{6.7b}$$

For the special case without precipitation ($\Gamma = 0$), these two can be combined in a way that allows us to calculate the fluxes that would be needed to attain a certain salinity ratio (Knudsen, 1900),

$$Q_{out} = \frac{fwb}{\frac{S_{out}}{S_{in}} - 1} \text{ and } \mathrm{Q_{in}} = \frac{fwb}{1 - \frac{S_{in}}{S_{out}}} \tag{6.8}$$

If the basin has already reached saturation, Γ will become non-zero and must be considered. There are scenarios for which we can calculate values for Γ as a function of other parameters of the system. The simplest case is a scenario in which both the in- and the outflow are saturated in a salt, either gypsum or halite. While the salinity can increase, the concentration of the salt in question cannot, leading to the precipitation of the excessive mass. Applying eq. (6.7) to only the concentration of a single salt for a

system in balance gives an expression for the precipitation rate in that special case. We thus have,

$$c[salt]_{in} = c[salt]^{sat} \; and \; \mathrm{c[salt]_{out}} = c[salt]^{sat}$$

with which eq. (6.7b) yields,

$$\Gamma_{salt} = (Q_{in} - Q_{out}) * c[salt]^{sat}$$

Combined with eq. (6.7a) we find,

$$\Gamma_{salt} = fwb * c[salt]^{sat} \tag{6.9}$$

For a more realistic scenario, where the inflow is below saturation while the basin has reached that threshold, the number of unknowns increases, and the precipitation becomes dependent on the magnitude of the outflux and the concentration of the influx The conditions for the concentrations can now be written as

$$c_{in} < c[salt]^{sat} \;\; and \;\; c[salt]_{out} = c[salt]^{sat}$$

Inserting those conditions into eq. (6.7b) and substituting Q_{in} again with eq. (6.7a) gives

$$\Gamma_{\mathrm{salt}} = Q_{out} c_{in} + fwb * c_{in} - Q_{out} * c[salt]^{sat}$$

Which can be rewritten in a way to express it in dependence of the ratio between the concentrations of the in- and outflow

$$\Gamma_{salt} = c[salt]_{in} * \left(Q_{out} * \left(1 - \frac{c[salt]^{sat}}{c[salt]_{in}} \right) + fwb \right) \tag{6.10}$$

With eq. (6.10) it is now possible to explore the rate of precipitation for a set of scenarios that are not only defined by their fwb but also by Q_{out} and c_{in}. To compare the results of eqs. (9) and (10) to literature values they need to be expressed as rate of sedimentation (i.e., thickness of deposit per unit of time rather than mass). For this we need the density of the deposit, $\rho_{deposit}$ (Table 6.2), and the area, $A_{deposit}$, covered by the deposit of interest. It is then also possible to calculate the duration of the period of deposition for each Γ, from an observed volume of the deposit,

$$T_{prec} = \frac{V_{deposit} * \rho_{deposit}}{\Gamma_{salt}} \tag{6.11}$$

Applying eq. (6.11) to the total volume of the deposit gives the total timespan during which this salt would need to precipitate at a given rate to form the observed deposit. To get the average duration of precipitation per precessional cycle (23 kyr) the volume needs to be divided by the number of total cycles during which it formed.

It is worth noting that the depositional process used in our modelling is pure evaporative and does not take into consideration more complex bio-geochemical processes that might have played a role in the PLG formation, at least locally where low salinity values were obtained from water inclusions in PLG gypsum crystals (e.g. Piedmont Basin, Italy; Natalicchio et al., 2014; Calabria, Italy; Costanzo et al., 2019), although the reliability of the salinities obtained from fluid inclusions measurements was recently questioned (Bigi et al., 2022). With the modelling approach presented here we also do not the influence of erosion into account.

6.4. Results

In this section we apply the theory as described in section 6.3.2 to the data that was presented in section 6.3.1 to identify the key processes that are needed to explain the MSC deposits in the CMD. We find that a saline flow into as well as from the CMD is needed to form the gypsum deposit, while the halite deposit could have formed from a disconnected CMD filled with saturated brine undergoing a water level drop.

6.4.1. Water and evaporites volume considerations

As a first step, we calculate the volumes of water required to precipitate the observed volume of evaporites, V_G for gypsum and V_H for halite, and compare these to the (reconstructed) volume of the CMD. This will allow us to judge whether the evaporites could have formed by concentration of the water contained within the CMD or whether an additional influx of water and salt must be invoked.

For a range of water volumes (m^3) representing the CMD at a given water level, we calculate the concentration ($kg\ m^{-3}$) the water would attain if the mass of the observed evaporite (in kg) was dissolved in it. If the calculated concentration is lower than the concentration at which the water is saturated in the salts ($CaSO_4$, gypsum; $NaCl$, halite), then the water volume is big enough to hold the volume of the evaporite in a dissolved state. The minimal volume of water needed is determined as the volume at which the calculated concentration equals halite or gypsum saturation and was defined by eq. (6.1) and can be calculated with data as listed in Table 6.2.

The results, depicted in Figure 6.5, show that for the halite deposit this minimal water volume $V_{min} = \frac{9.633*10^{10}\ m^3 * 2200\ kg\ m^{-3}}{272.1\ kg\ m^{-3}} \approx 780\ km^3$ which is about equal to the capacity of the CMD below the level of the sill lying at -850 m (sill 01 in Figure 6.3). If instead we take the observed mass of halite and assume this to be dissolved in the volume of water comprised by the CMD below each horizontal level (i.e., water level below 0; Figure 6.5), we find the basin water to attain saturation values once the level is lowered to the depth of the sills (orange line in Figure 6.5). This is of course consistent with the V_{min} calculation and confirms its result.

In a similar type of calculation, we take the volume of water comprised by the basin at sill depth (Table 6.3) and assume saturation concentration of gypsum and halite respectively. This way we compute the maximum volume of gypsum or halite that can be precipitated from a disconnected basin. These calculations show that only a fraction of the observed gypsum volume (0.9%) of the BU1/2 (Table 6.1) could precipitate from the water volume available below sill depth, while more than 100% of the observed halite volume could be stored in the basin volume below the sill.

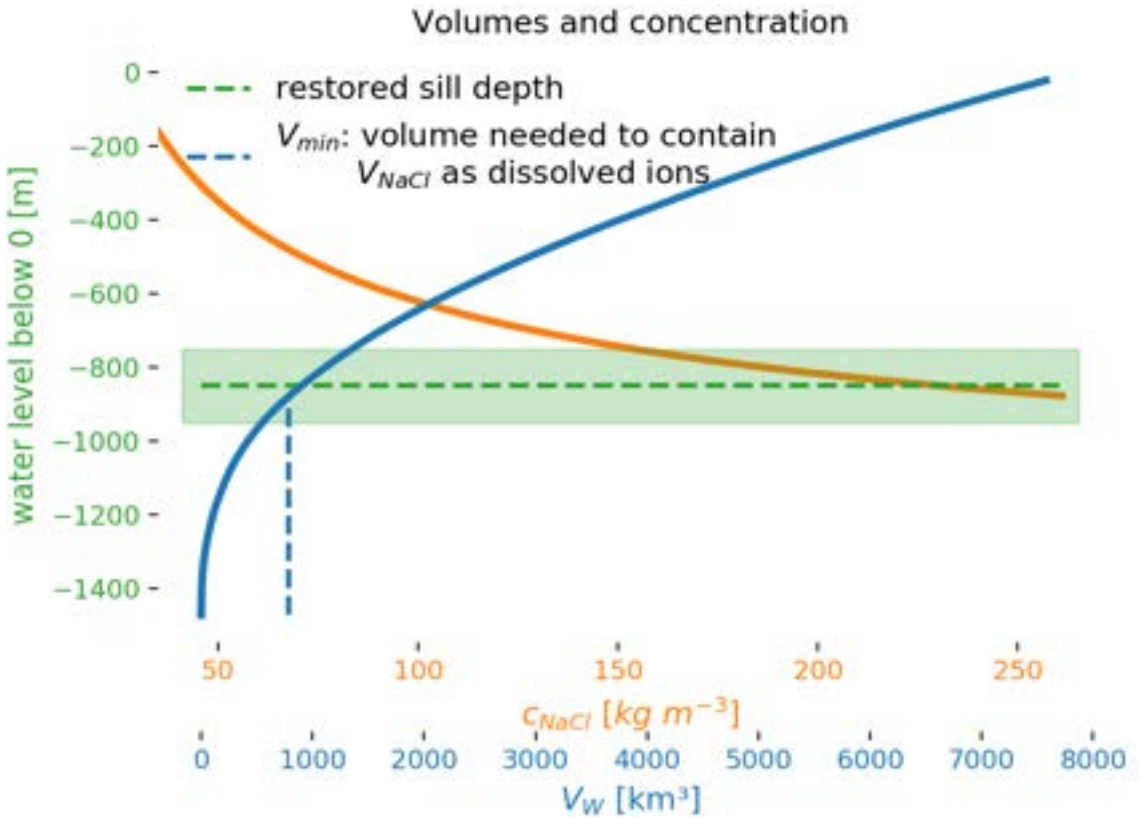

Figure 6.5. With water level on the vertical axis, the solid blue line gives the water volume of the pre-Messinian CMD below each level (see blue horizontal axis). The dashed green line depicts the level of the sills, with an uncertainty of ±50 m (green area). The water volume of the CMD below sill depth (i.e., at the crossing between the solid blue and dashed green lines) is about equal to the volume of halite-saturated water required to form the observed halite deposit (V_{min}) which is indicated with the vertical blue dashed line. Also shown as a function of water level is the concentration that the basin waters would attain if the observed mass of halite were dissolved in it (solid orange line and orange horizontal axis). Since the volume of water decreases with a lower water level, the resulting concentration increases until it reaches $c[NaCl]^{sat} = 271\ kg\ m^{-3}$ at a depth of -879m, which corresponds to a water volume of $V_{min} = 780\ km^3$ (see text for details).

The results indicate that the gypsum deposit is too massive to originate from a disconnected basin, even if it was saturated in gypsum, while the halite deposit could have precipitated from a disconnected basin saturated in halite (Table 6.4). The calculation does not inform us about the timespan over which the halite deposit was formed. This can be determined by the time it would take until a disconnected CMD would reach a new equilibrium between river inflow and net evaporation, which is addressed in the next section (section 6.4.2).

Unit	Percentage of observed volume that can be precipitated from a CMD filled to the sill (-850 m) with water at saturation
BU1/2	0.9 % (1.1 %)
BU3	2.2 % (2.8 %)
BU1/2+BU 3	0.6 % (0.7 %)
Halite	141 % (170 %)

Table 6.3. The maximum volumes of gypsum and halite that can be precipitated from the CMD as a disconnected basin. The calculations use the available water volume below sill depth at -850 m and -800 m according to pre-MSC hypsometry and saturation concentration for Gypsum (145 $kg\ m^{-3}$) and Halite (350 $kg\ m^{-3}$). For each deposit or combinations of deposits, the volume of water in the basin is adjusted to account for the predating deposits that occupies accommodation space.

6.4.2. Desiccation of an isolated basin

The only realistic process that could isolate the CMD is a water level drop in the Mediterranean Sea that lowers the level of the surrounding waters below the level of the sills. Bringing the level below that sill would cancel the exchange of saline water through the connections and the later evolution of the CMD would be independent of the rest of the sea. In this section we investigate such a scenario (Figure 6.4-A).

For such an isolated basin the new balance is described by the fwb, as defined in eq. (6.3) and thus dependent on the river influx R and loss of water to the atmosphere $(E - P) * A$. As long as more water is lost than added, the CMD experiences a drawdown that is not depending on the drawdown of the Mediterranean Sea. This process changes the surface area that is available for net evaporation and continues until a new stable state is reached where the flux to the atmosphere is of the

same size as the river inflow, which may, to first approximation, be considered constant. These two fluxes thus determine the water level in the new steady state that is defined by fwb=0 (eq. 6.3), as well as the time needed to reach it. The results are depicted in Figure 6.6, which shows that the timespan on which the process takes place is less than 1 kyr. The fastest change occurs in an extreme scenario without any river input at all (solid lines). In that case the steady state of a completely desiccated basin is reached after less than 900 yr. A river input of $R = 1\ m^3 s^{-1}$ is close to the present-day situation (Garcia et al., 2017) and would lead to a stable state after less than 1000 yr (dashed lines). In contrast to the first scenario, the basin would not completely desiccate, and the remaining water would have a depth of 8 m. A ten times higher river input of $R = 10\ m^3 s^{-1}$, leads to a larger remaining volume and a remaining water depth of 140 m. In theory there is also a corresponding river influx R for each net-evaporation $(E - P) * A$, and vice versa, that would prevent a drawdown for the disconnected basin, i.e., $fwb = 0$ for a basin with its surface at sill depth. To achieve this, a net evaporation of 0.75 $m\ yr^{-1}$ would have to be balanced by an unrealistically high influx of 340 $m^3 s^{-1}$, while inversely, the more realistic influx of 1 $m^3 s^{-1}$ (Table 6.3; Garcia et al., 2017) would require a net-evaporation as low as 0.002 $m\ yr^{-1}$. Both combinations are unrealistic, which implies that a disconnected CMD would experience a drawdown, until the surface area is small enough for the river inflow to balance the net-evaporation. The loss of freshwater during that time would lead to an increase in salinity because the dissolved ions stay in the system.

In the previous section (section 6.4.1), simply looking at volumes, it was argued that the halite deposit could have formed from a situation where the CMD was already at, or close to, halite saturation at the moment of disconnection. In that case, the water within the CMD would become oversaturated during a drawdown leading to the precipitation of the surplus ions (eq. 6.4). However, it follows from the reasoning in the current section that the resulting halite deposit will be smaller in mass and volume than the observed one, since the inflow from rivers prevents a complete desiccation. For a scenario with a high river inflow of $R = 10\ m^3 s^{-1}$ only 2.3% percent of the initial water volume remains in the basin and since a disconnected CMD at halite saturation could precipitate 144 % of the observed halite volume, this effect is small enough to be ignored. The question yet to be answered is if and how the CMD could reach halite saturation before it was disconnected.

	CMD	Valencia Basin	Reference
Present-day area (m2)	11.83E+9	57.60E+9	This work
Maximum paleo-depth (m)	1500	1800	Heida et al., 2021
Sills paleo-depth (m)	Sill02 = 700 Sill01 = 850	No sill (open basin)	This work
River inflow (m3/s)	≤ 10 [a] Present-day	500 [b] Paleo	[a] Garcia et al., (2017) [b] Urgeles et al., (2011)
Evaporation rate (m/a) [b](for the model)**	0.25 – 1.5 [a] 1.04 [b]	0.25-1.5 [a]	[a] Estrani et al., (2011) [b] Simon & Meijer, (2017)
Strait parameter g ($m^3/s/sqrt(kg/m^3)$)	10^5 Present-day	-	Barcelo-Llull et al., (2019)

Table 6.4. Table showing the morphometric parameters of the study area used as input for our modelling. **Evaporation rates are present-day values (Estrany et al., 2011; Simon and Meijer, 2017) assumed to be similar to those during the MSC.

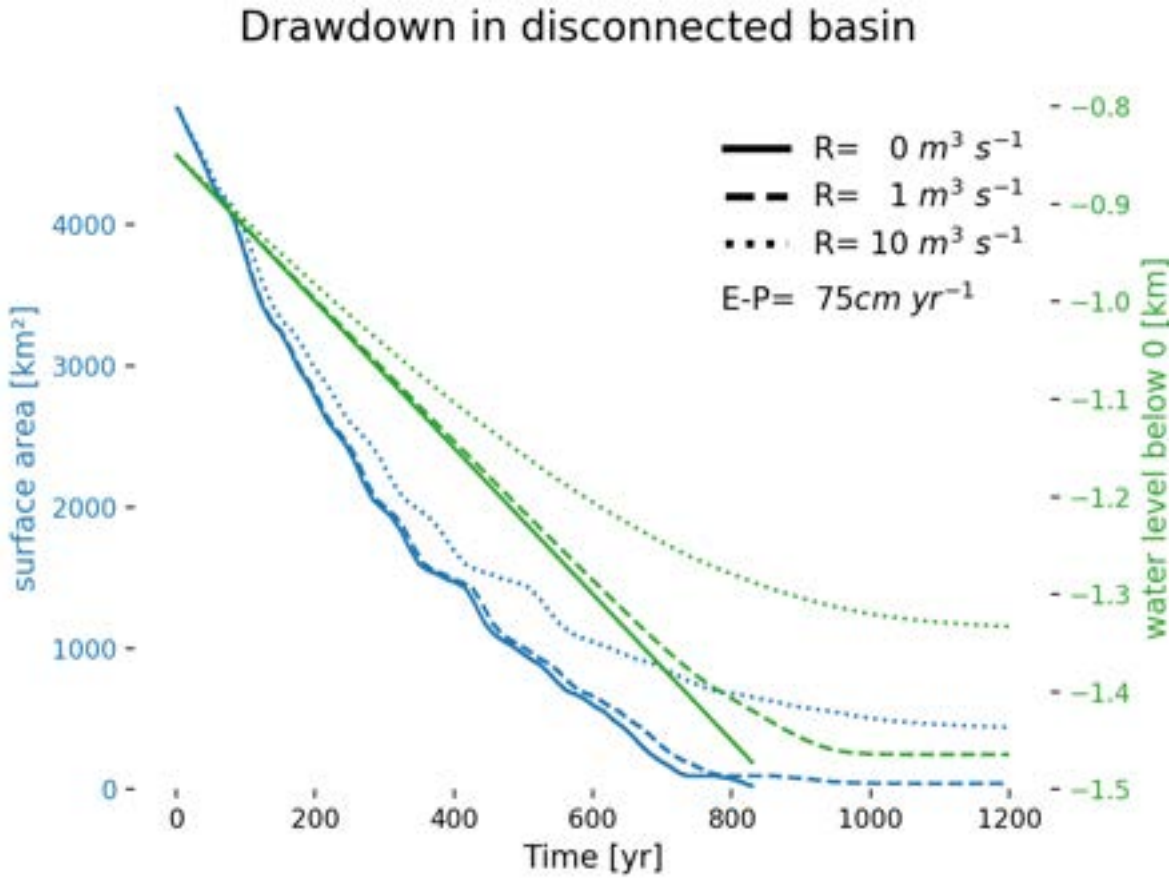

Figure 6.6. Model results for desiccation of the CMD. This figure shows the change over time in water level (green) and surface area (blue) for three different strengths of river inflow, R [$m^3 s^{-1}$] for a disconnected basin at a given net-evaporation, E-P [cm/yr]. As soon as the CMD is disconnected from the surrounding waters, the negative freshwater budget causes the water level to fall further below the sill depth (850 m). The basin only desiccates completely if there is no inflow from rivers (solid lines), for non-zero values of R (dashed, dotted) the system will reach a balance where it loses as much through evaporation as it gains by river input.

6.4.3. Full basin, inflow only

To understand if it is possible that the CMD reached halite saturation before the end of Stage 1 (i.e., the end of gypsum deposition) we consider the fastest change in concentration possible for a basin with constant volume (eq. 6.5). The same is applied to the Valencia Basin, which allows us to compare the behavior of the two basins. For this scenario, we will not assume a drawdown but keep the water level steady at 0 m. To preserve volume, all water lost to the atmosphere is replaced by saline water that is flowing into the basins from the open Mediterranean (Figure 6.4-B). This process adds ions to the water volume of the basins which can only be removed by precipitation, since there is no saline outflux. Unless $fwb = (E - P) * A - R < 0$, the salinity will increase (Figure 6.7). The rate of this increase is dependent on the fwb, the water volume of the basin as well as the salinity S_0 of the inflow. Since S_0 is the same for the CMD and the

VB, the difference in the rate of change between the CMD and VB is dependent on the ratio between their volume and the corresponding fwb. The latter is also dependent on the surface area of the basin in question (Table 6.3). We find that for the VB the net-evaporation needed to balance a realistic river inflow is 0.27 $m\ yr^{-1}$, which is 100 times higher than for the CMD. The much larger volume of the VB explains why this basin experiences a different rate of salinity increase for the same net-evaporation rate E-P even when, for the CMD, a very high river input (10 $m^3 s^{-1}$ instead of ~ 1 $m^3 s^{-1}$ taken from Garcia et al., 2017; Table 6.3) is chosen (Figure 6.7). The slow salinification of the VB in comparison to the CMD even for higher values of E-P might be an indicator that the salinity of the VB was lower than the one of the CMD.

$S_{in}[\mathrm{kg\ m^{-3}}]$	E-P [m/yr]	$T[CaSo_4]_{vol}$ [kyr]	$T[NaCl]_{sat}$ [kyr]	$T[NaCl]_{vol}$ [kyr]
37	25	182	21	0.62
145	75	15	1	0.16

Table 6.5. Comparison of the time the CMD would need to deposit the gypsum deposit ($T[CaSO_4]_{vol}$) or halite deposit ($T[NaCl]_{vol}$) compared to the time it would reach halite saturation ($T[NaCl]_{sat}$) for the same conditions and the scenario as described in Figure 6.7 and shown in Figure 6.4-B.

Focusing on the CMD, it follows from Figure 6.7 (see also Table 6.5) that the time needed to form the observed halite deposit, $T[NaCl]_{vol}$, is short enough for this to have happened during Stage 2 (~50 kyr). The same applies to the time needed to reach halite saturation, $T[NaCl]_{sat}$. With $T[NaCl]_{sat} = 21\ kyr$ for the slowest scenario tested, this time span is shorter than the duration of Stage 1, meaning that the basin would have reached halite saturation even before the beginning of Stage 2. However, $T[NaCl]_{sat}$ is much shorter than the time needed to precipitate the gypsum of BU1/2, i.e., duration $T[CaSO_4]_{vol}$. This means that in this scenario the basin would reach halite saturation before the observed volume of the gypsum deposit could be precipitated, which indicates that the inflow-only scenario is incompatible with the observed presence of gypsum and halite.

To find out whether there is a set-up where halite saturation is reached only after the full volume of the BU1/2 has been deposited, $T[NaCl]_{sat}$ as described in eq. (6.5) must be equal to $T[CaSo_4]_{Vol}$ which can be derived from eq. (6.10). This leaves us with an expression which is not dependent of the fwb and shows that for an inflow salinity of $S_0 = 35.05\ \mathrm{kg\ m^{-3}}$ the volume of the CMD would have to be 8.3 times larger than its volume at normal sea level. This again indicates that the gypsum and halite cannot have formed by the same mechanism (i.e., blocked outflow). It is likely that the formation of the gypsum deposit requires a more complex mechanism than the one considered here.

A saline outflow would not only keep the salinity from quickly rising to halite saturation values but would also be more realistic for a basin with two wide connections to surrounding waters.

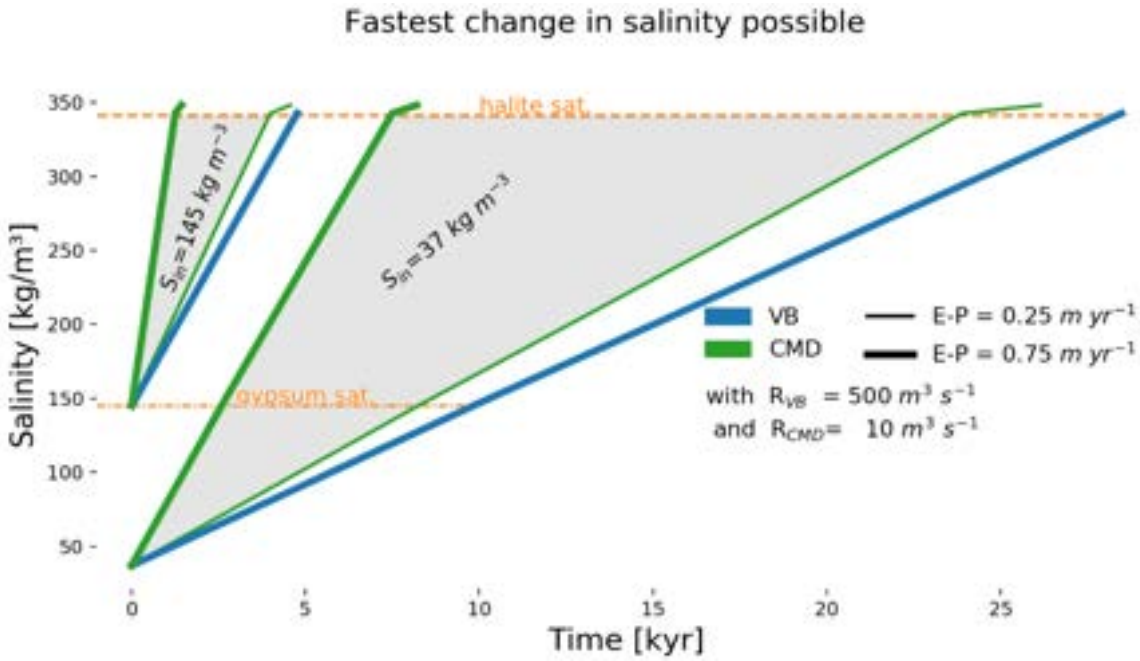

Figure 6.7. Fastest change in salinity possible for CMD and Valencia Basin (VB). All fresh water that is removed from the system due to a positive freshwater budget is replaced by saline water representing an inflow. No saline outflow is applied. The increase in salinity is shown for the CMD (green lines) and VB (blue lines) for two different inflow salinities (Sin=37 $kg\ m^{-3}$; Sin= 145 $kg\ m^{-3}$) as well as for two different net-evaporation rates (E-P= 0.25 $m\ yr^{-1}$, thin lines; EP= 0.75 $m\ yr^{-1}$, thick lines). The grey swaths filling the space between the thick and the thin green line resemble the family of functions with the same S_{in} but varying freshwater budget.

6.4.4. Two-way exchange

The presence of an outflow from the CMD to the surrounding western Mediterranean would have allowed the CMD to maintain a salinity in the range of gypsum saturation for a longer period of time than in a blocked outflow scenario. To explore this new scenario, we now quantify the size of the volume flux of water out of the basin for the case that the basin stabilizes just below gypsum saturation, while maintaining constant volume. Let us consider the two extremes of the mathematical solution, a non-existent and an infinite outflow. The first, a non-existent outflow, would lead to the situation described in Figure 6.7, with ever-increasing salinity. In the second extreme, the salinity of the basin would be the same as that of the inflow. In between these two extremes there exists an outflow strength for every inflow salinity such that the basin maintains gypsum saturation. If the outflow is larger than the calculated value, gypsum saturation will not be reached. We thus compute the maximal outflux that would still allow for

gypsum saturation. The absolute value of this maximal outflux as given by (eq. 6.8) is dependent on the salinity of the inflow as well as the fwb of the basin. The latter is defined by a given $E - P$, the surface area as well as a river inflow which is set to $R = 2\ m^3 s^{-1}$.

The results of this calculation are shown in Figure 6.8 as a function of the inflow salinity and the level of the water surface. The three swaths represent families of curves that describe a range of $E - P$ and are defined by a given outflow strength. Swaths corresponding to a relatively large outflow sit at higher inflow salinity, since with relatively large exchange the basin salinity is close to that of the adjacent water. If the basin is to attain gypsum saturation, the salinity of the inflow must already be close to that.

For a given value of the outflow, i.e., within a given swath in Figure 6.8, the curves shift towards higher inflow salinity for lower E-P, with the lowest E-P defining the right-hand border of the swath. When E-P is small, fwb is small, the inflow thus exceeds the outflow by a smaller amount (equation 6.7a) and its salinity must be higher to still achieve saturation. The slope of the curves towards the right in Figure 6.8, i.e., the shift to higher inflow salinity for lower water level, is explained by the same mechanism. The change in fwb is in that case caused by the decrease in surface area for lower water levels. Thus, a given E-P then corresponds to a smaller fwb and less net input of salt to the basin. Comparing the fwb for a water level at sea level to a water level at the depth of the sills ($-850\ m$) shows a decrease of about 50%, (e.g. $E - P = 0.25\ m\ yr^{-1}$, $R = 10\ m^3 s^{-1}$, decrease= 53%). The influence of drawdown is thus smaller than one order of magnitude.

For low inflow salinities, the fluxes needed for the basin to reach gypsum saturation ($S_{in} < 80\ \mathrm{kg\ m^{-3}}$) are several orders of magnitude smaller than the ones that are measured today (~0.1 Sv; Barcelló-Lull, 2019). This means that in a situation where the inflow salinity is less than $140\ \mathrm{kg\ m^{-3}}$ the fluxes to and from the basin would need to decrease several orders of magnitude for the basin to stay at gypsum saturation, independently of drawdown and net evaporation. Without any external factors that decrease the magnitude of the fluxes, like a strong slow-down of the circulation, the only way for the CMD to reach gypsum saturation is when the salinity of the surface to intermediate layer of the Western Mediterranean Sea is already very close to saturation. The same applies to reaching halite saturation in the basin.

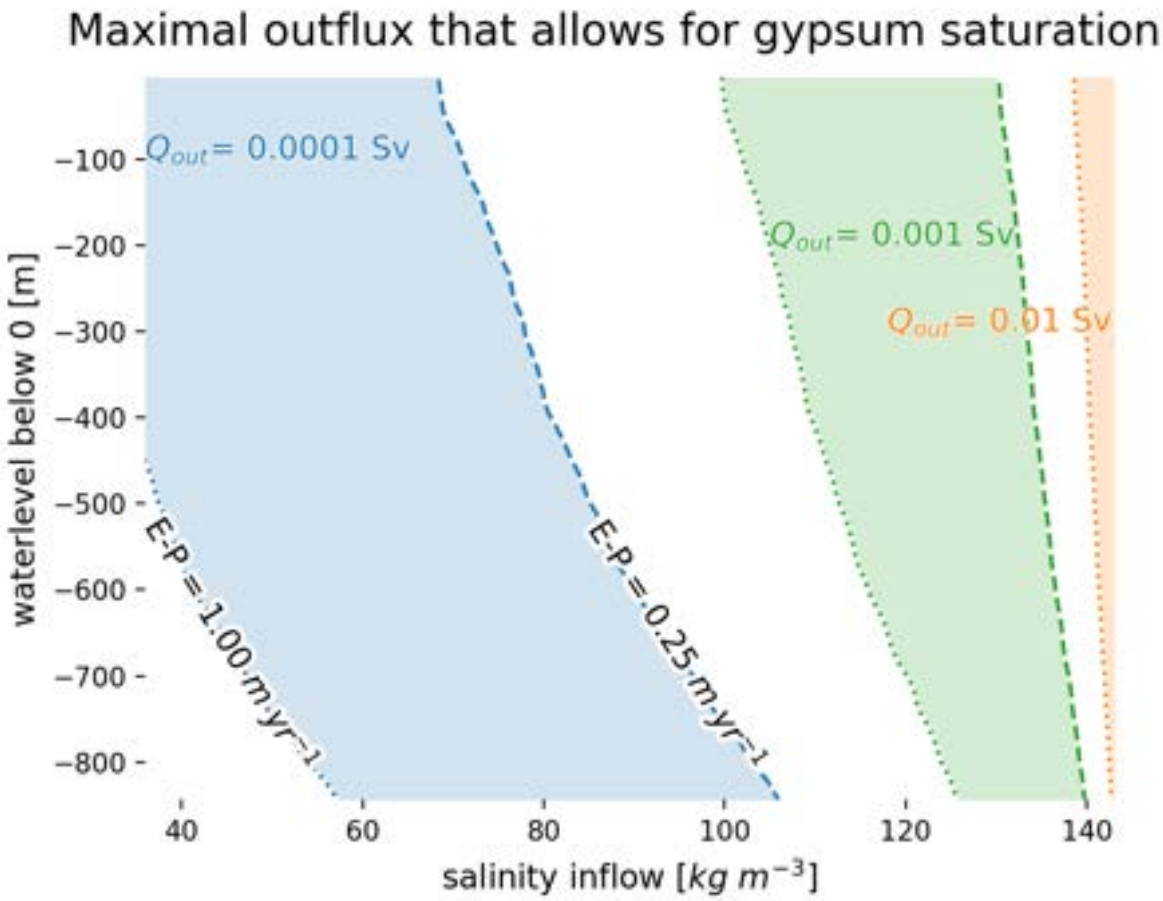

Figure 6.8. Model estimation of the precipitation of gypsum in the CMD as a function of water level and salinity in the Mediterranean, and the magnitude of the water flow into the CMD. With two-way flow across the sills that connect it to the western Mediterranean, the CMD will reach a constant salinity. This graph illustrates the conditions under which the CMD stabilizes exactly at gypsum saturation (calculated with equation 6.8). Each colored swath corresponds to a certain magnitude of the outflow and comprises the curves obtained for a range of E-P from 0.25 to 1.00 m/yr. The swaths are plotted as a function of inflow salinity on the horizontal axis. The vertical axis gives the level of the water surface: since the area subject to evaporation becomes less upon drawdown, the water level together with E-P determines freshwater budget. The path for $Q_{out} = 0.1\ Sv$ is too thin to be properly displayed in this figure and would be located in a narrow band close to an inflow salinity of $145\ kg\ m^{-3}$.

6.4.5. Precipitation of gypsum

In the previous section (section 6.4.4) we focused on the situation right before precipitation and the fluxes which would be needed to maintain this. We now calculate precipitation rates resulting from specific combinations of outflow, fwb and salinity of the inflow (eq. 6.9). To reduce the number of unknowns we now look at a full basin and consider a single value for E-P. This is allowed since it is already known from previous calculations that a drawdown only has a minimal effect on the system (see section 6.4.2). Net evaporation also has an influence, but just like drawdown, this influence is minor and does not change the overall behaviour of the system.

Based on equations 6.9 and 6.10 we can calculate first the precipitation rate (Γ) and then the duration of precipitation that follows from this precipitation rate as being required to explain the observed volume of gypsum. The lower the precipitation rate, the longer it would take to precipitate the observed volume and for the mathematically correct but unrealistic solution this time span would tend to infinity. To avoid this type of solution the results are filtered to be within geologically realistic limits. From previous studies it is known that a realistic margin for the precipitation rate of gypsum ranges from 1 $m\ kyr^{-1}$ (Orti Cabo et al., 1984) to $100\ m\ kyr^{-1}$

(Schreiber and Hsü, 1980), while the duration of precipitation per precessional cycle cannot be longer than the length of the cycle itself (assumed to be 23 kyr).

The results are shown in Figure 6.9 (compare with section 6.4.4; Figure 6.8). The grey line indicates the minimum inflow salinity that would lead to gypsum saturation for a given outflux strength. The higher the magnitude of the outflow, the higher the salinity of the inflow needs to be for the basin to reach gypsum saturation. Precipitation starts when this salinity (145 $kg\ m^{-3}$) is exceeded and the duration of precipitation itself ranges between 0.8 and 5 kyr per cycle and thus lasts between 5% to 20% of a precessional cycle. For lower magnitudes of outflow, for example, it becomes clear that the higher the inflow salinity is, the shorter the duration of precipitation per cycle. This can be explained by the increasing amount of excess ions that are transported into the basin for higher salinities. The same observation is valid for halite (Figure 6.10) and will be discussed in section 6.5.2.

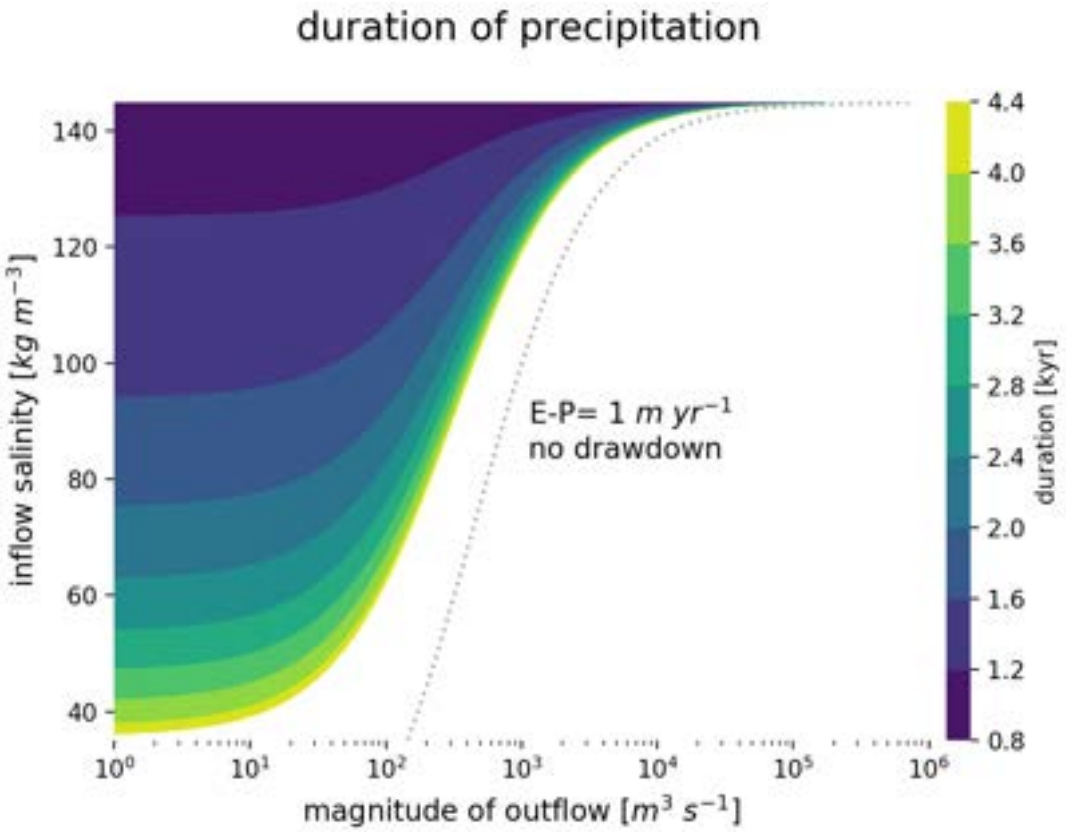

Figure 6.9. Duration of the period required to precipitate the observed volume of gypsum in the CMD, for different values of the outflow and the salinity of the inflow, when no drawdown is applied and E-P = 1 $m\ yr^{-1}$. The grey dotted line indicates the minimum inflow salinity that is needed for the CMD to reach gypsum saturation for a given outflow magnitude. For each pair of outflow strength (x-axis, logarithmic) and inflow salinity (y-axis, linear) the timespan per cycle that is needed to precipitate the observed gypsum volume of the BU1/2 is calculated. The results are clipped by limiting the precipitation rate between $1\ m\ kyr^{-1} < \Gamma < 100\ m\ kyr^{-1}$.

Another interesting aspect is that, the stronger the outflow through the connections is, the smaller the range of possible salinities leading to a realistic precipitation rate. This means that knowing the actual strength of the fluxes would not only provide us with a range of inflow salinities and thus salinity of the upper layer of the Mediterranean Sea at that time, but also that the higher those fluxes are, the smaller the range of possible salinities is. While for an outflux of $Q_{out} = 10\ m^3 s^{-1}$ an inflow salinity of $[40\ kg\ m^{-3}, 145\ kg\ m^{-3}]$ could lead to the observed BU1/2, this range would be limited to $[144\ kg\ m^{-3}, 145\ kg\ m^{-3}]$ for $Q_{out} = 10^5\ m^3 s^{-1}$. The latter is close to the strength that is measured today (Barcelló-Llull et al., 2019).

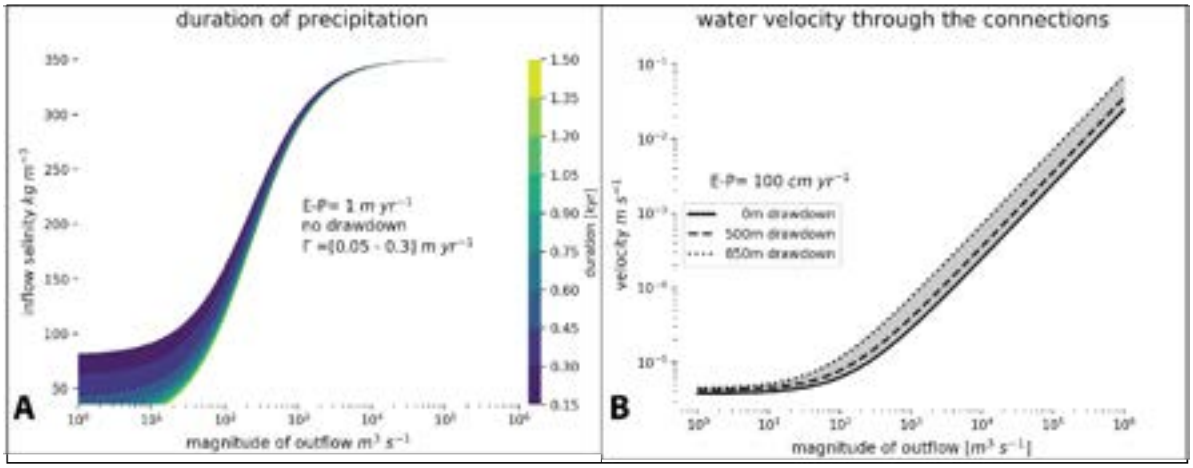

Figure 6.10. A: Duration of precipitation for the halite deposit in the CMD in analogy to Figure 6.9. The limits for the precipitation rate (Γ) are benchmarked by those of the Dead Sea (Table 6.2) with ± 2 order of magnitudes to cover broader boundaries. B: velocity of water fluxes through the connection in dependence of drawdown and magnitude of outflow.

6.5. Discussion

In this section, we discuss the significance of our results on the MSC events in the CMD and in the Western Mediterranean. Sub-section 6.5.1 focuses on the first stage of the MSC, known also as the PLG stage (5.97-5.60 Ma). The main outcome from sub-section 6.5.1 is that during stage 1 of the MSC, the salinity of the upper water layer of the Western Mediterranean reached gypsum saturation for relatively 'brief' periods of precessional cycles, and provided the CMD with the necessary Ca^{2+} and SO_4^{2-} ions to deposit the observed gypsum volume through a two-way exchange of fluxes.

Sub-section 6.5.2 focuses on stage 2 of the MSC (5.60-5.55 Ma). The main outcome from this sub-section is that the only way possible to deposit the observed halite volume in the CMD during this stage is a scenario in which it is disconnected from the open Mediterranean. This requires a high amplitude base-level drawdown of at least ~850 m, in which halite saturation is reached both in the CMD and in the Western Mediterranean only when the water level was significantly lowered (Figure 6.11).

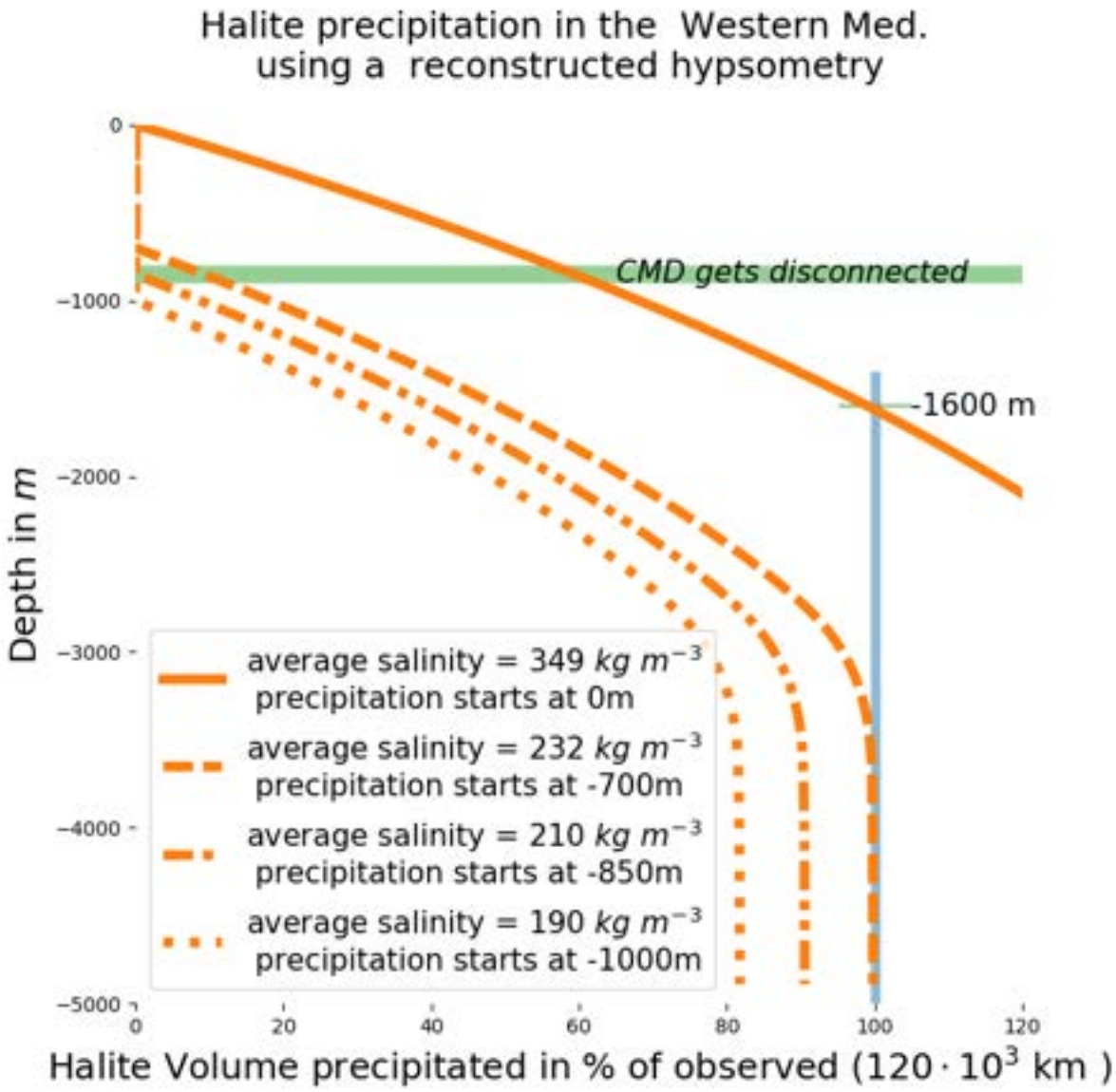

Figure 6.11. Halite volume that would form from a drawdown in the Western Mediterranean. The orange lines show the precipitated volume of halite in function of the amplitude of the drawdown. The shape of the curves is determined by the hypsometry of the basin and the average salinities of the water column before drawdown. AS the drawdown is progresses, the water volume of the basin is reduced so that it reaches halite saturation and precipitation begins. The green bar indicates the depth at which the CMD would have become disconnected, and the thin green line marks the depth at which the full deposit would have formed from a full water column at halite saturation.

6.5.1. The pre-halite lower gypsum in the CMD: Stage 1 of the MSC

The pre-Halite MSC units of the CMD (BU1 and BU2) are interpreted as Lower Gypsum belonging to stage 1 of the MSC (Table 6.1; see section 6.2.3 and Raad et al., 2021). The estimated volume of the evaporitic gypsum content of both units is ~3 x 10^{+11} m^3. Due to estimation uncertainties, related mainly to the limited seismic coverage in some parts of the CMD (Figure 6.2) and assumptions on the internal lithology of BU1 and BU2, there

is a chance that this volume has been slightly underestimated, but this would not change the following line of reasoning which is based on qualitative results. Even an underestimation of 30% of the gypsum volume would only have a noticeable influence on the duration of precipitation, changing the interval from 5% - 20% to 6.5%-20%.

Our results show that the volume of pre-halite gypsum observed in the CMD (Table 6.1) is too high to precipitate from a disconnected basin scenario. A CMD filled with water at gypsum saturation concentration (145 $kg\ m^{-3}$) up to the sill depth would produce a volume of gypsum that is far too small with respect to the observed volume (0.9%; Table 6.4). This implies that if the CMD was ever disconnected from the surrounding waters, gypsum should have started deposition before the disconnection happened, i.e., when the CMD was still supplied with an input of Ca^{2+} and SO_4^{2-} ions. In this case, two possible scenarios can be considered: (1) A basin with only an influx from the surrounding Mediterranean waters into the CMD without an outflux; (2) A CMD with 2-way fluxes from and into the surrounding Mediterranean waters. For the first case (1), our results presented in Figure 6.7 show that even in the slowest possible scenario (E-P=0.25 $m\ yr^{-1}$), the salinity of the CMD would increase very rapidly jumping to gypsum saturation in about 7 kyr and continuing to halite saturation concentration in 21 kyr, thus not allowing enough time for the observed gypsum volume to precipitate ($\boldsymbol{T}[\boldsymbol{CaSO_4}]_{\boldsymbol{vol}}$=182 kyr; Table 6.5). In the second case (2), a saline outflux would slow down the rapid salinity increase in the CMD giving longer timespans for the gypsum to precipitate. Figure 6.8 shows that in this scenario, for the CMD to stabilize at gypsum saturation, the saline influx should be very close to if not exactly at gypsum saturation concentration (between 140 and 145 $kg\ m^{-3}$; Figure 6.8) for an outflux which is equal to or one order of magnitude less than the one measured today across the silled channels (0.1 and 0.01 Sv, respectively; Figure 6.8). This is mainly due to the small volume of the CMD compared to its large connection to the surrounding waters (Figure 6.3) through the wide and deep channels, which maintains the salinity of the CMD equal to the salinity of the upper layer of the Mediterranean waters. Unless a drastic decrease in the fluxes caused by a more sluggish circulation (e.g., slowdown of the currents due to a base-level drop) of the Mediterranean currents took place, the CMD will have had almost the same salinity as the upper Mediterranean water layer, as is true for the present-day situation (Barcello Llull et al., 2019). To our knowledge, until present, no studies showed or quantified such a decrease in the Mediterranean currents and its consequences during the MSC. Our calculations also show that gypsum precipitation could not have persisted for the whole duration of a precessional cycle. Instead, the duration of gypsum deposition is restricted to 5% to 20% (i.e., 0.8-4.4 kyr/23 kyr) of a precessional cycle (Figure 6.9).

Our inferences have several important implications for what might have happened in the Mediterranean during stage 1 of the MSC. One important implication is that the saturation concentration of gypsum must have been reached in the upper layers of the

open Western Mediterranean (Figure 6.12), at least during the dry periods of precessional cycles (i.e., insolation minima). Several studies showed that, due to the negative fresh water budget that characterizes the Mediterranean Basin, a reduction of the strait efficiency in the proximity of Gibraltar would lead to a drastic increase of the salinity of the Mediterranean waters (Meijer and Krijgsman, 2005; Blanc, 2006; Topper and Meijer, 2013; Meijer, 2021). The drop in diversity until the complete disappearance of planktic foraminifera in the Mediterranean during summer insolation minima, is, for example, one indication that surface waters reached salinities above the maximum tolerance of these organisms (Sierro et al., 1999; Blanc-Valleron et al., 2002; Sierro et al., 2003; Bulian et al., 2021). One might argue that the salinity tolerance of planktic foraminifera generally does not exceed 50 $kg\ m^{-3}$ (Bijma et al., 1990), meaning that salinities in the Mediterranean water column did not necessarily reach gypsum saturation. This might be true for most of the duration of each precessional cycle of stage 1, but salinity probably peaked reaching gypsum saturation during relatively short timespans (Figure 6.9). Indeed, Topper & Meijer, (2015) showed that the salinity of the open Mediterranean waters could rise to gypsum saturation, following a restriction with the Atlantic Ocean, in timespans that are as fast as 3 kyr.

Our result, thus, contradicts what has been proposed by Lugli et al. (2010) who suggested that gypsum saturation concentration was reached only in silled marginal basins whose salinity increase and the subsequent gypsum deposition was due to circulation restrictions imposed by the presence of the sill itself. This observation has been indeed also supported by Meijer, (2021) who showed that in the case of a Mediterranean-marginal basin connection through sills, a strait efficiency as small as 10^3 $m^3\ s^{-1}$ should occur in order for the marginal basins to reach gypsum saturation with a Mediterranean at normal salinity. This extremely low strait efficiency value is 'unrealistic' as it is in the order of magnitude of a large river flowing to the Mediterranean at present. Also De Lange & Krijgsman, (2010) suggested that gypsum saturation and precipitation took place at all shallow-water depths when the upper Mediterranean waters were at gypsum saturation. In our opinion, the example of the CMD provides evidence that there is no need for a 'shallow' structural sill for gypsum to deposit. Most of the basins from which the shallow sill control idea comes from are basins now lying onshore and that underwent complex post-MSC tectonic evolution since the formation of the evaporites. Restoring their structural setting, including sill depths, at the MSC time is not straightforward and needs sophisticated tectonic reconstructions. Moreover, the few places in the offshore Western Mediterranean area where PLG was recovered in boreholes, are open shelves not or partially surrounded by sills (e.g., Alicante shelf and Valencia Basin; Soria et al., 2008; del Olmo, 2011; Ochoa et al., 2015; and offshore Western Algeria in the Arzew borehole; Burollet et al., 1978). It follows that PLG could have been deposited almost everywhere in the Mediterranean Basin during stage 1, including open shelves (Krijgsman & Meijer, 2008; De Lange & Krijgsman, 2010), with probably selenitic gypsum dominating in the shallow oxygenated

water layer and cumulate gypsum below a certain water depth limited by the depth of anoxia level (Figure 6.12) (De Lange & Krijgsman, 2010; Dela Pierre et al., 2011; Natalicchio et al., 2021). In the CMD this facies change could be marked by the passage from the MSC seismic unit BU1 to BU2 (Raad et al., 2021; see section 6.2.3). In the deep basin, the so-called Lower Unit (LU) (Montadert et al., 1978; Bache et al., 2009; Lofi et al., 2011) could thus be the sediment resulting from this phase constituting of gypsum cumulates, clastic gypsum and dolostones (Figure 6. 12). Local conditions such as high river inflow might have prevented gypsum formation by locally reducing the salinity (e.g., Ebro delta in the VB; Figure 6.7). Other local geo-chemical and geo-biological factors might have also prevented the formation of gypsum locally in deep basin context (e.g., reduced supply of gypsum from the water column and higher rates of bacterial sulfate reduction, deriving from permanent seafloor anoxia and larger availability of organic matter; Natalicchio et al., 2021; Guibourdenche et al., 2022). In shallow water where freshwater dilution did not play a role, the absence of PLG must mean that it has been removed after deposition. This removal of PLG could be due to two different causes. (1) It might have been redeposited into deeper settings due to gravitational instability (De Lange & Krijgsman, 2010). Such a process combined with local tectonic activity, might be at the origin of the Resedimented Lower Gypsum (RLG) observed in some basins (Roveri et al., 2006; Manzi et al., 2021), but could have happened in any moment after the gypsum's deposition and not necessarily during stage 2 of the MSC (Figure 6.12), as also supported by observations from the MSC PLG in Cyprus by Artiaga et al. (2021); (2) It could have been the result of subaerial erosion during the main MSC water level drawdown which amplitude has been recently revised to 1.5 km in the Western Mediterranean (Heida et al., 2021). Indeed, present-day denudation rates measured in gypsum (by denudation), including MSC gypsum from the Sorbas Basin (Calaforra et al., 1993; Sanna et al., 2015; Table 6.2), vary from low (0.20 $mm\ yr^{-1}$) to high (3.16 $mm\ yr^{-1}$). Such rates make it realistic to assume that even hundreds of meters of Gypsum could have been eroded during stages 2 and 3 of the MSC (total duration of ~270 kyr), during which the water level was lowered, and the shelves underwent intense erosion as attested by the Messinian Erosion Surface (Lofi et al., 2005, 2011; Urgeles et al., 2011). It remains unclear, however, why PLG is preserved only locally. Subaerial erosion and/or slope instability may have been more efficient on some margins compared to others.

Interpretation of stratigraphic and/or borehole data from onshore (Caltanissetta Basin, Manzi et al., 2021; Piedmont Basin, Dela Pierre et al., 2011) and offshore (Levant Basin, Manzi et al., 2018) 'intermediate to deep basins' contradicts the presence of gypsum in the distal domain of such basins, where the distal equivalent of stage 1 'marginal' PLG is represented by organic shales (Foraminifer Barren Interval, FBI; Manzi et al., 2018).

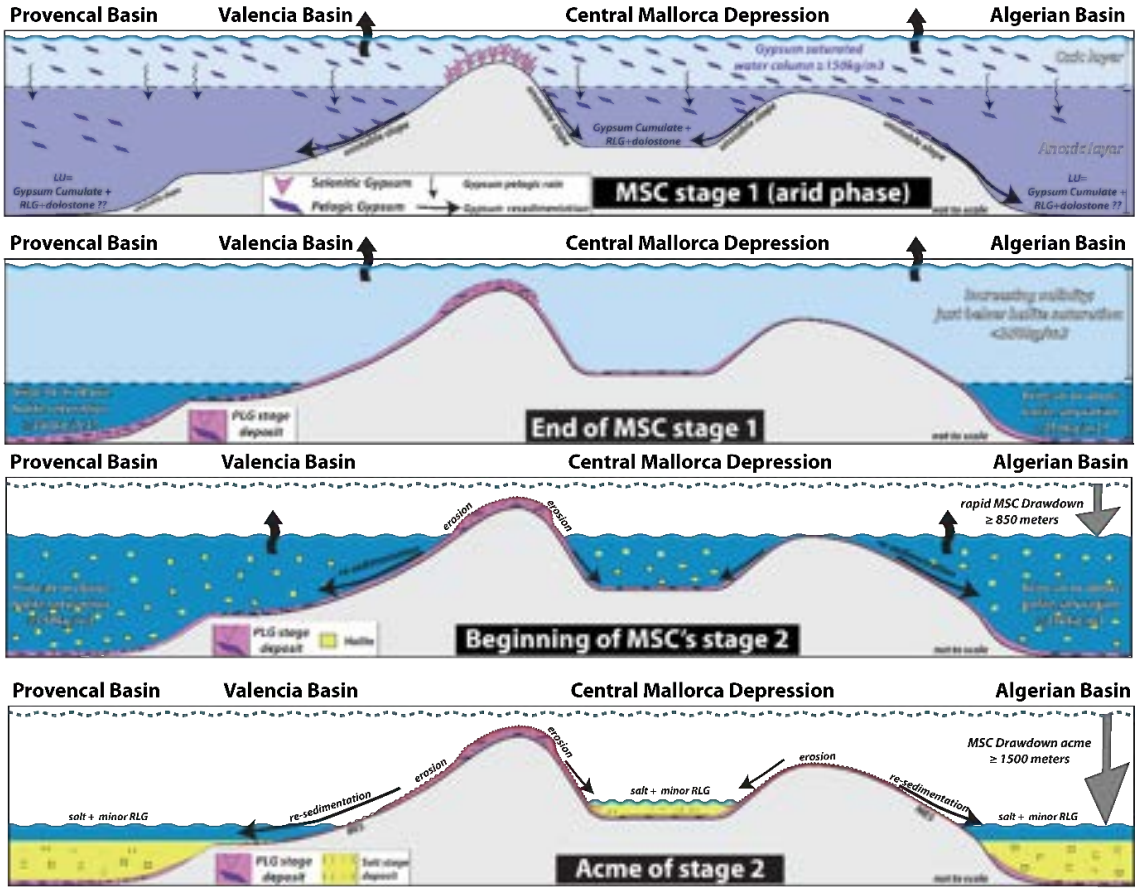

Figure 6.12. Schematic representation of the depositional conditions in the Western Mediterranean during stages 1 and 2 of the MSC according to our modelling results. The non-silled Valencia Basin does not currently contain halite (Maillard et al., 2006). Erosion rates measured in exposed halite can be as high as 20 $mm\ yr^{-1}$ (Frumkin, 1994; Mottershead et al., 2005) suggesting that halite may have been subsequently redeposited in the deeper Provencal Basin following the acme of the drawdown (Heida et al., 2021).

This interpretation has been recently modified, at least for the Piedmont Basin, where Natalicchio et al. (2021) inferred the presence of Gypsiferous Mudstones in the distal domain of the basin. Regarding the deep Levant Basin, Meilijson et al. (2018) have already opposed such interpretation by putting the halite as stage 1 distal equivalent of the PLG. In addition, very recent XRD data from the deep Levant Basin's halite shows important inclusions of calcium sulfates within the halite (Aloisi et al., in prep - personal communication).

The duration of gypsum sedimentation within a precessional cycle is also of relevance. Lugli et al. (2010) suggested that time spans for gypsum formation within a precessional cycle could have been restricted to the peak of the aridity phase of the cycle (i.e., few thousands of years), which is in accordance with our calculations. Indeed, the relatively high deposition rates of gypsum (Table 6.2), compared to the low sedimentation rates of the terrigenous intercalations between consecutive gypsum beds (Lugli et al., 2010) makes it realistic that the sedimentation of the latter occupies most of the precessional cycles.

6.5.2. Halite in the CMD: Stage 2 of the MSC

The salt unit of the CMD is interpreted as halite belonging to stage 2 of the MSC (Table 6.1; see section 6.2.3 and Raad et al., 2021) and it has an estimated volume of ~9.63 x 10^{+10} m^3. The seismic data coverage imaging the halite in the CMD is sufficient to assume that the volume estimation is reliable, and any error in the volume estimation would not exceed ± 5% of our observed volume (Figure 6.2).

Contrary to the gypsum volume, our calculations show that the observed halite volume in the CMD can be deposited in a disconnected basin scenario. A CMD filled up to sill depth with water at halite saturation concentration (350 $kg\ m^{-3}$) would produce a volume of halite that is even bigger than observed (140%; Table 6.4). Three possible scenarios can reproduce our observations: (1) A CMD that undergoes evaporation and progressive drawdown with the consequent increase in salinity, reaching halite saturation concentration when the sea surface reaches the level of the sill (~850 m; sill 01 in Figure 6.3) and the basin disconnects from the Mediterranean; (2) A full CMD at normal sea level having a stratified water column with depth-increasing salinities, where halite saturation is reached only at depths comparable to the depth of the deeper sill (sill 01 in Figure 6.3); (3) The volume of the halite deposit is not correlated to the volume of water at halite saturation and only appears to be by chance.

In the first scenario (1), our results show that blocking the outflow of ions from the CMD toward the Mediterranean (Figure 6.7) is enough to reach the halite saturation rapidly in the basin. Knowing that by the end of stage 1 the inflow salinity from the Mediterranean waters must have been very close to or even at gypsum saturation (see previous section 6.5.1.), the time to reach halite saturation can be as short as 1 kyr (Figure 6.7 and Table 6.5). This process of salinity increase must have been accompanied by a drawdown that reached at least the depth of the deep sill (~850 m; sill 01 in Figure 6.3) and disconnected the CMD from the Mediterranean. Once the halite saturation is reached and the CMD is disconnected from the Mediterranean, the CMD starts precipitating the halite. The drawdown in the CMD now proceeds independently from the drawdown of the rest of the surrounding Mediterranean. Figure 6.6 shows that a quasi-desiccation in the CMD, and the subsequent halite deposition, would take place rapidly (~1.2 kyr in the slowest case scenario) and that even the highest possible fresh water input by river would have a negligible effect on the amount of halite deposited.

In the second scenario (2), the basin is filled with water at halite saturation up to the sill depth and overlaid with a ~800 m thick column of relatively fresher water (<350 $kg\ m^{-3}$), sealing the brine off against atmospheric influence (i.e., evaporation). The brine, hence, is not affected by a sink of freshwater and needs a source of ions to surpass halite saturation and precipitate halite (see mechanism in Simon & Meijer, 2017). Such a source of ions would need an area at the surface where water is so dense, that it is

transported to the depth. This means that the stratification that characterizes this scenario would have to be broken at least locally and at least intermittently. Given the limited horizontal dimensions of the basin and the resulting salinity gradient in this case (due to its connection to the open Mediterranean), such a scenario is unlikely to take place in the CMD. This also applies to the double diffusion as a process (Arnon et al., 2016; Ouillon et al., 2019), in which the vertical salinity difference needs to be so small that the effect of temperature on density and saturation point cannot be ignored anymore (see mechanism in Arnon et al., 2016). In this case, in fact, the CMD would have to be inversely stratified with slightly higher salinity in the (warm) surface layer at least part of the year. Furthermore, the volume of the deposited halite would not depend on the water volume of the deep layer, but on the transports of ions into said volume. The more ions are imported to the volume, the more halite will be deposited. Such mechanisms observed in present-day evaporative basins (e.g., Dead Sea; Lensky et al., 2005; Sirota et al., 2018), are associated to high deposition rate of halite that can reach 0.15 $m\ yr^{-1}$ (Table 6.2). Consequently, in such a scenario, the time needed to deposit the whole observed halite volume in the CMD is less than 2 kyr in the slowest case scenario, which is only 4% of the duration of stage 2 (~50 kyr). Therefore, even if this mechanism is stopped (by drawdown and disconnection), an excess volume of halite would be produced, which is not observed in the present-day halite volume.

Scenario 3 (3) is similar, with the only difference being that the whole basin is assumed to be at halite saturation and long enough to precipitate the observed halite deposit. In this scenario, the inflow salinity has either to be very close to halite saturation or the fluxes from the Mediterranean to be small enough to increase the salinity locally in the CMD. Figure 6.10-A shows that the magnitude of the fluxes from the CMD to the Mediterranean (eq. 6.7a) has to be 10^2 $m^3 s^{-1}$ or smaller to reach halite saturation in the CMD when the Mediterranean inflow is still at gypsum saturation. With the cross sections of the connections between the CMD and the rest of the Mediterranean through the channels, this would require extremely slow horizontal velocities in the order of v=10^-6 $m^3 s^{-1}$ and smaller (Figure 6.10-B), which is the same order of magnitude as vertical velocities of the present-day global ocean (Liang et al., 2017). Horizontal velocities, however, tend to be much larger (e.g. River flows: $v_{river} \approx 10^0\ m\ s^{-1}$, Schulze et al., 2005; horizontal ocean currents: $v_{current} \approx 10^1\ m\ s^{-1}$, Lumpkin & Johnson, 2013; wind induced surface currents of the Dead Sea: $V_{DeadSea} \approx 10^{-2} - 10^{-1}\ m\ s^{-1}$, Padon & Ashkenazy, 2018). There is no reason to assume that the horizontal currents in the Western Mediterranean became slower than the sinking speed that is observed in the present-day global circulation. It is thus reasonable to assume that the inflow salinity in this scenario was at halite saturation. Again, given the short period of time needed to precipitate the halite deposit (Figure 6.10-A), this high salinity inflow only needs to be reached for 150 yrs -1500 yrs to deposit the observed volume. The longer the connection lasts, the larger the deposited halite volume, which

is something that we do not observe in the present-day halite volumes, hinting again that the CMD has to disconnect from the Mediterranean.

Our results supporting a quasi-desiccation of the CMD seem consistent with previously reported observations. Starting locally from the CMD itself, Raad et al. (2021) evidenced the presence of an erosional event truncating within the top of the halite unit in the depocenter of the CMD. The authors interpreted this erosion as due to subaerial exposure and/or dissolution of halite in relatively shallow water. Since our calculations show that no complete desiccation is possible due to river input (Figure 6.6), the subaqueous but shallow origin should be preferred. However, we cannot exclude that the salt was subaerially exposed on the flanks of the depocenter while a residual water body was present in its deeper part.

A similar observation from another intermediate-depth basin, the Caltanissetta Basin of Sicily, also supports an important sea level drawdown during the halite stage, where an erosional surface with desiccation cracks is cutting the top of a K- and Mg- salt rich level (Decima and Wezel, 1973; Garcia-Veigas et al., 1995; Lugli et al., 1999; Rouchy and Caruso, 2006). Some authors associated this erosional surface to the local desiccation of the Caltanissetta Basin (Roveri et al., 2008; Manzi et al., 2012) during stage 2. This is consistent with our interpretation and we propose that the Sicilian salt may have deposited during stage 2 in the Caltanissetta basin in a similar way to the one described above for the CMD (scenario 1), as both basins are classified as intermediate-depth and their MSC record share many similarities (Raad et al., 2021).

	Western Mediterranean	Eastern Mediterranean	Reference
Area covered by Halite (m2)	5.38E+11	2.80E+11	Lofi, (2018)
FWB (m3/a)	-2.5*(10E+15)E-3		Simon et al., (2017)
Volume of MSC evaporites (m3) *	977E+12		Haq et al., (2020)

Table 6.6. The area and volume of the halite in the Mediterranean area. FWB = Fresh water budget (calculated for both Western and Eastern Mediterranean). * The volume of evaporites from Haq et al. (2020) includes pre-halite, halite and post-halite MSC units.

As long as the CMD is connected to the main Mediterranean basin, its water level will follow that of the Mediterranean. Studies showed evidences of a drawdown of even higher amplitudes than the depth of 850 m of our sill, varying from ~1500 m (Urgeles et al., 2011; Heida et al., 2021) up to quasi-desiccation of the deep basins (Ryan, 1978; Pellen et al., 2019). This means that the drawdown might have continued further in the Mediterranean, whereas the CMD had its own base level evolution as explained in section 6.4.2 and shown in Figure 6.6. With the aim of evaluating the present-day observed halite volume in the frame of the consensus model (CIESM, 2008; Roveri et al., 2014a) we performed a simple calculation, similar to the one done for the CMD but on the scale of the whole Mediterranean, using the parameters shown in Table 6.6 and the mechanism in Figure 6.4-B. We keep a restricted Mediterranean-Atlantic connection, allowing for an Atlantic inflow with a salinity of 35 $kg\ m^{-3}$ replacing the net-freshwater loss (i.e., no drawdown; Meijer, 2012) for the whole MSC stage 2 duration (~50 kyr as assumed in Roveri et al., 2014a) where the Mediterranean waters are at halite saturation. Results of our calculations show that we would precipitate x1.5 times the observed deep basin evaporite volume (977 x 10^{+12} m^3, Table 6.6) calculated by Haq et al. (2020). This is not a contradiction to the results of Krijgsman & Meijer (2008), who used the same approach but estimated the volume of halite by combining the areal extent of halite as indicated by the distribution map of Rouchy and Caruso (2006), a thickness of 1000 m in the western basin and 3500 m in the eastern basin (after Lofi et al., 2005). Their calculated volume was close to the estimated one. Note that the volume given by Haq et al. (2020) includes the pre- and post-halite MSC units and it is thus an overestimation of the deep basin halite volume. Thus, we would expect to accumulate a volume of halite that could be at least two-times bigger than the observed one. However, the volume estimation by Haq et al. (2020) is more reliable and thus our calculation could be considered an improvement to Krijgsman & Meijer (2008). As for the CMD, our calculation suggests that the open Mediterranean could not have remained connected to the Atlantic during the whole duration of stage 2. Consequently, a drawdown must have occurred upon the Mediterranean's disconnection from the Atlantic because of the negative water budget that characterizes the Mediterranean (e.g., Meijer, 2006; Krijgsman & Meijer, 2008) and desiccation and refilling of the Mediterranean could have taken place very rapidly (within one precessional cycle; Meijer & Krijgsman, 2005). Of course, this calculation is very simplistic since it overlooks some factors such as the sill effect between the Eastern and Western Mediterranean (Blanc 2000, 2006; Topper & Meijer, 2013), and the fact that the salt in the deep basin might have started deposition already during stage 1, at least in the eastern basin (Meilijson et al., 2019, 2022). Although, in their modelling of the MSC halite stage, Topper and Meijer (2013) tested the efficiency of the Siculo-Tunisian sill between the eastern and western Mediterranean basins and arrived to the same conclusion that a high amplitude drawdown (~ 1500 m) must have happened at the end of halite deposition in the deep basin (see their Figure 10).

Another step to place the results obtained in the CMD in the wider context of the wider MSC events in the Western Mediterranean Basin, is comparing the obtained halite volumes formed during water level drop in the CMD, to those in the deep basin of the Western Mediterranean. The deep basin halite volume in the Western Mediterranean has been estimated at around $120x10^3$ km^3 (Heida et al., 2021), which is considerably smaller than previous estimates (Haq et al., 2020). Using the reconstructed hypsometry of the western basin at the beginning of halite deposition derived from the paleo-bathymetry published in Heida et al. (2021), we can calculate the volume of halite that would result for different average starting salinities for the Western Mediterranean (Figure 6.11) for a disconnected basin that experiences drawdown (as in Figure 6.4A). For a low starting salinity model (190-210 kg m^{-3}) and halite saturation reached after a drawdown of ~850 m, a large drop in water level (>3000 m) is required to obtain >85% of the halite volume. A fully desiccated basin, which is physically impossible since the system would reach an equilibrium before (comparable to Figure 6.6), would also not lead to the total volume. This volume is only reached for a water column that starts precipitating after a drawdown of ~700 m or sooner which implies an average Salinity of 232 kg m^{-3} or higher (Figure 6.11). For a salinity of 350 kg m^{-3}, i.e., halite saturation, the drawdown needed to form the western Mediterranean MU halite is even reduced to 1600 m. This type of calculation simplifies a complex basin to one uniform water column and thus ignores effects like horizontal salinity differences, dynamic changes during the drawdown, and a continuous (even though reduced) supply of ions from the Atlantic to the deep Western Mediterranean Basin. This however, as well as our calculations on the CMD itself, strongly indicate that halite did not start depositing before the beginning of the drawdown.

6.6. Chapter Conclusions

We carried out numerical modelling of the Messinian Salinity Crisis (MSC) evaporites accumulation in the Central Mallorca Depression (CMD) using physics-based models built on conservation of mass of water and salt and a simplified model for the flow in sea straits. The interpretation of a widespread seismic dataset covering the CMD allowed the estimation of the volumes of the MSC evaporites that are used to constrain both our isostatic and evaporite precipitation models. According to the results and observations, we conclude the following:

- During stage 1 of the MSC (5.97-5.60 Ma), the upper water layer of the Mediterranean had to be at gypsum saturation salinity to supply the CMD with Ca^{2+} and SO_4^{2-} ions needed to deposit the observed volume of PLG. Gypsum deposition likely occurred only during part of precessional cycles (maximum duration of ~4.5 kyr).
- The need of shallow topographic sills in the deposition of PLG appears not to be a pre-requirement, and PLG deposition was not necessarily limited to 200 m water depth but was rather constrained by the depth at which anoxia starts.
- Our results suggest that during stage 1, gypsum possibly deposited almost everywhere in the Mediterranean, including on open shelves. PLG may have successively been removed at any time by subaerial erosion or slopes instabilities, and re-sedimented in deeper contexts.
- The deep basin's Lower Unit, traditionally associated to the MSC could thus at least partly be made of cumulatic and resedimented gypsum.
- Following the gypsum deposition, a phase of rapid base level drawdown commenced (beginning of stage 2; 5.60-5.55 Ma) accompanied with increasing salinities. The outflow of ions from the CMD toward the Mediterranean is blocked allowing halite saturation to be reached rapidly in the basin. After a period as short as ~1.5 kyr, the drawdown reached the depth of the basin sill lying at ~850 mbsl, leading to the complete disconnection of the CMD, and to halite precipitation.
- The base level in the CMD successively evolved separately from rest of the western Mediterranean Sea, still ongoing a drawdown. A quasi-desiccation in the CMD has likely been reached, and halite locally subaerially exposed while a residual water body was present in the deepest part.
- In the deep western Mediterranean basins, halite saturation was likely reached earlier than in the CMD in a basin strongly stratified before the beginning of the drawdown. Salt deposition however, probably started after the beginning of the base-level drawdown, implying that salt deposition started in a relatively deep-water context and ended when the acme of the drawdown was reached. Halite emplacement in the deep basin could have been completed before the end of stage 2.

On a larger basin scale, during stage 1 of the MSC, a normal, even though restricted, connection between the Atlantic and Mediterranean must have persisted, with no significant base level drop. This connection must have been further restricted until total interruption during stage 2, leading to the important base-level drop and the deposition of halite. Such drawdown must have led to the disconnection between the Western and Eastern Mediterranean basins during this stage, but halite deposition is not necessarily synchronous in both basins due to the further restriction imposed to the eastern basin by the Siculo-Tunisian sill as attested by several studies.

Even though many observations from the Balearic Promontory and the Western Mediterranean are coherent with the 3-step MSC consensus model, our results also highlight that some aspects of such model (e.g., limiting the PLG deposition to shallow >200 m silled basins; and the synchronous onset of the RLG and halite) may need to be reconsidered in future studies.

Chapter 7: General Discussion

7.1. Water levels during MSC: connecting the dots

In this chapter, I will build the results obtained from the subbasins studied in this volume into the framework of a pan-Mediterranean Messinian Salinity Crisis, to discuss how they can guide us towards a coherent and comprehensive model for the progression of the MSC. To this purpose, I will start by discussing the consistencies in results presented in the various chapters, and then highlight the key differences and their implications. I will then go into the plausible mechanisms that can explain the observations presented in the previous four chapters.

7.1.1. Basin-wide large-scale drawdown

Based on our starting hypothesis that erosion markers, halite extent and Upper Unit deposits are all features constraining subaerial exposure and coastline location, we have consistently obtained large Mediterranean Sea level drawdown ranging from -600 to -1500 m, as neither evaporite distribution nor erosive surfaces are consistent with formation under constant high water levels. Even though the shoreline markers used in our baselevel constraints are based on features with very different formation histories, they allow for comparison between subbasins. Every subbasin investigated has erosional features/paleoshoreline indicators that upon reconstruction are positioned at depths of at least 500 m, well beyond eustatic sea level variations and not explainable by tectonic vertical motions since the Messinian. The only shoreline that can conclusively be linked to the MSC Stage 2 (the Mobile Unit pinch-out in the Western Mediterranean, see Chapter 4) is also the deepest paleoshoreline at -1500 m, although this does not exclude the possibility of short-lived deeper drawdown in the either subbasin. After this initial drawdown, marking the moment of complete disconnection of the Atlantic inflow into the Mediterranean, water level remains substantially lowered with large variations between subbasins. A factor that is shown to be very important in controlling the basin depth and water level estimate during the lowstand phase is the flexural-isostatic rebound in response to the evaporation of a large portion of the water column. As illustrated in Chapter 3, this rebound affects the Atlantic-Mediterranean connectivity by preventing the reconnection of the Atlantic and Mediterranean after the initial onset of a drawdown.

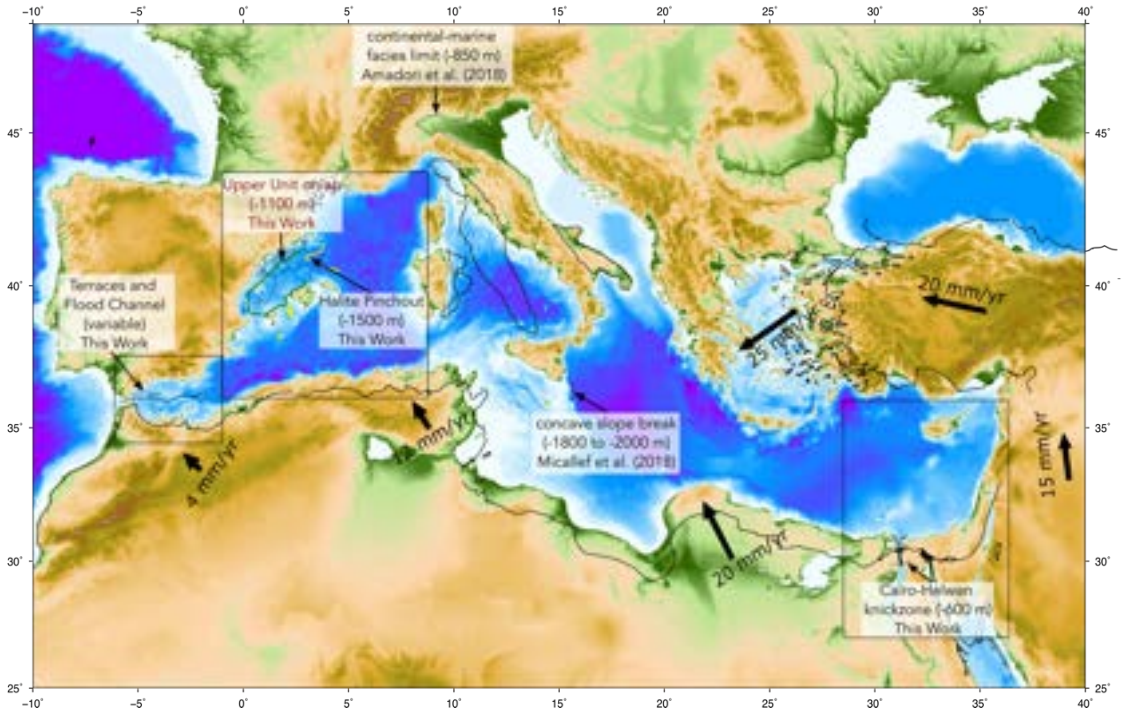

Figure 7.1. Locations of shoreline markers used in this volume and in two recently published papers based on a similar methodology, using TISC to calculate isostatic vertical motions on a regional scale. The black line shows the approximate position of the mayor tectonic plates relative to Eurasia during the Messinian, by rotating the modern shoreline using plate velocities as shown by the black arrows (from Serpelloni et al. [2013] and Garcia-Castellanos et al. [2020]). Base map shows restored Messinian topography in the three regions studied in this volume, and modern bathymetry where such reconstruction is not available.

7.1.2. Variability of water-level results between subbasins

The topographic reconstructions presented in this work for regions covering the Eastern and Western ends of the Mediterranean highlight the complexity of interpreting the Messinian erosion and water-level markers, and the clear differences that exist between the different parts of the sea. From the results presented in chapters 3, 4 and 5 a distinct image arises of a Mediterranean realm under lateral and temporal variation after the initial disconnection from the Atlantic water supply.

While the Nile canyon records a relatively minor water level drop at around 600 m, previous work by Micallef et al. (2018) resulted in water-level estimate of 1800-2000 m below global sea level on the Malta Escarpment. As the Ionian and Levant basins were in all likelihood connected, large variations must have occurred within the basin in order to explain these two highly disparate water-level markers. Meanwhile, in the Western Mediterranean the Upper Unit onlap onto the Bottom Erosion Surface is found at a level of 1100 m depth, and the halite pinchout at 1500 m. The magnitude of the inferred drawdown, both in the western and eastern basins, is such that we can assume a

hydrological divide at the Sicily Sill during the lowstand phase, barring large and unidentified vertical motions having uplifted the Sicily Sill since the MSC. This separation of the Eastern and Western basins can also explain the large difference in reconstructed shoreline depth from -600 m (Nile Canyon, Chapter 5) and <-1100 m (Valencia Basin, Chapter 4). An independent water-level estimate East of the Sicily Sill on the Malta Escarpment was reconstructed to significantly deeper levels of 1800-2000 mbsl (Micallef et al., 2018b). An overview of recent drawdown estimates based on planform flexural-isostatic reconstructions (all using TISC) is presented in Figure 7.1, illustrating the variety of results. A key factor towards interpreting these results lies in accounting for the nature of the shoreline indicators used to arrive at a water level estimate for each stage of the MSC and subbasin.

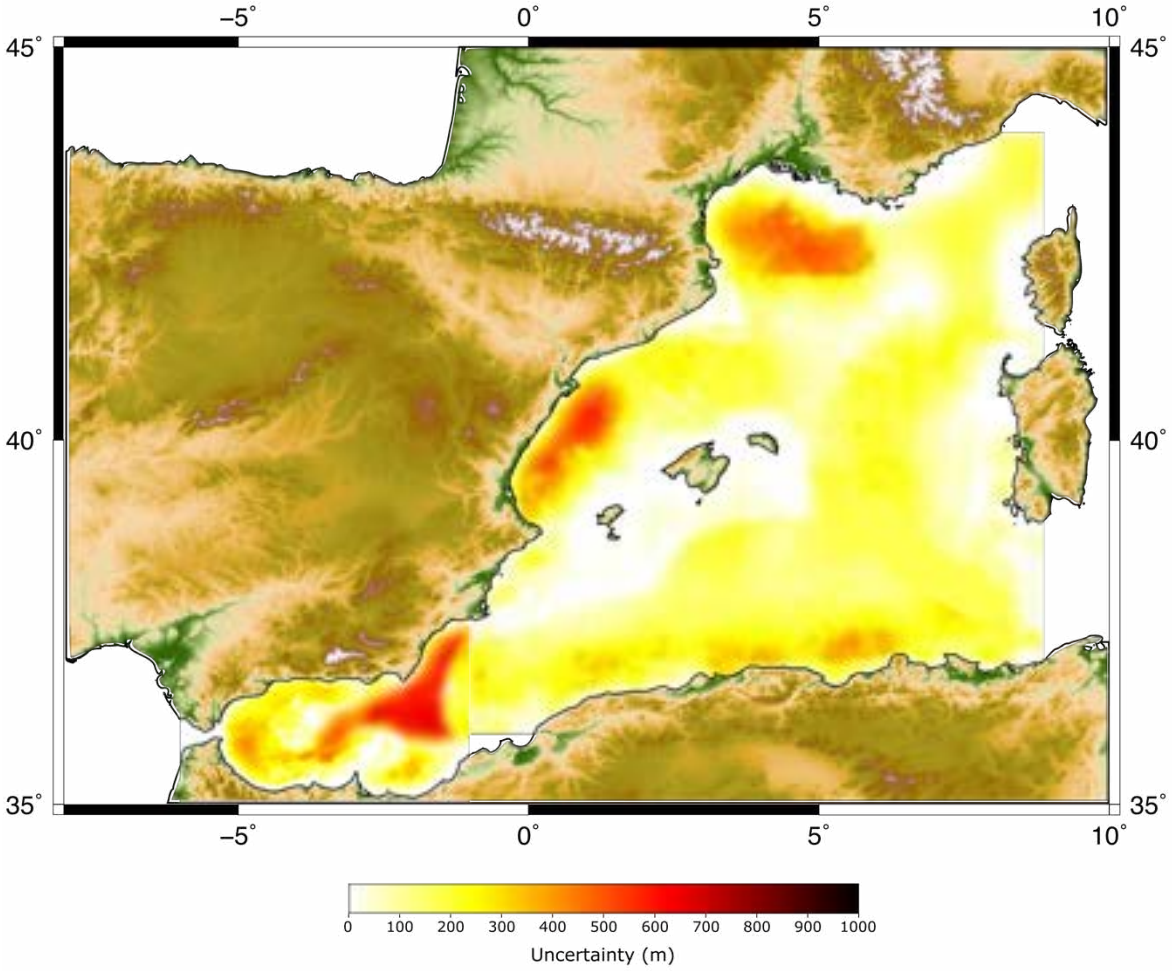

Figure 7.2. Map showing the uncertainty around model topography results (deepest model topography - shallowest model topography) for the Base Pliocene. Largest uncertainty occurs in the Alboran Volcanic Arc and in the region with thick Pre- and Post-Messinian sediment sequences (Ebro and Rhône deltas). This uncertainty only results from our applied model steps, and does not include possible tectonic deformation outside of the uplift on the Alboran Ridge as discussed in Chapter 3.

The variations between paleoshoreline depth are consistently bigger than the uncertainty of the paleobathymetric reconstruction in the region where they are defined, meaning that uncertainty of the modelled bathymetry is not a plausible explanation for the differences in paleoshoreline depth. Uncertainty is largest in specific regions with very thick sediment layers (like the West Alboran Basin, Ebro delta and Gulf of Lions) or active and recent volcanism (like the East Alboran Volcanic Arc). The total uncertainty in paleobathymetry (deepest model reconstruction – shallowest model reconstruction) for the Base Pliocene surface is presented in Figure 7.2 for the Western Mediterranean basins. An overview of the drawdown estimates from previous studies and results presented in this work is provided in Figure 7.3.

Halite represents a highly mobile component of the evaporitic sequence in two senses: It deforms plastically and is able to migrate significant distances under the effect of gravity and overburden, and it is soluble causing it to both to rapidly deposit during an evaporative drawdown and easily dissolve when exposed to less saline water, be it meteoric, riverine or marine in origin. The paleoshoreline investigated in the Western Mediterranean Valencia Basin related to the limit of the Mobile Unit halite deposit can therefore be assumed to have formed on a relatively short time span, representing the water level during a short-lived but dramatic main lowstand of the Mediterranean water level just after the last Atlantic-Mediterranean connection closed. From the stratigraphic relationship between this unit, the associated Bottom Erosion Surface also formed during this lowstand before the Upper Unit was deposited, and the Upper Unit containing anhydrite/gypsum onlapping onto this surface it is clear that variations in water level took place during the lowstand stage. In the Western Mediterranean, stage 3 materials were therefore deposited under different circumstances (in terms of water level and salinity) than the Mobile Unit. After the initial drawdown, the equilibrium water level (where total water input from precipitation and inflow from rivers and other basins equals the evaporation over the water surface) must have changed by hundreds of meters in order to form the observed paleoshoreline at the limit of the Upper Unit, inundating the previously exposed Valencia Basin. An open question remains as to the exact nature of the UU in the Valencia Basin, that has been confirmed to contain anhydrite/gypsum by the sampling of DSDP Leg 13, but the number of gypsum/marl cycles or alternations recorded in the Valencia Basin are unclear from seismic stratigraphy, and no borehole data that gives insight into the number of cycles is available in the north-eastern sector of the basin. In the southwest sector of the Valencia Basin, well-to-seismic ties on the Ibiza Marino drill site indicated a hiatus of 41 kyr below the MSC units. At this site, only the top part of the UU is deposited, and its thickness is less than 60 m with no clearly identified internal cyclicity (Ochoa, 2016, Chapter 7), although this well is located towards the margin where the UU is thinnest. As the top and bottom of the Upper Unit in the Valencia Basin cannot be explicitly linked to a specific cycle in the onshore Upper Gypsum, the moment in time represented by the

onlap of the Upper Unit is uncertain. It could represent the water level just before the flooding and reestablishment of open marine conditions at the Miocene-Pliocene transition, but it might also be representative of the last gypsum deposit formed under low water level during a Stage 3 with highly fluctuating water level, not necessarily representing the final moments before reflooding. A more detailed correlation of the UU stratigraphy in the Valencia Basin to the onshore Stage 3/Lago Mare deposits would be required to answer these questions. Overall, the UU onlap paleoshoreline in the Valencia Basin represents an evaporite accumulation process that persisted over multiple precession cycles, and can therefore be assumed to be representative of a persistent lowered water level in the Western Mediterranean, higher than the water level during the formation of the Bottom Erosion Surface and halite pinchout shoreline. Potential periodic higher water level phases might have occurred during insolation minima, corresponding to humid phases and associated with deposition of "Lago Mare" sediment on the basin margins.

The erosional terraces mapped in the Alboran Basin and reconstructed to their original depth in Chapter 3 are difficult to associate with any specific moment during the MSC on the scale of precession cycles. Just from their internal paleodepth distribution, it is clear that they were not formed under a single uniform water level. The coastal erosion processes associated with terrace formation act relatively rapidly on geological timescales, and we can assume that these terraces represent variable base level over the course of the MSC lowstand phase, or during basin reflooding.

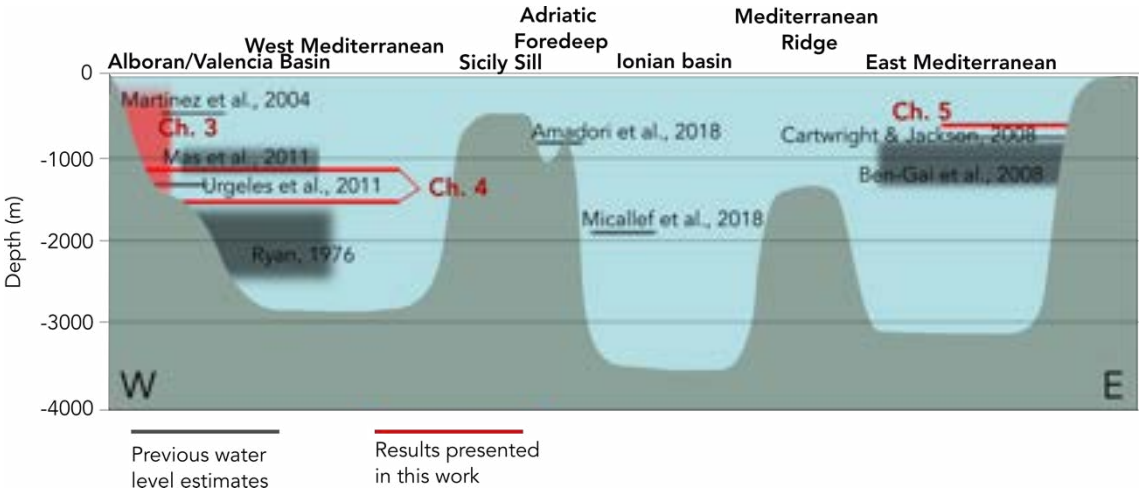

Figure 7.3. Schematic W-E profile of the Mediterranean, with drawdown estimates from of previous studies (same as Figure 1.5) and this work.

The Nile Canyon shoreline restoration in Chapter 5 supporting a water level drop of only 600 m is based on geological features which provide some clues to the required duration of the drawdown in this region. The restored knickzone, with a height of 400 m, represents a relatively short region of cascading waterfalls excavated by the significant erosive capacity of the Nile River. Downstream, the gently sloping flat channel continuous for another 60 km northwards before reaching the inferred shoreline where

it steeps again into the submarine domain. The rates of knickzone migration depend on a wide range of factors, including catchment area, discharge, rates of tectonic deformation or base level variations, and bedrock lithology (Whittaker and Boulton, 2012), but with river discharge being the dominant controlling factor on knickpoint migration rate (Castillo et al., 2013). In modern catchments it has been estimated to range between 0.2-2 mm/yr, but retreat of large waterfalls exceeds such rates significantly, and retreat rates vary widely depending on drainage area, gradients, and bedrock properties (Howard et al., 1994). For the knickpoint to retreat 60 km from the new shoreline upon baselevel drop to it final position, the lowstand must have persisted over a significant timespan, ranging from a few tens of thousands of years, to potentially >100 kyr if incision rates are lower. Upon restoration of the water level, the canyon was "frozen" and filled with Pliocene-Quaternary sediment. It is probable that the Nile Canyon baselevel represents a long-lived lowstand that persisted throughout a large part of the third stage of the MSC, although as noted in section 5.6, erosional features in deeper parts of the Levant Basin (i.e., on the Nahr Menashe deposits as reported by Madof et al., 2019 or the shore platforms restored to 1900 m depth by Micallef et al., 2018) might be indicative of lower water levels during part of the MSC.

Basin	Shoreline indicator	Type	Depth shoreline (m)	Timing formation	Duration formation
Alboran Basin	Terraces	morphology	250 - >1500	Stage 2/3?	Kyr?
West Mediterranean	Upper Unit onlap	sedimentary	1100	Stage 3	Multiple precession cycles
	Mobile Unit pinchout	sedimentary	1500	Stage 2	Potentially <1 precession cycle
East Mediterranean	Knickzone	morphology	600	Stage 3?	10s-100s kyr

Table 7.1 Overview of duration and timing shoreline indicators for the Western and Eastern Mediterranean subbasins presented in this work.

The different timescales on which these paleoshoreline indicators for outlined above (see Table 7.1) point towards a plausible explanation on the differences of the restored baselevels in Chapters 3,4 and 5 to stem from temporal and spatial variations in water level during the second and third stages of the MSC. They illustrate key differences between the Eastern and Western Mediterranean Basins, that are also reflected in the Messinian stratigraphy.

7.2. Implications for conditions during evaporite deposition

One of the main questions left to be answered about the MSC related to the chronological relationship between the onshore PLG and UG and the deep basin MU and UU deposits. The depth distribution and volume of the halite found in the Western Mediterranean provide an important clue towards decoding the enigmatic conditions during their deposition. In Chapter 4 I provide a new volume estimate of the Mobile Unit (halite) in the Western Mediterranean of 120x 10e3 km^3. This estimate is significantly smaller than previous estimates by Haq et al. (2020) and Ryan (2009), as it considers a basinwide interpretation of only the Mobile Unit, and does not rely on extrapolation from 2D seismic data. It should be taken into account that the halite volume estimate is only based on the region where relatively high density data coverage is available, excluding part of the Ligurian basin (where in the basin axis considerable salt thickness is present (Lofi, 2018)) and the Tyrrhenian Basin which was hydrologically connected to the Western Mediterranean during the MSC (albeit considerably smaller volume, as extension and subsidence in this basin continues well after the Miocene) which also contains some limited salt volume. Nevertheless, as these contributions are limited, they do not substantially (>10%) affect the accuracy of the new halite volume estimate. From this new estimate, a plausible solution to one of the big questions posed at the initial discovery of the Mediterranean Salt Giant, namely the large volume of halite compared to the ions contained in a marine basin can be postulated. Instead of requiring multiple cycles of desiccation and filling, which was proposed by Hsü et al. (1973) but almost immediately raised concerns (Ryan, 2009). The new halite volume estimate, combined with the reconstructed hypsometry, indicates that the entire Western Mediterranean halite volume could be deposited from a single drawdown, under the condition that average salinity was close to halite saturation at the onset of the drawdown (see Chapter 6). While the contribution to hypsometry changes due to the convergence between the African and Eurasian plates is not considered in the reconstructions in Chapters 3 and 4 (see Figure 7.4 for modern and reconstructed hypsometry), we can estimate this effect from modern convergence rates in the region. In Figure 7.1 the estimated position of the African plate during the Messinian is illustrated. While in the Alboran Basin the post-Messinian convergence is limited (although it did strongly affect the morphology of the basin), in the Western Mediterranean the convergence rate implies a total post-Messinian shortening of up to 65 km, constituting about 10% of the current basin width, and therefore Messinian basin volume that would also be in the order of 10% larger than our reconstructed hypsometry, depending on how and where this convergence has been accommodated, which was likely on the incipient subduction zone on the Algerian Margin. This larger Messinian surface area and volume makes it more likely that the entire Western Mediterranean halite volume could have been produced during a single drawdown in

the order of 1.5 km. The time required for the halite deposition in the Western Mediterranean is then limited by the rate of evaporative water loss, but can be much shorter than the 50 kyr "stratigraphic gap" in the onshore MSC record assigned to MSC Stage 2 according to the "consensus model" (CIESM, 2008). This suggests that the "Lower Unit" in the Western Mediterranean deep basins is the equivalent to the marginal/intermediate Stage 1 deposits (PLG), possibly containing evaporites.

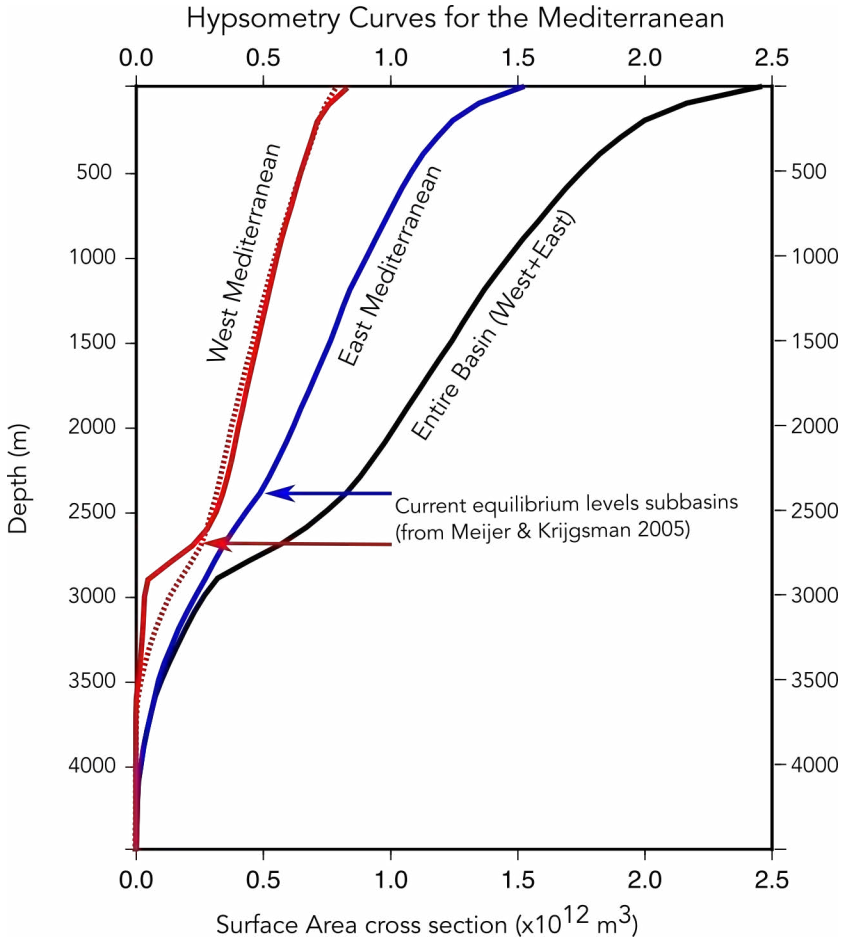

Figure 7.4. Hypsometry curves for the entire (black), Eastern (blue) and Western (red) Mediterranean basins. Solid lines are based on modern bathymetry from GEBCO 2014 global bathymetry grid, while the dotted line is based on the reconstructed topography of the Western Mediterranean before the onset of halite deposition and drawdown presented in Chapter 4. Illustrated are the equilibrium levels for the Western and Eastern Mediterranean based on modern hypsometry and climate as computed by Meijer & Krijgsman 2005.

Strongly elevated salinity levels are the logical result of progressive restriction at the Atlantic-Mediterranean gateway (Meijer, 2012), and the effect of progressive restriction is noted in sediment core isotope data (Bulian et al., 2021) long before the onset of evaporite deposition. As the Atlantic-Mediterranean gateway is progressively restricted, salinity increases and the total ion content (and therefore the evaporite deposition

potential) of the Mediterranean basins increases. As the sill gets closer to the Atlantic sea-level, periodical blocking of outflow would induce rapid salinity increase possibly surpassing gypsum saturation in parts of the basin. In the Eastern Mediterranean, which at high water level forms the terminal basin in this evaporative system, salinity could increase much further than in the Western Mediterranean, as it is already supplied with more saline water from the Western Basin and further salinified by the large freshwater deficit in this region.

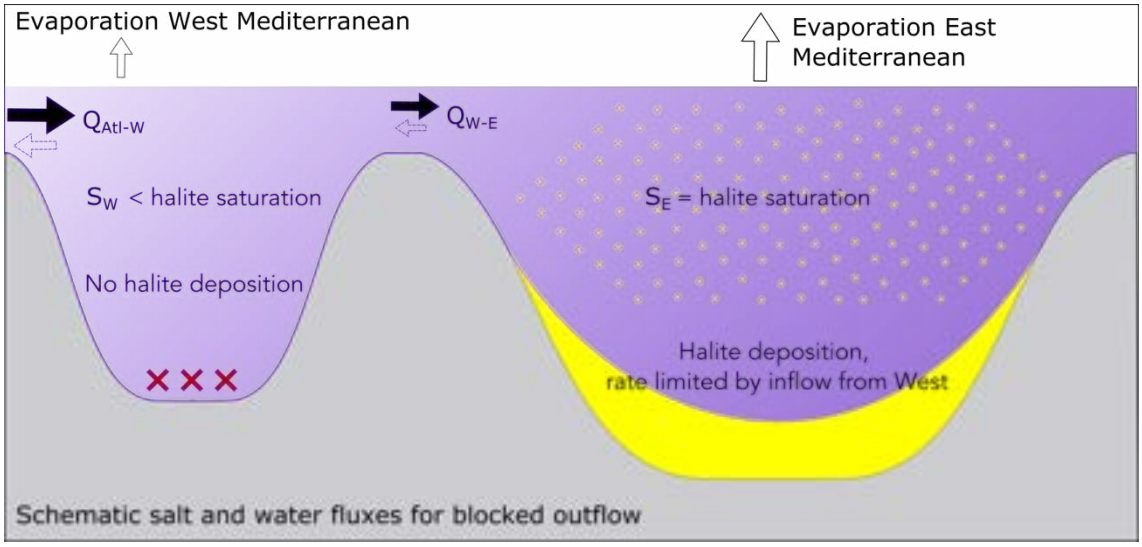

Figure 7.5. Cartoon showing the water and salt exchange between Atlantic, West Mediterranean and East Mediterranean before full closure and drawdown. If the saline outflow to the Atlantic is blocked, salinity in both basins depends on the ratio of evaporation between the two basins. An equilibrium state (where salinity is constant) is expected where the Eastern Basin is at halite saturation, depositing the excess ions entering from the West, while the Western Basin is at a much lower salinity because the inflow from the Atlantic exceeds the evaporation over the sub-basin.

The limit of Western Mediterranean salinity is decided by the ratio of surface area between East and West, and the mixing rate between the two basins, as illustrated in Figure 7.5 and the following equations:

$$Q_{Atl-W} = E_w + E_E \tag{7.1}$$

$$Q_{Atl-W} \cdot S_{Atl} = Q_{W-E} \cdot S_W \tag{7.2}$$

$$S_W = \frac{Q_{Atl-W}}{Q_{W-E}} \cdot S_{Atl} = \frac{E_w + E_E}{E_E} \cdot S_{Atl} \tag{7.3}$$

Where:

Q_{Atl-W}	=	Net flow Atlantic-West Mediterranean	(m^3/sec)
Q_{W-E}	=	Net flow West-East Mediterranean	(m^3/sec)
E_W	=	Evaporation West Mediterranean	(m^3/sec)
E_E	=	Evaporation East Mediterranean	(m^3/sec)
S_{Atl}	=	Salinity Atlantic	(g/l)
S_W	=	Salinity West Mediterranean	(g/l)
S_E	=	Salinity East Mediterranean	(g/l)

In the scenario presented in Figure 7.5, where no outflow takes place from the Mediterranean to Atlantic or East- to West Mediterranean, and the water level is maintained by inflow from the Atlantic, the volume entering into the Western Mediterranean (Q_{Atl-W}) must necessarily compensate the net evaporation in both the Western and Eastern Mediterranean (eq. 7.1). Equation 7.2 assumes a steady state, where the salinity of the Western Basin does not change, and all salts brought into the Western Mediterranean are transported into the eastern basin through Q_{W-E}. This places a limitation on the salinity of the Western Basin that is controlled by the ratio between the net evaporation over the eastern and western basins, which can be assumed to be proportional to the ratio of surface areas between these basins. For the current surface area ratio (approximately 1:3) the salinity of the Western Mediterranean in this steady state without and outflow is limited to ~1.3*S_{Atl}, or approximately 50 g/l. This is well below the salinity needed for gypsum saturation of 250 g/l (Lugli, 2009), but low-salinity gypsum precipitation from benthic microbial mats could explain the formation of gypsum in marginal basins from undersaturated water (Aloisi et al., 2022). Salinity in the Western Basin can be higher if significant mixing takes place between the Eastern and Western basins through a backflow over the Sicily Sill, possibly creating salinity stratification in the Western Basin with a relatively low salinity surface layer and anoxic saline brine in the deep basin. This steady-state approach can explain why the Western Basin salinity remains below halite saturation until the inflow from the Atlantic is blocked and drawdown starts, as suggested by the results obtained from the box-model in Chapter 6, while the Eastern Basin could be already at halite saturation before the drawdown.

The absence of halite in the Valencia Basin, which was deeper than both the CMD and the Cogedor basins in our reconstruction of the pre-evaporite stage, also requires an explanation consistent with the results from the other basins. In Figure 7.6 I show the current and pre-evaporite depths of these small basins along with the thickness of halite

preserved, while in Figure 7.7 an overview of the different preservation stages of halite in the Western Mediterranean subbasins is illustrated. Halite thickness seems to be related primarily to the height of the limiting sill between a subbasin and the deep Mediterranean. While the Cogedor and Formentera basin, which are delimited by sills of insignificant height compared to their basin centres, contain small halite thicknesses (<100 m), the Central Mallorca Depression where the basin centre was over 400 m deeper than the lowest sill before halite deposition (see Chapters 4 and 6).

The results presented in this thesis show the potential for further investigation along the lines of hydrogeochemical box modelling constrained by topographic reconstructions. Open questions remain as to whether it is possible to restrict the Atlantic-Mediterranean gateway enough to provoke a significant water level drop without preconditioning the water column to be completely saturated, as is suggested by the relationship of halite volume and paleohypsometry and channel depth if the Central Mallorca Depression as outlined in Chapter 6. The presence of halite in the Cogedor Basin in the western end of the Balearic Promontory suggests that halite saturation salinity was reached well before the water level dropped to 800 m (see Chapter 4), directly contradicting the result of Chapter 6. This discrepancy can be explained in a number of ways:

- Limiting channel depth of the CMD during the MSC was affected by post-MSC tectonics or volcanism in a way not identified in previous studies of the post-MSC tectonics (Maillard et al., 2022). The sill was deeper than our estimate, limiting the potential of halite preservation during the lowstand and explaining the relatively small halite volume in the CMD.
- Halite was partially exported from the CMD after deposition by a different mechanism, like dissolution and outflow during periods of relatively high water-level during which the CMD was hydrologically connected with the deep basin above sill level.
- The halite identified in the Cogedor Basin was not deposited simultaneously with that in the CMD and deep basins, and does not indicate precipitation at high water levels. The basin could be filled with other types of evaporites. It is unlikely that halite here would be sourced from local evaporation while the basin was already isolated from the deep basin, due to the absence of a significant silled volume that could have retained a potential large brine volume.

Considering the natural response of a basin upon blocking of the saline outflow, and the requirement of saturation at high water level to explain the Western Mediterranean halite volume when drawdown is limited to 1.5 km (see Chapter 6) it appears likely that the halite volume preserved in the CMD has not been completely preserved. Dissolution during stages of high water-level and relatively low salinity appears to be the most likely explanation, but further investigation of this hypothesis is required. This remain a problematic aspect of the model, as it seems unlikely that halite in the Cogedor Basin would not be affected by suck a process, unless the water level fluctuations were big

enough to connect the CMD to the deep basin, but not the Cogedor basin situated some hundreds of meters higher. The Formentera Basin, situated at depths close to the deep basin halite, was potentially covered by brine throughout the MSC explaining its preservation.

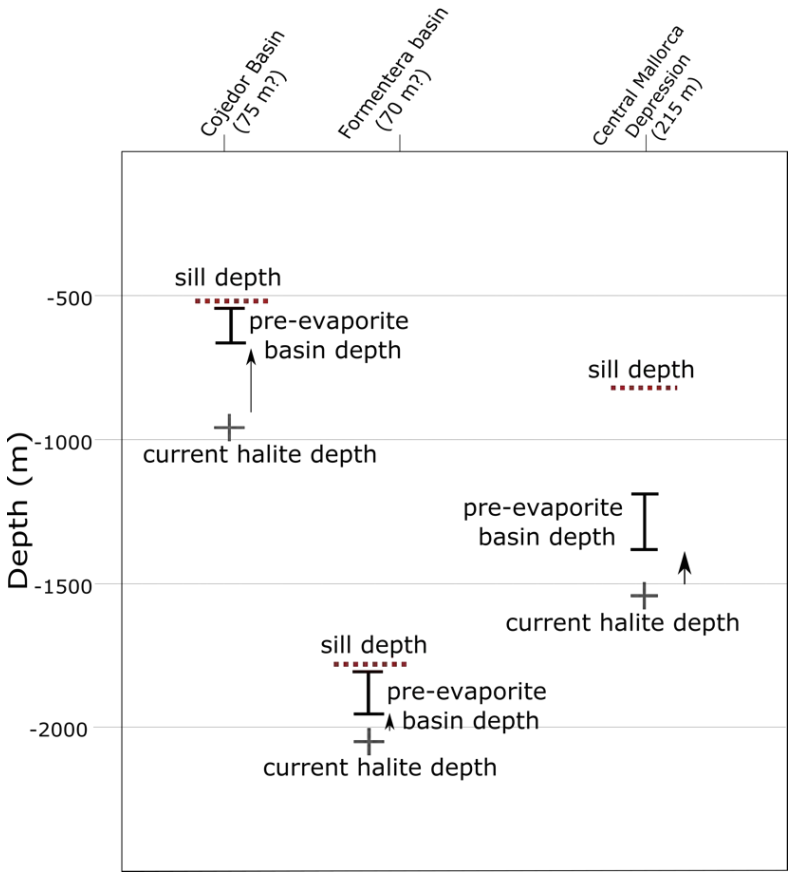

Figure 7.6. Interpretation of the control son halite preservation in different domains of the Balearic Promontory. A: comparison of halite thickness in small isolated basins vs. their current and reconstructed depth.

7.3. Water budgets and baselevel variation

Based on the impact of a desiccation on the Gibraltar arc region (as outlined in Chapter 3) it seems implausible that Atlantic waters were responsible for the water level variations observed both in the record of erosional surfaces and in the Lago Mare deposits found near modern sea level. The freshwater budget of the Mediterranean catchments is sensitive to climate, and varied on a precession scale as illustrated by modelling work (Simon et al., 2017).

The influx of paratethyan fauna during the final stage of the MSC has been recognized throughout the Mediterranean, together with the shift from a hypersaline to a hyposaline, lacustrine environment alternating with gypsum precipitation (Andreetto et

al., 2021). The implications of the connectivity between the Paratethys and Mediterranean while the Mediterranean was disconnected from the Atlantic, when seen from a water budget perspective, are huge and largely unrecognized in literature on the MSC. The catchment area of the Paratethys, including that of the modern Volga and Don rivers exceeds that of the Mediterranean basin (see Fig. 1.2).

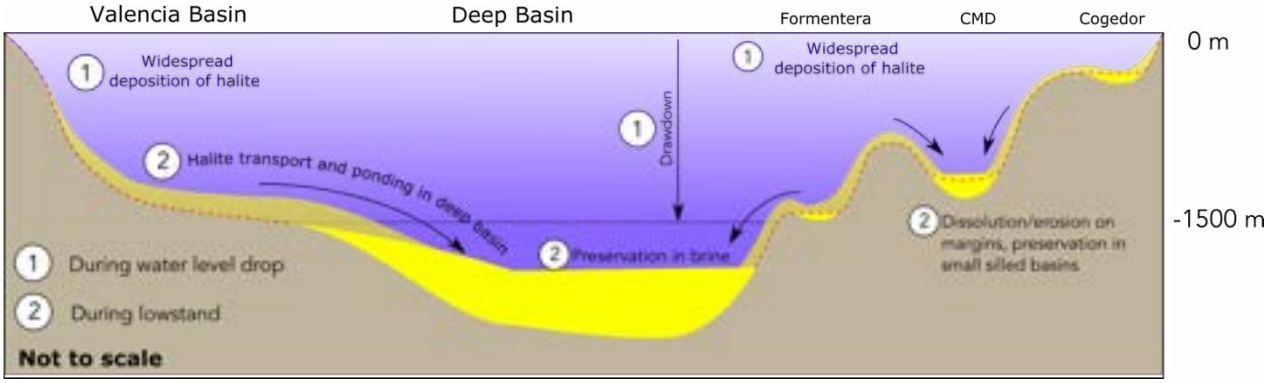

Figure 7.7. Comparison between open, semi-closed and closed basins, and their capacity to retain halite deposited during a drawdown after subaerial exposure, depending on relative height of their sills.

Large regressions in the Paratethys are recognized in the Late Miocene where the lake was reduced to 1/3 of its surface area, having a marked impact on climate, hydrology and vegetation in the region (Palcu et al., 2021), while in the Eastern Paratethys a latest Miocene climatic shift to a positive hydrological budget has been proposed to have caused a transgressive event in the region (Krijgsman et al., 2010). The terminal separation of the Paratethys into its current remnants, the Caspian and Black Seas similarly took place in the late Miocene, and the Caspian Sea underwent a prolonged period of partial desiccation during which the northern part of the basin was subject to canyon incision and the Productive Series, a km thick sediment unit with large hydrocarbon potential, was deposited in the South Caspian basin. The current connection between the Black Sea and Mediterranean through the Dardanelles Sill sees similar hydrodynamic configuration as the Strait of Gibraltar, with a saline flow from the Mediterranean to the Black Sea in the deep, and a low-salinity surface flow from the Black Sea to the Mediterranean, forming a net contributor to the Mediterranean water budget (Özsoy et al., 1996; Ozturk and Altas, 2021). By looking at the Mediterranean hypsometry and freshwater budget without inflow from the Atlantic, we can calculate the depth at which the evaporation over a water body equals the input of fresh water into the basin (equilibrium water level), that has been explored in detail by Meijer and Krijgsman (2005), showing that an isolated Mediterranean under modern hydrological conditions would evaporate down to a depth of over 2 km. In this analysis, a net inflow from the Black Sea is considered that is approximately 2x as big as the Nile prior to damming. However, if we consider that the Paratethys waters, which included the catchment of the Volga River, this flow could have been responsible for a much larger

freshwater contribution from the Paratethys into the Mediterranean at the time of the Messinian Salinity Crisis. A fall of the Paratethys water level associated with stage 2 of the MSC at glacial cycles TG12-14 (Krijgsman et al., 2010) could have provoked a reorganization of Paratethyan drainage systems, rising Mediterranean equilibrium levels without input from the Atlantic. This concept is illustrated in Figure 7.8, where I show a range of equilibrium levels for the Mediterranean, also subdivided into East and West, varying the net evaporation over the basin and adding the 8000 m^3/sec, modern Volga discharge to the freshwater budget for the curves of the Eastern Mediterranean and the entire Mediterranean.

Including extra freshwater input from the Paratethys raises equilibrium levels for the Eastern Mediterranean significantly. From these boundary conditions, the freshwater budget for the Eastern Mediterranean could be positive over parts of a precession cycle, and equilibrium level in the Eastern Mediterranean could easily be above the level of the Sicily Sill, causing overspill from the Eastern to Western Mediterranean. As such a contribution is hard to quantify, its effect on the isolated Western Mediterranean equilibrium level is not shown. However, we can compare the equilibrium level in the Western Basin for its modern hypsometry with its supposed hypsometry after compensating for a large drawdown, in which case the deep basin seafloor is several hundreds of meters shallower due to the loss of surface loading by the water column (see Chapter 4). In that scenario, the equilibrium level of -1500 m is reached when the net evaporation over the surface is a bit over 0.4 m/yr. While this may be slightly low, it should be taken into account that effective evaporation is reduced significantly (by around 30%, Myers and Bonython, 1958; Topper and Meijer, 2013) in brine at halite saturation compared to normal seawater. The halite-pinchout paleoshoreline reconstructed for Stage 2 at -1500 m might therefore not be far from the natural water level the basin would tend to upon isolation. Based on these concepts, a variation in water level large enough to explain the spread of restored paleoshoreline depth presented in this thesis could be explained by changes in the freshwater budget by climate oscillations and changes in Paratethys discharge into the Mediterranean.

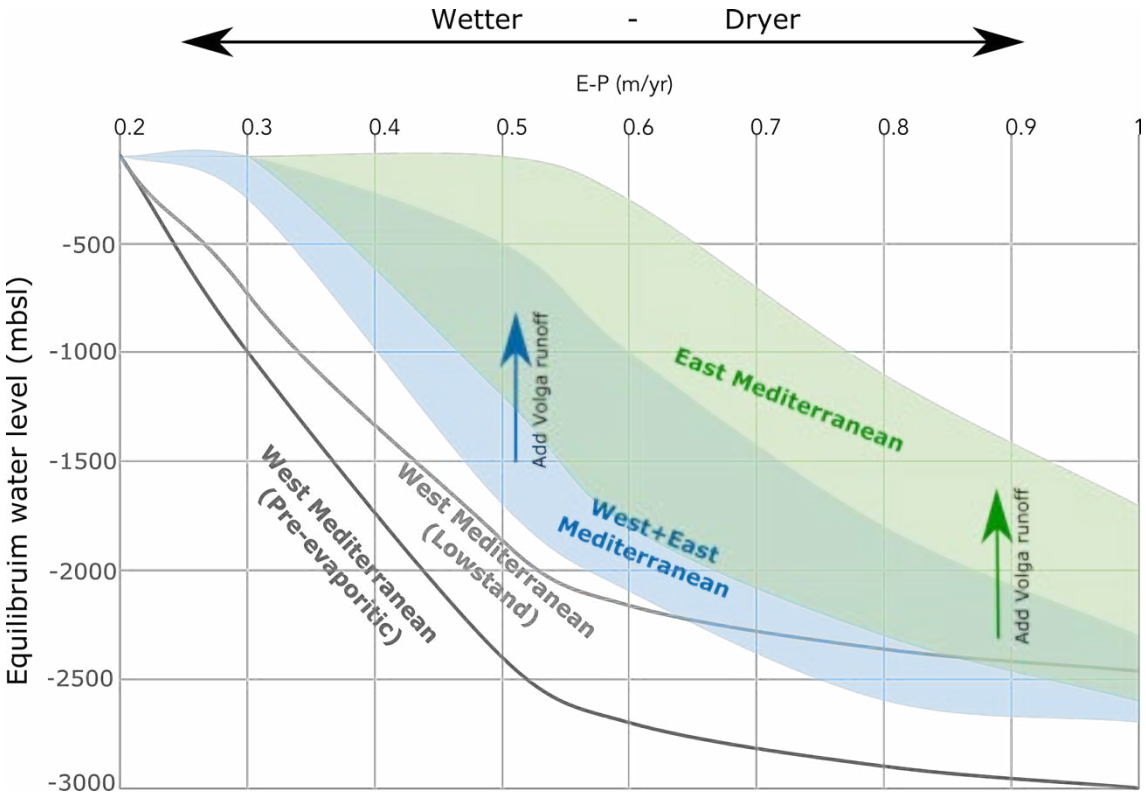

Figure 7.8. Range of equilibrium level based on the hypsometry of the modern Eastern Mediterranean (green), modern East+West Mediterranean (blue) and reconstructed West Mediterranean (grey) for a range of E-P values. Shown is the impact on the subbasin equilibrium level of net evaporation changes due to climatic variation (wetter versus dryer conditions along the x-axis), and the raising of equilibrium water level by introducing a large freshwater contribution from the Paratethys (in this figure, the impact of adding 8000 m^3/sec Volga runoff is shown for reference. Within this parameter range, it is possible for the East Mediterranean to have a positive freshwater budget.

After connection of the Paratethys, the Eastern Mediterranean would be maintained at a higher base level, possibly explaining the long-term incision of the Nile Canyon, where the water level would be determined by the depth of the Sicily Sill. In the Western Mediterranean, water level would be more variable depending on the magnitude of outflow from East to West. Such scenarios require further detailed investigation, with reliable quantification of freshwater budgets as a foundation. Alternative explanations involving limited water inflow from the Atlantic after a drawdown are deemed unlikely considering the self-isolating effect at the Gibraltar arc upon drawdown (Govers, 2009; Chapter 3) and the erosive capacity of a stream that cannot be maintained with stable limited discharge over hundreds of thousands of years, but rather would cause catastrophic flooding (Garcia-Castellanos et al., 2020).

7.4. Future perspective

The SaltGiant project has provided large steps towards reaching a comprehensive model for the progression of the Messinian Salinity Crisis, with most results converging on the need for large water level fluctuations during Stages 2 and 3 of the MSC, as also illustrated in this work. Important questions remain regarding the sources of water into the Mediterranean during these stages, where isotopic composition and palaeontological data suggest a contribution of marine (Atlantic) waters (Andreetto, 2022), but sustained Atlantic inflow during stages of low water level is unlikely considering the stability of the eroding sill on the required timescale (García-Castellanos and Villaseñor, 2011).

7.4.1. Numerical Modelling

Numerical modelling approaches are one of the most important components towards constraining the required water sources in a brine undergoing phases of dilution and concentration. Similarly, models of the plausible evolution of equilibrium water levels in the Mediterranean undergoing climate variations and reconfiguration of the catchments draining into the Mediterranean and Paratethys are required to understand the implications for the connectivity between subbasins over the course of the MSC. Numerical box models based on realistic hypsometry, like those presented in Chapter 6 of this work have the potential to provide a host of new insight on these topics. Ideally, such modelling efforts would also be supported by more accurate knowledge on the depth of the sills separating subbasins, specifically the Sicily Sill. The depth of the Sicily Sill controls the dynamics of the drawdown and reflooding stages (determining the stable water level during basin overtopping) as well as the ease of establishing connectivity between east and west during the lowstand stage. The flexural-isostatic and global water level implications of precession-scale (21 kyr) variations in water level have significant implications for vertical motions in the deep Mediterranean Basins and their margins, possibly weakening and deforming these margins as proposed in Chapter 4. It is possible that with fast variations in water level, flexural-isostatic compensation of the changing water load is not fully developed over every climate cycle, and that this affects the accuracy of the restoration of paleoshoreline indicators that were formed over short periods. Glacial-isostatic models can help us predict these effects and can be another independent tool towards test MSC water level scenarios.

7.4.2. Drilling of MSC record

The importance of new scientific drilling of the Messinian evaporites has been clear to a large part of the community for well over a decade. Access to samples from the halite unit and the underlying sediments remains limited, and is crucial to understand the chronology of the MSC events in the deep Mediterranean Basins east and west of the Sicily Sill, as well as their emplacement relative to evaporite deposits in marginal basins and Sicily. Multiple drilling campaigns have been proposed in recent years, for example

on the Balearic Promontory ("DREAM", Lofi et al., 2017), although drilling hazards associated with drilling through thick halite deposits, addressed in Work Package 3 of SaltGiant project, remain an issue. An amphibious drilling project focussed on the Atlantic-Mediterranean gateway area (IMMAGE, Flecker, 2018) has been scheduled for late 2023, hopefully providing data that will help resolve the evolution of the marine gateways before and during the MSC. Another proposed drilling project (BlackGate, Krijgsman et al., 2022) would focus on the other end of the Mediterranean, and the gateways controlling the connectivity with the Paratethys domain, the importance of which has been discussed at length in this work. Results from these future campaigns will provide further context and boundary conditions to arrive at an integrated model for the MSC.

7.4.3. Global impact of the MSC

Another interesting, and undervalued aspect of the MSC is the impact these events must have had on the global ocean and climate. A km-scale drop in the Mediterranean water level would provide a large water level contribution to the global ocean, potentially raising average global sea level by about 10 meters. While such an effect has been proposed in the South Atlantic (Aharon et al., 1993) this impact has not been clearly identified in the global record. The rapid sequestration of a significant portion of global ocean salinity into a Salt Giant also affects climate by weakening greenhouse forcing, which can cause several degrees of planetary cooling (Shields and Mills, 2021). The global record of proxy markers for salinity and climate at the end of the Miocene would be a good target to try and identify the possible MSC signal, although it might be difficult to distinguish these effects from normal eustatic variations. Results of drilling in the vicinity of the Strait of Gibraltar on the Atlantic side (IMMAGE) might provide a clear record of such impacts, as the variations in Mediterranean Outflow Waters will be directly recorded there. This will also add to the ongoing efforts to determine quantitatively the impact of the MSC on biodiversity in the Mediterranean (Agiadi, in prep; Butiseacă et al., 2022).

7.4.4. The Dead Sea: a potential analogue?

A final line of investigation that has been explored over the recent years and has already led to important insights on the processes of evaporite deposition is the identification of modern-day hypersaline environments as possible analogues to the Mediterranean during the MSC. The Dead Sea, while different in crucial ways to the Mediterranean in terms of dimensions and water budget, has the potential to explore the impacts of seasonal variability, freshwater plumes and the exposure of margins during a water level drop, in real time. Comparison in specific contexts, such as the Valencia Basin and Central Mallorca Depression, combined with quantitative analyses of precipitation and dissolution potential can help us understand the sometimes puzzling depth distribution of evaporite preservation in the Mediterranean.

Chapter 8: General Conclusions

The aim of this thesis was to reach a better understanding of the timing and magnitude of water level variations during the Messinian Salinity Crisis, and their implications for conditions during evaporite deposition. This has been done through a quantitative reconstruction of the Mediterranean subbasins, constraining the depth of paleoshoreline markers from these reconstructions, and examining the plausible basin connectivity and environmental conditions that led to evaporite deposition.

The results show that the Western Mediterranean was of considerable depth before the onset of the MSC, similar to the modern bathymetry. Shoreline terraces were formed at a wide range of depths from 250 to 1500 m in the West Alboran Basin, although these cannot be linked univocally to the drawdown stage of the MSC and their formation by a flooding event cannot be excluded. The mostly submarine paleotopography obtained for the Alboran Volcanic Arc indicates that marine corridors should have allowed for water exchange between the West Alboran and the rest of the Mediterranean, and that therefore the shallower Gibraltar tectonic arc was the most likely position for the topographic barrier separating the Atlantic Ocean and the Mediterranean Sea.

In the Valencia Basin, the relationship of MSC stratigraphy and erosional surfaces allow identification of two paleoshoreline levels, one formed originally at -1500 m related to the halite “Mobile Unit” (MU) and the Bottom Erosion Surface, and one at -1100 m related to the “Upper Unit” (gypsum/anhydrite) deposits. This, like the variable terrace depth in the Alboran Basin, indicates variations in the West Mediterranean water levels from the onset of the lowstand stage to the eventual reflooding at the base of the Pliocene. The presence of halite in small silled basins at a wide depth range on the Balearic Promontory shows that halite was originally deposited in shallower regions than suggested by its modern preservation. However, it is unclear whether the shallow halite deposits were formed only in these silled basins due to local brine accumulation, or if halite was formed on all of the later exposed margins and subsequently eroded everywhere but in the silled basins.

In the Eastern Mediterranean, re-examination of the Nile Canyon allowed identification of a morphological expression of a shoreline in the form of a 400 m high knickzone formed as a response the drop in Messinian baselevel. Downstream from the knickzone, a gently sloping subaerial river canyon transitions into a steeper, subaqueous canyon, with this change in the character of the canyon geometry being interpreted as an expression of the paleoshoreline formed during the Messinian lowstand. This shoreline was reconstructed to a level 600 m below sea level, which implies a significantly larger water level drop than can be explained by eustatic sea-level variations, but this new estimate is 2-4 times smaller than previous water level reported based on the Nile

Canyon incision. The difference between the Nile Canyon paleoshoreline depth and previous estimates based on coastal erosion features on the Malta Escarpment and the potentially subaerially exposed Nahr Menashe deposit in the deep Levant Basin suggests, similarly to the Western Mediterranean, strong changes in water level during the lowstand stage of the Messinian during which the connection to the global ocean was closed, probably controlled by climatic-induced changes in the water budget of each subbasin.

The box-model of the hydrological and salinity budget of the Central Mallorca Depression based on the restored Messinian bathymetry illustrates how the Stage 1 gypsum deposits in this unique basin formed over a large depth range under high water level, in a Mediterranean that had surface waters with high salinity. In contrast, based on its preserved volume the halite observed in the CMD was formed in a basin undergoing significant drawdown, suggesting that halite saturation was reached when the CMD disconnected from the surrounding deep basin when the water level drop reached approximately -800 m. However, the presence of the aforementioned halite basins on the Balearic Promontory suggests that at least in some areas halite saturation was reached already at higher water level, before the drawdown reached -500 m depth relative to the global sea level. The box model also shows that the entire halite volume in the Western Mediterranean could potentially be formed during the drawdown from the brine present in the basin at the time of disconnection.

Based on the results and ideas presented above I tentatively propose the following model for the evolution of Mediterranean water level and connectivity, illustrated in Figure 8.1:

- After deposition of the Primary Lower Gypsum in a full Mediterranean, progressive restriction at the strait of Gibraltar initiated Stage 2 with the complete disconnection between the Atlantic Ocean and Mediterranean Sea and a major water level drop down to -1500 m below global sea level during which the majority of the Western Mediterranean halite volume was deposited. In the Eastern Mediterranean the initial water level drop might have been even larger, potentially reaching -1900 m. Rebound in response to the water level drop at the Gibraltar Arc region would prevent the reconnection of the Atlantic inflow by eustatic sea-level variation and initiate a ~220 kyr phase of endorheism in the Mediterranean.

- After the initial drawdown, Stage 3 is characterized by erosion at the margins and deposition of the Upper Unit evaporites indicating both lateral and temporal variation in water level. In the Eastern Mediterranean, a long-lived base level is recorded at -600 m below global sea level potentially related to the depth of the Sicily Sill, but water level might have periodically fluctuated depending on the water budget of the Paratethys and East Mediterranean. In the Western Mediterranean, a multi-precession cycle water level is recorded in the UU of the Valencia Basin at -1100 m, and variable water levels are recorded in erosional terraces of the Alboran Basin. The lower water level in the Western Mediterranean compared to the East can be related to lack of large plausible catchment areas that would have provided extra fresh water to this basin after isolation, and therefore the water level would vary depending on climate and periodic overtopping of the Eastern Basin. Normal marine conditions are established only after reopening of the Atlantic-Mediterranean connection at the Strait of Gibraltar and the reflooding of the Mediterranean.

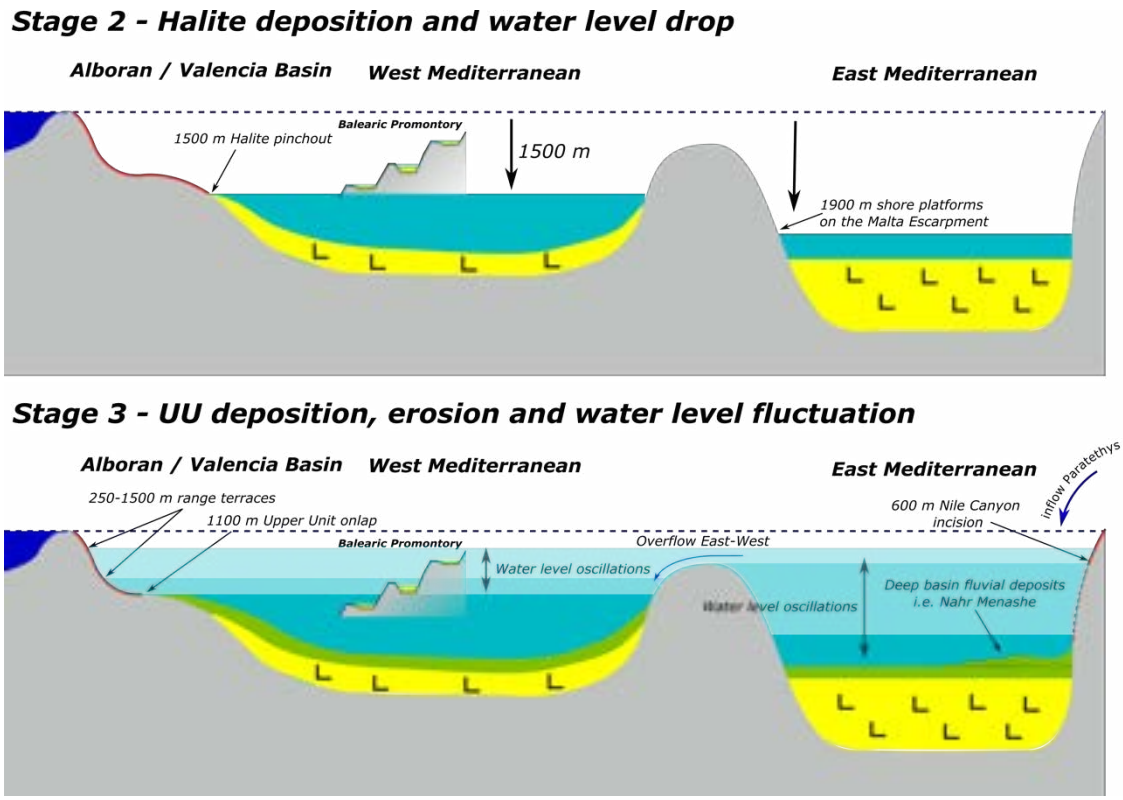

Figure 8.1. Cartoon depicting the model of MSC water level variations and evaporite deposition based on the results presented in this work and previous publications. Yellow indicates halite deposits; green is for upper unit gypsum/anhydrite deposits. Shoreline markers restored in this work (Halite pinchout, Upper Unit onlap, terraces and Nile Canyon incision) and previous publications (Nahr Menashe deposits [Madof et al., 2019] and shore platforms on the Malta Escarpment [Micallef et al., 2018]) are indicated.

Acknowledgements

A huge thanks goes out to my supervisors at Geosciences Barcelona, Daniel Garcia-Castellanos and Ivone Jiménez Munt. Thank you for the all your guidance, and the incredible patience and support throughout the process of writing this thesis, allowing me to find my own rhythm and way through the challenges and controversies, and for the openness to explore collaborations and follow my curiosity. No matter how challenging the moment, I always left our discussions feeling more confident and optimistic about our work.

To Johanna Lofi, Agnès Maillard, Jerry Mitrovica, Sophie Coulson, thank you for the generous hosting during the international stays, and everything learned.

All members of the extended SaltGiant community are thanked for the many discussions and learning moments during the workshops, fieldtrips and training events that are at the heart of this thesis. Special thanks my fellow ESRs Athina, Bea, Federico, Francesca, Gaia, Jimmy, Laetitia, Maria, Mariam, Michael, Simon R., Simon B. and Ronja for all the fun times over the years and the amazing stuff I learned from all of you. You guys have made the last four years truly special, and I feel like I gained a new family. Very special thanks to Fadl Raad, fellow ESR and closest collaborator over the last years. Your self-appointed title of honorary supervisor is well deserved, and this thesis would not be the same without your teachings both on seismic interpretation and our many great Lebanese dinners.

Thanks to my amazing friends and colleagues in Barcelona, Martyna, Erandi, Estefania, Mario, Ajay, Kittiphon, Angel, Olaya, Alejandra, Lara, Wentao, Vito, Gabriel, the Irenes, Erik, Marc and the rest for the fun times over the past four years. Every beer, padel game and mountain trip has made the writing process that much easier.

Muchísimas gracias a los del Geociencias Barcelona, que me han ayudado en todas las luchas de la vida de “Guiri” en España, Chelo, Paco, Marc, Oscar, y por supuesto a Xavi por alegrarme cada mañana entrando a la oficina.

Aan mijn vrienden Floris, Nelly, Milo, Jurriaan en de rest terug in Nederland, jullie zijn een geweldige steun geweest, zelfs van een afstand.

To my parents and siblings, and to Ignacio, for everything.

This work in this thesis was undertaken in the context of the SaltGiant European Training Network funded by the European Commission through under grant agreement Horizon2020-765256.

Bibliography

Acosta, J., Ancochea, E., Canals, M., Huertas, M.J., Uchupi, E., 2004a. Early Pleistocene volcanism in the Emile Baudot Seamount, Balearic Promontory (western Mediterranean Sea). Mar. Geol. 207, 247–257. https://doi.org/10.1016/j.margeo.2004.04.003

Acosta, J., Canals, M., Carbó, A., Muñoz, A., Urgeles, R., Muñoz-Martín, A., Uchupi, E., 2004b. Sea floor morphology and Plio-Quaternary sedimentary cover of the Mallorca Channel, Balearic Islands, western Mediterranean. Mar. Geol. 206, 165–179. https://doi.org/10.1016/j.margeo.2004.02.008

Acosta, J., Muñoz, A., Herranz, P., Palomo, C., Ballesteros, M., Vaquero, M., Uchupi, E., 2001. Geodynamics of the Emile Baudot Escarpment and the Balearic Promontory, western Mediterranean. Mar. Pet. Geol. 18, 00003–00004.

Agiadi, K. , In Prep. Late Miocene Mediterranean Marine Ecosystem Crisis

Aharon, P., Goldstein, S.L., Wheeler, C.W., Jacobson, G., 1993. Sea-Level Events in the South-Pacific Linked With the Messinian Salinity Crisis. Geology 21, 771–775. https://doi.org/10.1130/0091-7613(1993)021

Ahmed, A., Ahmed, E.B., Marc, G., Hans-Jürg, M., Marcus, S., Hala, Z., 2001. Tectonic Evolution of the Eastern Mediterranean Basin and its Significance for the Hydrocarbon Prospectivity of the Nile Delta Deepwater Area. GeoArabia 6, 363–384. https://doi.org/10.2113/geoarabia0603363

Aloisi, G., Guibourdenche, L., Natalicchio, M., Caruso, A., Haffert, L., El Kilany, A., & Dela Pierre, F. (2022). The geochemical riddle of “low-salinity gypsum” deposits. Geochimica et Cosmochimica Acta, S0016703722001600. https://doi.org/10.1016/j.gca.2022.03.033

Alvarez, W., 1972. Rotation of the Corsica–Sardinia Microplate. Nat. Phys. Sci. 235, 103–105. https://doi.org/10.1038/physci235103a0

Amadori, C., Garcia-Castellanos, D., Toscani, G., Sternai, P., Fantoni, R., Ghielmi, M., Di Giulio, A., 2018. Restored topography of the Po Plain-Northern Adriatic region during the Messinian base-level drop-Implications for the physiography and compartmentalization of the palaeo-Mediterranean basin. Basin Res. https://doi.org/10.1111/bre.12302

Amblas, D., Canals, M., Gerber, T.P., 2015. The long-term evolution of submarine canyons: insights from the NW Mediterranean. CIESM Monogr. 47, 171–181.

Andreetto, F., 2022. High-amplitude water-level fluctuations at the end of the Mediterranean Messinian Salinity Crisis: Implications for gypsum formation, connectivity and global climate. Earth Planet. Sci. Lett. 15.

Andreetto, F., Aloisi, G., Raad, F., Heida, H., Flecker, R., Agiadi, K., Lofi, J., Blondel, S., Bulian, F., Camerlenghi, A., Caruso, A., Ebner, R., Garcia-Castellanos, D., Gaullier, V., Guibourdenche, L., Gvirtzman, Z., Hoyle, T.M., Meijer, P.T., Moneron, J., Sierro, F.J., Travan, G., Tzevahirtzian, A., Vasiliev, I., Krijgsman, W., 2021. Freshening of the Mediterranean Salt Giant: controversies and certainties around the terminal (Upper Gypsum and Lago-Mare) phases of the Messinian Salinity Crisis. Earth-Sci. Rev. 216, 103577. https://doi.org/10.1016/j.earscirev.2021.103577

Andreetto, F., Matsubara, K., Beets, C.J., Fortuin, A.R., Flecker, R., Krijgsman, W., 2020. High Mediterranean water-level during the Lago-Mare phase of the Messinian Salinity Crisis: insights from the Sr isotope records of Spanish marginal basins (SE Spain). Palaeogeogr. Palaeoclimatol. Palaeoecol. 562, 110139. https://doi.org/10.1016/j.palaeo.2020.110139

Arnon, A., Selker, J.S., Lensky, N.G., 2016. Thermohaline stratification and double diffusion diapycnal fluxes in the hypersaline Dead Sea. Limnol. Oceanogr. 61, 1214–1231. https://doi.org/10.1002/lno.10285

Artiaga, D., García-Veigas, J., Cendón, D.I., Atalar, C., Gibert, L., 2021. The Messinian evaporites of the Mesaoria basin (North Cyprus): A discrepancy with the current chronostratigraphic understanding. Palaeogeogr. Palaeoclimatol. Palaeoecol. 584, 110681. https://doi.org/10.1016/j.palaeo.2021.110681

Auzende, J.M., Olivet, J.L., Bonnin, J., 1972. Une structure compressive au nord de l’Algérie? Deep Sea Res. Oceanogr. Abstr. 19, 149–155. https://doi.org/10.1016/0011-7471(72)90047-2

Awad, S.R., 2019. Groundwater hydrogeology and quality in Helwan area and its vicinities in Egypt. Water Sci.

33, 10–21. https://doi.org/10.1080/11104929.2019.1624307

Babel, M., Schreiber, B., 2014. Geochemistry of Evaporites and Evolution of Seawater, in: Treatise on Geochemistry: Second Edition. pp. 483–560. https://doi.org/10.1016/B978-0-08-095975-7.00718-X

Bache, F., Olivet, J.L., Gorini, C., Rabineau, M., Baztan, J., Aslanian, D., Suc, J.P., 2009. Messinian erosional and salinity crises: View from the Provence Basin (Gulf of Lions, Western Mediterranean). Earth Planet. Sci. Lett. 286, 139–157. https://doi.org/10.1016/j.epsl.2009.06.021

Bache, F., Popescu, S.M., Rabineau, M., Gorini, C., Suc, J.P., Clauzon, G., Olivet, J.L., Rubino, J.L., Melinte-Dobrinescu, M.C., Estrada, F., Londeix, L., Armijo, R., Meyer, B., Jolivet, L., Jouannic, G., Leroux, E., Aslanian, D., Reis, A.T.D., Mocochain, L., Dumurdžanov, N., Zagorchev, I., Lesić, V., Tomić, D., Namik Çağatay, M., Brun, J.P., Sokoutis, D., Csato, I., Ucarkus, G., Çakir, Z., 2012. A two-step process for the reflooding of the Mediterranean after the Messinian Salinity Crisis. Basin Res. 24, 125–153. https://doi.org/10.1111/j.1365-2117.2011.00521.x

Badji, R., Charvis, P., Bracene, R., Galve, A., Badsi, M., Ribodetti, A., Benaissa, Z., Klingelhoefer, F., Medaouri, M., Beslier, M.-O., 2015. Geophysical evidence for a transform margin offshore Western Algeria: a witness of a subduction-transform edge propagator? Geophys. J. Int. 200, 1029–1045. https://doi.org/10.1093/gji/ggu454

Balaguer, P., Fornós, J.J., 2003. Erosive processes at Eastern Mallorca seacliffs (Illes Balears, western Mediterranean): Evaluation of erosion rates by granular disgregation, Preliminary data. Bolleti Soc. Hist. Nat. Balears 46.

Barber, P.M., 1981. Messinian subaerial erosion of the proto-Nile Delta. Mar. Geol. 44, 253–272. https://doi.org/10.1016/0025-3227(81)90053-0

Barceló-Llull, B., Pascual, A., Ruiz, S., Escudier, R., Torner, M., Tintoré, J., 2019. Temporal and Spatial Hydrodynamic Variability in the Mallorca Channel (Western Mediterranean Sea) From 8 Years of Underwater Glider Data. J. Geophys. Res. Oceans 124, 2769–2786. https://doi.org/10.1029/2018JC014636

Baringer, M.O., Price, J.F., 1999. A review of the physical oceanography of the Mediterranean outflow. Mar. Geol. 155, 63–82. https://doi.org/10.1016/S0025-3227(98)00141-8

Bartrina, M.T., Cabrera, L., Jurado, M.J., Guimerà, J., Roca, E., 1992. Evolution of the central Catalan margin of the Valencia trough (western Mediterranean). Tectonophysics 203, 219–247. https://doi.org/10.1016/0040-1951(92)90225-U

Bellucci, M., Pellen, R., Leroux, E., Bache, F., Garcia, M., Do Couto, D., Raad, F., Blondel, S., Rabineau, M., Gorini, C., Moulin, M., Maillard, A., Lofi, J., Del Ben, A., Camerlenghi, A., Poort, J., Aslanian, D., 2021. A comprehensive and updated compilation of the seismic stratigraphy markers in the Western Mediterranean Sea. https://doi.org/10.17882/80128

Ben Moshe, L., Ben-Avraham, Z., Enzel, Y., Schattner, U., 2020. Estimating drawdown magnitudes of the Mediterranean Sea in the Levant basin during the Lago Mare stage of the Messinian Salinity Crisis. Mar. Geol. 427, 106215–106215. https://doi.org/10.1016/j.margeo.2020.106215

Ben-Gai, Y., Ben-Avraham, Z., Buchbinder, B., Kendall, C.G.S.C., 2005. Post-Messinian evolution of the Southeastern Levant Basin based on two-dimensional stratigraphic simulation. Mar. Geol. 221, 359–379. https://doi.org/10.1016/j.margeo.2005.03.003

Bertoni, C., Cartwright, J.A., 2007. Major erosion at the end of the Messinian Salinity Crisis: evidence from the Levant Basin, Eastern Mediterranean. Basin Res. 19, 1–18. https://doi.org/10.1111/j.1365-2117.2006.00309.x

Bertoni, C., Cartwright, J.A., 2006. Controls on the basinwide architecture of late Miocene (Messinian) evaporites on the Levant margin (Eastern Mediterranean). Sediment. Geol. 188–189, 93–114. https://doi.org/10.1016/j.sedgeo.2006.03.019

Bessis, F., 1986. Some remarks on the study of subsidence of sedimentary basins Application to the Gulf of Lions margin (Western Mediterranean). Mar. Pet. Geol. 3, 37–63. https://doi.org/10.1016/0264-8172(86)90055-3

Bigi, D., Lugli, S., Manzi, V., Roveri, M., 2022. Are fluid inclusions in gypsum reliable paleoenvironmental indicators? An assessment of the evidence from the Messinian evaporites. Geology. https://doi.org/10.1130/G49475.1

Bijma, J., Faber, W.W., Hemleben, C., 1990. Temperature and salinity limits for growth and survival of some planktonic foraminifers in laboratory cultures. J. Foraminifer. Res. 20, 95–116.

Blanc, P.L., 2006. Improved modelling of the Messinian Salinity Crisis and conceptual implications.

Palaeogeogr. Palaeoclimatol. Palaeoecol. 238, 349–372. https://doi.org/10.1016/j.palaeo.2006.03.033

Blanc, P.L., 2002. The opening of the plio-quaternary gibraltar strait: Assessing the size of a cataclysm. Geodin. Acta 15, 303–317. https://doi.org/10.1080/09853111.2002.10510763

Blanc, P.L., 2000. Of sills and straits: A quantitative assessment of the Messinian Salinity Crisis. Deep-Sea Res. Part Oceanogr. Res. Pap. 47, 1429–1460. https://doi.org/10.1016/S0967-0637(99)00113-2

Blanckenhorn, M., 1921. Handbuch der regionalen geologie, bd., vii, abt. 9, Heft 23, Agypten.

Blanc-Valleron, M.-M., Pierre, C., Caulet, J.P., Caruso, A., Rouchy, J.-M., Cespuglio, G., Sprovieri, R., Pestrea, S., Di Stefano, E., 2002. Sedimentary, stable isotope and micropaleontological records of paleoceanographic change in the Messinian Tripoli Formation (Sicily, Italy). Palaeogeogr. Palaeoclimatol. Palaeoecol. 185, 255–286. https://doi.org/10.1016/S0031-0182(02)00302-4

Bohorquez, P., Carling, P.A., Herget, J., 2016. Dynamic simulation of catastrophic late Pleistocene glacial-lake drainage, Altai Mountains, central Asia. Int. Geol. Rev. 58, 1795–1817. https://doi.org/10.1080/00206814.2015.1046956

Boonma, K., 2021. Geodynamic modelling of lithosphere subduction and the topographic response to slab tearing. Application to the Gibraltar Arc. Universitat de Barcelona, Barcelona, Spain.

Booth-Rea, G., R. Ranero, C., Grevemeyer, I., 2018. The Alboran volcanic-arc modulated the Messinian faunal exchange and salinity crisis. Sci. Rep. 8, 13015–13015. https://doi.org/10.1038/s41598-018-31307-7

Booth-Rea, G., Ranero, C.R., Martínez-Martínez, J.M., Grevemeyer, I., 2007. Crustal types and Tertiary tectonic evolution of the Alborán sea, western Mediterranean: ALBORÁN SEA CRUSTAL TYPES. Geochem. Geophys. Geosystems 8, n/a-n/a. https://doi.org/10.1029/2007GC001639

Bourillot, R., Vennin, E., Rouchy, J.M., Blanc-Valleron, M.M., Caruso, A., Durlet, C., 2010. The end of the Messinian Salinity Crisis in the western Mediterranean: Insights from the carbonate platforms of south-eastern Spain. Sediment. Geol. 229, 224–253. https://doi.org/10.1016/j.sedgeo.2010.06.010

Bourillot, R., Vennin, E., Rouchy, J.M., Durlet, C., Rommevaux, V., Kolodka, C., Knap, F., 2009. Structure and evolution of a Messinian mixed carbonate-siliciclastic platform: The role of evaporites (Sorbas Basin, South-east Spain). Sedimentology 57, 477–512. https://doi.org/10.1111/j.1365-3091.2009.01092.x

Bulian, F., Sierro, F.J., Ledesma, S., Jiménez-Espejo, F.J., Bassetti, M.-A., 2021. Messinian West Alboran Sea record in the proximity of Gibraltar: Early signs of Atlantic-Mediterranean gateway restriction. Mar. Geol. 434, 106430. https://doi.org/10.1016/j.margeo.2021.106430

Burollet, P.F., Said, A., Trouve, P., 1978. Slim holes drilled on the Algerian shelf. Initial Rep. Deep Sea Drill. Proj. Government Press, 1181–1184.

Burov, E.B., Diament, M., 1995. The effective elastic thickness (Te) of continental lithosphere: what does it really mean? J. Geophys. Res. https://doi.org/10.1029/94JB02770

Burrus, J., 1984. Contribution to a geodynamic synthesis of the Provençal Basin (North-Western Mediterranean). Mar. Geol. 55, 247–269.

Butiseacă, G. A., van der Meer, M. T. J., Kontakiotis, G., Agiadi, K., Thivaiou, D., Besiou, E., Antonarakou, A., Mulch, A., & Vasiliev, I. (2022). Multiple crises preceded the Mediterranean Salinity Crisis: Aridification and vegetation changes revealed by biomarkers and stable isotopes. Global and Planetary Change, 217, 103951. https://doi.org/10.1016/j.gloplacha.2022.103951

Calaforra, J.M., dell'Aglio, A., Forti, P., 1993. Preliminary data on the chemical corrosion in gypsum karst: 1-The Sorbas region (Spain). XI Int. Congr. Speleol., Beijing, China 77–99.

Camerlenghi, A., Accettella, D., Costa, S., Lastras, G., Acosta, J., Canals, M., Wardell, N., 2009. Morphogenesis of the SW Balearic continental slope and adjacent abyssal plain, Western Mediterranean Sea. Int. J. Earth Sci. 98, 735–750. https://doi.org/10.1007/s00531-008-0354-8

Camerlenghi, A., Del Ben, A., Hübscher, C., Forlin, E., Geletti, R., Brancatelli, G., Micallef, A., Saule, M., Facchin, L., 2019. Seismic markers of the Messinian salinity crisis in the deep Ionian Basin. Basin Res. 1–23. https://doi.org/10.1111/bre.12392

Cameselle, A.L., Urgeles, R., 2017. Large-scale margin collapse during Messinian early sea-level drawdown: the SW Valencia trough, NW Mediterranean. Basin Res. 29, 576–595. https://doi.org/10.1111/bre.12170

Cameselle, A.L., Urgeles, R., De Mol, B., Camerlenghi, A., Canning, J.C., 2014. Late Miocene sedimentary architecture of the Ebro Continental Margin (Western Mediterranean): Implications to the Messinian Salinity Crisis. Int. J. Earth Sci. 103, 423–440. https://doi.org/10.1007/s00531-013-0966-5

Capella, W., Barhoun, N., Flecker, R., Hilgen, F.J., Kouwenhoven, T., Matenco, L., Sierro, F.J., Tulbure, M.A., Yousfi, M.Z., Krijgsman, W., 2018. Palaeogeographic evolution of the late Miocene Rifian Corridor (Morocco): Reconstructions from surface and subsurface data. Earth-Sci. Rev. 180, 37–59. https://doi.org/10.1016/j.earscirev.2018.02.017

Capella, W., Spakman, W., van Hinsbergen, D.J.J., Chertova, M.V., Krijgsman, W., 2020. Mantle resistance against Gibraltar slab dragging as a key cause of the Messinian Salinity. Terra Nova 32, 141–150. https://doi.org/10.1111/ter.12442

Capó, A., Garcia, C., 2019. Basin filling evolution of the central basins of Mallorca since the Pliocene. Basin Res. 31, 948–966. https://doi.org/10.1111/bre.12352

Carballo, A., Fernandez, M., Torne, M., Jiménez-Munt, I., Villaseñor, A., 2015. Thermal and petrophysical characterization of the lithospheric mantle along the northeastern Iberia geo-transect. Gondwana Res. 27, 1430–1445. https://doi.org/10.1016/j.gr.2013.12.012

Cartwright, J.A., Jackson, M.P.A., 2008. Initiation of gravitational collapse of an evaporite basin margin: The Messinian saline giant, Levant Basin, eastern Mediterranean. Bull. Geol. Soc. Am. 120, 399–413. https://doi.org/10.1130/B26081X.1

Castillo, M., Bishop, P., Jansen, J.D., 2013. Knickpoint retreat and transient bedrock channel morphology triggered by base-level fall in small bedrock river catchments: The case of the Isle of Jura, Scotland. Geomorphology 180–181, 1–9. https://doi.org/10.1016/j.geomorph.2012.08.023

Chertova, M.V., Spakman, W., Geenen, T., van den Berg, A.P., van Hinsbergen, D.J.J., 2014. Underpinning tectonic reconstructions of the western Mediterranean region with dynamic slab evolution from 3-D numerical modeling: western Mediterranean slab evolution. J. Geophys. Res. Solid Earth 119, 5876–5902. https://doi.org/10.1002/2014JB011150

Chumakov, I.S., 1973. Pliocene and Pleistocene deposits of the Nile Valley in Nubia and Upper Egypt, in: Ryan, W.B.F., Hsü, K.J. (Eds.), Initial Reports of the Deep Sea Drilling Project, 13. . U.S. Gov. Print. Off., Washington, DC, pp. 1242–1243.

Chumakov, I.S., 1967. Pliocene and Pleistocene deposits of the Nile Valley: Nubia and Upper Egypt (In Russian). Acad. Sci. USSR Trans. Geol. Inst. 170.

CIESM, 2008. The Messinian Salinity Crisis from mega-deposits to microbiology - A consensus report, CIESM Workshop Monographs, CIESM Workshop Monographs.

Clauzon, G., 1982. Le canyon messinien du Rhone; une preuve decive du “desiccated deep-basin model” (Hsue, Cita and Ryan, 1973). Bull. Société Géologique Fr. S7-XXIV, 597–610. https://doi.org/10.2113/gssgfbull.S7-XXIV.3.597

Clauzon, G., 1978. The Messinian Var canyon (Provence, southern France) — Paleogeographic implications. Mar. Geol., Messinian erosional surfaces in the Mediterranean 27, 231–246. https://doi.org/10.1016/0025-3227(78)90033-6

Clauzon, G., 1973. The eustatic hypothesis and the pre-Pliocene cutting of the Rhone valley. Initial Rep. Deep Sea Drill. Proj. 13, Part 2, 1251–1256.

Clauzon, G., Suc, J.P., Couto, D.D., Jouannic, G., Melinte-Dobrinescu, M.C., Jolivet, L., Quillévéré, F., Lebret, N., Mocochain, L., Popescu, S.M., Martinell, J., Doménech, R., Rubino, J.L., Gumiaux, C., Warny, S., Bellas, S.M., Gorini, C., Bache, F., Rabineau, M., Estrada, F., 2015. New insights on the Sorbas Basin (SE Spain): The onshore reference of the Messinian Salinity Crisis. Mar. Pet. Geol. 66, 71–100. https://doi.org/10.1016/j.marpetgeo.2015.02.016

Clauzon, G., Suc, J.P., Gautier, F., Berger, A., Loutre, M.F., 1996. Alternate interpretation of the Messinian salinity crisis: Controversy resolved? Geology 24, 363–366. https://doi.org/10.1130/0091-7613(1996)024<0363:AIOTMS>2.3.CO;2

Cloetingh, S., Burov, E.B., 1996. Thermomechanical structure of European continental lithosphere: Constraints from rheological profiles and EET estimates. Geophys. J. Int. 124, 695–723. https://doi.org/10.1111/j.1365-246X.1996.tb05633.x

Comas, M.C., Platt, J.P., Soto, J.I., Watts, A.B., 1999. The origin and tectonic history of the Alboran Basin: insights from leg 161 results, in: Proceedings of the Ocean Drilling Program, 161 Scientific Results, Proceedings of the Ocean Drilling Program. Ocean Drilling Program. https://doi.org/10.2973/odp.proc.sr.161.1999

Comas, M.C., Zahn, R., Klaus, A., et al. (Eds.), 1996. Proceedings of the Ocean Drilling Program, 161 Initial Reports, Proceedings of the Ocean Drilling Program. Ocean Drilling Program. https://doi.org/10.2973/odp.proc.ir.161.1996

Comas, M C, Zahn, R., Klaus, A., Mascle, J., Lohmann, G.P., Clift, P.D., 1996. Proceedings of the Ocean Drilling

Program, Initial Reports, Proceedings of the Ocean Drilling Program, Initial Reports. Ocean Drilling Program. https://doi.org/10.2973/odp.proc.ir.159.1996

Conesa, G., Badinot, J.F., 1999. Early Messinian carbonate platforms from Sorbas Basin (SE Spain): sedimentary setting, microfaunas and palaeoenvironments. Rev. Micropaléontologie 42, 255–267.

Corbí, H., Peral, J.J., Pérez-Valera, F., Soria, J.M., Tent-Manclús, J.E., 2017. Late Miocene vertical movements in the Sierra Nevada and Granada Basin linking zone (Betic Cordillera, Spain): insights from marine microfossils. J. Iber. Geol. 43, 615–630. https://doi.org/10.1007/s41513-017-0042-2

Cornée, J.J., Saint Martin, J.P., Conesa, G., Münch, P., André, J.P., Saint Martin, S., Roger, S., 2004. Correlations and sequence stratigraphic model for Messinian carbonate platforms of the western and central Mediterranean. Int. J. Earth Sci. 93, 621–633. https://doi.org/10.1007/s00531-004-0400-0

Costanzo, A., Cipriani, M., Feely, M., Cianflone, G., Dominici, R., 2019. Messinian twinned selenite from the Catanzaro Trough, Calabria, Southern Italy: field, petrographic and fluid inclusion perspectives. Carbonates Evaporites 34, 743–756. https://doi.org/10.1007/s13146-019-00516-0

Coulson, S., Pico, T., Austermann, J., Powell, E., Moucha, R., Mitrovica, J.X., 2019. The role of isostatic adjustment and gravitational effects on the dynamics of the Messinian salinity crisis. Earth Planet. Sci. Lett. 525, 115760–115760. https://doi.org/10.1016/j.epsl.2019.115760

Dabrio, C.J., Polo Camacho, M.D., 1995. Oscilaciones eustáticas de alta frecuencia en el Neógeno superior de Sorbas (Almería, sureste de España). GeoActa 18, 75–78.

Dal Cin, M., Del Ben, A., Mocnik, A., Accaino, F., Geletti, R., Wardell, N., Zgur, F., Camerlenghi, A., 2016. Seismic imaging of Late Miocene (Messinian) evaporites from Western Mediterranean back-arc basins. Pet. Geosci. 22, 297–308. https://doi.org/10.1144/petgeo2015-096

Dannowski, A., Kopp, H., Grevemeyer, I., Lange, D., Thorwart, M., Bialas, J., Wollatz-Vogt, M., 2020. Seismic evidence for failed rifting in the Ligurian Basin, Western Alpine domain. Solid Earth 11, 873–887. https://doi.org/10.5194/se-11-873-2020

De Lange, G.J., Boelrijk, N.A.I.M., Catalano, G., Corselli, C., Klinkhammer, G.P., Middelburg, J.J., Müller, D.W., Ullman, W.J., Van Gaans, P., Woittiez, J.R.W., 1990. Sulphate-related equilibria in the hypersaline brines of the Tyro and Bannock Basins, eastern Mediterranean. Mar. Chem., Anoxic Brines of the Mediterranean Sea 31, 89–112. https://doi.org/10.1016/0304-4203(90)90032-8

de Lange, G.J., Krijgsman, W., 2010. Messinian salinity crisis: A novel unifying shallow gypsum/deep dolomite formation mechanism. Mar. Geol. 275, 273–277. https://doi.org/10.1016/j.margeo.2010.05.003

Decima, A., Wezel, F., 1973. Late Miocene Evaporites of the Central Sicilian Basin, Italy. https://doi.org/10.2973/DSDP.PROC.13.144-1.1973

Decima, A., Wezel, F.C., 1967. Late Miocene Evaporites of the Central Sicilian Basin , Italy, Deep Sea Drilling Project Initial Reports Volume 13.

del Olmo, W.M., 2011. The Messinian in the Gulf of Valencia and Alboran Sea (Spain): paleogeography and paleoceanography implications. Rev. Soc. Geológica Esp. 24, 22.

Dela Pierre, F., Bernardi, E., Cavagna, S., Clari, P., Gennari, R., Irace, A., Lozar, F., Lugli, S., Manzi, V., Natalicchio, M., 2011. The record of the Messinian salinity crisis in the Tertiary Piedmont Basin (NW Italy): the Alba section revisited. Palaeogeogr. Palaeoclimatol. Palaeoecol. 310, 238–255.

Denizot, G., 1952. Le Pliocène dans la vallée du Rhône. Géocarrefour 27, 327–357.

Dewey, J.F., Helman, M.L., Knott, S.D., Turco, E., Hutton, D.H.W., 1989. Kinematics of the western Mediterranean. Geol. Soc. Lond. Spec. Publ. 45, 265–283. https://doi.org/10.1144/GSL.SP.1989.045.01.15

Diaz, J., Torne, M., Vergés, J., Jiménez-Munt, I., Martí, J., Carbonell, R., Schimmel, M., Geyer, A., Ruiz, M., García-Castellanos, D., Alvarez-Marrón, J., Brown, D., Villaseñor, A., Ayala, C., Palomeras, I., Fernandez, M., Gallart, J., 2021. Four decades of geophysical research on Iberia and adjacent margins. Earth-Sci. Rev. 222, 103841. https://doi.org/10.1016/j.earscirev.2021.103841

Do Couto, D., Gorini, C., Jolivet, L., Lebret, N., Augier, R., Gumiaux, C., d'Acremont, E., Ammar, A., Jabour, H., Auxietre, J.-L., 2016. Tectonic and stratigraphic evolution of the Western Alboran Sea Basin in the last 25 Myrs. Tectonophysics 677–678, 280–311. https://doi.org/10.1016/j.tecto.2016.03.020

Do Couto, D., Gumiaux, C., Jolivet, L., Augier, R., Lebret, N., Folcher, N., Jouannic, G., Suc, J.P., Gorini, C., 2015. 3D modelling of the Sorbas Basin (Spain): New constraints on the Messinian Erosional Surface morphology. Mar. Pet. Geol. 66. https://doi.org/10.1016/j.marpetgeo.2014.12.011

Docherty, J.I.C., Banda, E., 1992. A note on the subsidence history of the northern margin of the Alboran Basin. Geo-Mar. Lett. 12, 82–87. https://doi.org/10.1007/BF02084916

Driussi, O., Briais, A., Maillard, A., 2015a. Evidence for transform motion along the South Balearic margin and implications for the kinematics of opening of the Algerian basin. Bull. Société Géologique Fr. 186, 353–370. https://doi.org/10.2113/gssgfbull.186.4-5.353

Driussi, O., Maillard, A., Ochoa, D., Lofi, J., Chanier, F., Gaullier, V., Briais, A., Sage, F., Sierro, F., Garcia, M., 2015b. Messinian Salinity Crisis deposits widespread over the Balearic Promontory: Insights from new high-resolution seismic data. Mar. Pet. Geol. 66, 41–54. https://doi.org/10.1016/j.marpetgeo.2014.09.008

Dronkert, H., 1985. Evaporite Models and Sedimentology of Messinian and Recent Evaporites, GUA papers of geology. Series 1.

Dronkert, H., 1976. Late miocene evaporites in the Sorbas Basin and adjoining areas. MemSocGeol It 16, 341–361.

Druckman, Y., Buchbinder, B., Martinotti, G.M., Tov, R.S., Aharon, P., 1995. The buried Afiq Canyon (eastern Mediterranean, Israel): a case study of a Tertiary submarine canyon exposed in Late Messinian times. Mar. Geol. 123, 167–185. https://doi.org/10.1016/0025-3227(94)00127-7

Duggen, S., Hoernle, K., Klügel, A., Geldmacher, J., Thirlwall, M., Hauff, F., Lowry, D., Oates, N., 2008. Geochemical zonation of the Miocene Alborán Basin volcanism (westernmost Mediterranean): geodynamic implications. Contrib. Mineral. Petrol. 156, 577–593. https://doi.org/10.1007/s00410-008-0302-4

Duggen, S., Hoernle, K., van den Bogaard, P., Harris, C., 2004. Magmatic evolution of the Alboran region: The role of subduction in forming the western Mediterranean and causing the Messinian Salinity Crisis. Earth Planet. Sci. Lett. 218, 91–108. https://doi.org/10.1016/S0012-821X(03)00632-0

Dumitru, O.A., Austermann, J., Polyak, V.J., Fornós, J.J., Asmerom, Y., Ginés, J., Ginés, A., Onac, B.P., 2021. Sea-level stands from the Western Mediterranean over the past 6.5 million years. Sci. Rep. 1–10. https://doi.org/10.1038/s41598-020-80025-6

Dumitru, O.A., Austermann, J., Polyak, V.J., Fornós, J.J., Asmerom, Y., Ginés, J., Ginés, A., Onac, B.P., 2019. Constraints on global mean sea level during Pliocene warmth. Nature 574, 233–236. https://doi.org/10.1038/s41586-019-1543-2

Escutia, C., Maldonado, A., 1992. Palaeogeographic implications of the Messinian surface in the Valencia trough, northwestern Mediterranean Sea. Tectonophysics 203, 263–284. https://doi.org/10.1016/0040-1951(92)90227-W

Esteban, M., Braga, J.C., Martín, J.M., Santisteban, C., 1996. Western Mediterranean reef complexes., in: Models for Carbonate Stratigraphy from Miocene Reef Complexes of Mediterranean Regions, Concepts in Sedimentology and Paleontology. SEPM, Tulsa, OK, pp. 55–72.

Estrada, F., Ercilla, G., Gorini, C., Alonso, B., Vázquez, J.T., García-Castellanos, D., Juan, C., Maldonado, A., Ammar, A., Elabbassi, M., 2011. Impact of pulsed Atlantic water inflow into the Alboran Basin at the time of the Zanclean flooding. Geo-Mar. Lett. 31, 361–376. https://doi.org/10.1007/s00367-011-0249-8

Estrada, F., Galindo-Zaldívar, J., Vázquez, J.T., Ercilla, G., D'Acremont, E., Alonso, B., Gorini, C., 2018. Tectonic indentation in the central Alboran Sea (westernmost Mediterranean). Terra Nova 30, 24–33. https://doi.org/10.1111/ter.12304

Estrany, J., Garcia, C., Walling, D., Ferrer, L., 2011. Fluxes and storage of fine-grained sediment and associated contaminants in the Na Borges River (Mallorca, Spain). Catena 87, 291–305. https://doi.org/10.1016/j.catena.2011.06.009

Etheve, N., Mohn, G., Frizon de Lamotte, D., Roca, E., Tugend, J., Gómez-Romeu, J., 2018. Extreme Mesozoic Crustal Thinning in the Eastern Iberia Margin: The Example of the Columbrets Basin (Valencia Trough). Tectonics 37, 636–662. https://doi.org/10.1002/2017TC004613

Faccenna, C., Becker, T.W., 2020. Topographic expressions of mantle dynamics in the Mediterranean. Earth-Sci. Rev. 209, 103327. https://doi.org/10.1016/j.earscirev.2020.103327

Faccenna, C., Becker, T.W., Auer, L., Billi, A., Boschi, L., Brun, J.P., Capitanio, F.A., Funiciello, F., Horvàth, F., Jolivet, L., Piromallo, C., Royden, L., Rossetti, F., Serpelloni, E., 2014. Mantle dynamics in the Mediterranean. Rev. Geophys. 52, 283–332. https://doi.org/10.1002/2013RG000444

Faccenna, C., Glišović, P., Forte, A., Becker, T.W., Garzanti, E., Sembroni, A., Gvirtzman, Z., 2019. Role of dynamic topography in sustaining the Nile River over 30 million years. Nat. Geosci. 12, 1012–1017. https://doi.org/10.1038/s41561-019-0472-x

Faccenna, C., Piromallo, C., Crespo-Blanc, A., Jolivet, L., Rossetti, F., 2004. Lateral slab deformation and the origin of the western Mediterranean arcs. Tectonics 23. https://doi.org/10.1029/2002TC001488

Flecker, R., 2018. Investigating Miocene Mediterranean-Atlantic Exchange Africa, Morocco, Europe, Spain. ICDP Int. Cont. Sci. Drill. Program.

Flecker, R., Krijgsman, W., Capella, W., de Castro Martíns, C., Dmitrieva, E., Mayser, J.P., Marzocchi, A., Modestu, S., Ochoa, D., Simon, D., Tulbure, M.A., van den Berg, B., van der Schee, M., de Lange, G., Ellam, R., Govers, R., Gutjahr, M., Hilgen, F., Kouwenhoven, T., Lofi, J., Meijer, P., Sierro, F.J., Bachiri, N., Barhoun, N., Alami, A.C., Chacon, B., Flores, J.A., Gregory, J., Howard, J., Lunt, D., Ochoa, M., Pancost, R., Vincent, S.J., Yousfi, M.Z., 2015. Evolution of the Late Miocene Mediterranean-Atlantic gateways and their impact on regional and global environmental change. Earth-Sci. Rev. 150, 365–392. https://doi.org/10.1016/j.earscirev.2015.08.007

Fortuin, A.R., Krijgsman, W., Hilgen, F.J., Sierro, F.J., 2000. Late Miocene Mediterranean desiccation: topography and significance of the 'Salinity Crisis' erosion surface on-land in southeast Spain: Comment. Sediment. Geol. 133, 167–174. https://doi.org/10.1016/S0037-0738(00)00040-3

Frumkin, A., 1994. Hydrology and denudation rates of halite karst. J. Hydrol. 162, 171–189. https://doi.org/10.1016/0022-1694(94)90010-8

Galdeano, A., Rossignol, J.C., 1977. Contribution de l'aeromagnetisme a l'etude du golfe de Valence (Mediterranee occidentale). Earth Planet. Sci. Lett. 34, 85–99. https://doi.org/10.1016/0012-821X(77)90109-1

Gallart, J., Vidal, N., Estévez, A., Pous, J., Sàbat, F., Santisteban, C., Surinach, E., Group, E.V.T., 1995. The ESCI-València Troug Vertical reflection Experiment: a Seismic Image of the Crust from the NE Iberian Peninsula to the Western Mediterranean. Rev. Soc. Geol. Espana 8 (4), 401–415.

Garcia, C., Amengual, A., Homar, V., Zamora, A., 2017. Losing water in temporary streams on a Mediterranean island: Effects of climate and land-cover changes. Glob. Planet. Change 148, 139–152. https://doi.org/10.1016/j.gloplacha.2016.11.010

Garcia-Castellanos, D., 2002. Interplay between lithospheric flexure and river transport in foreland basins: Lithospheric flexure and fluvial transport. Basin Res. 14, 89–104. https://doi.org/10.1046/j.1365-2117.2002.00174.x

Garcia-Castellanos, D., D., Estrada, F., F., Jiménez-Munt, I., I., Gorini, C., Fernandez, M., Vergés, J., Vicente, D., R., 2009a. Catastrophic flood of the Mediterranean after the Messinian salinity crisis. Nature 462, 778–782.

Garcia-Castellanos, D., Fernández, M., Torne, M., 2002. Modeling the evolution of the Guadalquivir foreland basin (southern Spain). Tectonics 21. https://doi.org/10.1029/2001TC001339

Garcia-Castellanos, D., Fernàndez, M., Torne, M., 1997. Numerical modeling of foreland basin formation: A program relating thrusting, flexure, sediment geometry and lithospehre rheology. Comput. Geosci. 23, 993–1003. https://doi.org/10.1016/S0098-3004(97)00057-5

Garcia-Castellanos, D., Jiménez-Munt, I., 2015. Topographic evolution and climate aridification during continental collision: Insights from computer simulations. PLoS ONE 10, 1–32. https://doi.org/10.1371/journal.pone.0132252

Garcia-Castellanos, D., Micallef, A., Estrada, F., Camerlenghi, A., Ercilla, G., Periáñez, R., Abril, J.M., 2020. The Zanclean megaflood of the Mediterranean – Searching for independent evidence. Earth-Sci. Rev. 201, 103061–103061. https://doi.org/10.1016/j.earscirev.2019.103061

Garcia-Castellanos, D., Vergés, J., Gaspar-Escribano, J., Cloetingh, S., 2003. Interplay between tectonics, climate, and fluvial transport during the Cenozoic evolution of the Ebro Basin (NE Iberia). J. Geophys. Res. Solid Earth 108. https://doi.org/10.1029/2002JB002073

Garcia-Castellanos, D., Villaseñor, A., 2011. Messinian salinity crisis regulated by competing tectonics and erosion at the Gibraltar arc. Nature 480, 359–363. https://doi.org/10.1038/nature10651

García-Dueñas, V., Balanyá, J.C., Martínez-Martínez, J.M., 1992. Miocene extensional detachments in the outcropping basement of the northern Alboran Basin (Betics) and their tectonic implications. Geo-Mar. Lett. 12, 88–95. https://doi.org/10.1007/BF02084917

Garcia-Veigas, F.J., Ortí, F., Rosell, L., Ayora, C., Rouchy, J.M., Lugli, S., 1995. The Messinian salt of the Mediterranean: geochemical study of the salt fromthe Central Sicily Basin and comparison with the Lorca Basin (Spain). Bull. Soc. Geol. Fr. 166, 699–710.

García-Veigas, J., Cendón, D.I., Gibert, L., Lowenstein, T.K., Artiaga, D., 2018. Geochemical indicators in Western Mediterranean Messinian evaporites:

Implications for the salinity crisis. Mar. Geol. 403, 197–214. https://doi.org/10.1016/j.margeo.2018.06.005

Gargani, J., 2004. Modelling of the erosion in the Rhone valley during the Messinian crisis (France). Quat. Int. 121, 13–22. https://doi.org/10.1016/j.quaint.2004.01.020

Gargani, J., Rigollet, C., 2007. Mediterranean Sea level variations during the Messinian salinity crisis. Geophys. Res. Lett. 34, 0–4. https://doi.org/10.1029/2007GL029885

Gargani, J., Rigollet, C., Scarselli, S., 2010. Isostatic response and geomorphological evolution of the Nile valley during the Messinian salinity crisis. Bull. Soc. Geol. Fr. 181, 19–26. https://doi.org/10.2113/gssgfbull.181.1.19

Gaspar-Escribano, J.M., Garcia-Castellanos, D., Roca, E., Cloetingh, S., 2004. Cenozoic vertical motions of the Catalan Coastal Ranges (NE Spain): The role of tectonics, isostasy, and surface transport: VERTICAL MOTIONS CCR (NE SPAIN). Tectonics 23, n/a-n/a. https://doi.org/10.1029/2003TC001511

Gaullier, V., Loncke, L., Vendeville, B.C., Deverchere, J., Droz, L., Obone Zeu Obame, E.M., Mascle, J., 2008. Salt Tectonics in the deep Mediterranean: indirect clues for understanding the Messinian Salinity Crisis. in: The Messian Salinity Crisis from mega-deposits to microbiology - a consensus report.

Gelabert, B., Sàbat, F., Rodríguez-Perea, A., 2002. A new proposal for the late Cenozoic geodynamic evolution of the western Mediterranean. Terra Nova 14, 93–100. https://doi.org/10.1046/j.1365-3121.2002.00392.x

Ghielmi, M., Minervini, M., Nini, C., Rogledi, S., Rossi, M., Vignolo, A., 2010. Sedimentary and tectonic evolution in the eastern Po-Plain and northern Adriatic Sea area from Messinian to Middle Pleistocene (Italy). RENDICONTI LINCEI 21, 131–166. https://doi.org/10.1007/s12210-010-0101-5

Ghielmi, M., Minervini, M., Nini, C., Rogledi, S., Rossi, M.E., 2013. Late Miocene-Middle Pleistocene sequences in the Po Plain - Northern Adriatic Sea (Italy): The stratigraphic record of modification phases affecting a complex foreland basin. Mar. Pet. Geol. 42, 50–81. https://doi.org/10.1016/j.marpetgeo.2012.11.007

Gibert, L., Scott, G.R., Montoya, P., Ruiz-Sánchez, F.J., Morales, J., Luque, L., Abella, J., Lería, M., 2013. Evidence for an African-Iberian mammal dispersal during the pre-evaporitic Messinian. Geology 41, 691–694. https://doi.org/10.1130/G34164.1

Gladstone, R., Flecker, R., Valdes, P., Lunt, D., Markwick, P., 2007. The Mediterranean hydrologic budget from a Late Miocene global climate simulation. Palaeogeogr. Palaeoclimatol. Palaeoecol. 251, 254–267. https://doi.org/10.1016/j.palaeo.2007.03.050

Gómez de la Peña, L., R. Ranero, C., Gràcia, E., Booth-Rea, G., 2021. The evolution of the westernmost Mediterranean basins. Earth-Sci. Rev. 214, 103445. https://doi.org/10.1016/j.earscirev.2020.103445

Gómez de la Peña, L., R. Ranero, C., Gràcia, E., Booth-Rea, G., Azañón, J.M., Tinivella, U., Yelles-Chaouche, A., 2022. Evidence for a developing plate boundary in the western Mediterranean. Nat. Commun. 13, 4786. https://doi.org/10.1038/s41467-022-31895-z

Gómez de la Peña, L., Ranero, C.R., Gràcia, E., 2018. The Crustal Domains of the Alboran Basin (Western Mediterranean). Tectonics 37, 3352–3377. https://doi.org/10.1029/2017TC004946

Gorini, C., Montadert, L., Rabineau, M., 2015. New imaging of the salinity crisis: Dual Messinian lowstand megasequences recorded in the deep basin of both the eastern and western Mediterranean. Mar. Pet. Geol. 66, 278–294. https://doi.org/10.1016/j.marpetgeo.2015.01.009

Govers, R., 2009. Choking the Mediterranean to dehydration: The Messinian salinity crisis. Geology 37, 167–170. https://doi.org/10.1130/G25141A.1

Govers, R., Meijer, P., Krijgsman, W., 2009. Regional isostatic response to Messinian Salinity Crisis events. Tectonophysics 463, 109–129. https://doi.org/10.1016/j.tecto.2008.09.026

Govers, R., Wortel, M.J.R., 1995. Extension of stable continental lithosphere and the initiation of lithospheric scale faults. Tectonics 14, 1041–1055. https://doi.org/10.1029/95TC00500

Granot, R., 2016. Palaeozoic oceanic crust preserved beneath the eastern Mediterranean. Nat. Geosci. 9, 701–705. https://doi.org/10.1038/ngeo2784

Grevemeyer, I., Gràcia, E., Villaseñor, A., Leuchters, W., Watts, A.B., 2015. Seismicity and active tectonics in the Alboran Sea, Western Mediterranean: Constraints from an offshore-onshore seismological network and swath bathymetry data. J. Geophys. Res. Solid Earth 120, 8348–8365. https://doi.org/10.1002/2015JB012073

Gueguen, E., Doglioni, C., Fernandez, M., 1998. On the post-25 Ma geodynamic evolution of the western Mediterranean. Tectonophysics 298, 259–269. https://doi.org/10.1016/S0040-1951(98)00189-9

Guerra-Merchán, A., Serrano, F., Hlila, R., El Kadiri, K., Sanz de Galdeano, C., Garcés, M., 2014. Tectono-sedimentary evolution of the peripheral basins of the Alboran Sea in the arc of Gibraltar during the latest Messinian-Pliocene. J. Geodyn. 77, 158–170. https://doi.org/10.1016/j.jog.2013.12.003

Guibourdenche, L., Cartigny, P., Dela Pierre, F., Natalicchio, M., Aloisi, G., 2022. Cryptic sulfur cycling during the formation of giant gypsum deposits. Earth Planet. Sci. Lett. 593, 117676. https://doi.org/10.1016/j.epsl.2022.117676

Gvirtzman, Z., Manzi, V., Calvo, R., Gavrieli, I., Gennari, R., Lugli, S., Reghizzi, M., Roveri, M., 2017. Intra-Messinian truncation surface in the Levant Basin explained by subaqueous dissolution. Geology 45. https://doi.org/10.1130/G39113.1

Haq, B., Gorini, C., Baur, J., Moneron, J., Rubino, J.L., 2020. Deep Mediterranean's Messinian evaporite giant: How much salt? Glob. Planet. Change 184, 103052–103052. https://doi.org/10.1016/j.gloplacha.2019.103052

Hardie, L.A., Lowenstein, T.K., 2004. Did the Mediterranean Sea Dry Out During the Miocene? A Reassessment of the Evaporite Evidence from DSDP Legs 13 and 42A Cores. J. Sediment. Res. 74, 453–461. https://doi.org/10.1306/112003740453

Hassan, M.Y., Issawi, B., Zaghloul, E.A., 1978. Geology of the area east of Beni Suef, eastern Desert, Egypt. Ann Geol Surv Egypt 8, 129–126.

Haviv, I., Enzel, Y., Whipple, K.X., Zilberman, E., Matmon, A., Stone, J., Fifield, K.L., 2010. Evolution of vertical knickpoints (waterfalls) with resistant caprock: Insights from numerical modeling. J. Geophys. Res. 115, F03028. https://doi.org/10.1029/2008JF001187

Hayford, J.F., 1909. Geodesy: The Figure of the Earth and Isostasy from Measurements in the United States. Government Printing Office, Washingtom, D.C.

Heida, H., Garcia-Castellanos, D., Jiménez-Munt, I., Estrada, F., Ercilla, G., Do Couto, D., Ammar, A., Submitted. Paleotopography, sea level drop and erosion in the Alboran Basin during the Messinian Salinity Crisis from a flexural-isostatic reconstruction.

Heida, H., Raad, F., Garcia-Castellanos, D., Jiménez-Munt, I., Maillard, A., Lofi, J., 2021a. Flexural-isostatic reconstruction of the Western Mediterranean during the Messinian Salinity Crisis: Implications for water level and basin connectivity. Basin Res. bre.12610. https://doi.org/10.1111/bre.12610

Hersey, J.B., 1965. Sedimentary basins of the Mediterranean Sea., in: Submarine Geology and Geophysics. S Butterworths London., pp. 75–91.

Howard, A.D., Dietrich, W.E., Seidl, M.A., 1994. Modeling fluvial erosion on regional to continental scales. J. Geophys. Res. Solid Earth 99, 13971–13986. https://doi.org/10.1029/94JB00744

Hsü, K.J., 1983. The Mediterranean was a desert. Princeton University Press, Princeton, New Jersey.

Hsü, K.J., 1973. The desiccated deep-basin model for the Messinian events. Drooger CW Ed Messin. Events Mediterr. N.-Holl. Publ Co Amst. 60–67.

Hsü, K.J., Cita, M.B., Ryan, W.B.F., 1971. 43 . The origin of the Mediterranean evaporites. Initial Rep. Deep Sea Drill. Program xxx, 1203–1231.

Hsü, K.J., Ryan, W.B.F., Cita, M.B., 1973. Late Miocene dessication of the Mediterranean. Nature 242, 240–244.

Jiménez-Munt, I., Torne, M., Fernàndez, M., Vergés, J., Kumar, A., Carballo, A., García-Castellanos, D., 2019. Deep Seated Density Anomalies Across the Iberia-Africa Plate Boundary and Its Topographic Response. J. Geophys. Res. Solid Earth 124, 13310–13332. https://doi.org/10.1029/2019JB018445

Jolivet, L., Augier, R., Robin, C., Suc, J.P., Rouchy, J.M., 2006. Lithospheric-scale geodynamic context of the Messinian salinity crisis. Sediment. Geol. 188–189, 9–33. https://doi.org/10.1016/j.sedgeo.2006.02.004

Jolivet, L., Menant, A., Roche, V., Le Pourhiet, L., Maillard, A., Augier, R., Do Couto, D., Gorini, C., Thinon, I., Canva, A., 2021. Transfer zones in Mediterranean back-arc regions and tear faults. BSGF - Earth Sci. Bull. 192, 11. https://doi.org/10.1051/bsgf/2021006

Just, J., Hübscher, C., Betzler, C., Lüdmann, T., Reicherter, K., 2011. Erosion of continental margins in the Western Mediterranean due to sea-level stagnancy during the Messinian Salinity Crisis. Geo-Mar. Lett. 31, 51–64. https://doi.org/10.1007/s00367-010-0213-z

Kaban, M.K., Chen, B., Tesauro, M., Petrunin, A.G., El Khrepy, S., Al-Arifi, N., 2018. Reconsidering Effective Elastic Thickness Estimates by Incorporating the Effect of Sediments: A Case Study for Europe. Geophys. Res. Lett. 45, 9523–9532. https://doi.org/10.1029/2018GL079732

Kellner, A., Brink, G.J., El Khawaga, H., 2018. Depositional history of the western Nile Delta, Egypt: Late Rupelian to Pleistocene. AAPG Bull. 102, 1841–1865. https://doi.org/10.1306/02161817234

Knudsen, M., 1900. Ein hydrographischer lehrsatz. Ann. Hydrogr. Marit. Meteorol. 28, 316–320.

Kozary, M.T., Dunlap, J.C., Humphrey, W.E., 1968. Incidence of saline deposits in geologic time. Geol. Soc. Am. Spec. Pap. 88, 43–57.

Krijgsman, W., Capella, W., Simon, D., Hilgen, F.J., Kouwenhoven, T.J., Meijer, P.Th., Sierro, F.J., Tulbure, M.A., van den Berg, B.C.J., van der Schee, M., Flecker, R., 2018. The Gibraltar Corridor: Watergate of the Messinian Salinity Crisis. Mar. Geol. 403, 238–246. https://doi.org/10.1016/j.margeo.2018.06.008

Krijgsman, W., Fortuin, A.R., Hilgen, F.J., Sierro, F.J., 2001. Astrochronology for the Messinian Sorbas basin (SE Spain) and orbital (precessional) forcing for evaporite cyclicity. Sediment. Geol. 140, 43–60. https://doi.org/10.1016/S0037-0738(00)00171-8

Krijgsman, W, Hilgen, F.J., Raffi, I., Sierro, F.J., Wilson, D.S., 1999. Chronology, causes and progession of the Messinian salinity crisis. Nature 400, 652–655.

Krijgsman, W., Meijer, P.T., 2008. Depositional environments of the Mediterranean "Lower Evaporites" of the Messinian salinity crisis: Constraints from quantitative analyses. Mar. Geol. 253,73–81. https://doi.org/10.1016/j.margeo.2008.04.010

Krijgsman, W., Stoica, M., Vasiliev, I., Popov, V.V., 2010. Rise and fall of the Paratethys Sea during the Messinian Salinity Crisis. Earth Planet. Sci. Lett. 290, 183–191. https://doi.org/10.1016/j.epsl.2009.12.020

Krijgsman, W., Vasiliev, I., Beniest, A., Lyons, T., Lofi, J., Tari, G., Slomp, C. P., Cagatay, N., Triantaphyllou, M., Flecker, R., Palcu, D. V., McHugh, C., Artz, H., Henry, P., Lloyd, K., Citci G., Sipahioglu, Ö., & Sakelariou, D. (2022) Mediterranean-Black Sea gateway exchange: Scientirfic drilling workshop on the BlackGate project. Scientific Drilling

Kumar, A., Fernàndez, M., Vergés, J., Torne, M., Jiménez-Munt, I., 2021. Opposite Symmetry in the Lithospheric Structure of the Alboran and Algerian Basins and Their Margins (Western Mediterranean): Geodynamic Implications. J. Geophys. Res. Solid Earth 126. https://doi.org/10.1029/2020JB021388

La Violette, P.E., 1994. Seasonal and Interannual Variability of the Western Mediterranean Sea. American Geophysical Union.

Lachenbruch, A.H., Morgan, P., 1990. Continental extension, magmatism and elevation; formal relations and rules of thumb. Tectonophysics 174, 39–62. https://doi.org/10.1016/0040-1951(90)90383-J

Lacombe, H., Richez, C., 1982. The Regime of the Strait of Gibraltar, in: Nihoul, J.C.J. (Ed.), Elsevier Oceanography Series, Hydrodynamics of Semi-Enclosed Seas. Elsevier, pp. 13–73. https://doi.org/10.1016/S0422-9894(08)71237-6

Leeder, M.R., 2009. Sedimentology and Sedimentary Basins: From Turbulence to Tectonics. John Wiley & Sons.

Leila, M., Moscariello, A., 2019. Seismic stratigraphy and sedimentary facies analysis of the pre- and syn-Messinain salinity crisis sequences, onshore Nile Delta, Egypt: Implications for reservoir quality prediction. Mar. Pet. Geol. 101, 303–321. https://doi.org/10.1016/j.marpetgeo.2018.12.003

Lensky, N.G., Dvorkin, Y., Lyakhovsky, V., Gertman, I., Gavrieli, I., 2005. Water, salt, and energy balances of the Dead Sea. Water Resour. Res. 41. https://doi.org/10.1029/2005WR004084

Leprêtre, A., Klingelhoefer, F., Graindorge, D., Schnurle, P., Beslier, M.O., Yelles, K., Déverchère, J., Bracene, R., 2013. Multiphased tectonic evolution of the Central Algerian margin from combined wide-angle and reflection seismic data off Tipaza, Algeria. J. Geophys. Res. Solid Earth 118, 3899–3916. https://doi.org/10.1002/jgrb.50318

Leroux, E., Aslanian, D., Rabineau, M., 2019. Atlas of the stratigraphic markers in the Western Mediterranean with focus on the Messinian, Pliocene and Pleistocene of the Gulf of Lion. Commission de la carte géologique du monde.

Liang, X., Spall, M., Wunsch, C., 2017. Global Ocean Vertical Velocity From a Dynamically Consistent Ocean State Estimate. J. Geophys. Res. Oceans 122, 8208–8224. https://doi.org/10.1002/2017JC012985

Little, O.H., 1936. Recent geological work in the Faiyum and in the adjoining portion of the Nile Valley. Inst. Français d'Archéologie Orientale.

Liu, J.T., Hsu, R.T., Hung, J.-J., Chang, Y.-P., Wang, Y.-H., Rendle-Bühring, R.H., Lee, C.-L., Huh, C.-A., Yang, R.J., 2016. From the highest to the deepest: The Gaoping River–Gaoping Submarine Canyon dispersal system. Earth-Sci. Rev. 153, 274–300. https://doi.org/10.1016/j.earscirev.2015.10.012

Lofi, J., 2018. Seismic Atlas of the Messinian Salinity Crisis markers in the Mediterranean Sea - Volume 2. CGMW and Mémoires de la Société Géologie de France.

Lofi, J., Camerlenghi, A., Aloisi, G., Maillard, A., Garcia-Castellanos, D., Huebscher, C., Kuroda, J., 2017. The" DREAM" IODP project to drill the Mediterranean Salt Giant on the Balearic Promontory. EGU Gen. Assem. Conf. Abstr. 13670).

Lofi, J., Déverchère, J., Gaullier, V., Gillet, H., Gorini, C., Guennoc, P., Loncke, L., Maillard, A., Sage, F., Thinon, I., World, C. for the G.M. of the, 2011a. Seismic Atlas of the Messinian Salinity Crisis markers in the Mediterranean and Black Seas, Memoires de la Société Géologique de France.

Lofi, J., Gorini, C., Berné, S., Clauzon, G., Dos Reis, A.T., Ryan, W.B.F., Steckler, M.S., 2005. Erosional processes and paleo-environmental changes in the Western Gulf of Lions (SW France) during the Messinian Salinity Crisis. Mar. Geol. 217, 1–30. https://doi.org/10.1016/j.margeo.2005.02.014

Lofi, J., Sage, F., Deverchere, J., Loncke, L., Maillard, A., Gaullier, V., Thinon, I., Gillet, H., Guennoc, P., Gorini, C., 2011b. Refining our knowledge of the Messinian salinity crisis records in the offshore domain through multi-site seismic analysis. Bull. Soc. Geol. Fr. 182, 163–180. https://doi.org/10.2113/gssgfbull.182.2.163

Loget, N., Van Den Driessche, J., 2006. On the origin of the Strait of Gibraltar. Sediment. Geol. 188–189, 341–356. https://doi.org/10.1016/j.sedgeo.2006.03.012

Loget, N., Van Den Driessche, J., Davy, P., 2005. How did the Messinian Salinity Crisis end? Terra Nova 17, 414–419. https://doi.org/10.1111/j.1365-3121.2005.00627.x

Loncke, L., Gaullier, V., Mascle, J., Vendeville, B., Camera, L., 2006. The Nile deep-sea fan: An example of interacting sedimentation, salt tectonics, and inherited subsalt paleotopographic features. Mar. Pet. Geol. 23, 297–315. https://doi.org/10.1016/j.marpetgeo.2006.01.001

Lonergan, L., White, N., 1997. Origin of the Betic-Rif mountain belt. Tectonics 16, 504–522. https://doi.org/10.1029/96TC03937

Lüdmann, T., Wiggershaus, S., Betzler, C., Hübscher, C., 2012. Southwest Mallorca Island: A cool-water carbonate margin dominated by drift deposition associated with giant mass wasting. Mar. Geol. Complete, 73–87. https://doi.org/10.1016/j.margeo.2011.09.008

Lugli, S., 2009. Evaporites, in: Gornitz, V. (Ed.), Encyclopedia of Paleoclimatology and Ancient Environments, Encyclopedia of Earth Sciences Series. Springer Netherlands, Dordrecht, pp. 321–325. https://doi.org/10.1007/978-1-4020-4411-3_84

Lugli, S., Gennari, R., Gvirtzman, Z., Manzi, V., Roveri, M., Schreiber, B.C., 2013. Evidence of Clastic Evaporites In the Canyons of the Levant Basin (Israel):

Implications For the Messinian Salinity Crisis. J. Sediment. Res. 83, 942–954. https://doi.org/10.2110/jsr.2013.72

Lugli, S., Manzi, V., Roveri, M., Schreiber, B.C., 2015. The deep record of the Messinian salinity crisis: Evidence of a non-desiccated Mediterranean Sea. Palaeogeogr. Palaeoclimatol. Palaeoecol. 433, 201–218. https://doi.org/10.1016/j.palaeo.2015.05.017

Lugli, S., Manzi, V., Roveri, M., Schreiber, C.B., 2010a. The Primary Lower Gypsum in the Mediterranean: A new facies interpretation for the first stage of the Messinian salinity crisis. Palaeogeogr. Palaeoclimatol. Palaeoecol. 297, 83–99. https://doi.org/10.1016/j.palaeo.2010.07.017

Lugli, S., Schreiber, B., Triberti, B., 1999. Giant polygons in the Realmonte Mine (Agrigento, Sicily); evidence for the desiccation of a Messinian halite basin. J. Sediment. Res. 69, 764–771. https://doi.org/10.2110/jsr.69.764

Lumpkin, R., Johnson, G.C., 2013. Global ocean surface velocities from drifters: Mean, variance, El Niño–Southern Oscillation response, and seasonal cycle. J. Geophys. Res. Oceans 118, 2992–3006. https://doi.org/10.1002/jgrc.20210

Madof, A.S., Bertoni, C., Lofi, J., 2019. Discovery of vast fluvial deposits provides evidence for drawdown during the late Miocene Messinian salinity crisis. Geology 47, 171–174. https://doi.org/10.1130/G45873.1

Mahmoud, H.H., Tawfik, M.Z., 2015. Impact of the geologic setting on the groundwater using geoelectrical sounding in the area southwest of Sohag – Upper Egypt. J. Afr. Earth Sci. 104, 6–18. https://doi.org/10.1016/j.jafrearsci.2015.01.004

Maillard, A., Driussi, O., Lofi, J., Briais, A., Chanier, F., Hübscher, C., Gaullier, V., 2014. Record of the Messinian Salinity Crisis in the SW Mallorca area (Balearic Promontory, Spain). Mar. Geol. 357, 304–320. https://doi.org/10.1016/j.margeo.2014.10.001

Maillard, A., Gaullier, V., Lézin, C., Chanier, F., Odonne, F., Lofi, J., 2020a. New onshore/offshore evidence of the Messinian Erosion Surface from key areas: The Ibiza-Balearic Promontory and the Orosei-Eastern Sardinian margin. BSGF - Earth Sci. Bull. 191, 9–9. https://doi.org/10.1051/bsgf/2020007

Maillard, A., Gorini, C., Mauffret, A., Sage, F., Lofi, J., Gaullier, V., 2006. Offshore evidence of polyphase erosion in the Valencia Basin (Northwestern Mediterranean): Scenario for the Messinian Salinity Crisis. Sediment. Geol. 188–189, 69–91. https://doi.org/10.1016/j.sedgeo.2006.02.006

Maillard, A., Jolivet, L., Lofi, J., Thinon, I., Couëffé, R., Canva, A., Dofal, A., 2020b. Transfer zones and associated

volcanic province in the eastern Valencia Basin: Evidence for a hot rifted margin? Mar. Pet. Geol. 119, 104419–104419. https://doi.org/10.1016/j.marpetgeo.2020.104419

Maillard, A., Mauffret, A., 2013. Structure and present-day compression in the offshore area between alicante and ibiza island (eastern iberian margin). Tectonophysics 591, 116–130. https://doi.org/10.1016/j.tecto.2011.07.007

Maillard, A., Mauffret, A., 1999. Crustal structure and riftogenesis of the Valencia Trough (north-western Mediterranean Sea). Basin Res. 11, 357–379. https://doi.org/10.1046/j.1365-2117.1999.00105.x

Maillard, A., Mauffret, A., 1993. Structure et volcanisme de la fosse de Valence (M{é}diterran{é}e nord-occidentale). Bull Société Géologique Fr 164, 365–383.

Maillard, A., Mauffret, A., Watts, A.B., Torné, M., Pascal, G., Buhl, P., Pinet, B., 1992. Tertiary sedimentary history and structure of the Valencia trough (western Mediterranean). Tectonophysics 203, 57–75. https://doi.org/10.1016/0040-1951(92)90215-R

Maillard, A., Raad, F., Chanier, F., Heida, H., Lofi, J., Mas, G., Garcia-Castellanos, D., 2022. Plio-Quaternary strike-slip tectonics in the Central Mallorca Depression, Balearic Promontory: Land–sea correlation. Tectonophysics 829, 229295. https://doi.org/10.1016/j.tecto.2022.229295

Malinverno, A., Ryan, W.B.F., 1986. Extension in the Tyrrhenian Sea and shortening in the Apennines as result of arc migration driven by sinking of the lithosphere. Tectonics 5, 227–245.

Mancilla, F. de L., Booth-Rea, G., Stich, D., Pérez-Peña, J.V., Morales, J., Azañón, J.M., Martin, R., Giaconia, F., 2015. Slab rupture and delamination under the Betics and Rif constrained from receiver functions. Tectonophysics 663, 225–237. https://doi.org/10.1016/j.tecto.2015.06.028

Manzi, V., Gennari, R., Hilgen, F., Krijgsman, W., Lugli, S., Roveri, M., Sierro, F.J., 2013. Age refinement of the Messinian salinity crisis onset in the Mediterranean. Terra Nova 25, 315–322. https://doi.org/10.1111/ter.12038

Manzi, V., Gennari, R., Lugli, S., Persico, D., Reghizzi, M., Roveri, M., Schreiber, B.C., Calvo, R., Gavrieli, I., Gvirtzman, Z., 2018. The onset of the Messinian salinity crisis in the deep Eastern Mediterranean basin. Terra Nova 30, 189–198.

Manzi, V., Gennari, R., Lugli, S., Persico, D., Roveri, M., Gavrieli, I., Gvirtzman, Z., 2021. Synchronous onset of the Messinian salinity crisis and diachronousevaporite deposition: New evidences from the deep Eastern Mediterranean basin. Palaeogeogr. Palaeoclimatol. Palaeoecol. 584, 110685. https://doi.org/10.1016/j.palaeo.2021.110685

Manzi, V., Gennari, R., Lugli, S., ROVERI, M., Scafetta, N., Schreiber, B.C., 2012. High-Frequency Cyclicity In the Mediterranean Messinian Evaporites: Evidence For Solar–Lunar Climate Forcing. J. Sediment. Res. 82, 991–1005. https://doi.org/10.2110/jsr.2012.81

Manzi, V., Lugli, S., Lucchi, F.R., Roveri, M., 2005. Deep-water clastic evaporites deposition in the Messinian Adriatic foredeep (northern Apennines, Italy): Did the Mediterranean ever dry out? Sedimentology 52, 875–902. https://doi.org/10.1111/j.1365-3091.2005.00722.x

Manzi, V., Lugli, S., Roveri, M., Charlotte Schreiber, B., 2009. A new facies model for the Upper Gypsum of Sicily (Italy): Chronological and palaeoenvironmental constraints for the Messinian salinity crisis in the Mediterranean. Sedimentology 56, 1937–1960. https://doi.org/10.1111/j.1365-3091.2009.01063.x

Manzi, V., Lugli, S., Roveri, M., Dela Pierre, F., Gennari, R., Lozar, F., Natalicchio, M., Schreiber, B.C., Taviani, M., Turco, E., 2016. The Messinian salinity crisis in Cyprus: a further step towards a new stratigraphic framework for Eastern Mediterranean. Basin Res. 28, 207–236. https://doi.org/10.1111/bre.12107

Manzi, Vinicio, Roveri, M., Argnani, A., Cowan, D., Lugli, S., 2021. Large-scale mass-transport deposits recording the collapse of an evaporitic platform during the Messinian salinity crisis (Caltanissetta basin, Sicily). Sediment. Geol. 424, 106003. https://doi.org/10.1016/j.sedgeo.2021.106003

Manzi, V., Roveri, M., Gennari, R., Bertini, A., Biffi, U., Giunta, S., Iaccarino, S.M., Lanci, L., Lugli, S., Negri, A., Riva, A., Rossi, M.E., Taviani, M., 2007. The deep-water counterpart of the Messinian Lower Evaporites in the Apennine foredeep: The Fanantello section (Northern Apennines, Italy). Palaeogeogr. Palaeoclimatol. Palaeoecol. 251, 470–499. https://doi.org/10.1016/j.palaeo.2007.04.012

Martí, J., Mitjavila, J., Roca, E., Aparicio, A., 1992. Cenozoic Magmatism of the Valencia trough (western Mediterranean): relationships between structural evolution and volcanism. Tectonophysics 203, 145–165.

Martín, J.M., Braga, J.C., Betzler, C., 2001. The Messinian Guadalhorce corridor: the last northern, Atlantic-

Mediterranean gateway. Terra Nova 13, 418–424. https://doi.org/10.1046/j.1365-3121.2001.00376.x

Martínez-García, P., Comas, M., Lonergan, L., Watts, A.B., 2017. From Extension to Shortening: Tectonic Inversion Distributed in Time and Space in the Alboran Sea, Western Mediterranean: Tectonic Inversion in the Alboran Sea. Tectonics 36, 2777–2805. https://doi.org/10.1002/2017TC004489

Martínez-Martínez, J.M., Azañón, J.M., 1997. Mode of extensional tectonics in the southeastern Betics (SE Spain): Implications for the tectonic evolution of the peri-Alborán orogenic system. Tectonics 16, 205–225. https://doi.org/10.1029/97TC00157

Marzocchi, A., Flecker, R., Baak, C.G.C. van, Lunt, D.J., Krijgsman, W., 2016. Mediterranean outflow pump: An alternative mechanism for the Lago-mare and the end of the Messinian Salinity Crisis. Geology 44, 523–526. https://doi.org/10.1130/G37646.1

Mas, G., Fornós, J.J., 2020. The Messinian Salinity Crisis in Mallorca: New insights for a Western Mediterranean stratigraphic scenario. Mar. Pet. Geol. 122, 104656. https://doi.org/10.1016/j.marpetgeo.2020.104656

Mas, G., Fornós, J.J., 2013. Late Messinian Lago-Mare deposits of the island of Mallorca (Western Mediterranean). Implications on the MSC events.

Mas, G., Fornós, J.J., 2011. The Messinian Salinity Crisis Record in the Palma Basin (Mallorca, Balearic Islands , Western Mediterranean).

Mas, G., Maillard, A., Alcover, J.A., Fornós, J.J., Bover, P., Torres-Roig, E., 2018. Terrestrial colonization of the Balearic Islands: New evidence for the Mediterranean sea-level drawdown during the Messinian Salinity Crisis. Geology 46, 527–530. https://doi.org/10.1130/G40260.1

Mauffret, A., 1977. Etude géodynamique de la marge des îles Baléares.

Mauffret, A., Frizon de Lamotte, D., Lallemant, S., Gorini, C., Maillard, A., 2004. E-W opening of the Algerian Basin (Western Mediterranean). Terra Nova 16, 257–264. https://doi.org/10.1111/j.1365-3121.2004.00559.x

Mauffret, A., Pascal, G., Maillard, A., Gorini, C., 1995. Tectonics and deep structure of the north-western Mediterranean Basin. Mar. Pet. Geol. 12, 645–666. https://doi.org/10.1016/0264-8172(95)98090-R

Mayer-Eymar, K., 1867. Catalogue systématique et descriptif des fossiles des terrains tertiaires qui se trouvent du Musée fédéral de Zürich. Zürich.

McCaffrey, M.A., Lazar, B., Holland, H.D., 1987. The evaporation path of seawater and the coprecipitation of Br (super -) and K (super +) with halite. J. Sediment. Res. 57, 928–937. https://doi.org/10.1306/212F8CAB-2B24-11D7-8648000102C1865D

McKenzie, D., 1978. Some remarks on the development of sedimentary basins. Earth Planet. Sci. Lett. 40, 25–32. https://doi.org/10.1016/0012-821X(78)90071-7

McKenzie, D.P., 1967. Some remarks on heat flow and gravity anomalies. J. Geophys. Res. 72, 6261–6273. https://doi.org/10.1029/jz072i024p06261

Medaouri, M., Déverchère, J., Graindorge, D., Bracene, R., Badji, R., Ouabadi, A., Yelles-Chaouche, K., Bendiab, F., 2014. The transition from Alboran to Algerian basins (Western Mediterranean Sea): Chronostratigraphy, deep crustal structure and tectonic evolution at the rear of a narrow slab rollback system. J. Geodyn. 77, 186–205. https://doi.org/10.1016/j.jog.2014.01.003

Meijer, P., 2021. (Paleo)oceanography of semi-enclosed seas with a focus on the Mediterranean region; Insights from basic theory. Earth-Sci. Rev. 221, 103810. https://doi.org/10.1016/j.earscirev.2021.103810

Meijer, P., 2006. A box model of the blocked-outflow scenario for the Messinian Salinity Crisis. Earth Planet. Sci. Lett. 248, 486–494. https://doi.org/10.1016/j.epsl.2006.06.013

Meijer, P, Krijgsman, W., 2005. A quantitative analysis of the desiccation and re-filling of the Mediterranean during the Messinian Salinity Crisis. Earth Planet. Sci. Lett. 240, 510–520. https://doi.org/10.1016/j.epsl.2005.09.029

Meijer, P., 2012. Hydraulic theory of sea straits applied to the onset of the Messinian Salinity Crisis. Mar. Geol. 326–328, 131–139. https://doi.org/10.1016/j.margeo.2012.09.001

Meilijson, A., Hilgen, F., Sepúlveda, J., Steinberg, J., Fairbank, V., Flecker, R., Waldmann, N.D., Spaulding, S.A., Bialik, O.M., Boudinot, F.G., Illner, P., Makovsky, Y., 2019. Chronology with a pinch of salt: Integrated stratigraphy of Messinian evaporites in the deep Eastern Mediterranean reveals long-lasting halite deposition during Atlantic connectivity. Earth-Sci. Rev. 194, 374–398. https://doi.org/10.1016/j.earscirev.2019.05.011

Meilijson, A., Liu, J., Makovsky, Y., 2022. In and Out of the Salt: How to Overcome Stratigraphic Uncertainty in Evaporitic Systems? A Case Study from the MSC in the Deep Levant Basin. pp. 213–216. https://doi.org/10.1007/978-3-030-72547-1_47

Meilijson, A., Steinberg, J., Hilgen, F., Bialik, O.M., Waldmann, N.D., Makovsky, Y., 2018. Deep-basin evidence resolves a 50-year-old debate and

demonstrates synchronous onset of Messinian evaporite deposition in a non-desiccated Mediterranean. Geology 46, 243–246. https://doi.org/10.1130/G39868.1

Micallef, A., Camerlenghi, A., Garcia-Castellanos, D., Cunarro Otero, D., Gutscher, M.A., Barreca, G., Spatola, D., Facchin, L., Geletti, R., Krastel, S., Gross, F., Urlaub, M., 2018a. Evidence of the Zanclean megaflood in the eastern Mediterranean Basin. Sci. Rep. 8, 1–8. https://doi.org/10.1038/s41598-018-19446-3

Micallef, A., Camerlenghi, A., Georgiopoulou, A., Garcia-Castellanos, D., Gutscher, M.A., Lo Iacono, C., Huvenne, V.A.I., Mountjoy, J.J., Paull, C.K., Le Bas, T., Spatola, D., Facchin, L., Accettella, D., 2018b. Geomorphic evolution of the Malta Escarpment and implications for the Messinian evaporative drawdown in the eastern Mediterranean Sea. Geomorphology 327, 264–283. https://doi.org/10.1016/j.geomorph.2018.11.012

Miller, K.G., Kominz, M.A., Browning, J.V., Wright, J.D., Mountain, G.S., Katz, M.E., Sugarman, P.J., Cramer, B.S., Christie-Blick, N., Pekar, S.F., 2005. The Phanerozoic Record of Global Sea-Level Change. Science 310, 1293–1298.

Modestou, S., Simon, D., Gutjahr, M., Marzocchi, A., Kouwenhoven, T.J., Ellam, R.M., Flecker, R., 2017. Precessional variability of 87Sr/86Sr in the late Miocene Sorbas Basin: An interdisciplinary study of drivers of interbasin exchange. Paleoceanography 32, 531–552. https://doi.org/10.1002/2016PA003061

Montadert, L., Letouzey, J., Mauffret, A., 1978. Messinian Event: Seismic Evidence. Initial Rep. Deep Sea Drill. Proj. 42, 1037–1050. https://doi.org/10.2973/dsdp.proc.42-1.154.1978

Mottershead, D.N., DUANE, W., Inkpen, R., J.S.Wright, 2005. Subaerial karstic erosion of small scale saltrock terrains, Cardona, Spain.

Myers, D.M., Bonython, C.W., 1958. The theory of recovering salt from sea-water bysolar evaporation. J. Appl. Chem. 207–219.

Natalicchio, M., Dela Pierre, F., Lugli, S., Lowenstein, T.K., Feiner, S.J., Ferrando, S., Manzi, V., Roveri, M., Clari, P., 2014. Did late miocene (Messinian) gypsum precipitate from evaporated marine brines?

Insights from the piedmont basin (Italy). Geology 42, 179–182. https://doi.org/10.1130/G34986.1

Natalicchio, M., Pellegrino, L., Clari, P., Pastero, L., Dela Pierre, F., 2021. Gypsum lithofacies and stratigraphic architecture of a Messinian marginal basin (Piedmont Basin, NW Italy). Sediment. Geol. 425, 106009. https://doi.org/10.1016/j.sedgeo.2021.106009

Negredo, A., Fernàndez, M., Torné, M., Doglioni, C., 1999. Numerical modeling of simultaneous extension and compression: The Valencia trough (western Mediterranean). Tectonics 18, 361–374. https://doi.org/10.1029/1998TC900026

Negro, F., Agard, P., Goffé, B., Saddiqi, O., 2007. Tectonic and metamorphic evolution of the Temsamane units, External Rif (northern Morocco): implications for the evolution of the Rif and the Betic–Rif arc. J. Geol. Soc. 164, 829–842. https://doi.org/10.1144/0016-76492006-112

Netzeband, G.L., Hübscher, C.P., Gajewski, D., 2006. The structural evolution of the Messinian evaporites in the Levantine Basin. Mar. Geol. 230, 249–273. https://doi.org/10.1016/j.margeo.2006.05.004

Norman, S.E., Chase, C.G., 1986. Uplift of the shores of the western mediterranean due to messinian desiccation and flexural isostasy. Nature 322, 450–451. https://doi.org/10.1038/322450a0

Ochoa, D., Sierro, F.J., Lofi, J., Maillard, A., Flores, J.A., Suárez, M., 2015a. Synchronous onset of the Messinian evaporite precipitation: First Mediterranean offshore evidence. Earth Planet. Sci. Lett. 427, 112–124. https://doi.org/10.1016/j.epsl.2015.06.059

Ochoa Lozano, D.P., 2016. Astrobiochronological Constraints on Margin to deep basin correlations across the Balearic Promontory and the Valencia Basin. Universidad de Salamanca, Spain.

Ogniben, L., 1957. Secondary Gypsum of the Sulphur Series, Sicily, and the So-called Integration. SEPM J. Sediment. Res. Vol. 27. https://doi.org/10.1306/74D7065F-2B21-11D7-8648000102C1865D

Orti Cabo, F., Pueyo Mur, J.J., Geisler-Cussey, D., Dulau, N., 1984. Evaporitic sedimentation in the coastal salinas of Santa Pola, Alicante, Spain.

Ott d'Estevou, P., Montenat, C., 1990. Le bassin de Sorbas-Tabernas, in: Les Bassins Neogenes Du Domaine Betique Oriental (Espagne). pp. 101–128.

Ouillon, R., Lensky, N.G., Lyakhovsky, V., Arnon, A., Meiburg, E., 2019. Halite precipitation from double-diffusive salt fingers in the Dead Sea: Numerical simulations. Water Resour. Res. 2019WR024818-2019WR024818. https://doi.org/10.1029/2019WR024818

Özsoy, E., Latif, M.A., Sur, H.I., Goryachkin, Y., 1996. A review of the exchange flow regime and mixing in the

Bosphorus Strait. Bull.-Inst. Oceanogr. MONACO-NUMERO Spec. 187–204.

Ozturk, M., Altas, F., 2021. The meteorological, hydrological and tidal components of Bosphorus flow. Reg. Stud. Mar. Sci. 48, 102060. https://doi.org/10.1016/j.rsma.2021.102060

Padon, O., Ashkenazy, Y., 2018. Non-hydrostatic effects in the Dead Sea. J. Mar. Syst. 187, 36–51. https://doi.org/10.1016/j.jmarsys.2018.06.007

Pagnier, H., 1976. Depth of deposition of Messinian selenitic gypsum in the Basin of Sorbas (SE Spain). Mem Soc Geol It 16 363-367 16, 363–367.

Palcu, D. V., Golovina, L. A., Vernyhorova, Y. V., Popov, S. V., & Krijgsman, W. (2017). Middle Miocene paleoenvironmental crises in Central Eurasia caused by changes in marine gateway configuration. *Global and Planetary Change*, *158*(September), 57–71. https://doi.org/10.1016/j.gloplacha.2017.09.013

Palcu, D.V., Patina, I.S., Șandric, I., Lazarev, S., Vasiliev, I., Stoica, M., Krijgsman, W., 2021. Late Miocene megalake regressions in Eurasia. Sci. Rep. 11, 11471. https://doi.org/10.1038/s41598-021-91001-z

Palomeras, I., Villaseñor, A., Thurner, S., Levander, A., Gallart, J., Harnafi, M., 2017. Lithospheric structure of Iberia and Morocco using finite-frequency Rayleigh wave tomography from earthquakes and seismic ambient noise: RAYLEIGH WAVE TOMOGRAPHY IN WM. Geochem. Geophys. Geosystems 18, 1824–1840. https://doi.org/10.1002/2016GC006657

Parsons, B., Sclater, J.G., 1977. An analysis of the variation of ocean floor bathymetry and heat flow with age. J. Geophys. Res. 82, 803–827. https://doi.org/10.1029/jb082i005p00803

Pellen, R., Aslanian, D., Rabineau, M., Suc, J.P., Gorini, C., Leroux, E., Blanpied, C., Silenziario, C., Popescu, S.M., Rubino, J.L., 2019a. The Messinian Ebro River incision. Glob. Planet. Change 181, 102988–102988. https://doi.org/10.1016/j.gloplacha.2019.102988

Pérez-Gussinyé, M., Watts, A.B., 2005. The long-term strength of Europe and its implications for plate-forming processes. Nature 436, 381–384. https://doi.org/10.1038/nature03854

Philobbos, E.R., Essa, M.A., Ismail, M.M., 2015. Geologic history of the Neogene "Qena Lake" developed during the evolution of the Nile Valley: A sedimentological, mineralogical and geochemical approach. J. Afr. Earth Sci. 101, 194–219. https://doi.org/10.1016/j.jafrearsci.2014.09.006

Pigott, J.D., Abdel-Fattah, M.I., 2014. Seismic stratigraphy of the Messinian Nile Delta coastal plain: Recognition of the fluvial Regressive Systems Tract and its

potential for hydrocarbon exploration. J. Afr. Earth Sci. 95, 9–21. https://doi.org/10.1016/j.jafrearsci.2014.02.003

Pinot, J.-M., López-Jurado, J.L., Riera, M., 2002. The CANALES experiment (1996-1998). Interannual, seasonal, and mesoscale variability of the circulation in the Balearic Channels. Prog. Oceanogr. 55, 335–370. https://doi.org/10.1016/S0079-6611(02)00139-8

Polyak, B.G., Fernàndez, M., Khutorskoy, M.D., Soto, J.I., Basov, I.A., Comas, M.C., Khain, V.Ye., Alonso, B., Agapova, G.V., Mazurova, I.S., Negredo, A., Tochitsky, V.O., de la Linde, J., Bogdanov, N.A., Banda, E., 1996. Heat flow in the Alboran Sea, western Mediterranean. Tectonophysics 263, 191–218. https://doi.org/10.1016/0040-1951(95)00178-6

Raad, F., Lofi, J., Maillard, A., Tzevahirtzian, A., Caruso, A., 2021. The Messinian Salinity Crisis deposits in the Balearic Promontory: An undeformed analog of the MSC Sicilian basins?? Mar. Pet. Geol. 124, 104777. https://doi.org/10.1016/j.marpetgeo.2020.104777

Raad, F., Ebner, R., Heida, H., Meijer, P., Lofi, J., Maillard, A. & Garcia-Castellanos, D. (2022). A song of volumes , surfaces and fluxes : The case study of the Central Mallorca Depression (Balearic Promontory) during the Messinian Salinity Crisis. *Basin Research*, *March*, 1–27. https://doi.org/10.1111/bre.12702

Réhault, J.P., Honthaas, C., Guennoc, P., Bellon, H., Ruffet, G., Cotten, J., Sosson, M., Maury, R.C., 2012. Offshore Oligo-Miocene volcanic fields within the Corsica-Liguria Basin: Magmatic diversity and slab evolution in the western Mediterranean Sea. J. Geodyn. 58, 73–95. https://doi.org/10.1016/j.jog.2012.02.003

Rehault, J.P., Mascle, J., Boillot, G., 1984. Evolution geodynamique de la Mediterrané depuis l'Oligocene. Mem. Della Soc. Geol. Ital. 27, 85–96.

Rico-García, A., 2007. El Neógeno superior marino en Vejer de la Frontera (Cádiz, SO España) y su evolución regresiva. GeoActa 4.

Riding, R., Braga, J.C., Martin, J.M., 1991. Oolite stromatolites and thrombolites, Miocene, Spain: analogues of Recent giant Bahamian examples. Sediment. Geol. 71, 121–127. https://doi.org/10.1016/0037-0738(91)90096-V

RIGW, 1997. Hydrogeological Map of Egypt, Beni Suef Map Sheet (Research Institute for Groundwater, Egypt).

Rios, J.M., 1968. Saline deposits of Spain. Geol. Soc. Am. Spec. Pap. 88, 59–74.

Rizzini, A., Vezzani, F., Cococcetta, V., Milad, G., 1978. Stratigraphy and sedimentation of a Neogene—Quaternary section in the Nile Delta area (A.R.E.). Mar. Geol. 27, 327–348. https://doi.org/10.1016/0025-3227(78)90038-5

Robert F. Schmalz (2), 1969. Deep-Water Evaporite Deposition: A Genetic Model. AAPG Bull. 53. https://doi.org/10.1306/5D25C7FD-16C1-11D7-8645000102C1865D

Robertson, A.H.F., Dixon, J.E., 1984. Introduction: aspects of the geological evolution of the Eastern Mediterranean. Geol. Soc. Lond. Spec. Publ. 17, 1–74. https://doi.org/10.1144/GSL.SP.1984.017.01.02

Roca, E., Guimerà, J., 1992. The Neogene structure of the eastern Iberian margin: Structural constraints on the crustal evolution of the Valencia trough (western Mediterranean). Tectonophysics 203, 203–218. https://doi.org/10.1016/0040-1951(92)90224-T

Rodríguez-Vidal, J., Cáceres, L.M., Finlayson, J.C., Gracia, F.J., Martínez-Aguirre, A., 2004. Neotectonics and shoreline history of the Rock of Gibraltar, southern Iberia. Quat. Sci. Rev. 23, 2017–2029. https://doi.org/10.1016/j.quascirev.2004.02.008

Rosell, L., Orti, F., Kasprzyk, A., Playa, E., Peryt, T.M., 1998. Strontium geochemistry of Miocene primary gypsum; Messinian of southeastern Spain and Sicily and Badenian of Poland. J. Sediment. Res. 68, 63–79. https://doi.org/10.2110/jsr.68.63

Rosenbaum, G., Lister, G.S., Duboz, C., 2002. Reconstruction of the tectonic evolution of the western Mediterranean since the Oligocene. J. Virtual Explor. 8. https://doi.org/10.3809/jvirtex.2002.00053

Rouchy, J.M., Caruso, A., 2006. The Messinian salinity crisis in the Mediterranean basin: A reassessment of the data and an integrated scenario. Sediment. Geol. 188–189, 35–67. https://doi.org/10.1016/j.sedgeo.2006.02.005

Rouchy, J.-M., Saint Martin, J.-P., 1992. Late Miocene events in the Mediterranean as recorded by carbonate-evaporite relations. Geology 20, 629–632. https://doi.org/10.1130/0091-7613(1992)

Roveri, Marco, Flecker, R., Krijgsman, W., Lofi, J., Lugli, S., Manzi, V., Sierro, F.J., Bertini, A., Camerlenghi, A., De Lange, G., Govers, R., Hilgen, F.J., Hübscher, C., Meijer, P.T., Stoica, M., 2014. The Messinian Salinity Crisis: Past and future of a great challenge for marine sciences. Mar. Geol. 352, 25–58. https://doi.org/10.1016/j.margeo.2014.02.002

Roveri, M., Gennari, R., Lugli, S., Manzi, V., 2009. The Terminal Carbonate Complex: the record of sea-level changes during the Messinian salinity crisis. GeoActa 8, 63–77.

Roveri, M., Gennari, R., Lugli, S., Manzi, V., Minelli, N., Reghizzi, M., Riva, A., Rossi, M.E., Schreiber, B.C., 2016. The Messinian salinity crisis: open problems and possible implications for Mediterranean petroleum systems. Pet. Geosci. 22, 283–290. https://doi.org/10.1144/petgeo2015-089

Roveri, M., Lugli, S., Manzi, V., Schreiber, B.C., 2008. The Messinian Sicilian stratigraphy revisited: new insights for the Messinian salinity crisis. Terra Nova 20, 483–488.

Roveri, M., Manzi, V., Bergamasco, A., Falcieri, F.M., Gennari, R., Lugli, S., Schreiber, B.C., 2014. Dense shelf water cascading and Messinian Canyons: A new scenario for the Mediterranean salinity crisis. Am. J. Sci. 314, 751–784. https://doi.org/10.2475/05.2014.03

Roveri, M., Manzi, V., Lugli, S., Schreiber, B., Caruso, A., Rouchy, J.-M., Iaccarino, S., Gennari, R., Vitale, F., Lucchi, F., 2006. Clastic vs. primary precipitated evaporites in the Messinian Sicilian basins. Ateneo Parm. Acta Nat. Organo Della Soc. Med. E Sci. Nat. Parma 42, 125–199.

Ryan, W.B., 1978. Messinian badlands on the southeastern margin of the Mediterranean Sea. Mar. Geol. 27, 349–363.

Ryan, W.B.F., 2011. Geodynamic responses to a two-step model of the Messinian salinity crisis. Bull. Soc. Geol. Fr. 182, 73–78. https://doi.org/10.2113/gssgfbull.182.2.73

Ryan, W.B.F., 2009. Decoding the mediterranean salinity crisis. Sedimentology 56, 95–136. https://doi.org/10.1111/j.1365-3091.2008.01031.x

Ryan, W.B.F., 2008. Modeling the magnitude and timing of evaporative drawdown during the Messinian salinity crisis. Stratigraphy 5, 227–243.

Ryan, W.B.F., 1976. Quantitative evaluation of the depth of the western Mediterranean before, during and after the Late Miocene salinity crisis. Sedimentology 23, 791–813. https://doi.org/10.1111/j.1365-3091.1976.tb00109.x

Ryan, W.B.F., 1973. Geodynamic implications of the Messinian crisis of salinity - Google Scholar. Messin. Events Mediterr.

Ryan, W.B.F., Cita, M.B., 1978. The nature and distribution of Messinian erosional surfaces — Indicators of a several-kilometer-deep Mediterranean in the Miocene. Mar. Geol. 27, 193–230. https://doi.org/10.1016/0025-3227(78)90032-4

Sàbat, F., Gelabert, B., Rodríguez-Perea, A., Giménez, J., 2011. Geological structure and evolution of Majorca: Implications for the origin of the Western Mediterranean. Tectonophysics 510, 217–238. https://doi.org/10.1016/j.tecto.2011.07.005

Sàbat, F., Roca, E., Muñoz, J.A., Vergés, J., Santanach, P., Sans, M., Massana, E., Estévez, A., Santisteban, C., 1997. Role of extension and compression in the evolution of the eastern margin of Iberia: the ESCI-Valencia Trough seismic profile. Rev. Soc. Geológica Esp. 8, 431–448.

Sagy, Y., Gvirtzman, Z., Reshef, M., Makovsky, Y., 2015. The enigma of the Jonah high in the middle of the Levant basin and its significance to the history of rifting. Tectonophysics 665, 186–198. https://doi.org/10.1016/j.tecto.2015.09.037

Said, R., 1981. The Geological Evolution of the River Nile. Springer-Verl. Berl.

Sallam, E., Issawi, B., Osman, R., Ruban, D., 2018. Deposition in a changing paleogulf: evidence from the Pliocene–Quaternary sedimentary succession of the Nile Delta, Egypt. Arab. J. Geosci. 11. https://doi.org/10.1007/s12517-018-3919-2

Sammartino, M., Aronica, S., Santoleri, R., Buongiorno Nardelli, B., 2022. Retrieving Mediterranean Sea Surface Salinity Distribution and Interannual Trends from Multi-Sensor Satellite and In Situ Data. Remote Sens. 14, 2502. https://doi.org/10.3390/rs14102502

Samperi, L., Giorgio, M., Kamaldeen, O.O., Alba, Z., Nicolas, W., Sabrina, N., Pauselli, C., Francesco, B., 2020. Estimation of the physical, petrophysical and mineralogical properties of Messinian salt rocks, Sicily: Implications for multidisciplinary applications. Mar. Pet. Geol. 112, 104032–104032. https://doi.org/10.1016/j.marpetgeo.2019.104032

Sandford, K.S., Arkell, W.J., 1929. Paleolithic man and the Nile-Faiyum divide.

Sanna, L., De Waele, J., Calaforra, J.M., Forti, P., 2015. Long-term erosion rate measurements in gypsum caves of Sorbas (SE Spain) by the Micro-Erosion Meter method. Geomorphology 228, 213–225. https://doi.org/10.1016/j.geomorph.2014.09.009

Schettino, A., Turco, E., 2006. Plate kinematics of the Western Mediterranean region during the Oligocene and Early Miocene. Geophys. J. Int. 166, 1398–1423. https://doi.org/10.1111/j.1365-246X.2006.02997.x

Schreiber, B.C., Hsü, K.J., 1980. Evaporites. Dev. Pet. Geol., (Ed G.D. Hobson), 2 87–138.

Schulze, K., Hunger, M., Döll, P., 2005. Simulating river flow velocity on global scale. Adv. Geosci. 5, 133–136.

Sclater, J.G., Christie, P.A.F., 1980. Continental stretching: an explanation of the post-mid-cretaceous subsidence of the central north sea basin. J. Geophys. Res. 85, 3711–3739.

Segev, A., Rybakov, M., Lyakhovsky, V., Hofstetter, A., Tibor, G., Goldshmidt, V., Ben Avraham, Z., 2006. The structure, isostasy and gravity field of the Levant continental margin and the southeast Mediterranean area. Tectonophysics 425, 137–157. https://doi.org/10.1016/j.tecto.2006.07.010

Selli, R., 1960. The Mayer-Eymar Messinian 1867 proposal for a neostratotype, in: Report of the Twenty-First Session Norden. International Geological Congress, pp. 311–333.

Serpelloni, E., C. Faccenna, G. Spada, D. Dong and S. D. P. Williams (2013), Vertical GPS ground motion rates in the Euro-Mediterranean region: New evidence of velocity gradients at different spatial scales along the Nubia-Eurasia plate boundary, J. Geophys. Res. Solid Earth, 118, 6003–6024, doi:10.1002/2013JB010102.

Shields, G.A., Mills, B.J.W., 2021. Evaporite weathering and deposition as a long-term climate forcing mechanism. Geology 49, 299–303. https://doi.org/10.1130/G48146.1

Sierro, F., Flores, J.A., Francés, G., Vazquez, A., Utrilla, R., Zamarreño, I., Erlenkeuser, H., Bárcena, M.Á., 2003. Orbitally-controlled oscillations in planktic communities and cyclic changes in western Mediterranean hydrography during the Messinian. Palaeogeogr. Palaeoclimatol. Palaeoecol. 190, 289–316. https://doi.org/10.1016/S0031-0182(02)00611-9

Sierro, F.J., Flores, J.A., Zamarreño, I., Vázquez, A., Utrilla, R., Francés, G., Hilgen, F.J., Krijgsman, W., 1999. Messinian pre-evaporite sapropels and precession-induced oscillations in western Mediterranean climate. Mar. Geol. 153, 137–146. https://doi.org/10.1016/S0025-3227(98)00085-1

Simon, D., Marzocchi, A., Flecker, R., Lunt, D.J., Hilgen, F.J., Meijer, P.T., 2017. Quantifying the Mediterranean freshwater budget throughout the late Miocene: New implications for sapropel formation and the Messinian Salinity Crisis. Earth Planet. Sci. Lett. 472. https://doi.org/10.1016/j.epsl.2017.05.013

Simon, D., Meijer, P.T., 2017. Salinity stratification of the Mediterranean Sea during the Messinian crisis: A first model analysis. Earth Planet. Sci. Lett. 479. https://doi.org/10.1016/j.epsl.2017.09.045

Sirota, I., Enzel, Y., Lensky, N.G., 2018. Halite focusing and amplification of salt layer thickness: From the Dead Sea to deep hypersaline basins. Geology 46, 851–854. https://doi.org/10.1130/G45339.1

Soria, J.M., Martín, J., Corbí, H., Dinarès-Turell, J., Lancis, C., Tent-Manclús, J., Yébenes, A., 2008. The Bajo Segura Basin (SE Spain): implications for the Messinian Salinity Crisis in the Mediterranean margins. Stratigraphy 5, 259–265.

Spakman, W., Chertova, M.V., Van Den Berg, A., Van Hinsbergen, D.J.J., 2018. Puzzling features of western Mediterranean tectonics explained by slab dragging. Nat. Geosci. 11. https://doi.org/10.1038/s41561-018-0066-z

Speranza, F., Villa, I.M., Sagnotti, L., Florindo, F., Cosentino, D., Cipollari, P., Mattei, M., 2002. Age of the Corsica-Sardinia rotation and Liguro-Provençal Basin spreading: New paleomagnetic and Ar/Ar evidence. Tectonophysics 347, 231–251. https://doi.org/10.1016/S0040-1951(02)00031-8

Steckler, M.S., ten Brink, U.S., 1986. Lithospheric strength variations as a control on new plate boundaries: examples from the northern Red Sea region. Earth Planet. Sci. Lett. 79, 120–132. https://doi.org/10.1016/0012-821X(86)90045-2

Stein, C.A., Stein, S., 1992. A model for the global variation in oceanic depth and heat flow with lithospheric age. Nature 359, 123–129. https://doi.org/10.1038/359123a0

Steinberg, J., Gvirtzman, Z., Garfunkel, Z., 2014. Flexural response of a continental margin to sedimentary loading and lithospheric rupturing: The mountain ridge between the Levant Basin and the Dead Sea Transform. Tectonics 33, 166–186. https://doi.org/10.1002/2013TC003330

Sternai, P., Caricchi, L., Garcia-Castellanos, D., Jolivet, L., Sheldrake, T.E., Castelltort, S., 2017. Magmatic pulse driven by sea-level changes associated with the Messinian salinity crisis. Nat. Geosci. 10, 783–787. https://doi.org/10.1038/ngeo3032

Stoica, M., Krijgsman, W., Fortuin, A., Gliozzi, E., 2016. Paratethyan ostracods in the Spanish Lago-Mare: More evidence for interbasinal exchange at high Mediterranean sea level. Palaeogeogr. Palaeoclimatol. Palaeoecol. 441, 854–870. https://doi.org/10.1016/j.palaeo.2015.10.034

Tateo, F., Sabbadini, R., Morandi, N., 2000. Palygorskite and sepiolite occurrence in Pliocene lake deposits along the River Nile: evidence of an arid climate. J. Afr. Earth Sci. 31, 633–645. https://doi.org/10.1016/S0899-5362(00)80011-1

ten Brink, U.S., Schoenberg, N., Kovach, R.L., Ben-Avraham, Z., 1990. Uplift and a possible moho offset across the Dead Sea transform. Tectonophysics 180, 71–85. https://doi.org/10.1016/0040-1951(90)90373-G

Tesauro, M., Kaban, M.K., Cloetingh, S.A.P.L., 2009. How rigid is Europe's lithosphere? Geophys. Res. Lett. 36, 2–7. https://doi.org/10.1029/2009GL039229

Tibor, G., Ben-Avraham, Z., 2005. Late Tertiary paleodepth reconstruction of the Levant margin off Israel. Mar. Geol. 221, 331–347. https://doi.org/10.1016/j.margeo.2005.03.005

Topper, R., Flecker, R., Meijer, P., Wortel, M., 2011. A box model of the Late Miocene Mediterranean Sea: Implications from combined Sr-87/Sr-86 and salinity data. Paleoceanography 26. https://doi.org/10.1029/2010PA002063

Topper, R.P.M., Meijer, P.T., 2013. A modeling perspective on spatial and temporal variations in Messinian evaporite deposits. Mar. Geol. 336, 44–60. https://doi.org/10.1016/j.margeo.2012.11.009

Topper, R.P.M., Meijer, P.T., 2015. The precessional phase lag of Messinian gypsum deposition in Mediterranean marginal basins. Palaeogeogr. Palaeoclimatol. Palaeoecol. 417, 6–16. https://doi.org/10.1016/j.palaeo.2014.10.025

Torné, M., Pascal, G., Buhl, P., Watts, A.B., Mauffret, A., 1992. Crustal and velocity structure of the Valencia trough (western Mediterranean), Part I. A combined refraction/ wide-angle reflection and near-vertical reflection study. Tectonophysics 203, 1–20. https://doi.org/10.1016/0040-1951(92)90212-O

Tortochaux, F., 1968. Occurance and Structure of Evaporites in North Africa. Geol. Soc. Am. Spec. Pap. 88, 108–138.

Urgeles, R., Camerlenghi, A., Garcia-Castellanos, D., De Mol, B., Garcés, M., Vergés, J., Haslam, I., Hardman, M., 2011. New constraints on the Messinian sealevel drawdown from 3D seismic data of the Ebro Margin, western Mediterranean. Basin Res. 23, 123–145. https://doi.org/10.1111/j.1365-2117.2010.00477.x

Vai, G.B., Lucchi, F.R., 1977. Algal crusts, autochthonous and clastic gypsum in a cannibalistic evaporite basin: a case history from the Messinian of Northern Apennines. Sedimentology 24, 211–244. https://doi.org/10.1111/j.1365-3091.1977.tb00255.x

van Baak, C.G.C., Krijgsman, W., Magyar, I., Sztanó, O., Golovina, L.A., Grothe, A., Hoyle, T.M., Mandic, O., Patina, I.S., Popov, S.V., Radionova, E.P., Stoica, M., Vasiliev, I., 2017. Paratethys response to the Messinian salinity crisis. Earth-Sci. Rev. 172, 193–223. https://doi.org/10.1016/j.earscirev.2017.07.015

Van Ceuvering, J.A., Berggren, W.A., Drake, R.E., Aguirre, E., Curtis, G.H., 1976. The terminal Miocene event. Mar. Micropaleontol. 1, 263–286.

van der Beek, P.A., Cloetingh, S., 1992. Lithospheric flexure and the tectonic evolution of the Betic Cordilleras (SE Spain). Tectonophysics 203, 325–344. https://doi.org/10.1016/0040-1951(92)90230-4

Van Hinsbergen, D.J.J., Vissers, R.L.M., Spakman, W., 2014. Origin and consequences of western Mediterranean subduction, rollback, and slab segmentation. Tectonics 33, 393–419. https://doi.org/10.1002/2013TC003349

Vargas-Yáñez, M., Juza, M., Balbín, R., Velez-Belchí, P., García-Martínez, M.C., Moya, F., Hernández-Guerra, A., 2020. Climatological Hydrographic Properties and Water Mass Transports in the Balearic Channels From Repeated Observations Over 1996–2019. Front. Mar. Sci. 7.

Vasiliev, I., Mezger, E.M., Lugli, S., Reichart, G.J., Manzi, V., Roveri, M., 2017. How dry was the Mediterranean during the Messinian salinity crisis? Palaeogeogr. Palaeoclimatol. Palaeoecol. 471, 120–133. https://doi.org/10.1016/j.palaeo.2017.01.032

Vergés, J., Fernàndez, M., 2012. Tethys–Atlantic interaction along the Iberia–Africa plate boundary: The Betic–Rif orogenic system 29.

Vergés, J., Sàbat, F., 1999. Constraints on the Neogene Mediterranean kinematic evolution along a 1000 km transect from Iberia to Africa. Geol. Soc. Lond. Spec. Publ. 156, 63–80. https://doi.org/10.1144/GSL.SP.1999.156.01.05

Villaseñor, A., Chevrot, S., Harnafi, M., Gallart, J., Pazos, A., Serrano, I., Córdoba, D., Pulgar, J.A., Ibarra, P., 2015. Subduction and volcanism in the Iberia–North Africa collision zone from tomographic images of the upper mantle. Tectonophysics 663, 238–249. https://doi.org/10.1016/j.tecto.2015.08.042

Walcott, R.I., 1970. Flexural rigidity, thickness, and viscosity of the lithosphere. J. Geophys. Res. 75, 3941–3954. https://doi.org/10.1029/JB075i020p03941

Warren, J.K., 2010. Evaporites through time: Tectonic, climatic and eustatic controls in marine and nonmarine deposits. Earth-Sci. Rev. 98, 217–268. https://doi.org/10.1016/j.earscirev.2009.11.004

Watts, A.B., 2001. Isostasy and flexure of the lithosphere. Cambridge University Press, Cambridge ; New York.

Watts, A.B., Ryan, W.B.F., 1976. Flexure of the Lithosphere and Continental Margin Basins. Tectonophysics 36, 25–44.

Watts, A.B., Torné, M., 1992a. Subsidence history, crustal structure, and thermal evolution of the Valencia Trough: A young extensional basin in the western Mediterranean. J. Geophys. Res. 97, 20021–20021. https://doi.org/10.1029/92JB00583

Watts, A.B., Torné, M., 1992b. Crustal structure and the mechanical properties of extended continental lithosphere in the Valencia trough (western Mediterranean). J. Geol. Soc. 149, 813–827. https://doi.org/10.1144/gsjgs.149.5.0813

Watts, A.B., Torné, M., Buhl, P., Mauffret, A., Pascal, G., Pinet, B., 1990. Evidence for reflectors in the lower continental crust before rifting in the Valencia trough. Nature 348, 631–635. https://doi.org/10.1038/348631a0

Watts, A.B., Zhong, S.J., Hunter, J., 2013. The Behavior of the Lithosphere on Seismic to Geologic Timescales. Annu. Rev. Earth Planet. Sci. 41, 443–468. https://doi.org/10.1146/annurev-earth-042711-105457

Wees, J.D., Cloetingh, S., 1994. A Finite-Difference Technique to Incorporate Spatial Variations In Rigidity and Planar Faults Into 3-D Models For Lithospheric Flexure. Geophys. J. Int. 117, 179–195. https://doi.org/10.1111/j.1365-246X.1994.tb03311.x

Whittaker, A.C., Boulton, S.J., 2012. Tectonic and climatic controls on knickpoint retreat rates and landscape response times. J. Geophys. Res. Earth Surf. 117, 2011JF002157. https://doi.org/10.1029/2011JF002157

Yelles, A., Domzig, A., Déverchère, J., Bracène, R., Mercier de Lépinay, B., Strzerzynski, P., Bertrand, G., Boudiaf, A., Winter, T., Kherroubi, A., Le Roy, P., Djellit, H., 2009. Plio-Quaternary reactivation of the Neogene margin off NW Algiers, Algeria: The Khayr al Din bank. Tectonophysics 475, 98–116. https://doi.org/10.1016/j.tecto.2008.11.030

Yoshimura, T., Kuroda, J., Lugli, S., Tamenori, Y., Ogawa, N.O., Jiménez-Espejo, F.J., Isaji, Y., Roveri, M., Manzi, V., Kawahata, H., Ohkouchi, N., 2016. An X-ray spectroscopic perspective on Messinian evaporite from Sicily: Sedimentary fabrics, element distributions, and chemical environments of S and Mg. Geochem. Geophys. Geosystems 17, 1383–1400. https://doi.org/10.1002/2015GC006233

Zucker, E., Gvirtzman, Z., Steinberg, J., Enzel, Y., 2020. Salt tectonics in the Eastern Mediterranean Sea: Where a giant delta meets a salt giant. Geology 48, 134–138. https://doi.org/10.1130/G47031.1